A Thesis Submitted for the Degree of EngD at the University of Warwick

Permanent WRAP URL:

http://wrap.warwick.ac.uk/153811

warwick.ac.uk/lib-publications

COMPOSITES OF POLYMERS WITH 2D MATERIALS: BORON NITRIDE NANOSHEETS (BNNS) AND EXFOLIATED GRAPHITE NANOPLATELETS (GNP) BY MELT-MIXING

By Valentina Guerra

Engineer Doctorate (EngD) Dissertation

Sustainable Materials and Manufacturing (SMM CDT)

University of Warwick

WMG

International Institute for Nanocomposites Manufacturing (IINM)

June 2020

ABSTRACT

2D materials (nanomaterials) such as boron nitride nanosheets (BNNS) and exfoliated graphite/graphene nanoplatelets (GNP) are of increasing interest to both academia and industry due to their exceptional mechanical, thermal and electrical (GNP only) properties. Such properties could potentially be transferred to thermoplastic polymers, for the manufacture of functional composites for a variety of applications ranging from automotive to aerospace, electronics and energy. The morphology and geometry (*i.e.* thickness, platelet length, shape and, aspect ratio) of BNNS/GNP along with the surface chemistry, the state of filler dispersion/distribution in the polymer matrix, filler-filler/polymer-filler interfacial interactions and the processing methodology adopted to prepare the composites all affect the final properties. It is generally understood that high aspect ratio BNNS/GNP, strong polymer-filler interactions, and high levels of filler dispersion and distribution in the matrix are required to form a percolated 3D filler network in the matrix, essential to achieving enhanced mechanical, thermal and electrical (GNP) properties.

The inclusion of BNNS and GNP in commercial polyolefin such as polypropylene and high density polyethylene is a non-trivial task. BNNS/GNP tend to agglomerate upon mixing with the polymer matrix, due to the strong particle-particle interactions preferred over the particle-polymer interactions. In addition, the presence of functionalities and/or traces of additives derived from the manufacturing of the BNNS/GNP particles affect the state of distribution and dispersion thereof in the polymer matrix, thus the properties of the final composites (*e.g.* morphology, mechanical and rheological properties, thermal conductivity). Little information is available in the literature on the structure-properties correlation for composites of polymers, particularly polyolefin, with BNNS/GNP prepared by relevant industrial melt-mixing based processing techniques. This limits the application of such composites on industrial scale.

The present thesis focusses on the characterization of different grades of BNNS and GNP as provided by the industrial partner Thomas Swan & Co. Ltd (TS) and their application as functional additives in isotactic polypropylene (PP) and high density polyethylene (HDPE) prepared through extrusion and injection moulding. The complexity and challenges for the manufacturing of functional composites of PP and HDPE with TS BNNS/GNP lay on the morphology and surface chemistry of the filler particles, the mixing efficiency during extrusion, the melt-flow realised during injection moulding, the viscosity and crystallization mechanisms of the polymer matrices.

The chemical and physical characteristics of BNNS and GNP, prepared by high pressure homogenisation (HPH)- a process developed by TS- were determined and the morphology/crystalline structure (Scanning Electron Microscopy (SEM); X-Ray Diffraction (XRD); Raman spectroscopy), surface chemistry (X-Ray photoemission spectroscopy (XPS) and sessile tests) and thermal stability (Thermo-gravimetric analysis (TGA)) of both fillers reported. The pressure applied during HPH, the morphology of the bulk hexagonal boron nitride and graphite fed into the HPH, the solvent and the surfactant exploited for the exfoliation of the bulk materials all govern the final properties of the BNNS/GNP. The grades of fillers examined in this thesis showed a distribution of platelet sizes (from 100 nanometre (nm) up to tens of micrometre (μm)) layered as irregular flakes, with high crystalline structure and low defect concentration in the crystal lattice. The fillers contained functionalities and impurities on the surfaces (mostly derived from the surfactants used during HPH) which imparted hydrophilic characteristics to the particles. All the BNNS and GNP analysed were thermally stable under oxidative conditions up to 300-400°C.

Composites of PP and HDPE with both BNNS and GNP were prepared by 16 mm co-rotating twin-screws extruder followed by injection moulding, over a range of compositions with filler loadings up to 10wt%. The morphology, crystalline structure, rheological and mechanical properties of the as prepared composites were assessed by SEM, XRD, Differential Scanning Calorimetry (DSC), oscillatory rheology and tensile testing. The processing adopted to prepare the composites of PP/HDPE with the BNNS/GNP grades produced composites with different levels of filler particles dispersion and distribution.

The extent of dispersion and distribution of BNNS/GNP in PP appeared to be strongly affected by the mechanism of interactions with the surfactant present in trace amounts on the surfaces of the filler platelets, namely sodium cholate (SC), T and L. It was found that SC and L were more effective at distributing and dispersing BNNS in PP compared with T. On the other hand, SC was more effective at distributing GNP in PP than L. Consequently, an increase in the Young's modulus of PP by up to 20% was obtained when the BNNS with SC and L and, GNP with SC were added to PP. In contrast, a decrease in the Young's modulus of PP of *ca* 20% was observed when the BNNS prepared with T and GNP with L were included to PP.

The lateral dimension of the fillers play a key role in achieving rheological percolation. The BNNS particles with a lateral dimension up to 10 μm facilitated the formation of a 3D particle-particle network. However, no improvement in the thermal conductivity of the polymer was recorded due to the phonon-scattering at the polymer-filler interface, perhaps also caused by

the presence of surfactant on the filler surface and/or by the PP chain entanglements near the BNNS particles.

The BNNS and GNP had a nucleating effect on the PP, manifested by an increase in the crystallization temperature by up to 14°C higher than the T_c of the neat PP. The different grades of BNNS and GNP examined also promoted the crystallization of the β-crystals (polymorph) of PP, particularly at low filler content (≤0.5wt%).

The inclusion of the BNNS and GNP particles did not affect the morphology and crystalline structure of HDPE. A decrease in the Young's modulus of the HDPE of *ca* 20% was observed in presence of the fillers, probably due to the agglomeration of the BNNS/GNP as the HDPE crystallizes rapidly during injection moulding excluding the nanoparticles from the crystalline phase.

In summary, this work confirms the importance of the dual non-trivial technical challenges of promoting polymer-filler interactions and achieving effective dispersion and distribution of the nano-filler throughout the polymer matrix when manufacturing composites by relevant industrial technologies *i.e.* extrusion and injection moulding. The outputs of the present research supported TS to understanding the properties of their BNNS/GNP and the requirements for the optimal inclusion thereof in polymers matrices.

Acknowledgements

A special thank you to my family and friends Caterina Palange, Leonardo Baldassarre, Lorena Amoroso, Azzurra Miraglia and Derya Kaya for supporting me throughout these four years, during difficult times and memorable laughing moments.

TABLE OF CONTENTS

List of Figures

List of Tables

with infinite dimensions, used to calculate the crystallinity was taken as 287 J/g [30]. The results are an average of three measurements per each composition. The error calculated for T_m, T_c amd X_c (%) falls on the first decimal, which is not significant for the present study.

CHAPTER 1: INTRODUCTION

1.1-   Background

Nanomaterials are particles with at least one dimension in the range between 1 and 100 nm, subcategorized as 0D (*e.g.* fullerenes), 1D (*e.g.* carbon nanotubes (CNT), boron nitride nanotubes (BNNT)) and 2D materials (*e.g.* boron nitride nanosheets (BNNS), exfoliated graphite nanoplatelets (GNP), transition metal-dichalcogenides (MoS_2, WS_2, WTe_2)) depending on the shape and dimensions thereof [1-6].

The ultrafine dimensions of nanomaterials translate into high surface areas, resulting in many unique properties, including mechanical strength and thermal resistance. In addition, the highly crystalline structures typical of many nanoparticles ensures exceptional thermal and/or electrical properties [1, 2].

The need for light, functional and sustainable materials guides the research direction for polymer nanocomposites, a class of composites containing a polymeric matrix and a nanomaterial as functional additive (filler). The principle behind the design of polymer nanocomposites is the translation of the exceptional properties of the nanomaterial to the polymer matrix through the optimization of the *interfacial interactions* between the nanomaterial and the polymer in question, thus, generating a route or mechanism through which any external impulse (mechanical, thermal, electrical) can be transferred from the polymer to the nanoparticles. The 'transfer-mechanism' of any external stimuli relies on the intrinsic properties of the nanoparticle, as well as the chemical-physical properties of the host matrix [1-3, 6-9].

Among 2D materials, boron nitride nanosheets (BNNS) and exfoliated graphite/graphene nanoplatelets (GNP) are excellent candidates for manufacturing functional polymer nanocomposites with potential application across a wide range of industries such as automotive, aerospace, energy and electronics. BNNS/GNP have outstanding mechanical properties, thermal stability, thermal conductivity and electrical (GNP only) conductivity, ideal for improving the performance of the final composite (*e.g.* strength, toughness, thermal and electrical conductivity, barrier properties). Furthermore, the in service-life of the composite can be extended, thus reducing waste, reducing the environmental impact of both the manufacturing process and disposal [10-15].

This project explores the properties of BNNS and GNP, produced and provided by the industrial partner Thomas Swan & Co. Ltd (TS). Both have a number of target applications, including as functional fillers for polymers. Both BNNS and GNP are prepared by high pressure homogenisation (HPH), a proprietary technique developed by TS and described in the patent [16]. In HPH, the bulk material, *i.e.* hexagonal boron nitride or graphite, are fed into the homogeniser as a liquid dispersion. The head of the homogeniser imparts high pressures onto the solid particles, which are forced to pass through conduits inclosing the main body of the homogeniser, thus, delaminating the bulk particles of hexagonal boron nitride and graphite to obtain BNNS and GNP, respectively. The morphology of the bulk materials, the solvent/surfactant present in the liquid dispersion, as well as the pressure applied and the timing before harvesting the final product determine the morphology and geometry, crystalline structure and surface chemistry of the BNNS and GNP.

1.2- The research problem, strategy, sustainability and challenges

Thermoplastics are polymers that can be heated above their melting temperature (or glass transition temperature in the case of amorphous polymers) so as they can be shaped and formed as desired. The heating process is reversible and ideally it is possible to setup several heating-cooling cycles without damaging the structure of the polymer. Thermoplastic polymers can be classified as commodities (*e.g.* PE, PP, PVC, PS), technical thermoplastics (*e.g.* PA, PMMA, PPE, PET, PBT) and specialty thermoplastics (*e.g.* PEEK, PEI), used for a variety of applications such as car tailoring, cables, packaging, electronics, aeronautics and aerospace. The drawback of thermoplastics is their relatively low mechanical strength and resistance to creep when re-heated and re-used overtime, thus, lowering their in-service life. Furthermore, thermoplastic polymers are thermal and electrical insulators, which limits their application where high thermal and/or electrical conduction is required (*e.g.* electronics) [17-22].

The addition of BNNS and GNP could overcome some of these limitations related to thermoplastics. The key requirements to exploiting this potential are, filler geometry (platelets size, shape and thickness), filler surface chemistry, the extent of interfacial interactions between filler and polymer and the level of filler dispersion and distribution in the polymer matrix. It is now understood that large platelets of BNNS/GNP (up to tens of micrometres), intimate adhesion with the host polymer, uniform distribution/dispersion of BNNS/GNP in the

matrix- eventually as a percolated 3D network of filler particles- are essential to enhancing mechanical, thermal and electrical (GNP composites only) properties of the final composites. [17-22].

The challenges related to the application of the BNNS and GNP as functional additives in polymers are numerous. BNNS and GNP tend to agglomerate in the polymer matrix due to their high surface energy, typical of materials having high surface-areas, thus hindering homogeneous composites from being manufactured [23]. The surface chemistry as well as the geometrical features of BNNS and GNP depend on the processing adopted to prepare them, thus making each grade of BNNS and GNP unique. The mechanisms of the chemical-physical interactions between BNNS/GNP and the matrix change when using different polymers therefore, each polymer-filler system needs to be studied separately. In addition, the processing method adopted to prepare composites of thermoplastics and BNNS/GNP affect the properties of the final product. The relevant industrial technologies adopted to prepare functional thermoplastic composites are melt-mixing-based such as extrusion and injection moulding, since they are cost-effective, environmental friendly and allow for high throughput. Yet, there is little information available in the literature on the processing-structure-property relationships for composites of BNNS/GNP and thermoplastics prepared by such manufacturing techniques, a further challenge to this research [24-29].

1.3- EngD portfolio and Innovation report: structure

The EngD portfolio is constructed of reports describing the different phases of the EngD project. Table 1 summarises the reports written by the author.

Table 1.1: List of reports as written by the author and submitted for the EngD portfolio.

Report (Submission)	Title
1	Thermal conductivity of 2D nano-structured boron nitride (BN) and its composites with polymers.
2	Thermal conductivity of 2D nano-structured graphene platelets (GNP) composites with thermoplastics and their application in 3D printing.
3	2D Boron Nitride Nanosheets (BNNS) and graphene nanoplatelets (GNP) prepared by High-Pressure Homogenisation: Structure and Morphology.
4	Inclusion of 2D materials: X-BNNS-SC and X-GNP-SC as functional fillers for polypropylene (PP) and high density polyethylene (HDPE) prepared by micro-scale processing.
5	Application of X-BNNS-SC and X-GNP-SC as functional fillers for polypropylene (PP) and high density polyethylene (HDPE) prepared by melt processing.
6	X-BNNS-T and X-GNP-L as functional fillers for polypropylene (PP) prepared by melt mixing.
7	Application of Y-BNNS-L, Y-GNP-L and Z-GNP-T as functional fillers for polypropylene (PP) and high-density polyethylene (HDPE) by melt-mixing

Submission 1-2 are literature reviews of BNNS and GNP properties and their applications as functional filler in polymers, with a particular focus on the thermal conductivity of both BNNS/GNP alone and their composites. At the very beginning of this project the applications of BNNS/GNP composites of interest to TS were focused on thermal conductive devices (*e.g.* electronics). However, it became clear that a full study on the structure and properties of both BNNS and GNP prepared by HPH and their composites with polymers- which had not been done before - was required.

Submission 3 describes the main features of the first grades of BNNS and GNP produced, successively named as X-BNNS-SC and X-GNP-SC, to distinguish the different grades of BNNS and GNP as received by TS.

Submission 4 describes the results on the studies of composites of X-BNNS-SC/X-GNP-SC with isotactic polypropylene (PP) and high density polyethylene (HDPE) prepared by micro-scale processing (laboratory scale extruder and micro-injection moulding).

Submission 5 reports the results on the studies of composites of X-BNNS-SC/X-GNP-SC with PP and HDPE prepared with a parallel twin screw extruder, a 16-mm co-rotating twin screw extruder and micro-injection moulding.

Submission 6-7 report the main findings from studies on composites of PP (model polymer) with alterative grades of BNNS and GNP as provided by TS. A stand-alone study was performed on the electro-rheological properties of composites of HDPE at the University of Huelva (Spain) as part of the International Placement. The experimental is described in report 7.

The nomenclature of the different grades of BNNS/GNP and their composites is presented in Chapter 3.

The Innovation Report (Thesis) gathers and condenses the most relevant results of the project and is structured as follows:

Chapter 2 provides and overview of the technologies adopted to prepare BNNS and GNP and their properties (thermal, electrical, mechanical). The chapter also describes the main techniques exploited to manufacture composites of BNNS/GNP with thermoplastics, with a particular focus on the melt-mixing process and the properties of the BNNS/GNP composites with thermoplastics prepared by such techniques.

Chapter 3 reports the materials used in this project, *i.e.* the polymer matrices, PP and HDPE and the different BNNS and GNP grades provided by TS, along with the nomenclature used throughout the thesis. The chapter also describes the method adopted to prepare composites of BNNS/GNP with PP and HDPE and the techniques exploited for the characterization of the different grades of BNNS/GNP and their composites.

Chapter 4 describes the key properties of BNNS and GNP grades in terms of morphology, crystalline structure, surface chemistry and thermal stability. The chapter also describes the properties of PP and HDPE composites with the different BNNS and GNP grades, specifically, the morphology, crystalline structure, rheological and mechanical properties. An overview of the potential applications of thermoplastic-based composites using TS BNNS/GNP is given.

1.4- Contribution of the thesis: innovation, knowledge and industrial partner

The innovative aspect of the research is the use of unique forms of BNNS and GNP, particularly the former, prepared by the HPH process, as functional additives for polymers. This thesis and the associate journal papers are the first to be published on this topic. The ultimate target of the work is to create functional composites for important applications, including electronics and automotive. Furthermore, the innovative approach adopted throughout, *i.e.* the processing techniques used to manufacture the composites, *i.e.* extrusion and injection moulding, are industrially relevant, over and above the solution mixing approaches preferred by the majority of academic groups.

This Innovation report contributes to the knowledge base in this subject area significantly. The primary value of the present research is the knowledge derived from the characterization of the different grades of BNNS and GNP. Specifically, this thesis proposes mechanisms of correlations between processing, structure and properties of the composites with BNNS/GNP. The limited literature available on BNNS and GNP and their composites with thermoplastics prepared by extrusion and injection moulding (see Chapter 2) highlights the novelty of the work described in this thesis and it contributes to the understanding required for designing new functional and sustainable composite materials based on these two 2D nanomaterials.

The outputs from the research project were considered significant to TS in that it confirmed the importance of the following:

- BNNS/GNP surface chemistry as prepared by HPH, *i.e.* the solvent and surfactant used during the preparation, and the role the surfactant played when the filler was added to the polymer.
- The morphology of the bulk materials and the parameters set during HPH to achieve optimal exfoliation and produce the 2D materials with large platelets (known to a point to be required to achieve excellent composite mechanical and thermal properties).
- Build up the know-how on the properties of TS BNNS and GNP and their application in polymers.
- Identifying the key strengths of TS competitors so TS can better target their products to applications, other product development areas and potential clients.

1.5- Aims and objectives

The aims of the project are to:

I. Investigate the morphology, crystalline structure, surface chemistry and thermal properties of the BNNS and GNP.

II. Prepare composites of BNNS and GNP with thermoplastics, in particular, isotactic polypropylene (PP) and high density polyethylene (HDPE), by industrial relevant processing techniques, *i.e.* extrusion and injection moulding.

III. Investigate the morphology, structure, thermal, rheological and mechanical properties of the composites prepared.

IV. Correlate the structure and morphology of BNNS/GNP with the properties of the composites, *i.e.* structure-property relationships.

V. Propose explanations on the role of BNNS/GNP surface chemistry- *e.g.* surface functionalities and surfactants- on distribution/dispersion in the polymer matrix as well as on the crystalline, rheological and mechanical properties of the composites prepared.

VI. Identify possible applications of composites of BNNS/GNP and polymer for TS.

The objectives of the project are to:

I. Investigate the morphology, crystalline structure, surface chemistry and thermal properties of different grades of BNNS and GNP namely, X-BNNS-SC, X-BNNS-T, Y-BNNS-L, X-GNP-SC, X-GNP-L, Y-GNP-L by Scanning Electron Microscopy (SEM), X-Ray Diffraction (XRD), Raman spectroscopy, X-Ray Photoemission Spectroscopy (XPS), Sessile tests, Thermo-gravimetric analysis (TGA).

II. Measure the thermal stability of the BNNS, GNP, PP and HDPE by TGA to determine the temperature profiles for the manufacturing of composites.

III. Compound composites of PP and HDPE with the X-BNNS-SC and X-GNP-SC at 0-5 wt% using a laboratory scale (twin conical screw) extruder.

IV. Compound composites of PP and HDPE with X-BNNS-SC and X-GNP-SC at 0-10wt% by 16mm co-rotating twin-screw extruder.

V. Compound composites of PP (model polymer) with X-BNNS-T, Y-BNNS-L, X- GNP-L, Y-GNP-L at 0-10wt% using a16mm co-rotating twin-screw extruder.

VI. Prepare specimens for testing and characterization by micro-injection moulding.

VII.   Investigate the morphology, crystalline structure, thermal, rheological and mechanical properties of the as prepared composites by SEM, XRD, Differential Scanning Calorimetry (DSC), Oscillatory rheology, Tensile tests and thermal conductivity.

VIII.   Correlate the morphology and structure of the different grades of BNNS/GNP and processing set-up to the properties of the as prepared composites by XRD, DSC, Oscillatory rheology and Tensile tests.

IX.   Correlate the morphology and structure of the different grades of BNNS/GNP and processing set-up to the polymorphism of PP by XRD and DSC. In particular, determine the nucleating effect of the different grades of BNNS and GNP in PP by DSC.

References

[1] Kim WG, Nair S 2013 *Chem. Eng. Sci.* **104** 908-24.

[2] Huo CX, Yan Z, Song XF, Zeng HB 2015 *Science Bulletin* **60** 1994-2008.

[3] Akinwande D, et al. 2017 Extreme *Mechanics Letters* **13** 42-77.

[4] Loiseau A, Willaime F, Demoncy N, Schramchenko N, Hug G, Colliex C, Pascard H 1998 *Carbon* **36** 743-52.

[5] Zhi C, Bando Y, Tang C, Golberg D 2010 *Mater. Sci. Eng., R* **70** 92-111.

[6] Papageorgiou DG, Kinloch IA, Young RJ 2015 *Carbon* **95** 460-84.

[7] Potts JR, Dreyer DR, Bielawski CW, Ruoff RS 2011 *Polymer* **52** 5-25.

[8] Mosanenzadeh SG, Naguib HE 2016 *Compos. Part B-Eng.* **85** 24-30.

[9] Chow WS, Ishak ZAM 2020 *Express Polymer Letters* **14** 416-35.

[10] Lin Z, McNamara A, Liu Y, Moon K, Wong CP 2014 *Compos. Sci. Technol.* **90** 123-8.

[11] Wang X, Pakdel A, Zhang J, Weng Q, Tianyou Z, Zhi C, Golberg D 2012 *Nanoscale Res. Lett.* 7:662.

[12] Schwierz F. Graphene and beyond: Two-dimensional materials for transistor applications. In: George T, Dutta AK, Islam MS, editors. Micro- and Nanotechnology Sensors, Systems, and Applications Vii 2015.

[13] Kandanur SS, Rafiee MA, Yavari F, Schrameyer M, Yu ZZ, Blanchet TA, Koratkar N 2012 *Carbon* **50** 3178-83.

[14] Naskar AK, Keum JK, Boeman RG 2016 Nat *Nanotechnol.* **11** 1026-30.

[15] Du JH, Cheng HM 2012 *Macromol. Chem. Phys*. **213** 1060-77.

[16] Ladislaus Paul GL, McHale Ronan. 2017;WO 2017/064496 A1:1-11.

[17] Ahn K, Kim K, Kim M, Kim J 2015 *Ceram. Int.* **41** 2187-95.

[18] Zhang X, Shen L, Wu H, Guo S 2013 *Compos. Sci. Technol.* **89** 24-8.

[19] Takahashi S, Imai Y, Kan A, Hotta Y, Ogawa H 2014 J. *Alloys Compd.* **615** 141-5.

[20] Greco A, Timo A, Maffezzoli A 2012 *Materials* **5** 1972-85.

[21] Honaker K, Vautard F, Drzal LT 2017 *Materials Science and Engineering B-Advanced Functional Solid-State Materials* **216** 23-30.

[22] Mayoral B, Harkin-Jones E, Khanam PN, Al Maadeed MA, Ouederni M, Hamilton AR, Sun D 2015 *Rsc Adv* **5** 52395-409.

[23] Rong MZ, Zhang MQ, Ruan WH 2006 *Mater. Sci. Technol.* **22** 787-96.

[24] Quan H, Zhang BQ, Zhao Q, Yuen RKK, Li RKY 2009 *Compos Part A Appl Sci Manuf.* **40** 1506-13.

[25] Liu MF, Papageorgiou DG, Li SH, Lin KL, Kinloch IA, Young RJ 2018 *Compos Part A Appl Sci Manuf.* **110** 84-92.

[26] Mohd Bijarimi NS, Azizan Ramli, Said Nurdin, Waleed Alhadadi, Muhammad Zakir Muzakkar, Jamiluddin Jaafar 2020 *Indones. J. Chem.* **20** 276-81.

[27] Tarawneh MA, Yu LJ, Tarawni MA, Ahmad SH, Al-Banawi O, Batiha MA 2015 *World Journal of Engineering* **12** 437-42.

[28] Araby S, Zaman I, Meng QS, Kawashima N, Michelmore A, Kuan HC, Majewski P, Ma J, Zhang LQ 2013 *Nanotechnology* **24** 1-14.

[29] Sakai T 2013 *Polimery* **58** 847-57.

CHAPTER 2

LITERATURE REVIEW: COMPOSITES OF BORON NITRIDE NANOSHEETS (BNNS) AND EXFOLIATED GRAPHITE NANOPLATELETS (GNP) WITH THERMOPLASTIC POLYMERS PREPARED BY MELT MIXING

2.1- Introduction

Hexagonal boron nitride (h-BN) and graphite are extensively used as additives or precursor of functional fillers for polymers as they can have high thermal conductivity, electrical conductivity (graphite only), structural stability and mechanical properties [1-18]. h-BN is a synthetic material, consisting of equal number of boron (B) and nitrogen (N) atoms and is isoelectronic to graphite. Both h-BN and graphite show layered sp^2-bonded packed sheets arranged in the hexagonal crystal structure. In graphite the valence electrons are conjugated along the basal plane whereas in h-BN the valence electrons are localised around the N atoms, thus imparting to h-BN partial ionic characteristics with electrical insulating properties [2, 19]. The optical properties of h-BN and graphite reflect their structural difference as h-BN is white whereas graphite is black [20-25]. The layers of h-BN are perfectly arranged in the "registry" configuration where each atom of a layer eclipses the atoms of the upper and lower layers, whereas in graphite the layers are arrayed in the Bernal sequence (AB) [26]. Figure 1 shows the difference between h-BN and graphite layer configuration.
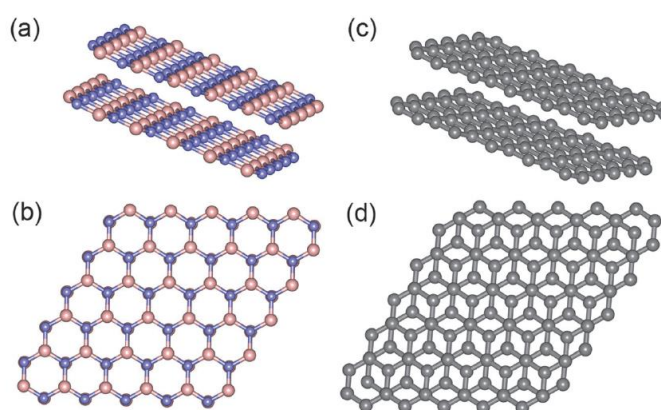
Figure 2.1: h-BN (a, b) with layers in registry-it is not possible to discern one layer from another. Graphite (c, d) with layers disposed according to Bernal crystal structure, where it is possible to distinguish two overlapping layers [26].

h-BN can be exfoliated and shaped in different nanostructures such as 2D BN nanosheets (BNNS)[21, 27-30] and 0D BN spherical nanoparticles (BNNP)[31, 32]. It is also possible to synthetize 1D BN nanotubes (BNNT) [33-37] by air plasma treatment or chemical vapour deposition (CVD).

Likewise, graphite can be exfoliated to form a few layered structure (2-5 layers), multilayered structure (5-10 layers), nanoplatelets (GNP, thickness less than 100nm), up to one single layer, known as graphene, a two-dimensional layer (2D material) having a honeycomb structure made of sp^2-hybridized carbon atoms arranged in regular hexagons, which can be rolled up to obtain 0D fullerenes or 1D nanotubes. The π-conjugation confers extraordinary mechanical, electrical and thermal properties, which have made graphene increasingly attractive in both academia and industry over the last few years. Presently, different procedures have been adopted to prepare graphene, however, it is difficult to obtain a perfect single layer or a few layered structure on an industrial scale. It is more realistic to discuss a GNP structure, which shows similar properties to graphene mono/multilayers [38].

The next section will provide an overview on the technologies adopted to prepare BNNS and GNP.

2.2- Methodologies adopted to prepare BNNS and GNP and their properties

Mechanical exfoliation or cleavage [39] of h-BN was initially used to exfoliate BNNS. The technique relies on the use of an adhesive tape to peel off BN layers from the bulk material, which are successively attached onto a substrate such as Si/SiO_2. The procedure is not viable on an industrial scale due to the strong interactions between BN layers, which makes the peeling step difficult on large scales [40, 41]. The introduction of an additional shear force, *e.g.* ball milling or sonication, in presence of a suitable solvent (N,N-dimethylformamide (DMF), chloroform, 1,2-dichloroethane and methanesulfonic acid (MSA)) or hydroxides (NaOH, KOH) may help break the Van der Waals interactions among the BN layers [26, 28, 41, 42]. The chemical reaction between boric acid (H_3BO_3) and urea ($CO(NH_2)_2$) at 900 °C under a nitrogen flux was adopted to synthesize BNNS [41, 43]. The reaction allows for the thickness to be tuned by adjusting the urea concentration [2]. Template-free solid phase reaction in the presence of $NaBF_4$, NH_4Cl and NaN_3 powders were also exploited to synthesize BNNS. The

reaction occurs in autoclave at 300°C for 20h, followed by further sonication to separate thin flakes of BNNS[44]. The chemical blowing of NH_3BH_3 at high temperatures (up to 1400°C) was proposed as an alternative technique to manufacture BNNS. It is basically a dehydrogenation reaction of the precursor to obtain BNNS, which have been reported to show a few layered structure with lateral dimensions of about 100µm [45, 46]. BNNS was also prepared by the combustion-annealing processes, where a viscous gel consisting of H_3BO_3, CH_4N_2O, NaN_3 and NH_4Cl in water was ignited at 600°C in a muffle furnace, followed by washing with water and ethanol, vacuum drying and annealing at 1000-1400°C under nitrogen [47]. An alternative approach for BNNS synthesis consists of a chemical reaction between B_2O_3, Zn, $N_2H_4 \cdot 2HCl$ in an autoclave at 500°C for 12h before washing with HCl, followed by filtration and dry [48]. In addition, substitution reactions from graphene sheets have been explored for the synthesis of BNNS. The principle of this technique relies on the substitution of an atom (or functional group) in a compound with another atom (group). B_2O_3 and graphene powders react in a graphite crucible in presence of molybdenum oxide (MoO_3) as reaction promoter, at 1650 ^{o}C for 30 mins under a nitrogen flux [49], which lead to the formation of BNNS by substituting the carbon atoms in the graphene precursor with the boron and nitrogen atoms from B_2O_3 and nitrogen flux respectively. BNNS has been also synthesized by chemical vapour deposition (CVD) using different precursors such as BF_3-NH_3, BCl_3-NH_3, borazine ($B_3N_3H_6$), trichloroborazine ($B_3N_3H_6$) or hexachloroborazine ($B_3N_3Cl_6$) [50-58] in presence of a transition metal such as Pt(111), Ru(001), Ni(111), Cu(111), Pd(111), Pd(110), Fe(110), Mo(110), Cr(110), Rh(111)[59-70], at high temperature (1000K). The reaction is basically a dehydrogenisation of the precursor and the morphology of the product depend on the metal used as the interfacial interaction between the precursor and the metal substrate are different [57]. By way of example, the morphology known as nanomesh (one corrugated BNNS layer) is obtained when using Rh(111) [59]. In some cases, the low-pressure CVD was adopted to synthesize BNNS from BH_3-NH_3 in presence of Cu as substrate at 70-90 ^{o}C, where little triangular island of the BNNS grow and merge with each other to form a complete layer on the metal [23, 71]. Electron irradiation was explored by Jin *et al.*[72] and Meyer *et al.* [73] in 2009 to fabricate a single layer of BNNS with the use of intensive electron beam irradiation, a method tested first in a TEM instrument.

Geim and Novoselov isolated a single layer of graphene for the first time in 2004 by mechanical exfoliation, with the aid of a tape to peel off single layers of graphene from bulk

graphite. The peeled layers were then transferred onto a substrate. It is an easy procedure but it does not allow for the production of a large quantity of material [39, 74]. Graphene was also prepared by CVD using Ni or Cu as metal substrates in presence of gaseous hydrocarbons (*e.g.* methane, ethylene, or liquids such as hexane or pentane) at high temperatures (1000K). The degradation of the precursors entailed the production of carbon atoms, which nucleate on the surface of the metal and grow to form a single layer of graphene, before being transferred onto the substrate of interest [75-78]. The liquid phase exfoliation was investigated as an alternative process to prepare GNP. The procedure involves three steps, namely the dispersion of the precursor in a suitable solvent (e.g. N-methyl-pyrrolidone (NMP), dimethyl-formamide (DMF), dimethylsulfoxide (DMSO), tetrahydrofuran (THF), aqueous surfactant suspensions or aqueous mixtures of inorganic salts such as NaCl and $CuCl_2$) by sonication, followed by ultracentrifugation to separate the thin flakes of GNP and purification to remove the solvent. The procedure is neither environmentally nor economically viable due to the use of large quantities of organic solvents and surfactants as well as long sonication times [79-85].

The erosion of a graphite electrode in presence of an electrolyte (e.g. $LiClO_4$) in a liquid solution and under electrical current is known as electrochemical exfoliation, an alternative approach to prepare GNP. It's a one-step procedure, yet, it exploits large amounts of surfactants and ionic liquids and, as a result less eco-friendly [86-90].

Ruoffs' group in 2006 reported the chemical reduction of graphene oxide (GO) as viable route to prepare GNP. The first step of the procedure requires the oxidation of graphite by either Hummers, Staudenmeier or Brodle methods, to produce the intermediary GO, which was further exfoliated by applying mechanical energy before being reduced by thermal annealing in presence of a reducing agent (e.g. hydrazine), crucial step to remove the oxidised groups. The use of hazardous materials such as hydrazine for reduction, along with the high stability of GO during the exfoliation step, make this procedure not viable on industrial scale [91-101]. The thermal exfoliation of acid-intercalated graphite (precursor) was also explored to prepare GNP. The precursor was fast heated at 1050 °C (> 2000 °C/min), which caused the evaporation of the intercalated acid, thus, the expansion and ultimately the exfoliation of graphene layers. This technique is commonly used to prepare high quantities of GNP with a thickness in the order of 10 nm [101-103].

Table 2.1 lists the properties of BNNS and GNP as reported in the literature.

Table 2.1: Chemical structure, thermal, electrical and mechanical properties of BNNS/GNP. The mechanical and thermal properties reported are theoretical values unless specified.

Characterisation	Properties		Ref.
	BNNS	*GNP*	*BNNS/GNP*
Colour	White	Black	[104]/[16]
Bonding	Covalent/ionic	Covalent	[104]//[16]
Electronic structure	5-6 eV band gap	0 eV band gap	[104]/[16]
Raman	E_{2g} (1360 cm^{-1})	D (~1350 cm^{-1}) G (~1580 cm^{-1}) D′(~1620 cm^{-1}) G′/2D (~2700 cm^{-1}) I_G/I_G < 2	[23, 105, 106]/[38, 107-109]
IR	B-N-B (bending, 800-830 cm^{-1}) B-N (stretching, 1370-1378 cm^{-1})	C=C (~1600 cm^{-1}) C=O (~1700 cm^{-1}) COOH (~3400 cm^{-1})	[110-112]/[113, 114]
UV	Sharp peak at 203nm	-	[23]
XPS	B*-N (190eV) B-OH (192.5 eV) B-N* (397.5 eV) N-H (400eV)	C=C (284.2 eV) C-C/C-H (284.8 eV) C-O (286 eV) C=O (287 eV) O=C-O (288.7 eV) π-π* (289.9 eV)	[23, 115, 116]/[117, 118]
XRD	(002) at 2θ=26°; lattice parameters: a=0.250nm, c=0.666nm; interlayer spacing:0.333nm	(002) at 2θ=26°; lattice parameters: a=0.250nm, c=0.666nm; interlayer spacing:0.333nm	[105, 110, 115]/[112, 117]
Mechanical properties	Elastic Modulus: 220-510 N/m^2	Elastic Modulus: 1-1.1 TPa	[104]/[16, 119]
Thermal conductivity @ RT	Up to 2000 W/mL 300-360 W/mK (experimental)	Up to 8000 W/mK	[104, 120]/[121]
Thermal stability	>600°C	>400ºC	[110]/[118]

At the present, BNNS and GNP cannot replace reinforcements such as carbon fibres (CF) to improve the performance of the final composites, particularly for mechanical properties. Indeed, it has been reported that CF can increase the polymer stiffness and strength up to one order of magnitude compared to the neat matrix, which has not currently achieved by admixing BNNS/GNP to thermoplastics. Yet, CF are expensive, and the processing used to prepare composites with polymers is less versatile than the processing used to prepare composites with BNNS/GNP, in terms of processing configuration (extrusion, fibre/polymer impregnation, cooling, shape/sizing of the final composites). Therefore, the study of composites of polymers with BNNS and GNP has intensified in the recent years since the addition of BNNS/GNP was proven to enhance the mechanical, electrical (GNP), thermal and barrier properties of the polymer matrix. Such composites could be exploited for a variety of industrial applications ranging from, automotive to aerospace, electronics and energy (*e.g.* capacitors, solar cells). Yet, there is still poor information about composites of GNP/ BNNS with thermoplastic polymers, which limits their uptake in the market. The next section is an overview on the processing adopted to manufacture composites of thermoplastics and BNNS/GNP as reported in the literature, with a particular focus on the properties of the thermoplastic composites obtained by melt mixing [119, 122-143].

2.3- Processing of composites of thermoplastic polymers with BNNS and GNP

The optimal distribution and dispersion of BNNS/GNP in thermoplastic polymers is a challenge when manufacturing functional and homogeneous composites, since BNNS/GNP tend to agglomerate upon mixing with the polymer matrix, due to high energetic state of the nanoplatelets [144-146]. The main techniques adopted to manufacture composites of thermoplastic polymers with BNNS and GNP are: in-situ polymerization, solution mixing, melt mixing.

In-situ polymerization requires the BNNS/GNP to be dissolved in the liquid monomer to facilitate the swelling of the platelets, thus, favouring the diffusion of the initiator. The reaction starts by applying heat or a radiation and occurs directly onto the BNNS/GNP surface. Therefore, in *in-situ* polymerization the polymer attaches on the BNNS/GNP surface as the polymerization occurs, resulting in intimate adhesion between the forming polymer and the filler particles, essential to transfer any external impulse (mechanical, electrical, thermal) from

the polymer to the BNNS/GNP throughout the composite [144, 147]. *In-situ* polymerization was adopted to prepare composites of BNNS with polystyrene (PS)[148], poly(methylmethacrylate) (PMMA)[149, 150], poly(caprolactone) [151], as well as to manufacture composites of GNP with PS and PMMA ([144] and references therein).

In solution mixing, BNNS/GNP are dissolved in a suitable solvent such as water, acetone, tetrahydrofuran (THF), dimethyl fomamide (DMF), toluene to facilitate the delamination of the platelets, before the addition of the polymer, which adheres on the delaminated BNNS/GNP layers. The evaporation of the solvent causes the reassembly of the BNNS/GNP sheets, thus sandwiching the polymer [144, 152, 153]. This processing requires up to 24 hours for the solvent to completely evaporate and the homogeneity of the final composites strongly depends on the mixing efficiency of the BNNS/GNP and polymer in the solvent (*e.g.* sonication)[145]. The solution mixing has been exploited largely for epoxy-resin composites, yet in some cases this procedure have been used to prepare composites of GNP with polypropylene (PP) [154] and poly(vinyl alcohol) (PVA) [155].

Melt mixing or melt compounding involves the mixing of the BNNS/GNP within the molten polymer matrix using extruders, internal mixers, two roll mills and injection moulding. Melt mixing is environmental friendly as it does not require solvents and it is industrially viable as it allows to scale-up large quantities (on the tons scale) of composites. The high shear stresses realized during melt mixing breaks BNNS/GNP agglomerates, thus, facilitating their dispersion and distribution in the polymer matrix. Different parameters govern melt mixing, for instance during extrusion, the screw speed, mixing time, screw configuration and temperature profile must be optimized to guarantee a constant output and homogeneous composites [156]. Usually, the higher the screw speed the better the distribution/dispersion of BNNS/GNP in the polymer, yet, if the screw speed is too severe, the platelets can be eroded, thus, reducing the aspect ratio of the filler particle which could be detrimental for the properties of the final composites (see next section). At a given temperature/screws profiles, the higher the concentration of BNNS/GNP the higher the viscosity of the polymer-filler system and the longer the residence time, which could promote the polymer degradation and BNNS/GNP particles erosion [145]. The screw configuration plays a key role in melt mixing. The screw elements, including the kneading elements, define the shear stress applied on the filler particles, thus determining the state of filler distribution and dispersion [157]. The temperature profile defines the molten state of the polymer matrix in terms of viscosity profile. The lower the temperature, the higher the viscosity which could prevent the BNNS/GNP from diffusing

through the molten polymer, thus lowering the optimal distribution and dispersion. Yet, high viscous states impart high shear stresses onto the filler particle, which promote the exfoliation thereof [144, 145, 147].

2.3.1- Composites of thermoplastic polymers with BNNS and GNP prepared by melt mixing.

Melt compounding is extensively used in industry to prepare composites of thermoplastic polymers with BNNS/GNP, yet, this topic has been poorly studied and reported in the literature. Table 2.2 shows, at the time of writing of the thesis, the published literature on composites of thermoplastics with BNNS/GNP prepared by melt mixing, including the mixing technology employed- *e.g*. extrusion, internal mixers, hot press injection moulding- the materials used, the properties attained and the comments as reported by the author of each individual paper listed.

Table 2.2: Composites of thermoplastic polymers with BNNS and GNP prepared by melt mixing: materials, procedures and properties. The comments reported refer to the remarks given by the authors of each individual paper listed. In case of hybrid filler systems, only carbonaceous materials and boron nitride derivatives have been considered.

Composites of thermoplastics with BNNS prepared by melt mixing				
Materials	**Procedure/Equipment**	**Mechanical Properties, Rheological and Barrier Properties**	**Comments**	**Ref.**
PA66+BN(20wt%)	Coating of BN with polysilazane by solution mixing Extruder + Hot press (composites manufacturing)	Increase of Young's modulus of 12% and 57% when adding non-coated BN and coated BN respectively.	Surface treatment of BN particles improved the adhesion with PA66 and the processing favoured the BN particle alignment in PA6, thus enhancing stress transfer.	[158]
PBT (polybutylene terephthalate) +BN(15wt%) PBT + BN(15wt%)+CF(15wt%) (BN: boron nitride particles, 5-11µm agglomerates, 3µm length, 0.1-0.2µm thickness; CF: carbon fibre, 200µm length, 10µm diameter)	Extruder + Injection moulding	Increase of Young's modulus up to 200% and 350% when adding BN and BN+CF respectively.	Synergistic effect of CF with BN increasing stiffness of PBT.	[159]
TPU+BN(3wt%) (BN: boron nitride particles, 100nm size)	Extruder + Hot press	Increase of Young's modulus up to 490%. Increase of Tensile strength of *ca* 50% (no error reported on the values).	π-π interaction between BN and TPU improved interfacial adhesion, thus stress transfer.	[160]
Estane (polyether based polyurethane) + BN (7.5wt%) (BN: boron nitride particles, 4-8nm size)	Extruder + Injection moulding	Increase of Young's modulus of 60%.	The chemical-physical interaction between BN and the matrix facilitated stress transfer.	[161]
SEBS(70) (styrene-ethylene-buthylene-styrene):EVA(30) (poly-(etlylene-co-vinyl acetate) +BN (50wt%) (BN: boron nitride particles, 7.5µm size)	Extruder + Hot press	Increase of Young's modulus of 500%.	The large size of BNNS facilitated the stress transfer.	[162]

Materials	Procedure/Equipment	Thermal and Morphological Properties	Comments	Ref.
PA66+BN(20wt%) (BN: boron nitride particles)	Coating of BN with polysilazane by solution mixing Extruder + Hot press (composites manufacturing)	Increased thermal conductivity up to 230%.	Surface treatment of BN particles improved the adhesion with PA66 and the processing favoured BN particle alignment in PA6, thus, enhancing heat transfer.	[158]
PPS (polyphenylene sulfide)+ BN(50wt%) +MWCNT (1wt%) (BN: boron nitride powder, MWCNT: multi walled carbon nanotube 10μm length, 20-100nm diameter)	H_2O_2 treatment of MWCNT Extruder + Injection moulding (composites manufacturing)	Increased thermal conductivity by 368% and 461% when adding BN and BN+MWCNT respectively.	MWCNT surface treatment enhanced adhesion with the BN particles and bridged BN and PPS domains, thus facilitating heat transfer.	[163]
PET+BNNS(3v%) (BNNS: boron nitride nanosheets, 1.7μm length, 4.5μm thickness)	Extruder + Hot press	Decrease of oxygen permeation rate by 75%.	The even dispersion/distribution of BNNS in PET decreased diffusion of oxygen.	[164]
PBT (polybutylene terephthalate)+ BN(15wt%) PBT + BN(15wt%)+CF(15wt%) (BN: boron nitride particles, 5-11μm agglomerates, 3μm length, 0.1-0.2μm thickness; CF: carbon fibre, 200μm length, 10μm diameter)	Extruder + Injection moulding	No improvement in thermal conductivity.	BN agglomerates increase thermal interface resistance. The breaking of CF into smaller fibres after extrusion and the random orientation of CF after injection moulding prevent the formation of a 3D thermal path.	[159]
PBT+BN(15wt%) (BN: boron nitride platelets, 10-60μm size, 0.1-2.5 μm thickness, surface area 0.3-10 m^2/g)	Extruder+ Injection moulding	No improvement in thermal conductivity.	BN agglomerates and the random orientation after processing lead to high thermal resistance.	[165]
PPS+BN(30wt%) (BN: boron nitride particle, 12μm size)	Extruder + injection moulding	Increase in thermal conductivity up to 500%.	High concentration of filler saturated the polymer matrix and generated a thermal path.	[166]

Materials	Procedure/Equipment	Thermal and Morphological Properties	Comments	Ref.
TPU+BN(3wt%) (BN: boron nitride particles, 100nm size)	Extruder + Hot press	Slight increase in thermal conductivity of 50%.	The π-π interaction between BN and TPU improved the interfacial adhesion, thus reducing the thermal resistance at the interface.	[160]
PVDF+BN(20wt%) PVDF+BN(20wt%)+CNT(2wt%) (BN: boron nitride particles; CNT: carbon nanotubes)	Solution mixing of PVDF, BN, CNT in DMF, drying. Lab scale compounder + Hot press (composites preparation)	Increase in thermal conductivity by 300% and 450% when adding BN and BN+MWCNT, respectively.	The pre-mix in DMF facilitated the dispersion of the filler in PVDF. CNT bridged the BN particles creating a 3D thermal path.	[167]
PE+BN (30wt%) (BN: boron nitride particles, 3-5µm size)	Extruder containing laminating/multiplying elements+ Hot press	Increase in thermal conductivity of 500%.	The processing adopted favoured the even distribution, dispersion and alignment of filler particles. Yet high concentration of BN are needed to form a thermal path.	[168]
PP+BN(40v%) (BN: boron nitride particles)	Extruder + Injection moulding	Increase in thermal conductivity 20 times higher than the neat matrix.	The filler alignment when processing the composites facilitating the formation of a thermal path. Yet, high concentration of BN are needed	[169]
PPS+BNNS (40wt%) (BNNS: boron nitride nanosheets)	Surface modification of BNNS with silane groups Extruder+ Injection moulding	Increase in thermal conductivity 20 times higher than the neat matrix	The filler surface modification improved the interfacial adhesion with PPS, yet high concentration of BN are needed to increase the thermal conductivity.	[170]
SEBS(70) (styrene-ethylene-buthylene-styrene):EVA(30) (poly-(etlylene-co-vinyl acetate) +BN (50wt%) (BN: boron nitride particles, 7.5µm size)	Extruder + Hot press	Increase in thermal conductivity up to 166%.	High filler loading are needed to improve thermal conduction, probably due to the BN small size.	[162]

Composite of thermoplastics with GNP prepared by melt mixing				
Materials	**Procedure/Equipment**	**Mechanical, Rheological and Barrier Properties**	**Comments**	**Ref.**
TPU+GNP (1wt%) (GNP: graphene nanoplatelets, 1-3 graphene monolayers, 10μm length, 1.0-2.0 nm thickness)	Internal Mixer + Hot Press	Increase in Young's modulus of 50%.	The improved state of dispersion of GNP could have caused an increase in the stiffness.	[171]
TPU+GNP (3.9v%) (GNP: exfoliated graphite nanosheets, 100nm thickness)	Pre-mix of TPU/GNP/DMF+ filtration/drying. Internal Mixer + Hot Press	Increase in Young's modulus of 300%. Increase of stiffness (E′, DMA) up to 200%. Decrease of T_g of *ca* 8°C.	The high stiffness of GNP caused an increase in Young modulus.	[172]
TPU+GNP(0.5wt%) TPU+GNP(0.25wt%)+CNS(0.25 wt%) (GNP: graphene nanoplatelets, 15μm length, ca 6nm thickness; CNS: carbon nanostructures, lakes-70 μm long and 10 μm thick, nanotube- diameter 9 nm)	Extrusion (masterbatch manufacturing at 6wt% each type of filler loading) + Internal mixer (dilution with matrix to desired composition)+Hot Press	No improvement in mechanical properties.	The GNP did not alter the elasticity of the TPU.	[173]
PP(80):PS(20)+GNP(1wt%) (GNP: exfoliate graphene nanoplatelets, thickness ca 6-8nm, surface area 120-150 m^2/g)	Internal Mixer + Hot Press	No improvement in mechanical properties.	Poor dispersion and interfacial adhesion between GNP and PP:PS obstructed stress-transfer (no mechanical reinforcement).	[174]
Alcryn*2265UT (thermoplastics elastomer, partially cross-linked chlorinated olefin interpolymer alloy) + GNP (11v%) (GNP: graphene nanoplatelets, 25μm length, 6-8nm thickness)	Internal Mixer + Injection moulding	Increase in Young's modulus of *ca* 450%.	The combination of large GNP platelets and interfacial interaction with the matrix facilitated stress transfer.	[175]
PET+GNP (1wt%) (GNP: graphene nanoplatelets, no information reported)	Internal Mixer+ Hot Press	Increase in flexural modulus of *ca* 64%.	The good adhesion between the filler and matrix improved the flexural modulus.	[176]

Materials	Procedure/Equipment	Mechanical, Rheological and Barrier Properties	Comments	Ref.
TPU+GNP (2wt%) (GNP: graphene nanoplatelets, size 11-15nm, surface are 50-80 m^2/g)	Lab. Scale compounder+ Injection moulding	Increase in Young's modulus of ca 35%. Increase in shape memory up to 100%.	Interfacial bonds between GNP and the polymer increased the stiffness and the elastic recovery.	[177]
HDPE+GNP(15wt%) (GNP: graphene nanoplatelets, 5μm length, 6nm thickness, surface area 120-150 m^2/g)	Extruder+ Injection moulding	Increase in flexural modulus of ca 112% and flexural strength at yield of ca 60%. Decrease of oxygen permeation by up to 50%. Decrease of fuel vapour permeation by up to 73%.	GNP particle size and distribution affected strass-transfer, thus the stiffness and the strength of the composites. The relative uniform filler distribution improved barrier properties.	[178]
PC+GNP(15wt%) PC+GNP(15wt%)+MWCNT(1wt%) (GNP: graphene nanoplatelets, 5μm length, 6-8nm thickness; MWCNT: multi-walled carbon nanotube, 9.5nm diameter, 1.5μm length)	Internal Mixer+ Hot Press	No improvement in Hardness	Filler particle agglomeration results in a lower Hardness value.	[179]
PC+GNP (2wt%) (GNP: graphene nanoplatelets, 5μm length, 6-8nm thickness, surface area 120-150 m^2/g)	Extruder+ Injection moulding	No improvement in the mechanical properties.	GNP agglomerated in PC, thus, limiting stress transfer.	[180]
TPEE (thermoplastic polyester elastomer) + GNP (0.1wt%) (GNP: graphene nanoplatelets, 8μm length, 10nm thickness, aspect ratio 500-2000)	Slag-bonded-PEG-g-GNP Internal Mixer+ Injection Moulding	Increase of Young's modulus of ca 56%.	Surface modification of GNP improved interfacial interaction with TPEE, thus, increasing the stiffness.	[181]

Materials	Procedure/Equipment	Mechanical, Rheological and Barrier Properties	Comments	Ref.
PA66+GNP (6wt%) PA66+GNP(3wt%)+MWCNT(3wt%) (GNP: graphene nanoplatelets, 100nm-1µm size, surface area 500 m^2/g; MWCNT: multi walled carbon nanotube, aspect ratio 67)	Lab. scale compounder+ Injection moulding	Increase in Young's modulus of *ca* 44% and *ca* 52% when adding GNP and GNP+MWCNT in PA66, respectively.	The even distribution of GNP and MWCNT facilitated the stress transfer. MWCNT prohibited the agglomeration of GNP.	[182]
PA6+GNP (20wt%) (GNP: graphene nanoplatelets, 18-24 layers, 5µm length, 6-8nm thickness, surface area 120-150 m^2/g)	Extruder+ Hot Press	Increase in Young's modulus of ca 376%. Increase in stiffness (G′, Oscillatory rheology) by up to 3 orders of magnitude.	Uniform dispersion of GNP assisted stress transfer resulting in increased stiffness.	[183]
PP+GNP (1.05v%) (GNP: graphene nanoplatelets, 0.1-5µm length, <5 nm thickness)	Ball milling GNP in solvent +centrifugation Internal mixer + Hot Press	Increase of complex viscosity (oscillatory rheology) by up to 200%.	The high aspect ratio and rigidity of GNP increased the complex viscosity of the final composites.	[184]
LLDPE+GNP (10wt%) (GNP: graphene nanoplatelets, 2-15 layers, 5µm length, 6-8nm thickness, 120-150 m^2/g)	Extruder+ Hot Press	No improvement in mechanical properties.	Agglomeration of GNP limited stress-transfer.	[185]
PP+GNP (5wt%) (GNP: graphite nanoplatelets, 2-15 layers, 5µm length, 6-8nm thickness, 120-150 m^2/g)	Extruder + Hot Press	Increase in Young's modulus of *ca* 130% .	The restriction of the polymer chains and entanglements around the GNP particles stiffened the final composites.	[186]
PP (70): NR (20) (natural rubber): LNR (liquid natural rubber) (10)+ GNP (1.5wt%) (GNP: graphene nanoplatelets, 5µm length, 5-15nm thickness)	Ultra-sonication LNR+GNP Internal mixer of PP+NR+LNR/GNP + Hot Press	Increase in Young's modulus by up to 33%.	Uniform dispersion of GNP and improved interfacial adhesion with the matrix and increased stress-transfer.	[187]

Materials	Procedure/Equipment	Mechanical, Rheological and Barrier Properties	Comments	Ref.
PLA+GNP(5wt%) (GNP: graphene nanoplatelets, 1-2μm length, 10-20nm thickness, surface area 750 m^2/g)	Batch Mixer + Hot Press	Increase in Young's modulus of *ca* 39%. Increase in stiffness (E′, DMA) by up to 40%.	The even distribution of GNP enabled a more efficient stress-transfer in spite of poor interfacial adhesion with the matrix and resulted in increased composite stiffness.	[188]
PP+GNs (3wt%) (GNs: graphene nanosheets, 1nm thickness)	Lab. scale extruder + Hot Press	Increase in Young's modulus of 100% and tensile strength of 81% (no error reported on the values) Increase of stiffness (G′, oscillatory rheology) up to 4 orders of magnitude.	The high aspect ratio and the intrinsic rigidity of GNP along with the favourable interactions with the polymer matrix promoted stress transfer at the polymer-GNP interface, and restricted polymer chain mobility (increase in stiffness).	[189]
PLA(30): ABS(70) + GNP(0.4wt%) (GNP: graphene nanoplatelets, 6-8nm thickness, 120-150 m^2/g)	Extruder+ Hot Press	Slight increase in Young's modulus of 14%.	The high aspect ratio of GNP favoured stress transfer.	[190]
PP (70): NR (20) (natural rubber): LNR (liquid natural rubber) (10)+ GNP (5wt%) (GNP: graphene nanoplatelets, <30 layers, 5-10μm length, 4-20nm thickness)	Ultrasonic bath LNR+GNP Internal mixer	Increase in Young's modulus of *ca* 157% and impact strength of *ca* 100%.	The strong interactions between GNP and the polymer matrix improved filler dispersion and the mechanical properties.	[191]
PP+GNP(5wt%) (GNP: graphene nanoplatelets, 6 nm thickness, 120-150 m^2/g)	Lab. scale compounder+ Injection moulding	Increase in Young's modulus up to 67%.	Strong polymer-filler interactions improved stress-transfer.	[192]

Materials	Procedure/Equipment	Mechanical, Rheological and Barrier Properties	Comments	Ref.
PP+GNP(20wt%) PE+GNP(20wt%) (GNP: graphene nanoplatelets, 2µm length, 10 nm thickness, aspect ratio 200)	Mixing batch+ Hot press ECMAE (equal-channel multiple-angular extrusion)+ Hot press	Increase of micro-hardness by up to *ca* 100% (ECMAE procedure) for both sets of composites with PP and PE.	The polymer chains were aligned during ECMAE, thus increasing matrix hardness.	[193]
EDPM+GNP (26.7v%) (GNP: graphene platelets, 3.56 nm thickness)	Two roll mill- Hot press	Increase in Young's modulus of *ca* 560% and tear strength of *ca* 400%.	The increase in mechanical strength is due to the high stiffness of GNP and the GNP particles acting as crosslinking points.	[194]
PP (75wt%)+MAPP (MA-g-PP) (5wt%) +KF (Kenaf Fibre) (20wt%)+ GNP (5phr) (GNP: exfoliated graphene nanoplatelets, 5µm length, 6nm thickness, surface area 158 m^2/g)	Extruder + Injection moulding	Increases in Young's modulus of *ca* 38%, flexural modulus of *ca* 1500% and flexural strength of *ca* 50%. Decrease in water adsorption of *ca* 83%.	PP modification with MA-g-PP promoted interactions with GNP thus increasing mechanical properties. Addition of KF prevents GNP from agglomerating and reduced the water uptake.	[195]
PP+GNP (9.3v%) (GNP: graphene nanoplatelets, 150µm length, 20nm thickness, surface area 50-80 m^2/g)	Extruder+ Injection Moulding	Increase in Young's modulus of *ca* 30% and flexural modulus of *ca* 80%.	The high aspect ratio and level pf GNP dispersion in the polymer improved stress-transfer.	[196]
PP+GNP (5.2 v%) (GNP: graphene nanoplatelets, 15µm length, 6-8nm thickness, surface area 120-150 m^2/g)	Lab. scale compounder + Injection moulding	Increase in Young's modulus of *ca* 54%.	GNP interacts to some extent with PP thus improving stress-transfer.	[197]
PLA+GNP (0.25wt%) (GNP: graphene nanoplatelets, 1-2µm length, <2nm thickness, surface area 750 m^2/g)	Internal mixer + Hot press	No improvement in mechanical properties.	GNP agglomerations thus lowering mechanical performance.	[198]

Materials	Procedure/Equipment	Mechanical, Rheological and Barrier Properties	Comments	Ref.
PP+ graphite (1wt%) (flake graphite 150µm size)	Extrusion (to prepare the PP+ graphite masterbatch at low mixing effect) + Capillary rheology (to exfoliate graphite in GNP)	Extensional flow increase with the extensional stress whereas the shear flow decrease with the shear stress (Capillary + Rotational rheology).	Exfoliation of graphite in PP to obtain PP+GNP a result of extensional stress rather than shear stress.	[199]
PET+GNP (1.5wt%) (GNP: exfoliated graphite nanoplatelets, 46µm length, 4.5nm thickness)	Extruder+ Hot press	Increase in Young's modulus of *ca* 26%. Reduction of oxygen permeability up to 99%.	GNP increases PET crystallinity thus, increasing the stiffness. The high aspect ratio of impermeable GNP flakes along with increased crystallinity in PET enhanced barrier properties.	[200]
PP+GNP (3v%) (GNP: exfoliated graphite nanoplatelets, <1µm length, <0.01µm thickness, aspect ratio <100, surface area 100m^2/g)	Lab. scale compounder + Injection moulding	Reduction of oxygen permeability of *ca* 20%.	The high aspect ratio of impenetrable GNP flakes enhanced barrier properties.	[201]
PLA(50):TPU(50)+GNP (3wt%) (GNP: graphene nanoplatelets, 2-10nm thickness)	Internal mixer + Hot press	Increase in elongation at break of *ca* 600% (no error reported on the values).	GNP interconnected in the PLA:TPU blend altered blend morphology	[202]
PLA+GNP (15wt%) PBAT (poly(butylene adipate-co terephthalate)) +GNP(15wt%) (GNP: graphene nanoplatelets, 6-8nm thickness, surface area 120-150 m^2/g)	Internal mixer + Hot press	Increase in Young's modulus of 67% and 350% when adding GNP to PLA and PBAT, respectively.	The high aspect ratio of GNP enhanced stress-transfer. The agglomeration of GNP in PLA at high content (weak interfacial interaction) lead to a lower increase in Young's modulus to a value less than that of PBAT.	[203]
PA11+GNP(5wt%) (GNP: graphene nanoplatelets, 4-5 layers, <2µm length, 8nm thickness)	Masterbatch manufacturing by extrusion. Extruder + Injection moulding (dilution with PA11 to the desired composition)	Increase in Young's modulus of 56% and tensile strength of 25%.	The high aspect ratio and degree of dispersion of GNP along with the increase in crystallinity in PA11 improved the stress-transfer.	[204]

Materials	Procedure/Equipment	Mechanical, Rheological and Barrier Properties	Comments	Ref.
LDPE+GNP(7.5wt%) (GNP: graphene nanoplatelets, 5μm length, 6-8nm thickness, surface area 120-150 m, surface area 120-160 m^2/g)	Sonication of GNP with LDPE powder (coating step) Extruder(masterbatch manufacturing) + Extruder (film manufacturing of desired composition)	Increase in Young's modulus up to 100% and yield strength up to 62%. Decrease of CO_2 permeability of 175%. Decrease of SF_6 permeability of 80.5%.	The alignment of GNP and polymer chains in the extrusion direction made the material rigid. Inclusion of GNP reduced polymer chain mobility and the concentration of voids, thus, enhancing the barrier properties.	[205]
PLA+GNP(3wt%) (GNP: exfoliate graphite nanoplatelets, 1-2μm length, 10-20 nm thickness, surface area 750 m^2/g)	Lab scale compounder + melt spun + Hot press	Increase in stiffness (storage modulus) up to 75%.	The increase in crystallinity and the rigidity of polymer chains upon GNP incorporation resulted in a stiffening effect.	[206]
PLA+GNP(3wt%) (GNP: graphene nanoplatelets, 5-25μm length, 6-8nm thickness, surface area 120-150 m^2/g)	Internal mixer + Hot press	Isothermal crystallization under quiescent conditions: increase in stiffness (storage modulus) up to 40%; decrease in crystallization induction time of 5 times (nucleating effect upon filler incorporation).	Under quiescent conditions, the crystallinity of the polymer increases upon GNP addition, thus, a stiffening effect is obtained. GNP has a nucleating effect on PLA.	[207]
PC+GNP(0.5wt%) (GNP: graphene nanoplatelets, 15μm length, 6-8nm thickness, 120-150 m^2/g)	Internal mixer + hot press/ foaming by drop pressure (0-20 bar) in presence of CO_2- one step foaming. Internal mixer + hot press/ saturation of composites in presence of CO_2 + heating at high temperatures (165°C) - two steps foaming.	Increase in stiffness (storage modulus) up to 150%. Increase in stiffness (storage modulus) by up to one order of magnitude (two step foaming). Decrease in stiffness (storage modulus) by up to 350% when comparing the one and two step foaming processes.	GNP affects the morphology of the cell-structure upon foaming, thus stiffness. Furthermore, in the one-step foaming the cells formed are smaller than in the two step foaming. Therefore, the latter are denser, which lead to a major increase in the stiffness.	[208]
PEEK+GNP(10wt%)	Internal mixer + Injection moulding	Increase in Young's modulus of 40% and creep resistance of *ca* 33%.	GNP evenly distributed in PEEK reinforcing the matrix and reducing the creep.	[209]

27

Materials	Procedure/Equipment	Mechanical, Rheological and Barrier Properties	Comments	Ref.
PP+GNP (3v%) (GNP: exfoliated graphite, 1µm length, 10nm thickness)	Lab. scale compounder + injection moulding	Increases in Young's modulus of *ca* 38%, flexural strength of *ca* 29% and impact strength of *ca* 83%.	The GNP well dispersed and reinforcing the matrix. The variation in GNP alignment and aspect ratio lead to higher impact strength.	[210]
PP+GNP(5wt%)+GF(15wt%) (GNP: graphite nanoplatelets, 5µm length, 10-20nm thickness; GF: glass fibre, 6.50mm length, 15.3µm diameter)	Lab. scale compounder + Injection moulding	Increases in Young's modulus up to 127%, tensile strength up to 13% and impact strength up to 65%.	The increase in interfacial shear strength when adding GNP+CF to PP enhanced the stress-transfer.	[211]
PET(70): PP(30): SEBS-g-MA (10phr) +GNP (3phr) (GNP: exfoliated graphite nanoplatelets, 5µm length, 10nm thickness)	Extruder + Injection moulding	Increases in Young's modulus up to 43%, tensile strength up to 37% and impact strength of 45%.	The uniform dispersion of GNP in the matrix enhanced stress-transfer.	[212]
PP+GNP(5v%) PP+GNP(4v%)+CNT(1v%) (GNP: graphene nanoplatelets, 5µm length, 7nm thickness; CNT: carbon nanotube, 1.5µm length, 9.5nm diameter)	Batch mixer + Hot press	No improvement in mechanical properties.	Poor adhesion between GNP and CNT with PP prevented the stress from being transferred throughout the composite.	[213]
HDPE+GNP(7.5wt%) (GNP: exfoliated graphene nanoplatelets, 5µm length, 6nm thickness, surface area 120-150 m^2/g)	Lab. scale extruder + Injection moulding	Increase in Young's modulus up to 150% and flexural modulus up to 75%. Decrease of oxygen permeation up to 50%.	The high aspect ratio and the limited aggregation of GNP enhanced stress transfer and barrier properties.	[214]
HDPE+ GNP (5wt%) (GNP: exfoliated graphene nanoplatelets, 15µm length, 6nm thickness, 120-150 m^2/g)	Solution mixing to coat GNP with paraffin or thermoplastic elastomer (ethylene-octene) Lab scale extruder + injection moulding (composites preparation)	Decrease in oxygen permeation of up to 42% and 33% when GNP was coated with paraffin and thermoplastic elastomer, respectively.	The uniform distribution of GNP enhanced the barrier properties.	[215]

Materials	Procedure/Equipment	Mechanical, Rheological and Barrier Properties	Comments	Ref.
PP+GNP (1wt%) (GNP: graphene nanoplatelets, 1µm length, <2µm thickness, surface area 750 m²/g)	Extruder + Hot spinning	Increase in Young's modulus of 22%.	The rigid GNP particles increased the stiffness of the matrix. Yet, the GNP tendency to aggregate limited interfacial adhesion with the matrix, thus, preventing efficient stress-transfer.	[216]
PA6+GNP (1wt%) (GNP: graphene nanoplatelets, grade H from XG Sciences, no other information available)	Extruder + Injection moulding	No improvement in mechanical properties.	GNP did not disperse properly in PA6, thus, limiting stress-transfer.	[217]
PA6 +GNP (2wt%) (GNP: graphene nanoplatelets, 6-8nm thickness, surface area 120-150 m²/g)	Extruder + Injection moulding	Increase in Young's modulus of 50% and tensile strength up to 30%.	The uniform distribution of GNP increased to some extent the stiffness of the composite.	[218]
PEI (polyetherimide)+GNP(5wt%) (GNP: graphene nanoplatelets, 15µm length)	Extruder+ Hot press	Increase in flexural modulus up to 30%.	The even distribution of GNP in the matrix increased the flexural strength of PEI.	[219]
PP+GNP (5wt%) (GNP: graphite nanoplatelets, 2x10µm size, <10nm thickness)	Extruder + Injection moulding	No improvement in mechanical properties.	The poor dispersion of GNP and/or the limited interfacial interactions with the matrix led to poor mechanical properties.	[220]
HDPE+ GNP (1wt%) (GNP: graphene nanoplatelets, surface area 500 m²/g)	Extruder	Increase in flexural strength of 60%.	The large GNP platelets facilitated the stress-transfer.	[221]
PLA+PEO (polyethylene oxide) +GNP (1wt%) (PEO:GNP=1:1) (GNP: graphene nanoplatelets, 5-10µm length, 4-20nm thickness)	Ultra-sonication of PEO+GNP freeze drying Extruder+ Injection moulding (PLA+PEO+GNP)	No improvement in mechanical properties.	The aggregation of GNP inhibits stress transfer.	[222]

Materials	Procedure/Equipment	Thermal and Morphological Properties	Comments	Ref.
TPU+GNP (3.9v%) (GNP: exfoliated graphite nanosheets, 100nm thickness)	Pre-mix of TPU/GNP/DMF+ filtration/drying Internal Mixer + Hot Press	Increase in ignition time of *ca* 50%.	The uniform distribution and dispersion of GNP hindered the diffusion of oxygen thus increasing the ignition time.	[172]
PP+GNP (1.05v%) (GNP: graphene nanoplatelets, 0.1-5µm length, <5 nm thickness)	Ball milling GNP in solvent +centrifugation Internal mixer + Hot Press	Increase in T_{deg} (TGA) of *ca* 9%.	The high aspect ratio GNP improved thermal stability.	[184]
PP+GNP (0.3v%) (GNP: graphene nanoplatelets, 8-100µm length, <100 nm thickness, surface area 35 m^2/g)	Ball milling GNP in solvent +centrifugation Internal mixer + Hot Press	Increase in T_c (DSC, 1st cooling) of *ca* 9% and $t_{1/2}$ (crystallization half time, optical microscopy) up to 67%.	The GNP nucleated the PP and the PP crystals grow from the large GNP surface.	[223]
LLDPE+GNP (10wt%) (GNP: graphene nanoplatelets, 2-15 layers, 5µm length, 6-8nm thickness, 120-150 m^2/g)	Extruder+ Hot Press	Increase in thermal conductivity of *ca* 50% (no error reported on the values).	The agglomeration of GNP generated a thermal path.	[185]
TPU+GNP (2wt%) (GNP: graphene nanoplatelets, size 11-15nm, surface are 50-80 m^2/g)	Lab. scale compounder+ Injection moulding	Increase in thermal conductivity of 20%.	The high concentration of GNP improved thermal conduction.	[177]
PC+GNP(15wt%) PC+GNP(15wt%)+ MWCNT(1wt%) (GNP: graphene nanoplatelets, 5µm length, 6-8nm thickness; MWCNT: multi-walled carbon nanotube, 9.5nm diameter, 1.5µm length)	Internal Mixer+ Hot Press	Increase in thermal conductivity of *ca* 160% and *ca* 240% when GNP and GNP+MWCNT added to PC, respectively (no error reported on the values).	High filler concentration and the hybrid interconnected GNP/ MWCNT network generated a thermal path.	[179]
PC+GNP (2wt%) (GNP: graphene nanoplatelets, 5µm length, 6-8nm thickness, surface area 120-150 m^2/g)	Extruder+ Injection moulding	Increase in thermal conductivity of *ca* 150% (no error reported on the values).	The uniform distribution of GNP increased thermal conduction of PC.	[180]

Materials	Procedure/Equipment	Thermal and Morphological Properties	Comments	Ref.
PP+GNP(7.5wt%) (GNP: graphite nanoplatelets, 5µm size, 6-8nm thickness, surface area 120-150 m²/g)	Laboratory scale compounder+ Hot Press	Increase in thermal conductivity of *ca* 100% (no error reported on the values).	GNP formed a 3D thermally conductive network.	[224]
PA6+GNP (20wt%) (GNP: graphene nanoplatelets, 18-24 layers, 5µm length, 6-8nm thickness, surface area 120-150 m²/g)	Extruder+ Hot Press	Increase in T_c (DSC, 1st cooling) of *ca* 4%.	GNP had a nucleating effect on PA6	[183]
PC (40%)+SAN(59%)+GNP(1%) (GNP: graphene nanoplatelets, 5µm length, 6-8nm thickness)	Lab. scale compounder	*Microscopy (SEM, TEM, Optical) -* GNP localize in the PC phase when blended with SAN. GNP located in both PC domains and at the SAN/PC interface.	The high speed mixing of SAN+GNP breaks GNP into smaller particles, which diffuse from the SAN phases to the PC domains and SAN/PC interface.	[225]
PP+GNP (5wt%) (GNP: graphite nanoplatelets, 2-15 layers, 5µm length, 6-8nm thickness, 120-150 m²/g)	Extruder + Hot Press	Increase in T_c (DSC, 1st cooling) of *ca* 14%.	GNP nucleated PP.	[186]
PP (70): NR (20) (natural rubber): LNR (liquid natural rubber) (10)+ GNP (1.5wt%) (GNP: graphene nanoplatelets, 5µm length, 5-15nm thickness)	Ultra-sonication LNR+GNP Internal mixer of PP+NR+LNR/GNP + Hot Press	Increase in thermal conductivity of *ca* 36% (no error reported on the values).	Modest increase in thermal conductivity achieved is caused by the interfacial thermal resistance between the filler and the matrix.	[187]
PP+GNs (3wt%) (GNs: graphene nanosheets, 1nm thickness)	Lab. scale extruder + Hot Press	Increase in T_c (DSC, 1st cooling) of *ca* 7%.	Heterogeneous nucleation of PP by GNP resulted in an increase in T_c.	[189]
PP+GNP(1v%) (GNP: exfoliated graphite nanoplatelets, >10 layers, 15µm length, 5nm thickness)	Lab. scale extruder + Injection moulding	Increase in T_c (DSC, 1st cooling) of *ca* 7% and crystallization rate (optical microscopy) up to 790%. β-nucleating effect of GNP for PP (XRD).	GNP nucleate PP. The shape and morphology of GNP affect the polymorphism of PP.	[226]

Materials	Procedure/Equipment	Thermal and Morphological Properties	Comments	Ref.
HDPE+GNP (15 v%) (GNP: exfoliated graphene nanoplatelets, 15μm length, <10nm thickness)	Lab. scale compounder + Injection moulding	Increases in T_c (DSC, 1st cooling) of *ca* 5%, T_{onset} (TGA) of *ca* 5% and thermal conductivity of *ca* 200%.	GNP nucleates HDPE, yet at high concentration, GNP aggregation limits polymer chain mobility to growing in larger crystals. The even dispersion of GNP along with the relative high aspect ratio increased the thermal conduction and thermal stability of HDPE.	[227]
PC+GNP(19wt%)+MWCNT(1wt%) (GNP: graphene nanoplatelets, 5μm length, 6-8nm thickness; MWCNT: multi walled carbon nanotube, >20μm length, 20-200nm diameter)	Internal Mixer+ Hot Press	Increase in thermal conductivity of *ca* 480%.	MWCNT bridged the gaps between GNP particles, thus creating a thermal path.	[228]
PP+GNP(20wt%) PE+GNP(20wt%) (GNP: graphene nanoplatelets, 2μm length, 10 nm thickness, aspect ratio 200)	Mixing batch+ Hot press ECMAE (equal-channel multiple-angular extrusion)+ Hot press	Decrease in thermal expansion up to 24% and 32% for composites of PP and PE respectively, prepared by mixing batch + hot press. Decrease in thermal expansion up to 6% and 11% for composites PP and PE respectively, prepared by ECMAE + hot press. Decrease in thermal expansion up to 100% for composites of PP and PE when comparing the samples prepared by mixing batch + hot press and ECMAE+ hot press. (No error reported on the values).	The ECMAE process aligned the polymer chains thus leading to a reduction in thermal expansion.	[193]

Materials	Procedure/Equipment	Thermal and Morphological Properties	Comments	Ref.
EDPM+GNP (26.7v%) (GNP: graphene platelets, 3.56 nm thickness)	Two roll mill- Hot press	Increase in thermal conductivity of *ca* 300% (no error reported on the values).	Strong GNP-GNP and GNP-polymer interactions reduce phonon scattering thus increasing thermal conduction.	[194]
PP (75wt%)+MAPP (MA-g-PP) (5wt%) +KF (Kenaf Fibre) (20wt%)+ GNP (5phr) (GNP: exfoliated graphene nanoplatelets, 5μm length, 6nm thickness, surface area 158 m^2/g)	Extruder + Injection moulding	Increase in thermal conductivity of *ca* 600% and decrease in thermal expansion of *ca* 100% (no error reported on the values of the composite).	The GNP interacted with the polymer matrix efficiently thus dissipating the applied heat.	[195]
PP+GNP (9.3v%) (GNP: graphene nanoplatelets, 150μm length, 20nm thickness, surface area 50-80 m^2/g)	Extruder+ Injection Moulding	Increase in T_c (DSC, 1st cooling) of *ca* 6%.	GNP nucleates PP.	[196]
PP+GNP (7.5v%) (GNP: graphite nanoplatelets, 5μm length, 6-8nm thickness, 120-150 m^2/g)	Lab. scale compounder + Hot Press	Increase in thermal conductivity up to 100% (no error reported on the values).	The combination of filler shape and aspect ratio facilitated the formation of a conductive path.	[229]
PP+GNP (25v%) (GNP: exfoliated graphite nanoplatelets, <1μm length, <0.01μm thickness, aspect ratio <100, surface area 100m^2/g)	Lab. scale compounder + Injection moulding	Increase in thermal conductivity of 500%.	The high concentration/distribution of GNP favoured heat dissipation.	[201]
PLA+GNP (15wt%) PBAT (poly(butylene adipate-co terephthalate)) +GNP(15wt%) (GNP: graphene nanoplatelets, 6-8nm thickness, surface area 120-150 m^2/g)	Internal mixer + Hot press	Increase in T_c (DSC, 1st cooling) of 17% and 22% when adding GNP to PLA and PBAT respectively.	GNP act as a nucleating agent for both polymers.	[203]
PET(60.87):PP(26.09):SEBS-g-MA(8.70) + GNP (5phr) (GNP: exfoliated graphite nanoplatelets, 5μm length, 6nm thickness)	Extruder + Hot press	Increase in thermal conductivity of 225% and time of ignition by 75%.	GNP randomly distributed in the matrix interconnect and form a thermal path.	[230]

Materials	Procedure/Equipment	Thermal and Morphological Properties	Comments	Ref.
PA11+GNP(5wt%) (GNP: graphene nanoplatelets, 4-5 layers, <2µm length, 8nm thickness)	Masterbatch manufacturing by extrusion. Extruder + Injection moulding (dilution with PA11 to the desired composition)	Increase in T_c of 6%.	Nucleating effect of GNP for PA11.	[204]
LDPE+GNP(7.5wt%) (GNP: graphene nanoplatelets, 5µm length, 6-8nm thickness, surface area 120-150 m, surface area 120-160 m²/g)	Sonication of GNP with LDPE powder (coating step) Extruder (masterbatch manufacturing) + Extruder (film manufacturing of desired composition)	Increase in thermal conductivity up to 900%.	The interfacial phonon scattering between GNP and LDPE is low in the direction thermal conductivity was measured due to the higher interfacial area of the GNP platelets in that direction.	[205]
HDPE+GNP(5wt%) (GNP: graphene nanoplatelets, 5µm length, 10nm thickness)	Pre-mix HDPE+GNP powder by ball mill Internal mixer (composite preparation)	Decrease of crystallization half-life by up to 30%.	Nucleating effect of GNP for HDPE.	[231]
LDPE (70): NR (20) (natural rubber): LNR (liquid natural rubber) (10)+ GNP (3wt%) (GNP: graphene nanoplatelets, 5-10 nm length, 4-20nm thickness, <30 layers)	Ultra-sonication LNR+GNP Internal mixer + Hot press (composites manufacturing)	Increase in thermal conductivity up to 50%.	GNP percolated to yield a 3D thermally conductive structure in the polymer, thus, lowering interfacial phonon scattering.	[232]
CBT (cyclic butylene terephthalate)+ GNP (10wt%) CBT+GNP(15wt%)+CF(5wt%) (GNP: graphene nanoplatelets, 5µm length, 6-8nm thickness; CF: carbon fibre, 200µm length)	Internal mixer + Hot press	No increase in thermal conductivity when GNP added to CBT. Increase in thermal conductivity of 25 times when adding GNP+CF to CBT.	Synergistic effect on thermal conduction when adding GNP and CF to CBT.	[233]
PP+GNP(0.5wt%) (GNP: graphene nanoplatelets, 1-6 layers, <10µm length, <5µm thickness, surface area 200 m²/g)	Extruder	No improvement in the decomposition temperature.	GNP did not form a 3D network.	[234]

Materials	Procedure/Equipment	Thermal and Morphological Properties	Comments	Ref.
PET(70):PP(30)+GNP(7.5 phr) (GNP: exfoliated graphite nanoplatelets, 5μm length, 10nm thickness)	Extruder + Hot press	Increase in thermal conductivity of 12%.	GNP dispersed and formed an interconnected thermal path.	[235]
Materials	**Procedure/Equipment**	**Electrical Properties**	**Comments**	**Ref.**
TPU+GNP (2wt%) TPU+GNP(1.5wt%)+CNS(0.5wt%) (GNP: graphene nanoplatelets, 15μm length, 6nm thickness; CNS: carbon nanostructures, branched carbon nanotube flakes, 70μm length, 10μm thickness, 9nm diameter)	Internal Mixer + Hot Press	No change in electrical resistance when adding GNP. Increase of 2 orders of magnitude when adding GNP+CNS to TPU (no error reported on the values).	CNS bridges the GNP particles to give an electrically conductive path.	[236]
HDPE+GNP(8v%) (GNP: graphene nanoplatelets, 15μm length, surface area 150 m^2/g)	Extruder + Hot Press	Increase in electrical conductivity by 5 orders of magnitude (no error reported on the values).	GNP percolated in a 3D electrical path.	[237]
PET+GNP (1wt%) (GNP: graphene nanoplatelets, no information reported)	Internal Mixer+ Hot Press	Increase in electrical conductivity by up to 1 order of magnitude.	The even dispersion of GNP facilitated the electrical transfer.	[176]
LLDPE+GNP (10wt%) (GNP: graphene nanoplatelets, 2-15 layers, 5μm length, 6-8nm thickness, 120-150 m^2/g)	Extruder+ Hot Press	Increase in electrical conductivity of 5 orders of magnitude (no error reported on the values).	The agglomeration of GNP generated an electrical path.	[185]
SEBS+GNP(16wt%) (GNP: graphene nanoplatelets, 25μm length, 6-8nm thickness, 120-150 m^2/g)	Internal Mixer+ Hot Press	Increase in electrical conductivity of 10 orders of magnitude (no error reported on the values).	The GNP gradually percolated to form a 3D electrical path, probably due to the limited interfacial interaction with the matrix.	[238]

Materials	Procedure/Equipment	Electrical Properties	Comments	Ref.
PC+GNP(15wt%) PC+GNP(15wt%)+MWCNT(1wt%) (GNP: graphene nanoplatelets, 5µm length, 6-8nm thickness; MWCNT: multi-walled carbon nanotube, 9.5nm diameter, 1.5µm length)	Internal Mixer+ Hot Press	Increase in electrical conductivity of 10 and 14 order of magnitude when adding GNP and GNP+ MWCNT to PC, respectively.	High filler concentration and the hybrid interconnected GNP/MWCNT network generated an electrical path.	[179]
TPU+GNP(0.5wt%) TPU+GNP(0.25wt%)+CNS(0.25wt%) (GNP: graphene nanoplatelets, 15µm length, ca 6nm thickness; CNS: carbon nanostructures, lakes-70 µm long and 10 µm thick, nanotube- diameter 9 nm)	Extruder (masterbatch manufacturing at 6wt% each type of filler loading) + Internal mixer (dilution with matrix to desired composition)+Hot Press	No change in the dielectric constant when adding GNP to TPU. Increase in the dielectric constant by up to 57% when adding GNP+CNS (no error reported on the values).	When adding CNS+GNP to TPU, a higher particle-particle interfacial polarization is attained, due to the high electrical conduction of CNT compared to GNP, thus increasing the dielectric constant.	[173]
PP+GNP(7.5wt%) (GNP: graphite nanoplatelets, 5µm size, 6-8nm thickness, surface area 120-150 m^2/g)	Lab. scale compounder+ Hot Press	Increase in volume resistivity of ca 9 orders of magnitude (no error reported on the values).	GNP formed a 3D electrical conducting network.	[224]
PA6+GNP (20wt%) (GNP: graphene nanoplatelets, 18-24 layers, 5µm length, 6-8nm thickness, surface area 120-150 m^2/g)	Extruder+ Hot Press	Decrease in volume resistivity of 6 orders of magnitude (no error reported on the values).	The even distribution of GNP generated an electrical conducting path.	[183]
PBAT (Poly(Butylene adipate-coterephthalate)) +GNP (15wt%) (GNP: graphene nanoplatelets, 6-8nm thickness, surface area 120-150 m^2/g)	Internal Mixer+ Hot Press	Increase in electrical conductivity of 8 order of magnitude. Increase in EMI shielding effectiveness up to 12 dB. (no error reported on the values).	GNP percolated to form a 3D electrically conductive network.	[239]
PP (70): NR (20) (natural rubber): LNR (liquid natural rubber) (10)+ GNP (1.5wt%) (GNP: graphene nanoplatelets, 5µm length, 5-15nm thickness)	Ultra-sonication LNR+GNP Internal mixer of PP+NR+LNR/GNP + Hot Press	Increase in electrical conductivity of 9 orders of magnitude (no error reported on the values).	The uniform distribution of GNP percolated to yield a 3D electrical structure.	[187]

Materials	Procedure/Equipment	Electrical Properties	Comments	Ref.
PP+GNP(1wt%):MWCNT(1wt%) (GNP: graphene nanoplatelets, 5µm length, 5-8nm thickness, surface area 120-150 m²/g; MWCNT: multi walled carbon nanotube, 1.5µm length, 9.5nm diameter, surface area 250-300 m²/g)	Extruder (masterbatch preparation of PP+GNP, PP+MWCNT) Extruder (PP/GNP+PP/MWCNT) + Hot Press	Increase in electrical conductivity up to 190-200%.	The different geometries of GNP and MWCNT facilitated the formation of a 3D interconnected network for electrical conduction.	[240]
PP+GNP (5 v%) (GNP: exfoliated graphite, 15µm length, <10nm thickness)	Extruder + Injection moulding	Increase in electrical conductivity of up to 8 orders of magnitude.	The processing adopted dispersed GNP in the matrix in a way that a 3D electrically conducting path formed.	[154]
HDPE+GNP (15 v%) (GNP: exfoliated graphene nanoplatelets, 15µm length, <10nm thickness)	Lab. scale compounder + Injection moulding	No change in electrical resistivity.	The GNP particles randomly aligned along the measurement direction, thus lowering the electrical conductivity.	[227]
PP (70): NR (20) (natural rubber): LNR (liquid natural rubber) (10)+ GNP (5wt%) (GNP: graphene nanoplatelets, <30 layers, 5-10µm length, 4-20nm thickness)	Ultra-sonication LNR+GNP Internal mixer of PP+NR+LNR/GNP + Hot Press	Increase in electrical conductivity of 8 orders of magnitude.	The GNP dispersed in the polymer matrix and formed a 3D electrical network.	[191]
EDPM+GNP (26.7v%) (GNP: graphene platelets, 3.56 nm thickness)	Two roll mill- Hot press	Decrease in electrical resistivity of 9 orders of magnitude (no error reported on the values).	GNP dispersed and formed a 3D network.	[194]
PC+GNP (0.48 wt%)+MWCNT (0.32wt%) (GNP+MWCNT=0.8wt%) (GNP: multilayer graphene nanoplatelets, 5-25µm length, 8-10nm thickness; MWCNT: multi walled carbon nanotube, 1.5µm length, 9.5nm diameter, surface area 250-300 m²/g)	Internal mixer+ Hot press	Increase in electrical conductivity of 12 order of magnitude (no error reported on the values).	GNP-MWCNT-GNP interactions along with the π-π interactions between the polymer matrix and fillers, facilitated the formation of a 3D electrically conductive network.	[241]

Materials	Procedure/Equipment	Electrical Properties	Comments	Ref.
PP+GNP (9.3v%) (GNP: graphene nanoplatelets, 150µm length, 20nm thickness, surface area 50-80 m²/g)	Extruder+ Injection Moulding	Electrical percolation threshold formed at 3vol% GNP	The large GNP aspect ratio allowed for a relatively low percolation threshold value.	[196]
PP+GNP (7.5v%) (GNP: graphite nanoplatelets, 5µm length, 6-8nm thickness, 120-150 m²/g)	Lab. scale compounder + Hot Press	Decrease in electrical resistivity of 11 order of magnitude (no error reported on the values).	The combination of filler shape and geometry facilitated electrical conduction.	[229]
PC+GNP (2 pph of resin) (GNP: graphene nanoplatelets, from Timenano, no other information reported)	Extruder+ Hot Press	No change in electrical resistivity.	The poly-dispersity of the GNP particles prevented a conductive network from being formed.	[242]
PLA+GNP (15wt%) PBAT (poly(butylene adipate-co terephthalate)) +GNP(15wt%) (GNP: graphene nanoplatelets, 6-8nm thickness, surface area 120-150 m²/g)	Internal mixer + Hot press	Increase in electrical conductivity of 14 and 10 orders of magnitude when adding GNP to PLA and PBAT, respectively.	The GNP percolated in the polymer matrix thus increasing the electrical conductivity.	[203]
PA11+GNP(5wt%) (GNP: graphene nanoplatelets, 4-5 layers, <2µm length, 8nm thickness)	Masterbatch manufacturing by extrusion. Extruder + Injection moulding (dilution with PA11 to the desired composition)	Increase in dielectric constant of 200%.	Homogeneous GNP dispersion in PA11 created sites with high polarizability, thus, increasing the dielectric constant.	[204]
PLA+GNP(3wt%) (GNP: exfoliate graphite nanoplatelets, 1-2µm length, 10-20 nm thickness, surface area 750 m²/g)	Lab scale compounder + melt spun + Hot press	No change in electrical properties.	The random distribution of GNP prevented the electrical network from being made.	[206]
TPU+GNP(0.5wt%)+CNS(1.5wt%) (GNP: graphene nanoplatelets, 15µm length, 6nm thickness; CNS: branched carbon nanotubes, flakes of 70µm length, 10µm thickness, 9m diameter)	Internal mixer + Hot press	Increase in electrical conductivity by up to 7 orders of magnitude. Increase in dielectric constant up to 4 order of magnitude.	CNS bridged the GNP particles forming a 3D conductive path.	[243]

Materials	Procedure/Equipment	Electrical Properties	Comments	Ref.
AS (acrylonitrile-styrene copolymer) + GNs (18wt%) (GNs: graphite nanosheets, 5-20μm length, 38-80 nm thickness, aspect ratio 200-500)	Sonication of AS and GNs for the masterbatch production. Extruder	Decrease in electrical resistance by up to 10 orders of magnitude.	The elongated shape of the GNs with uniform dispersion in AS facilitated the formation of a conductive path.	[244]
HDPE+GNP(15v%) (GNP: exfoliated graphene nanoplatelets, 15μm length, 5nm thickness)	Lab. scale compounder + Injection moulding	Decrease in electrical resistivity by up to 10 order of magnitude.	GNP dispersed in HDPE formed a conductive path, although high GNP content is required.	[245]
PP+GNP(5v%) PP+GNP(4v%)+CNT(1v%) (GNP: graphene nanoplatelets, 5μm length, 7nm thickness; CNT: carbon nanotube, 1.5μm length, 9.5nm diameter)	Batch mixer + Hot press	No change in electrical resistivity on adding GNP to PP. Reduction in electrical resistivity of up to 14 order of magnitude when adding GNP+CNT to PP.	GNP alone did not form an interconnected network in PP whereas the CNT bridged the GNP particles, thus enhancing electrical conduction.	[213]
LDPE (70): NR (20) (natural rubber): LNR (liquid natural rubber) (10)+ GNP (3wt%) (GNP: graphene nanoplatelets, 5-10 nm length, 4-20nm thickness, <30 layers)	Ultra-sonication LNR+GNP Internal mixer + Hot press (composites manufacturing)	Increase in electrical conductivity by up to 5 order of magnitude.	GNP formed an interconnected network with electrically conductive paths.	[232]
PEI (polyetherimide)+GNP(5wt%) (GNP: graphene nanoplatelets, 15μm length)	Extruder+ Hot press	No change in electrical conductivity.	GNP are evenly distributed in the matrix, yet the presence of polymer chains between the GNP particles along with the reduction of GNP lateral size after extrusion, prevented the filler particles from percolating a 3D electrical structure.	[219]

Materials	Procedure/Equipment	Electrical Properties	Comments	Ref.
PP+GNP(55wt%)+MWCNT(5wt%) (GNP: graphene nanoplatelets, 15µm & 2µm length, 5-8nm & 1-5nm thickness, surface area 120-150m^2/g & 500m^2/g; MWCNT: multi walled carbon nanotube, 9nm diameter, surface area 250-300 m^2/g)	Internal mixer + Hot press	Increase in electrical conductivity by up to 10 orders of magnitude.	Synergistic effect of GNP and MWCNT improving electrical conduction.	[246]
PLA(50):TPU(50)+GNP (3wt%) (GNP: graphene nanoplatelets, 2-10nm thickness)	Internal mixer + Hot press	Decrease in electrical resistivity by up to 6 order of magnitude.	GNP interconnected to form electrical paths, thus, decreasing electrical resistance.	[202]

As evident from Table 2.2, the manufacturing of functional composites of polymers and 2D materials such as BNNS and GNP depends on several aspects including; i) filler geometry, ii) filler-polymer interactions at the interface, iii) filler dispersion and distribution, iv) filler alignment and v) processing. These factors are coupled and affect the properties of the final composites differently, therefore each polymer-filler system needs to be studied as a unique case.

It is understood that the geometry of BNNS/GNP platelets in terms of shape, lateral dimensions, thickness and aspect ratio determine the mechanism of stress-transfer, phonon and electron scattering. Large platelets (tens of μm) with high aspect ratio (length/thickness, order of hundreds) are the most effective at withstanding mechanical stresses (*e.g.* tensile, flexural, impact), since they expose larger areas to the applied stress [175, 178, 184, 189, 190, 196, 203, 204, 214]. Large particles with regular and smooth surfaces minimize phonon and electron scattering, thus enhancing the thermal and electrical (for GNP composites as BNNS are electrical insulators) conductivity of the final material [184, 196, 219, 227, 229, 244]. In addition, composites with large and impermeable GNP platelets show improved barrier properties to gases and liquids such as oxygen, fuel and water [200, 201, 214].

The geometry of filler particles alone is not sufficient to improve the stress transfer to the matrix. The BNNS/GNP particles need to intimately adhere with the polymer to minimize interfacial resistance, responsible for localizations of high stress-concentration spots as well as phonon and electron scattering sites, thus, obstructing the dissipation of the mechanical stress, thermal and electrical impulses [158, 160, 161, 170, 181, 187, 191, 192, 194, 195, 197, 213, 241]. It follows that polymer-filler interactions at the interface play a key role when manufacturing functional composites. The mechanism of interactions between BNNS/GNP and the hosting polymer depends both on the chemical structure of the polymer and on the surface chemistry of the filler particles. By way of example, it has been reported that BNNS and GNP may interact with aromatic polymers by π-π interactions, which in some instances has been exploited as way of modifying the surface chemistry of BNNS and GNP in an effort to design functionalised particles to interact with the host matrix. Other studies report the modification of BNNS and GNP particles by chemical reactions between the oxidised groups present on the BNNS/GNP surface and either commercial products or *ad-hoc* synthetized structures [21, 146, 247-258] (the concentration of the oxidised groups onto BNNS/GNP surface depends on the process adopted to prepare BNNS/GNP). It follows that a study of composites of polymers with BNNS/GNP encompasses a wide range of chemistry (inorganic

and organic chemistry) variables, which add complexity to the manufacturing of functional materials on industrial scale.

The combination of BNNS/GNP particle geometry and dimensions along with particle-polymer interactions govern the state of filler dispersion and distribution possible in a given matrix for a given manufacturing procedure. Contrasting opinions are reported when describing the effect of BNNS and GNP dispersion and distribution on the properties of the final composites. In one sense, the higher the degree of dispersion and distribution, the higher the reinforcement of the matrix, due to both of polymer entanglements around the filler particles and to the intrinsic stiffness and rigidity of BNNS and GNP [172, 178, 179, 182, 183, 185-188, 194, 198, 209, 210, 212, 216-220]. In another sense, a high level of BNNS/GNP dispersion and distribution could reduce the free volume in the amorphous region of the polymer matrix and generate a tortuous path for gases and liquids to diffuse, thus enhancing barrier properties [164, 195, 205, 215]. On the other side, for a given level of dispersion, the higher the degree of BNNS and GNP distribution in the matrix, the higher the average particle-particle distance, which prevent a 3D network of filler particles from being formed, essential for thermal and electrical conduction [136, 219, 224]. In other words, as the average distribution of BNNS and GNP in the polymer increases, a dilution of filler particles occurs locally, thus increasing the phonon and electron scattering (thermal and electrical resistance). Certainly, the concentration of BNNS/GNP as well as the particle size and shape needs to be considered [176, 180, 204, 229, 235, 259] since for a given concentration and distribution state, the particle-particle distances of large particles shorten compared to the smaller particles. It is been understood that the combination of particles of different dimensions and geometry could bridge small particles together, thus, overcoming the limitation of particle-particle distance at high distribution state. The bridging phenomenon induces a synergistic effect in the mechanical reinforcement and could facilitate the percolation of a 3D thermal/electrical conductive path [159, 163, 167, 173, 179, 182, 191, 202, 203, 228, 232-234, 236, 237, 239, 243, 246]. It has been also reported that in some cases a discrete degree of agglomeration (lower distribution state) of BNNS/GNP particles could help the thermal/electrical conduction by generating a 3D segregated morphology where the filler particles exclude and space out the non-conductive polymer domains [185, 260].

The BNNS and GNP alignment along a specific direction contributes to mechanical reinforcement, yet, in some instances a random distribution is preferred, particularly when attempting to improve the performance of the composites under impact deformation. Indeed, a

random distribution of BNNS and GNP particles provide the final composites with higher toughness, which is not likely to occur if BNNS/GNP are aligned un-directionally [193, 205, 210]. The alignment of BNNS and GNP particles plays a decisive role in the thermal and electrical conduction [146, 168, 169, 206, 227]. BNNS and GNP are thermal and electrically (GNP) conductive along the basal plane but not along the thickness (anisotropic 2D materials) where phonon and electron (GNP) scattering occur. Therefore, BNNS and GNP need to align in a way that the basal plane is oriented parallel to the direction where the thermal/electrical conduction is desired [261-263].

The processing of polymer composites influences their properties as it contributes to the state of dispersion and distribution of BNNS/GNP as well as the morphology of the final composites [26]. As discussed earlier in this report, melt mixing is exploited ordinarily by industry to compound polymer composites, as it is cost-effective (high throughput), environmental friendly (no solvents) and relatively easy to set-up [264]. Particularly, extrusion is one of the most effective processes for dispersing and distributing BNNS/GNP in thermoplastics on large scale, since it is a continuous process that can impart sufficient shear stresses to break BNNS/GNP agglomerates [168, 240]. Yet, the crucial post-processing procedures essential to shape compounded materials can alter the state of filler dispersion and distribution as well as the morphology of the polymer. By way of example, it has been reported that injection moulding generates specimens with the so-called 'skin-core' morphology, a layered structure where the filler particles locate across the thickness at the centre of the specimen, but a polymer rich phase forms on the skin of the moulded part [265]. In some cases, injection moulding changes the polymorphism of the polymer matrix, thus, affecting composite properties. For instance, the combination of GNP particle dimension/shape and injection moulding parameters induced the β-polymorph of PP, known to be stiffer and tougher than the more common α-form [266-271].

Both BNNS and GNP could act as nucleating agents for polymers, which change the crystallization mechanism as well as crystallite shape and dimensions during processing of the composites, again affecting the properties of the resultant material [186, 189, 196, 203, 204, 223, 226, 227, 231, 268]. Clearly, the addition of BNNS/GNP changes the structure and morphology of the host polymer, therefore, each polymer-filler system (composite) requires a tailored strategy to ensure the optimum properties enhancements are achieved on inclusion of BNNS or GNP in polymers.

2.4-   Conclusions

BNNS and GNP have been prepared by using a plethora of technologies such as mechanical exfoliation, including ball milling and sonication in presence of appropriate solvents (liquid exfoliation), chemical reactions and chemical vapour deposition (CVD). Interest in BNNS and GNP is increasing as functional additives for thermoplastic polymers due to their high thermal conductivity, electrical conductivity (GNP only) structural stability and mechanical properties. Yet, the preparation of functional composites with thermoplastics and BNNS/GNP is a non-trivial task embracing an ensemble of factors which must be considered including, filler geometry and morphology (platelets shape, length, aspect ratio and thickness), surface chemistry, polymer-filler interfacial interactions, platelet alignment and processing methodology. The breakthrough required to get these composites to market and prepared using industrially relevant processing technologies (*e.g.* extrusion, injection moulding) has not been realised. The limited published literature available on this topic and the lack of an in-depth understanding of the processing-structure property relationships of such composites must be addressed urgently.

This thesis focuses on the study of different grades of BNNS and GNP provided by Thomas Swan & Co Ltd. (TS), as functional fillers for model thermoplastics, specifically isotactic polypropylene (PP) and high-density polyethylene (HDPE). As described in Chapter 1, the aim of the project is to propose a R&D strategy for the industrial partner that can be used moving forward as a reference for the optimization of preparation of BNNS and GNP and their applications as functional additives for polymers. Furthermore, the aim is to provide the industrial partner with a deeper knowledge about BNNS and its use as a filler in thermoplastics, which has been much less studied when compared with GNP (Table 2.2).

References

[1] Lin Z, McNamara A, Liu Y, Moon K, Wong CP 2014 *Compos. Sci. Technol.* **90** 123-8.

[2] Kiran MSRN, Raidongia K, Ramamurty U, Rao CNR 2011 *Scripta Mater.* **64** 592-5.

[3] Zhi C, Bando Y, Tang C, Kuwahara H, Golberg D 2009 *Adv. Mater.* **21** 2889-93.

[4] Wang X, Pakdel A, Zhang J, Weng Q, Tianyou Z, Zhi C, Golberg D 2012 *Nanoscale Res. Lett.* **7:662**.

[5] Jung J, Kim J, Uhm YR, Jeon JK, Lee S, Lee HM, Rhee CK 2010 *Thermochim. Acta* **499** 8-14.

[6] Kemaloglu S, Ozkoc G, Aytac A 2010 *Thermochim. Acta* **499** 40-7.

[7] Blase X, Rubio A, Louie SG, Cohen ML 1994 *Europhys. Lett.* **28** 335-40.

[8] Chen Y, Zou J, Campbell SJ, Le Caer G 2004 *Appl. Phys. Lett.* **84** 2430-2.

[9] Zettl A, Chang CW, Begtrup G 2007 *Phys. Status Solidi B* **244** 4181-3.

[10] Chang CW, Fennimore AM, Afanasiev A, Okawa D, Ikuno T, Garcia H, Li D, Majumdar A, Zettl A 2006 *Phys. Rev. Lett.* **97**.

[11] Chang CW, Han WQ, Zettl A 2005 *Appl. Phys. Lett.* **86**.

[12] Chopra NG, Zettl A 1998 *Solid State Commun.* **105** 297-300.

[13] Hernandez E, Goze C, Bernier P, Rubio A 1998 *Phys. Rev. Lett.* **80** 4502-5.

[14] Golberg D, Costa PMFJ, Lourie O, Mitome M, Bai X, Kurashima K, Zhi C, Tang C, Bando Y 2007 *Nano Lett.* **7** 2146-51.

[15] Suryavanshi AP, Yu MF, Wen JG, Tang CC, Bando Y 2004 *Appl. Phys. Lett.* **84** 2527-9.

[16] Jiang XF, Weng QH, Wang XB, Li X, Zhang J, Golberg D, Bando Y 2015 *Journal of Materials Science & Technology* **31** 589-98.

[17] Lee SM, Kang DS, Roh JS 2015 *Carbon Letters* **16** 135-46.

[18] Kopelevich Y, Esquinazi P 2007 *Adv. Mater.* **19** 4559-63.

[19] Kim K, Kim J 2014 *Ceram. Int.* **40** 5181-9.

[20] Gorbachev RV*, et al.* 2011 *Small* **7** 465-8.

[21] Lin Y, Williams TV, Connell JW 2010 *J. Phys. Chem. Lett.* **1** 277-83.

[22] Kim KK*, et al.* 2012 *Nano Lett.* **12** 161-6.

[23] Song L*, et al.* 2010 *Nano Lett.* **10** 3209-15.

[24] Shi Y*, et al.* 2010 *Nano Lett.* **10** 4134-9.

[25] Coleman JN*, et al.* 2011 *Science* **331** 568-71.

[26] Pakdel A, Bando Y, Golberg D 2014 *Chem. Soc. Rev.* **43** 934-59.

[27] Golberg D, Bando Y, Huang Y, Terao T, Mitome M, Tang C, Zhi C 2010 *ACS Nano* **4** 2979-93.

[28] Han WQ, Wu LJ, Zhu YM, Watanabe K, Taniguchi T 2008 *Appl. Phys. Lett.* **93** 3.

[29] Lin Y, Williams TV, Cao W, Elsayed-Ali HE, Connell JW 2010 *J. Phys. Chem. C* **114** 17434-9.

[30] Yu J, Qin L, Hao Y, Kuang S, Bai X, Chong YM, Zhang W, Wang E 2010 *ACS Nano* **4** 414-22.

[31] Zhi C, Meng W, Yamazaki T, Bando Y, Golberg D, Tang C, Hanagata N 2011 *J. Mater. Chem.* **21** 5219-22.

[32] Tang C, Bando Y, Huang Y, Zhi C, Golberg D 2008 *Adv. Funct. Mater.* **18** 3653-61.

[33] Chopra NG, Luyken RJ, Cherrey K, Crespi VH, Cohen ML, Louie SG, Zettl A 1995 *Science* **269** 966-7.

[34] Zhi C, Bando Y, Tang C, Golberg D 2010 *Mater. Sci. Eng., R* **70** 92-111.

[35] Wang JS, Kayastha VK, Yap YK, Fan ZY, Lu JG, Pan ZW, Ivanov IN, Puretzky AA, Geohegan DB 2005 *Nano Lett.* **5** 2528-32.

[36] Loiseau A, Willaime F, Demoncy N, Schramchenko N, Hug G, Colliex C, Pascard H 1998 *Carbon* **36** 743-52.

[37] Golberg D, Bando Y, Eremets M, Takemura K, Kurashima K, Yusa H 1996 *Appl. Phys. Lett.* **69** 2045-7.

[38] Allen MJ, Tung VC, Kaner RB 2010 *Chem. Rev.* **110** 132-45.

[39] Novoselov KS, Geim AK, Morozov SV, Jiang D, Zhang Y, Dubonos SV, Grigorieva IV, Firsov AA 2004 *Science* **306** 666-9.

[40] Charlier JC, Blase X, De Vita A, Car R 1999 *Appl. Phys. A* **68** 267-73.

[41] Pakdel A, Zhi CY, Bando Y, Golberg D 2012 *Mater. Today* **15** 256-65.

[42] Li LH, Chen Y, Behan G, Zhang HZ, Petravic M, Glushenkov AM 2011 *J. Mater. Chem.* **21** 11862-6.

[43] Nag A, Raidongia K, Hembram K, Datta R, Waghmare UV, Rao CNR 2010 *ACS Nano* **4** 1539-44.

[44] Lian G, Zhang X, Tan M, Zhang S, Cui D, Wang Q 2011 *J. Mater. Chem.* **21** 9201-7.

[45] Wang X, Pakdel A, Zhi C, Watanabe K, Sekiguchi T, Golberg D, Bando Y 2012 *J. Phys. Condens. Matter* **24** 314205.

[46] Wang X, Zhi C, Li L, Zeng H, Li C, Mitome M, Golberg D, Bando Y 2011 *Adv. Mater.* **23** 4072-6.

[47] Zhao Z, Yang Z, Wen Y, Wang Y 2011 *J. Am. Ceram. Soc.* **94** 4496-501.

[48] Pacile D, Meyer JC, Girit CO, Zettl A 2008 *Appl. Phys. Lett.* **92** 133107.

[49] Han W-Q, Yu H-G, Liu Z 2011 *Appl. Phys. Lett.* **98**.

[50] Pierson HO 1975 *J. Compos. Mater.* **9** 228-40.

[51] Rozenberg AS, Sinenko YA, Chukanov NV 1993 *J. Mater. Sci.* **28** 5528-33.

[52] Middleman S 1993 *Mater. Sci. Eng. A.* **163** 135-40.

[53] Adams AC 1981 *J. Electrochem. Soc.* **128** 1378-9.

[54] Auwarter W, Suter HU, Sachdev H, Greber T 2004 *Chem. Mater.* **16** 343-5.

[55] Muller F, Stowe K, Sachdev H 2005 *Chem. Mater.* **17** 3464-7.

[56] Constant G, Feurer R 1981 *J Less Common Met* **82** 113-8.

[57] Paffett MT, Simonson RJ, Papin P, Paine RT 1990 *Surf. Sci.* **232** 286-96.

[58] Archer NJ 1979 *Phys. Techn.* **10** 152-61.

[59] Corso M, Auwarter W, Muntwiler M, Tamai A, Greber T, Osterwalder J 2004 *Science* **303** 217-20.

[60] Auwarter W, Kreutz TJ, Greber T, Osterwalder J 1999 *Surf. Sci.* **429** 229-36.

[61] Huda MN, Kleinman L 2006 *Phys. Rev* **74**.

[62] Cavar E, Westerstrom R, Mikkelsen A, Lundgren E, Vinogradov AS, Ng ML, Preobrajenski AB, Zakharov AA, Martensson N 2008 *Surf. Sci.* **602** 1722-6.

[63] Goriachko A, He Y, Knapp M, Over H, Corso M, Brugger T, Berner S, Osterwalder J, Greber T 2007 *Langmuir* **23** 2928-31.

[64] Preobrajenski AB, Vinogradov AS, Martensson N 2005 *Surf. Sci.* **582** 21-30.

[65] Preobrajenski AB, Vinogradov AS, Ng ML, Cavar E, Westerstrom R, Mikkelsen A, Lundgren E, Martensson N 2007 *Phys. Rev* **75** 245412.

[66] Morscher M, Corso M, Greber T, Osterwalder J 2006 *Surf. Sci.* **600** 3280-4.

[67] Corso M, Greber T, Osterwalder J 2005 *Surf. Sci.* **577** L78-L84.

[68] Vinogradov NA, Zakharov AA, Ng ML, Mikkelsen A, Lundgren E, Martensson N, Preobrajenski AB 2012 *Langmuir* **28** 1775-81.

[69] Allan MP, Berner S, Corso M, Greber T, Osterwalder J 2007 *Nanoscale Res. Lett.* **2** 94-9.

[70] Mueller F, Huefner S, Sachdev H 2008 *Surf. Sci.* **602** 3467-76.

[71] Sutter P, Lahiri J, Albrecht P, Sutter E 2011 *ACS Nano* **5** 7303-9.

[72] Jin C, Lin F, Suenaga K, Iijima S 2009 *Phys. Rev. Lett.* **102**.

[73] Meyer JC, Chuvilin A, Algara-Siller G, Biskupek J, Kaiser U 2009 *Nano Lett.* **9** 2683-9.

[74] Geim AK, Novoselov KS 2007 *Nat Mater* **6** 183-91.

[75] Yu QK, Lian J, Siriponglert S, Li H, Chen YP, Pei SS 2008 *Appl. Phys. Lett.* **93** 113103/1-3.

[76] Zhang Y, Zhang LY, Zhou CW 2013 *Acc. Chem. Res.* **46** 2329-39.

[77] Suk JW, Kitt A, Magnuson CW, Hao YF, Ahmed S, An JH, Swan AK, Goldberg BB, Ruoff RS 2011 *ACS Nano* **5** 6916-24.

[78] Li XS, Magnuson CW, Venugopal A, Tromp RM, Hannon JB, Vogel EM, Colombo L, Ruoff RS 2011 *J. Am. Chem. Soc.* **133** 2816-9.

[79] Hernandez Y*, et al.* 2008 *Nat Nanotechnol.* **3** 563-8.

[80] Blake P*, et al.* 2008 *Nano Lett.* **8** 1704-8.

[81] Park S, An JH, Jung IW, Piner RD, An SJ, Li XS, Velamakanni A, Ruoff RS 2009 *Nano Lett.* **9** 1593-7.

[82] Paredes JI, Villar-Rodil S, Martinez-Alonso A, Tascon JMD 2008 *Langmuir* **24** 10560-4.

[83] Bourlinos AB, Georgakilas V, Zboril R, Steriotis TA, Stubos AK 2009 *Small* **5** 1841-5.

[84] Ciesielski A, Samori P 2014 *Chem. Soc. Rev.* **43** 381-98.

[85] Lotya M*, et al.* 2009 *J. Am. Chem. Soc.* **131** 3611-20.

[86] Raccichini R, Varzi A, Passerini S, Scrosati B 2015 *Nat Mater* **14** 271-9.

[87] Abdelkader AM, Cooper AJ, Dryfe RAW, Kinloch IA 2015 *Nanoscale* **7** 6944-56.

[88] Shih CJ*, et al.* 2011 *Nat Nanotechnol.* **6** 439-45.

[89] Ambrosi A, Pumera M 2016 *Chemistry-a European Journal* **22** 153-9.

[90] Low CTJ, Walsh FC, Chakrabarti MH, Hashim MA, Hussain MA 2013 *Carbon* **54** 1-21.

[91] Stankovich S, Dikin DA, Piner RD, Kohlhaas KA, Kleinhammes A, Jia Y, Wu Y, Nguyen ST, Ruoff RS 2007 *Carbon* **45** 1558-65.

[92] Wang GX, Yang J, Park J, Gou XL, Wang B, Liu H, Yao J 2008 *J. Phys. Chem. C* **112** 8192-5.

[93] Chen WF, Yan LF, Bangal PR 2010 *J. Phys. Chem. C* **114** 19885-90.

[94] Chua CK, Pumera M 2014 *Chem. Soc. Rev.* **43** 291-312.

[95] Zhang JL, Yang HJ, Shen GX, Cheng P, Zhang JY, Guo SW 2010 *Chem. Commun.* **46** 1112-4.

[96] Paredes JI, Villar-Rodil S, Fernandez-Merino MJ, Guardia L, Martinez-Alonso A, Tascon JMD 2011 *J. Mater. Chem.* **21** 298-306.

[97] Zhu CZ, Guo SJ, Fang YX, Dong SJ 2010 *ACS Nano* **4** 2429-37.

[98] Aunkor MTH, Mahbubul IM, Saidur R, Metselaar HSC 2016 *Rsc Adv* **6** 27807-28.

[99] Bo Z, Shuai XR, Mao S, Yang HC, Qian JJ, Chen JH, Yan JH, Cen K 2014 *Scientific Reports* **4** 1-8.

[100] Wang Y, Shi ZX, Yin J 2011 *ACS Appl. Mater. Interfaces* **3** 1127-33.

[101] Zhang HB, Wang JW, Yan Q, Zheng WG, Chen C, Yu ZZ 2011 *J. Mater. Chem.* **21** 5392-7.

[102] Xiang JL, Drzal LT 2011 *Carbon* **49** 773-8.

[103] McAllister MJ*, et al.* 2007 *Chem. Mater.* **19** 4396-404.

[104] Meng WJ, Huang Y, Fu YQ, Wang ZF, Zhi CY 2014 *J. Mater. Chem. C* **2** 10049-61.

[105] Sajjad M, Morell G, Feng P 2013 *ACS Appl. Mater. Interfaces* **5** 5051-6.

[106] Chubarov M, Pedersen H, Hogberg H, Filippov S, Engelbrecht JAA, O'Connel J, Henry A 2014 *Physica B Condens. Matter* **439** 29-34.

[107] Malard LM, Pimenta MA, Dresselhaus G, Dresselhaus MS 2009 *Physics Reports-Review Section of Physics Letters* **473** 51-87.

[108] Shimada T*, et al.* 2005 *Carbon* **43** 1049-54.

[109] Mafra DL, Samsonidze G, Malard LM, Elias DC, Brant JC, Plentz F, Alves ES, Pimenta MA 2007 *Phys. Rev* **76** 233407/1-4.

[110] Kostoglou N, Polychronopoulou K, Rebholz C 2015 *Vacuum* **112** 42-5.

[111] Jager S, Bewilogua K, Klages CP 1994 *Thin Solid Films* **245** 50-4.

[112] Kostoglou N*, et al.* 2016 *Mater. Des.* **110** 540-8.

[113] Bera M, Chandravati, Gupta P, Maji PK 2018 *J Nanosci Nanotechnol* **18** 902-12.

[114] Kim HS, Bae HS, Yu J, Kim SY 2016 *Scientific Reports* **6** 1-9.

[115] Nazarov AS, Demin VN, Grayfer ED, Bulavchenko AI, Arymbaeva AT, Shin HJ, Choi JY, Fedorov VE 2012 *Chem. Asian J.* **7** 554-60.

[116] Jia SL, Wang ZH, Ding N, Wong YLE, Chen XF, Qiu GY, Chan TWD 2016 *Anal. Chim. Acta* **936** 123-9.

[117] Stobinski L, Lesiak B, Malolepszy A, Mazurkiewicz M, Mierzwa B, Zemek J, Jiricek P, Bieloshapka I 2014 *J. Electron. Spectrosc. Relat. Phenom.* **195** 145-54.

[118] Shtein M, Nadiv R, Buzaglo M, Kahil K, Regev O 2015 *Chem. Mater.* **27** 2100-6.

[119] Papageorgiou DG, Kinloch IA, Young RJ 2015 *Carbon* **95** 460-84.

[120] Jo I, Pettes MT, Kim J, Watanabe K, Taniguchi T, Yao Z, Shi L 2013 *Nano Lett.* **13** 550-4.

[121] Nika DL, Askerov AS, Balandin AA 2012 *Nano Lett.* **12** 3238-44.

[122] Potts JR, Dreyer DR, Bielawski CW, Ruoff RS 2011 *Polymer* **52** 5-25.

[123] Schwierz F. Graphene and beyond: Two-dimensional materials for transistor applications. In: George T, Dutta AK, Islam MS, editors. Micro- and Nanotechnology Sensors, Systems, and Applications Vii2015.

[124] Bunch JS, van der Zande AM, Verbridge SS, Frank IW, Tanenbaum DM, Parpia JM, Craighead HG, McEuen PL 2007 *Science* **315** 490-3.

[125] Raju APA, Lewis A, Derby B, Young RJ, Kinloch IA, Zan R, Novoselov KS 2014 *Adv. Funct. Mater.* **24** 2865-74.

[126] Eda G, Chhowalla M 2010 *Adv. Mater.* **22** 2392-415.

[127] Yoo JJ, *et al.* 2011 *Nano Lett.* **11** 1423-7.

[128] Patchkovskii S, Tse JS, Yurchenko SN, Zhechkov L, Heine T, Seifert G 2005 *Proceedings of the National Academy of Sciences of the United States of America* **102** 10439-44.

[129] Wang X, Zhi LJ, Mullen K 2008 *Nano Lett.* **8** 323-7.

[130] Miao XC, Tongay S, Petterson MK, Berke K, Rinzler AG, Appleton BR, Hebard AF 2012 *Nano Lett.* **12** 2745-50.

[131] Akinwande D, Petrone N, Hone J 2014 *Nat. Commun.* **5** 1-12.

[132] Chang HY, Yang SX, Lee JH, Tao L, Hwang WS, Jena D, Lu NS, Akinwande D 2013 *ACS Nano* **7** 5446-52.

[133] Lee GH, *et al.* 2013 *ACS Nano* **7** 7931-6.

[134] Lee J, Ha TJ, Li HF, Parrish KN, Holt M, Dodabalapur A, Ruoff RS, Akinwande D 2013 *ACS Nano* **7** 7744-50.

[135] Das S, Gulotty R, Sumant AV, Roelofs A 2014 *Nano Lett.* **14** 2861-6.

[136] Zhou W, Qi S, Li H, Shao S 2007 *Thermochim. Acta* **452** 36-42.

[137] Mosanenzadeh SG, Naguib HE 2016 *Compos. Part B-Eng.* **85** 24-30.

[138] Moore AL, Shi L 2014 *Mater. Today* **17** 163-74.

[139] Zhi CY, Bando Y, Terao T, Tang CC, Kuwahara H, Golberg D 2009 *Adv. Funct. Mater.* **19** 1857-62.

[140] Yung KC, Liem H 2007 *J. Appl. Polym. Sci.* **106** 3587-91.

[141] Kandanur SS, Rafiee MA, Yavari F, Schrameyer M, Yu ZZ, Blanchet TA, Koratkar N 2012 *Carbon* **50** 3178-83.

[142] Naskar AK, Keum JK, Boeman RG 2016 *Nat Nanotechnol.* **11** 1026-30.

[143] Du JH, Cheng HM 2012 *Macromol. Chem. Phys.* **213** 1060-77.

[144] Kuilla T, Bhadra S, Yao DH, Kim NH, Bose S, Lee JH 2010 *Prog. Polym. Sci.* **35** 1350-75.

[145] Leung SN 2018 *Compos Part B Eng* **150** 78-92.

[146] Guerra V, Wan C, McNally T 2019 *Prog. Mater Sci.* **100** 170-86.

[147] Yu CP, Zhang J, Tian W, Fan XD, Yao YG 2018 *Rsc Adv* **8** 21948-67.

[148] Huang XY, Wang S, Zhu M, Yang K, Jiang PK, Bando Y, Golberg D, Zhi CY 2015 *Nanotechnology* **26**.

[149] Qin LL, Li GH, Hou J, Yu XY, Ding HL, Zhang QX, Wang NY, Qu XW 2015 *Polym. Compos.* **36** 1675-84.

[150] Cui ZH, Martinez AP, Adamson DH 2015 *Nanoscale* **7** 10193-7.

[151] Lee J, Jung H, Yu S, Cho SM, Tiwari VK, Velusamy DB, Park C 2016 *Chem Asian J* **11** 1921-8.

[152] Stankovich S, Dikin DA, Dommett GHB, Kohlhaas KM, Zimney EJ, Stach EA, Piner RD, Nguyen ST, Ruoff RS 2006 *Nature* **442** 282-6.

[153] Lee WD, Im SS 2007 *Journal of Polymer Science Part B-Polymer Physics* **45** 28-40.

[154] Kalaitzidou K, Fukushima H, Drzal LT 2007 *Compos. Sci. Technol.* **67** 2045-51.

[155] Liang JJ, Huang Y, Zhang L, Wang Y, Ma YF, Guo TY, Chen YS 2009 *Adv. Funct. Mater.* **19** 2297-302.

[156] Villmow T, Kretzschmar B, Potschke P 2010 *Compos. Sci. Technol.* **70** 2045-55.

[157] Dennis HR, Hunter DL, Chang D, Kim S, White JL, Cho JW, Paul DR 2001 *Polymer* **42** 9513-22.

[158] Ahn K, Kim K, Kim M, Kim J 2015 *Ceram. Int.* **41** 2187-95.

[159] Ng HY, Lu XH, Lau SK 2005 *Polym. Compos.* **26** 66-73.

[160] Cakmakci E, Kocyigit C, Cakir S, Durmus A, Kahraman MV 2014 *Polym. Compos.* **35** 530-8.

[161] Iyer S, Detwiler A, Patel S, Schiraldi DA 2006 *J. Appl. Polym. Sci.* **102** 5153-61.

[162] Kemaloglu S, Ozkoc G, Aytac A 2010 *Polym. Compos.* **31** 1398-408.

[163] Pak SY, Kim HM, Kim SY, Youn JR 2012 *Carbon* **50** 4830-8.

[164] Xie SB, Istrate OM, May P, Barwich S, Bell AP, Khana U, Coleman JN 2015 *Nanoscale* **7** 4443-50.

[165] Ng HY, Lu XH, Lau SK 2005 *Polym. Compos.* **26** 778-90.

[166] Kim K, Kim J 2016 *Polymer* **101** 168-75.

[167] Xiao YJ, Wang WY, Lin T, Chen XJ, Zhang YT, Yang JH, Wang Y, Zhou ZW 2016 *J. Phys. Chem. C* **120** 6344-55.

[168] Zhang XL, Shen LY, Wu H, Guo SY 2013 *Compos. Sci. Technol.* **89** 24-8.

[169] Takahashi S, Imai Y, Kan A, Hotta Y, Ogawa H 2014 *J. Alloys Compd.* **615** 141-5.

[170] Kim K, Oh H, Kim J 2018 *Rsc Adv* **8** 33506-15.

[171] Yuan D, Pedrazzoli D, Pircheraghi G, Manas-Zloczower I 2017 *Polym Plast Technol Eng* **56** 732-43.

[172] Quan H, Zhang BQ, Zhao Q, Yuen RKK, Li RKY 2009 *Compos Part A Appl Sci Manuf.* **40** 1506-13.

[173] Ke K, McMaster M, Christopherson W, Singer KD, Manas-Zloczower I 2019 *Compos Part B Eng* **166** 673-80.

[174] Parameswaranpillai J, Joseph G, Shinu KP, Jose S, Salim NV, Hameed N 2015 *Rsc Adv* **5** 25634-41.

[175] Liu MF, Papageorgiou DG, Li SH, Lin KL, Kinloch IA, Young RJ 2018 *Compos Part A Appl Sci Manuf.* **110** 84-92.

[176] Greco A, Timo A, Maffezzoli A 2012 *Materials* **5** 1972-85.

[177] Patel KK, Purohit R 2019 *Sensors and Actuators a-Physical* **285** 17-24.

[178] Honaker K, Vautard F, Drzal LT 2017 *Materials Science and Engineering B-Advanced Functional Solid-State Materials* **216** 23-30.

[179] Wegrzyn M, Ortega A, Benedito A, Gimenez E 2015 *J. Appl. Polym. Sci.* **132**.

[180] M. Mahmoodi MT, S. S. Park. Characterization and Micro End Milling of Graphene Nano Platelet (GNP) and Carbon Nanotube (CNT) Filled Nanocomposites. ICOMM 20132013.

[181] Qiu YX, Wu DF, Xie WY, Wang ZF, Peng S 2018 *Compos. Struct.* **197** 21-7.

[182] Doagou Rad S, Islam, A., & Søndergaard Jensen, J. . Investigation of the mechanical properties of GNP/MWCNT reinforced PA66 hybrid nanocomposites. 33rd International Conference of the Polymer Processing Society (PPS-33). Cancuun, Mexico2017.

[183] Mayoral B, Harkin-Jones E, Khanam PN, AlMaadeed MA, Ouederni M, Hamilton AR, Sun D 2015 *Rsc Adv* **5** 52395-409.

[184] Beuguel Q, Mija A, Vergnes B, Peuvrel-Disdier E 2018 *Polym. Eng. Sci.* **58** 1937-44.

[185] Khanam PN, AlMaadeed MA, Ouederni M, Mayoral B, Hamilton A, Sun D 2016 *Advanced Manufacturing-Polymer & Composites Science* **2** 67-73.

[186] B. Mayoral EH-J, N. Khanam, M.A. Al Maadeed, M. Ouederni, A. Hamilton, D. Sun1. Characterizing Biaxially Stretched Polypropylene/Graphene Nanoplatelet Composites. 21st International Conference on Composite Materials2017.

[187] Ruey Shan Chen MFHMR, Dalila Shahdan, Sahrim Ahmad 2019 *PLOS ONE* **14** 1-16.

[188] Scaffaro R, Botta L, Maio A, Gallo G 2017 *Compos Part B Eng* **109** 138-46.

[189] Mounir El Achaby F-EA, Sebastien Vaudreuil, Abou el Kacem Qaiss, Mostapha Bousmina, Omar Fassi-Fehri 2012 *Wiley Online Library*.

[190] Mohd Bijarimi NS, Azizan Ramli, Said Nurdin, Waleed Alhadadi, Muhammad Zakir Muzakkar, Jamiluddin Jaafar 2020 *Indones. J. Chem.* **20** 276-81.

[191] Tarawneh MA, Yu LJ, Tarawni MA, Ahmad SH, Al-Banawi O, Batiha MA 2015 *World Journal of Engineering* **12** 437-42.

[192] Siti R. Ahmad RJY, Ian A. Kinloch 2015 *International Journal of Chemical Engineering and Applications* **6** 1-5.

[193] Beloshenko VA, Voznyak AV, Voznyak Y, Novokshonova LA, Grinyov VG 2017 *Compos. Sci. Technol.* **139** 47-56.

[194] Araby S, Zaman I, Meng QS, Kawashima N, Michelmore A, Kuan HC, Majewski P, Ma J, Zhang LQ 2013 *Nanotechnology* **24**.

[195] Idumah CI, Hassan A 2016 *Synth. Met.* **212** 91-104.

[196] Jun YS, Um JG, Jiang GP, Lui G, Yu AP 2018 *Compos Part B Eng* **133** 218-25.

[197] Ahmad SR, Xue CZ, Young RJ 2017 *Materials Science and Engineering B-Advanced Functional Solid-State Materials* **216** 2-9.

[198] Goncalves C, Pinto A, Machado AV, Moreira J, Goncalves IC, Magalhaes F 2018 *Polym. Compos.* **39** E308-E20.

[199] Matsumoto K, Nakade Y, Sugimoto K, Tanaka T. An Investigation on Dispersion State of Graphene in Polypropylene/Graphite Nanocomposite with Extensional Flow Mixing. In: Maazouz A, editor. Proceedings of Pps-32: The 32nd International Conference of the Polymer Processing Society2017.

[200] Al-Jabareen A, Al-Bustami H, Harel H, Marom G 2013 *J. Appl. Polym. Sci.* **128** 1534-9.

[201] Kalaitzidou K, Fukushima H, Drzal LT 2007 *Carbon* **45** 1446-52.

[202] Nordin NM, Buys YF, Anuar H, Ani MH, Pang MM 2019 *Materials Today-Proceedings* **17** 500-7.

[203] Kashi S, Gupta RK, Kao N, Hadigheh SA, Bhattacharya SN 2018 *Journal of Materials Science & Technology* **34** 1026-34.

[204] Rashmi BJ, Prashantha K, Lacrampe MF, Krawczak P 2018 *Adv. Polym. Tech.* **37** 1067-75.

[205] Gaska K, Kadar R, Rybak A, Siwek A, Gubanski S 2017 *Polymers* **9**.

[206] Sullivan EM, Karimineghlani P, Naraghi M, Gerhardt RA, Kalaitzidou K 2016 *Eur. Polym. J.* **77** 31-42.

[207] Reghat M, Ghasemi I, Farno E, Azizi H, Namin PE, Karrabi M 2017 *Soft Materials* **15** 103-12.

[208] Gedler G, Antunes M, Velasco JI 2016 *Compos Part B Eng* **93** 143-52.

[209] Papageorgiou DG, Liu MF, Li ZL, Valles C, Young RJ, Kinloch IA 2019 *Compos. Sci. Technol.* **175** 60-8.

[210] Kalaitzidou K, Fukushima H, Drzal LT 2007 *Compos Part A Appl Sci Manuf.* **38** 1675-82.

[211] Alessandro Pegoretti DP, Kyriaki Kalaitzidou. Improving Interfacial Stress Transfer In Glass Fiber Polymer Composites Through Graphite Nanoplatelets. 20th International Conference on Composite Materials. Copenaghen2015.

[212] Inuwa IM, Hassan A, Samsudin SA, Haafiz MKM, Jawaid M, Majeed K, Razak NCA 2014 *J. Appl. Polym. Sci.* **131**.

[213] Al-Saleh MH 2015 *Synth. Met.* **209** 41-6.

[214] F. Vautard TH-S, L. T. Drzal. High Density Polyethylene-Exfoliated Graphene Nanoplatelet Nanocomposites For Automotive Fuel Line And Fuel Tanks Applications.

[215] K. Honaker FV, L.T. Drzal. Processing Methods Of High Density Polyethylene exfoliated Graphene Nanoplatelet Nanocomposites For Automotive Fuel Tanks Applications.

[216] La Mantia FP, Ceraulo M, Mistretta MC, Botta L 2018 *Polym. Test.* **71** 10-7.

[217] Meszaros L, Szakacs J, Ltd T. Elastic Recovery At Graphene Reinforced Pa 6 Nanocomposites2014.

[218] Nafi Yesildag CH, Maximilian Adamy, Christian Windeck. Properties of polyamide 6-graphenecomposites produced and processed on industrial scale. AIP Conference Proceedings 19142017.

[219] Wu H, Rook B, Drzal LT 2013 *Polym. Compos.* **34** 426-32.

[220] Luis C. Herrera-Ramírez PC, Juan P. Fernández-Blázquez, Ángel Fernández, Roberto Guzmán de Villoria 2015 *Composites of Science and Technology* **111** 9-16.

[221] Seretis GV, Manolakos DE, Provatidis CG 2018 *Compos Part B Eng* **145** 81-9.

[222] Zeng QQ, Wang YF, Wang YM, Cao W, Liu CT, Shen CY 2019 *Polym. Test.* **78**.

[223] Quentin Beuguel SAEB, Daniel Settipani, Gabriel Monge, Jean-Marc Haudin, et al.. 2018 *Polymer Crystallization* **1** 1-10.

[224] Krause B, Potschke P. Electrical And Thermal Conductivity Of Polypropylene Filled With Combinations Of Carbon Fillers. In: Holzer CH, Payer M, editors. Proceedings of the Regional Conference Graz 2015 - Polymer Processing Society Pps: Conference Papers2016.

[225] Liebscher M, Blais MO, Potschke P, Heinrich G 2013 *Polymer* **54** 5875-82.

[226] Kalaitzidou K, Fukushima H, Askeland P, Drzal LT 2008 *J. Mater. Sci.* **43** 2895-907.

[227] Jiang X, Drzal LT 2012 *Polym. Compos.* **33** 636-42.

[228] Yu J, Choi HK, Kim HS, Kim SY 2016 *Compos Part A Appl Sci Manuf.* **88** 79-85.

[229] Krause B, Rzeczkowski P, Potschke P 2019 *Polymers* **11**.

[230] Inuwa IM, Hassan A, Wang DY, Samsudin SA, Haafiz MKM, Wong SL, Jawaid M 2014 *Polym. Degrad. Stab.* **110** 137-48.

[231] Tarani E, Wurm A, Schick C, Bikiaris DN, Chrissafis K, Vourlias G 2016 *Thermochim. Acta* **643** 94-103.

[232] Tarawneh MA, Saraireh SA, Chen RS, Ahmad SH, Al-Tarawni MAM, Al-Tweissi M, Yu LJ *J. Appl. Polym. Sci.*

[233] Noh YJ, Kim SY 2015 *Polym. Test.* **45** 132-8.

[234] Liang JZ, Wang JZ, Tsui GCP, Tang CY 2018 *J. Thermoplast. Compos. Mater.* **31** 246-64.

[235] I. M. Inuwa AH, S. A. Shamsudin 2014 *The Malaysian Journal of Analytical Sciences,* **18** 466-77.

[236] Ke K, Bonab VS, Yuan D, Manas-Zloczower I 2018 *Carbon* **139** 52-8.

[237] Liu Y*, et al.* 2018 *J. Mater. Chem. C* **6** 2760-8.

[238] Kuester S, Demarquette NR, Ferreira JC, Soares BG, Barra GMO 2017 *Eur. Polym. J.* **88** 328-39.

[239] Kashi S, Hadigheh SA, Varley R 2018 *Polymers* **10**.

[240] Wegrzyn M, Galindo B, Benedito A, Gimenez E 2015 *J. Appl. Polym. Sci.* **132**.

[241] Maiti S, Khatua BB 2016 *Polym. Compos.* **37** 2058-69.

[242] Poosala A, Kurdsuk W, Aussawasathien D, Pentrakoon D 2014 *Chiang Mai Journal of Science* **41** 1274-86.

[243] Ke K, McMaster M, Christopherson W, Singer KD, Manas-Zloczower I 2019 *Compos Part A Appl Sci Manuf.* **126**.

[244] Chen GH, Chen XF, Wang HQ, Wu DJ 2007 *J. Appl. Polym. Sci.* **103** 3470-5.

[245] Jiang X, Drzal LT 2012 *J. Appl. Polym. Sci.* **124** 525-35.

[246] Dweiri R 2015 *Jordan Journal of Mechanical and Industrial Engineering* **9** 1-8.

[247] Wang W, Bando Y, Zhi C, Fu W, Wang E, Golberg D 2008 *J. Am. Chem. Soc.* **130** 8144-5.

[248] Zhi C, Bando Y, Tang C, Golberg D 2005 *J. Am. Chem. Soc.* **127** 17144-5.

[249] Cho EC, Huang JH, Li CP, Chang-Jian CW, Lee KC, Hsiao YS, Huang JH 2016 *Carbon* **102** 66-73.

[250] Guo H, Li X, Li BA, Wang JX, Wang SC 2017 *Mater. Des.* **114** 355-63.

[251] Ding P, Su SS, Song N, Tang SF, Liu YM, Shi LY 2014 *Carbon* **66** 576-84.

[252] Song N, Yang JW, Ding P, Tang SF, Shi LY 2015 *Compos Part A Appl Sci Manuf.* **73** 232-41.

[253] Ding P, Zhang J, Song N, Tang SF, Liu YM, Shi LY 2015 *Compos Part A Appl Sci Manuf.* **69** 186-94.

[254] Lin H, Pei LX, Zhang LZ 2018 *J. Appl. Polym. Sci.* **135** 46397/1-8.

[255] Xie B-H, Huang X, Zhang G-J 2013 *Ceram. Int.* **39** 8543-8.

[256] Hou J, Li GH, Yang N, Qin LL, Grami ME, Zhang QX, Wang NY, Qu XW 2014 *Rsc. Adv.* **4** 44282-90.

[257] Jin W, Zhang W, Gao Y, Liang G, Gu A, Yuan L 2013 *Appl. Surf. Sci.* **270** 561-71.

[258] Muratov DS, Kuznetsov DV, Il'inykh IA, Burmistrov IN, Mazov IN 2015 *Compos. Sci. Technol.* **111** 40-3.

[259] Burger N, Laachachi A, Ferriol M, Lutz M, Toniazzo V, Ruch D 2016 *Prog. Polym. Sci.* **61** 1-28.

[260] Du JH, Zhao L, Zeng Y, Zhang LL, Li F, Liu PF, Liu C 2011 *Carbon* **49** 1094-100.

[261] Yuan C, Xie B, Huang MY, Wu RK, Luo XB 2016 *Int. J. Heat Mass Transfer* **94** 20-8.

[262] Zhu DC, Ren YY, Liao GX, Jiang SL, Liu FH, Guo JJ, Xu GJ 2017 *J. Appl. Polym. Sci.* **134**.

[263] Guerra V, Wan C, McNally T, 2020 *Functional Composites Materials* **1** 1-11.

[264] Sakai T 2013 *Polimery* **58** 847-57.

[265] M. Bilewicz JCV, A.M. Cunha, L.A. Dobrzański 2006 *Journal of Achievements in Materials and Manufacturing Engineering* **15** 159-65.

[266] Varga J 2002 *J Macromol Sci Polymer B* **B41** 1121-71.

[267] KargerKocsis J, Varga J, Ehrenstein GW 1997 *J. Appl. Polym. Sci.* **64** 2057-66.

[268] Guerra V, Wan C, McNally T 2019 *Journal of Composites Science* **3** 38.

[269] Kalaitzidou K, Fukushima H, Askeland P, Drzal LT 2008 *J Mater Sci* **43** 2895-907.

[270] Dai J, Shen Y, Yang JH, Huang T, Zhang N, Wang Y 2014 *Colloid. Polym. Sci.* **292** 923-33.

[271] Tjong SC, Shen JS, Li RKY 1995 *Scr Metall Mater* **33** 503-8.

CHAPTER 3: MATERIALS AND METHODS

3.1- Materials and equipment

The BNNS and GNP were kindly provided by our industrial partner Thomas Swan & Co. Ltd (TS) and prepared by High-Pressure Homogenisation (HPH) (Chapter 1). The grades studied were X-BNNS-SC, X-BNNS-T, Y-BNNS-L, X-GNP-SC, X-GNP-L, Y-GNP-L. The letters X and Y indicate the bulk materials used in the HPH and define the different morphologies thereof. Specifically, X-BNNS-SC/X-BNNS-T and Y-BNNS-L were exfoliated from BN-X and BN-Y respectively, whereas X-GNP-SC/X-GNP-L and Y-GNP-L were exfoliated from graphite-X and graphite-Y respectively. The letters SC, T, L indicate the surfactants used during HPH. SC is sodium cholate, which is an ionic hygroscopic surfactant whose structure is reported in Figure 3.1, whereas T and L are non-ionic amphiphilic surfactants with a polyether-polyol structure containing aromatic units. In particular, the surfactant T presents a branched aromatic head whereas the surfactant L displays an aromatic head with no functionalities. The chemical structures of the surfactants T and L are not reported as confidential for the industrial partner.
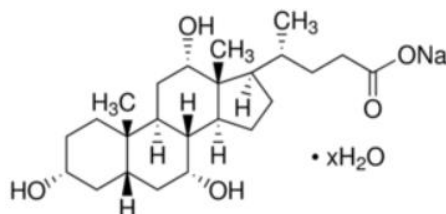
Figure 3.1: Sodium Cholate structure. The hydroxylic groups confer hydrophilic and hygroscopic characteristics to the molecule.

The grades of isotactic Polypropylene (PP) and high density polyethylene (HDPE) used are Exxon PP 1063L1, MFR=8.0g/10min and Exxon HDPE 6081, MFR=8.0g/10min. The materials were purchased from the distributor Plastribution, St Ives, Cambridgeshire, UK. The PP and HDPE pellets were cryo-milled in the freezer mill SPEXSamplePrep and dried overnight in an oven (50°C) before admixing them with BNNS and GNP.

3.1.1- Composites of PP and HDPE with X-BNNS-SC and X-GNP-SC by laboratory scale extruder and micro injection moulding.

The manufacturing of composites of PP and HDPE with X-BNNS-SC/X-GNP-SC by laboratory scale extruder was carried out as initial study phase to understanding the behaviour of these grades of BNNS and GNP (starting model grades) in the matrices on the small scale production.

PP and HDPE powders were individually mixed with X-BNNS-SC and X-GNP-SC at different loadings in a beaker before being fed to the extruder (the formulations prepared are reported in Table 3.2). The laboratory scale extruder used is a Thermo Scientific, HAAKE Lab II. The composites exiting from the extruder were directly fed in to the injection moulding tool (Micro-injection moulding Thermo Scientific, Multijet Plus) in order to prepare the specimens for testing and characterisation. Figure 3.2 shows the equipment utilised and Table 3.1 the processing parameters applied.

Laboratory scale extruder

Micro injection moulding

1- Extruder panel control
2- Feeder
3- Screws
4- Recycling
5- Recycling controller
6- Exit
7- Disk, Bar, Dumbell moulds
8- Thermal Conductivity mould
9- Harvesting cylinder
10- Injection moulding panel control
11- Mould holder
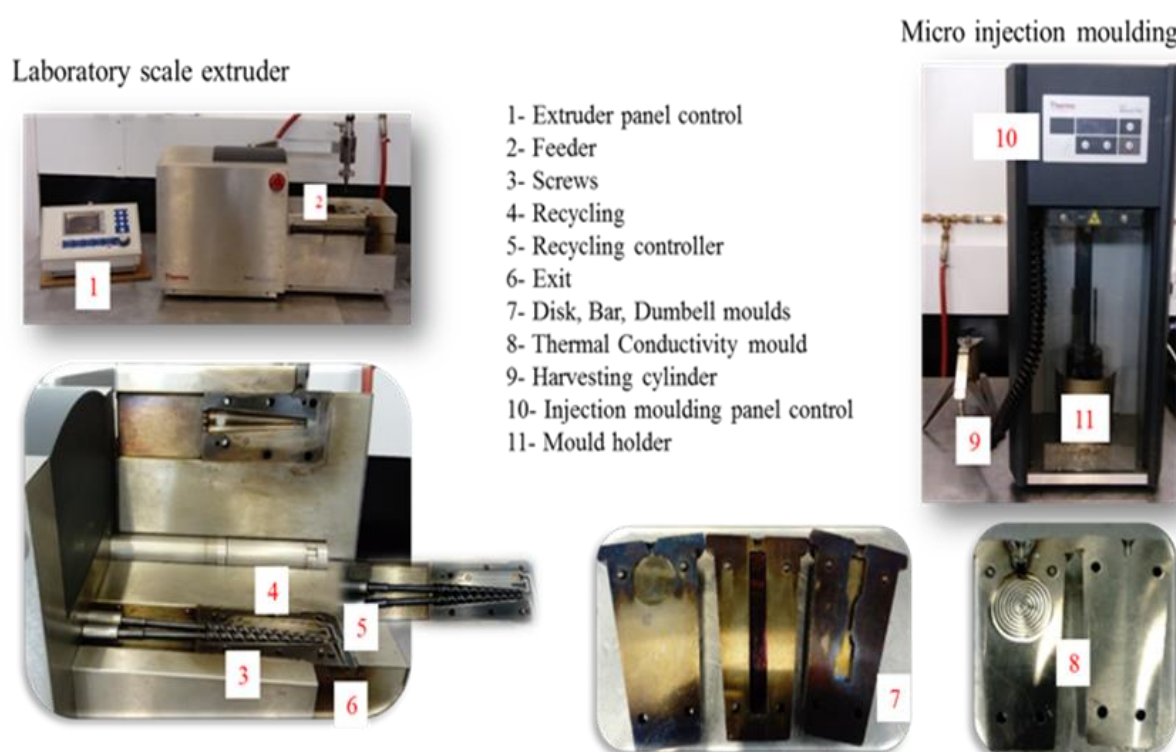
Figure 3.2. Laboratory scale extruder and micro-injection moulding used to prepare PP and HDPE composites with X-BNNS-SC and X-GNP-SC. The extruder reported shows a conical screws profile. The mould used to shape the final products are also reported. Specifically, the circle shape was used to mould the molten materials for rheology measurements and XRD analysis. The dumbbell was used to prepare the specimens for tensile testing.

Table 3.1: Processing conditions adopted to prepare PP and HDPE composites with X-BNNS-SC and X-GNP-SC by micro-processing.

System	T barrel (°C)	t harvesting (min)	T cylinder (°C)	T mould (°C)	Injection pressure (bar)	Post-injection pressure (bar)	t pressing (s)
PP+X-BNNS-SC	175	3-4 min	190-200	70	500-600	200	5
PP+X-GNP-SC							
HDPE+X-BNNS-SC	175		190-200	70			
HDPE+X-GNP-SC							

The processing temperatures set for extrusion and injection moulding were taken from between the melting and degradation points of the polymers, obtained by performing Differential Scanning Calorimetry (DSC) and thermo-gravimetric analysis (TGA) measurements on the raw materials. The temperature window was verified and set between 150-250 ºC for PP and 150-400 ºC for HDPE. The temperature in the extruder was set in a way that the polymer flowed with no bridging phenomenon at the feeding zone whereas the conditions for the injection moulding were set in a way that the polymer could flow through the cylinder to the mould without clogging and crystallize in regular, uniform, smooth and levelled specimens [1]. Table 3.2 lists the composites prepared by micro-processing.

Table 3.2: Composites of PP and HDPE. X-BNNS-SC and X-GNP-SC as provided by TS, prepared by micro-processing.

PP composites	
PP+X-BNNS-SC 0.1wt%	PP+X-GNP-SC 0.1wt%
PP+X-BNNS-SC 0.3wt%	PP+X-GNP-SC 0.3wt%
PP+X-BNNS-SC 0.5wt%	PP+X-GNP-SC 0.5wt%
PP+X-BNNS-SC 1wt%	PP+X-GNP-SC 1wt%
PP+X-BNNS-SC 3wt%	PP+X-GNP-SC 3wt%
PP+X-BNNS-SC 5wt%	PP+X-GNP-SC 5wt%
HDPE composites	
HDPE+X-BNNS-SC 0.1wt%	HDPE+X-GNP-SC 0.1wt%
HDPE+X-BNNS-SC 0.3wt%	HDPE+X-GNP-SC 0.3wt%
HDPE+X-BNNS-SC 0.5wt%	HDPE+X-GNP-SC 0.5wt%
HDPE+X-BNNS-SC 1wt%	HDPE+X-GNP-SC 1wt%
HDPE+X-BNNS-SC 3wt%	HDPE+X-GNP-SC 3wt%
HDPE+X-BNNS-SC 5wt%	HDPE+X-GNP-SC 5wt%

3.1.2- Composites of PP and HDPE with different grade of BNNS and GNP prepared by 16-mm co-rotating twin-screws extruder and micro-injection moulding

The 16mm co-rotating twin-screw extruder used in this work was a PRISM ThermoFischer Scientific, L/D = 40 for the production of composites on a few hundreds of grams scale (up to 500 g/h). The machine is a parallel twin-screw extruder and more industrially relevant than the micro-extruder (laboratory scale extruder). The advantage of the parallel twin-screw extruder over the conical extruder (laboratory scale extruder) was the ability to modulate the screw and temperature, key factors when distributing and dispersing BNNS/GNP evenly in PP/HDPE.

The screws were fitted with feed screw (FS) 45/45 forward and mixing elements of 3mm thickness, properly oriented to each other to guarantee optimal mixing conditions. The screw

configuration was based on the optimization of the highest mixing conditions (0–90°) with the lowest one (0°), as suggested by the manufacturer. The profile was set as follows:

- 10 FS followed by 0–90°/4/12, 0°/4/12, and 90–0°/4/12 mixing elements, with respect to the last FS element offset;
- 6 FS elements followed by 0°/6/18 mixing elements;
- 9 FS elements followed by 0°/4/12, 0–90°/8/24 mixing elements;
- 7 FS elements to close the screws assembling.

The PP/HDPE powder were individually mixed with the BNNS/GNP grades manually in a plastic bag before being placed in the feeder connected to the extruder. The molten composite filament was drawn from the extruder, cooled in a water bath, and pelletized using a laboratory pelletizer. The pellets were collected, dried in the oven at 50°C overnight and processed using the same micro-injection molding conditions as per Table 3.1.

Figure 3.2 shows a schematic of the equipment used along with a photograph of the screws and temperature profile set in the extruder.

											Volumetric feeder rate (%)	Screws speed (RPM)
T(°C) PP	205	200	195	195	190	190	185	185	180	170	15	100
T(°C) HDPE	210	205	205	200	200	195	190	185	180	170	15	100
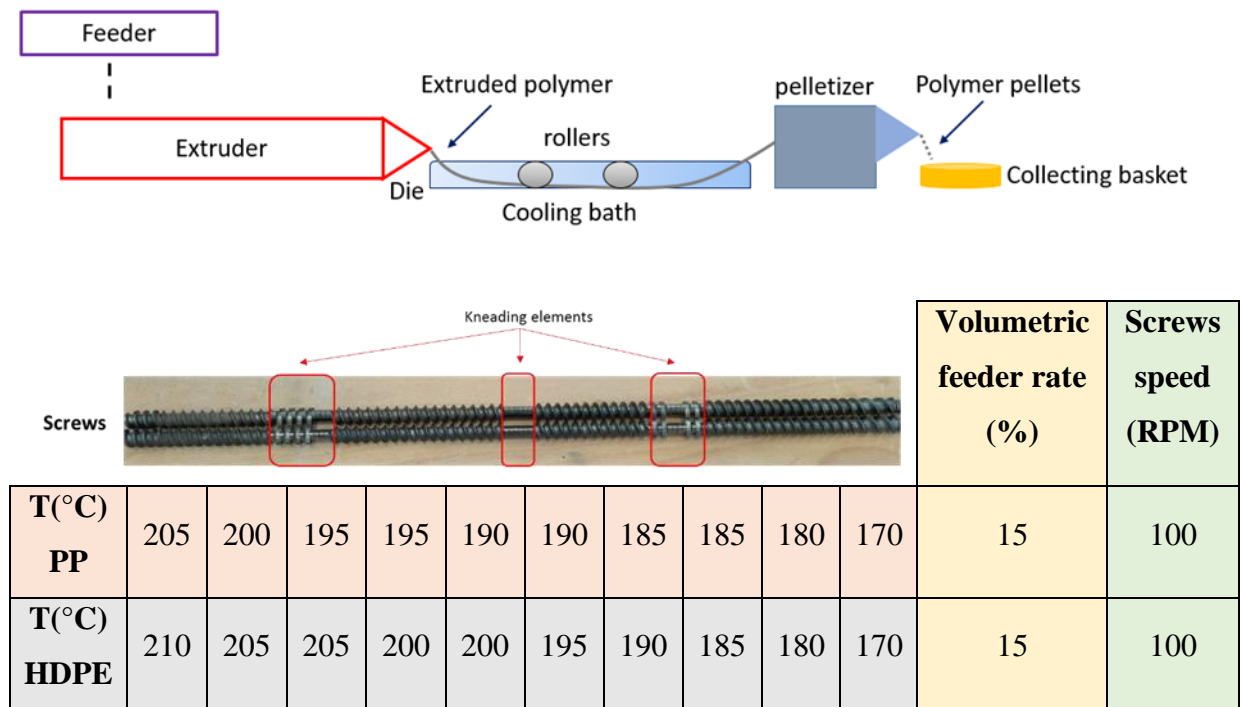
Figure 3.3: Schematic of the extrusion process adopted to prepare the composites of PP/HDPE with BNNS and GNP. The polymer/filler powders were fed into the extruder where melt mixing occurred. The filament exiting the extruder was cooled down in a water baths before

being pelletised. The screw and temperature profiles adopted when using the 16mm co-rotating twin screw extruder are also reported.

The temperatures selected for the extrusion and injection moulding were decided based on the window for the melting and degradation points of the polymers and BNNS/GNP studied, as reported in section 3.1.1. The temperature settings along the barrel were monitored (from the monitor attached to the extruder) and adjusted in a way that the actual profile matched with the set-points, the system equilibrated to a constant output and no bridging phenomenon occurred at the feeding zone [2]. It should be underlined that the study of different screws-profiles, die geometries, temperature profiles, feeding configurations is beyond this project.

Table 3.3 list the composites prepared by 16mm co-rotating twin-screws extruder and micro-injection moulding.

Table 3.3: composites of PP and HDPE with the BNNS/GNP grades as provided by TS, prepared by 16-mm co-rotating twin-screws extruder and micro-injection moulding. Only the PP was admixed with the entire set of BNNS/GNP as it was exploited as model polymer. The compositions were chosen based on data reported in the literature (see Chapter 2). The maximum filler loading was set at 10wt%, since higher loadings make the mixing more difficult due to an increase of the viscosity of the molten polymer.

Composites of PP		
PP+X-BNNS-SC 0.1wt%	PP+X-BNNS-T 0.1wt%	PP+Y-BNNS-L 0.1wt%
PP+X-BNNS-SC 0.3wt%	PP+X-BNNS-T 0.3wt%	PP+Y-BNNS-L 0.3wt%
PP+X-BNNS-SC 0.5wt%	PP+X-BNNS-T 0.5wt%	PP+Y-BNNS-L 0.5wt%
PP+X-BNNS-SC 1wt%	PP+X-BNNS-T 1wt%	PP+Y-BNNS-L 1wt%
PP+X-BNNS-SC 3wt%	PP+X-BNNS-T 3wt%	PP+Y-BNNS-L 3wt%
PP+X-BNNS-SC 5wt%	PP+X-BNNS-T 5wt%	PP+Y-BNNS-L 5wt%
PP+X-BNNS-SC 10wt%	PP+X-BNNS-T 10wt%	PP+Y-BNNS-L 10wt%
PP+X-GNP-SC 0.1wt%	PP+X-GNP-L 0.1wt%	PP+Y-GNP-L 0.1wt%
PP+X-GNP-SC 0.3wt%	PP+X-GNP-L 0.3wt%	PP+Y-GNP-L 0.3wt%
PP+X-GNP-SC 0.5wt%	PP+X-GNP-L 0.5wt%	PP+Y-GNP-L 0.5wt%
PP+X-GNP-SC 1wt%	PP+X-GNP-L 1wt%	PP+Y-GNP-L 1wt%
PP+X-GNP-SC 3wt%	PP+X-GNP-L 3wt%	PP+Y-GNP-L 3wt%
PP+X-GNP-SC 5wt%	PP+X-GNP-L 5wt%	PP+Y-GNP-L 5wt%

PP+X-GNP-SC 10wt%	PP+X-GNP-L 10wt%	PP+Y-GNP-L 10wt%
Composites of HDPE		
HDPE+X-BNNS-SC 0.1wt%	HDPE+X-GNP-SC 0.1wt%	HDPE+Y-BNNS-L 5wt%
HDPE+X-BNNS-SC 0.3wt%	HDPE+X-GNP-SC 0.3wt%	
HDPE+X-BNNS-SC 0.5wt%	HDPE+X-GNP-SC 0.5wt%	
HDPE+X-BNNS-SC 1wt%	HDPE+X-GNP-SC 1wt%	
HDPE+X-BNNS-SC 3wt%	HDPE+X-GNP-SC 3wt%	
HDPE+X-BNNS-SC 5wt%	HDPE+X-GNP-SC 5wt%	

3.2- Characterization of BNNS and GNP grades

Scanning Electron Microscopy (SEM) X-ray Diffraction (XRD) and Raman spectroscopy were used to determine the morphology and crystalline structure of the different grades of BNNS and GNP. As reported in the literature, particle shape and dimensions along with imperfections in the crystal lattice affect the properties of BNNS/GNP. Particularly, large and smooth platelets with low defect concentrations in the lattice structure are known to be required to optimise the mechanical properties, thermal and electrical (GNP only) conduction (Chapter 2) of the composites.

A Zeiss Sigma field emission instrument, provided with a Gemini column, was used to perform the SEM analysis. The images were recorded with the InLens detector at a working distance of up to 3.2 mm and an acceleration voltage of up to 5 kV. Before SEM imaging, the samples were placed on SEM stubs previously covered with carbon adhesive tape. The samples were then sputter coated (up to 10 nm) using a Pd/Pt metal target (Cressington 108 auto), to minimize charging effects on the surface of the samples due to the back scattering of the electron beam when hitting non-electrical conductive materials and under a weak argon atmosphere.

For Wide-angle X-ray Diffraction (WAXD, just named XRD afterwards) studies, a PANalytical Empyrean X-ray diffractometer was used. The instrument was equipped with a Co ($K_{\alpha 1}$ (λ) = 1.789 Å) source, a PIXcel^{3D} detector, a tube voltage of 45 kV and current of 40 amps. The tests were set in reflectance mode with a stage speed of 1 rps.

Raman spectroscopy was performed with a Renishaw inVia^{TM} Reflex confocal Raman microscope (Gonzo) equipped with a 532 nm solid state laser, x5, x20, x50 objectives, Renishaw CCD detector (Visible – NIR) and a 10 mW laser, which was spot focused on the samples with an exposure time up to 2 min and 5 collections.

The surface chemistry of the different grades of BNNS and GNP was investigated by X-Ray photoemission spectra (XPS) and Sessile tests. An understanding of the chemistry of the BNNS/GNP is essential since it in part determines the chemical-physical interactions with the polymer matrix. XPS measurements were performed using a Kratos Axis Ultra delay-line-detector XPS, provided with a magnetic immersion lens and charge neutralisation system with spherical mirror and concentric hemispherical analysers. The Al K_α monochromatic ray (1.487 keV; emission = 10 mA) with electrostatic lens (for BNNS grades) and hybrid lens (for GNP grades) was used for the survey spectra, registered in the range of binding energy 0-1200 eV (1eV per step). The core spectra were registered using the same Al K_α monochromatic ray and the same lenses used for the survey spectra. The B1s, N1s (for the BNNS grades), C1s and O1s (for the GNP grades) were detected in the range of 180-190 eV, 388-398 eV, 280-300 eV, 526-550 eV respectively. The detector was placed at 90° with respect to the samples and measurements taken on the nominal area of 300 μm-700 μm. The results were analysed using CasaXPS analysis software.

A Dyne Testing-ThetaLite instrument, provided with a camera and a light source for optical measurements, was used to perform sessile tests. The samples were pelletized before being placed onto the stage and the measurements started after a drop of distilled water (~6 μL) was placed onto the samples by using a manual dispenser. Five measurements were performed at five different points on the pellet. The images were recorded at room temperature, for 10 seconds and at 10% FPS. The Young-Laplace method was set for data elaboration.

The thermal stability of the different grades of BNNS and GNP was determined from TGA, data essential for the temperature set-up during extrusion with PP/HDPE. The analysis was performed with a Mettler Toledo TGA1-STARe system. The samples were placed in to 70 μL alumina pans and heated from room temperature to 800 °C at a constant heating rate of 10 K/ min under oxidative conditions.

3.3- Characterization of composites of PP and HDPE with BNNS and GNP grades.

The morphology and crystalline structure of the composites of PP/HDPE with the different grades of BNNS/GNP was investigated by SEM, XRD and DSC. Specifically, the SEM was exploited as way of visual screening of the BNNS/GNP distribution and morphology in the polymer matrix. XRD and DSC measurements were performed to assess the effect of BNNS/GNP on the crystalline structure and polymorphism of PP and HDPE.

The microscope used for SEM imaging is the same described in section 3.2. The images were collected with an InLens detector, a working distance up to 3.2 mm and an acceleration voltage up to 5 kV. The samples were cryo-fractured and placed on carbon adhesive tape mounted on an aluminium SEM stub. Before imaging, the samples were sputter coated (up to 10 nm) using a Pd/Pt metal target (Cressington 108 auto). The coating was applied to minimize charging on the surface of the samples.

The diffractometer used for the XRD analysis is the same as reported in section 3.2.

The DSC measurements were carried out in a Mettler Toledo DSC1. The fist heating cycle was realized from 25°C to 200°C at 10 K/min. The samples were held at 200°C for 2 min before a cooling step to 25°C at 10 K/min. The samples were held at 25°C for 1 min before a second heating ramp to 200°C at 10 K/min. Equation (3.1) was used to calculate the crystalline fraction of the samples:

$$X_c(\%) = \frac{\Delta H_c}{\Delta H_{c,\infty} \cdot \varphi_{(PP,HDPE)}} \quad (3.1)$$

where, $\varphi_{PP}, \varphi_{HDPE}$ is the mass fraction of PP or HDPE in the composites, ΔH_c is the enthalpy of crystallization during the first cooling and $\Delta H_{c,\infty}$ is the enthalpy of crystallisation of a theoretical PP/HDPE crystal of infinite dimensions (*i.e.* 207.1 J/g for PP and 293 J/g for HDPE [3]).

The degree of distribution and dispersion of BNNS/GNP in PP/HDPE was assessed by oscillatory rheology. Indeed, it has been understood that when the filler particles percolate in a 3D network in the polymer matrix, the rheology of the composite in question shifts from 'liquid-like' behaviour to more 'solid-like'. The extent of which BNNS/GNP distribute and disperse in PP/HDPE determines to a large extent the final properties of the composites, particularly it affect both the mechanical properties and thermal conductivity [4-6].

Oscillatory rheology measurements were performed using a controlled-stress rheometer, a Thermo-HAAKE MARS III which is fitted with an air convection oven set at a constant temperature (210°C for PP and its composites and 200°C for HDPE and its composites) and operating in plate-plate geometry (25 mm diameter, 1.4 mm gap). The optimal measurement temperature was chosen by performing a temperature sweep test at a frequency of 1Hz, a stress of 10 Pa, in the range of 180-220°C for PP and 180-250°C for HDPE. The thermal stability during the experiment was verified by performing a time-sweep test at a frequency of 1Hz, a stress of 10Pa, at 210°C for PP and 200°C for HDPE [4, 7].

Amplitude sweep tests were performed on the pure matrices and on the composites with the highest filler loading in order to check the range of linear viscoelasticity (LVE) passing from the neat polymer to the composites. In the amplitude sweep test the amplitude of shear stress was varied at constant frequency of 1Hz. The results were obtained by plotting G′ and G′′ as a function of shear stress and the LVE regime was determined as the range of shear stress where the moduli are constant. Then, the frequency sweep tests were performed by changing the frequency from 0.1 to 500 rad/s while the amplitude of shear stress was kept constant at a fixed value, chosen in the range of LVE. In particular, the value of stress of 10 Pa was chosen since for all the samples it fell within the LVE [4, 7].

The effect of BNNS and GNP onto the mechanical properties of the composites with PP/HDPE was assessed from tensile testing. The tensile tests were carried out using a Shimadzu tensile tester according to the standard ASTM-D638-02a, "Standard Test Method for Tensile Properties of Plastics". The instrument was fitted with a 10kN load cell and equipped with a twin TRViewX non-contact digital video extensometer having a 500 nm and a 120 nm field of view. The samples were deformed at 10mm/min. The Young's modulus was calculated using the secant method within the linear region before yield. The measurements were performed on an average of 6 specimens per composition. The data were statistically elaborated with the function t-student and only the values with $p \leq 0.05$ were considered for the evaluation.

Thermal conductivity measurements were performed to detect whether the inclusion of the BNNS/GNP altered the thermal conduction characteristics of the polymer matrices. The analysis were performed at Thomas Swan Advanced Materials Laboratory, using a MTPS instrument (reference thermal conductive material= water). The measurements were performed on three points on the front face of the samples and each value reported is the average of five measurements. Measurements at three points of the back face of the samples were also performed.

As part of the EngD programme, the Engineer researcher was required to attend an International placement. The author had a secondment at the University of Huelva, Spain to conduct electro-rheology measurements on the composites of HDPE with BNNS grades to better understand the effect of the filler particles on the rheology of the polymer matrix and to study the formation of a 3D filler network.

The electro-rheology measurements were performed on the composites of HDPE+X-BNNS-SC (5wt%) and HDPE+Y-BNNS-L (5wt%) to detect whether the application of an electrical stimulus could induce the alignment of the polarizable BNNS particles, thus facilitating the formation of a 3D network (rheological percolation) [8-13]. The two grades of BNNS were

chosen on the basis of their particle size (see Chapter 4). The instrument used was a strain-controlled rheometer Ares G2, fitted with a Peltier heating system, which could not heat above 150°C, therefore the author analysed the composites of HDPE only (PP melting point: *ca* 160°C). The Peltier system was coupled with an ER accessory, connected via cable to the upper plate of the rheometer. Therefore, after the positioning the sample between the upper plate and the Peltier base, a closed electric circuit was created. The strain sweep tests were performed at 150°C to detect the LVE and a value of γ (strain) of 0.01% was selected for the successive frequency sweep measurements. The frequency sweep experiments were performed at 150°C both without and with electric current for comparison. A preliminary ramp test at 150°C was performed to detect the minimum voltage to be applied to cause a structural change in the composites. Specifically a voltage of 1500V was applied throughout the electro-rheology measurements.

Electro-rheology measurements were also carried out on composites of HDPE+X-GNP-SC (5wt%). However, under electrical impulses, the X-GNP-SC particles could align and create an electrically conductive path, which interferes with the applied external electrical field. The internal electrical field could lead to a misreading of the experimental results, since the internal current could either oppose or align to the external current, thus, altering the effective applied electrical stimulus.

References

[1] Dominik V. Rosato DVR, Marlene G. Rosato. Injection Molding Handbook: Springer Science+Business Media , LLC.

[2] John R. Wagner Jr EMMI, Harold F.Giles Jr. Extrusion (Second Edition). The Definitive Processing Guide and Handbook: William Andrew, Elsevier. 2014.

[3] Jose S, Aprem AS, Francis B, Chandy MC, Werner P, Alstaedt V, Thomas S 2004 *Eur. Polym. J.* **40** 2105-15.

[4] Chin SJ, Vempati S, Dawson P, Knite M, Linarts A, Ozols K, McNally T 2015 *Polymer* **58** 209-21.

[5] Potschke P, Abdel-Goad M, Alig I, Dudkin S, Lellinger D 2004 *Polymer* **45** 8863-70.

[6] Meincke O, Kaempfer D, Weickmann H, Friedrich C, Vathauer M, Warth H 2004 *Polymer* **45** 739-48.

[7] Sabzi M, Jiang L, Liu F, Ghasemi I, Atai M 2013 *Journal of Materials Chemistry A* **1** 8253-61.

[8] Choi HJ, Jhon MS 2009 *Soft Matter* **5** 1562-7.

[9] Block H, Kelly JP 1988 *Journal of Physics D-Applied Physics* **21** 1661-77.

[10] Akhavan J 2007 *Proceedings of the Institution of Mechanical Engineers Part G-Journal of Aerospace Engineering* **221** 577-87.

[11] Deinega YF, Vinogradov GV 1984 *Rheol. Acta* **23** 636-51.

[12] Lee S, Yoon CM, Hong JY, Jang J 2014 *J. Mater. Chem. C* **2** 6010-6.

[13] Dong YZ, Kwon SH, Choi HJ, Puthiaraj P, Ahn WS 2018 *Acs Omega* **3** 17246-53.

CHAPTER 4: RESULTS AND DISCUSSION

4.1- Introduction

Composites of polymers with functional additives such as BNNS and GNP have been increasingly exploited in a variety of industries including electronics, automotive and aerospace, yet, the literature still lacks fundamental understanding of the effects of BNNS and GNP on composite structure and properties (*e.g.* thermal, electrical, rheological and mechanical). Very few publications are available on the manufacturing of thermoplastics-based composites with BNNS and GNP prepared by melt mixing, *e.g.* extrusion and injection moulding, which are presently the most industry relevant technologies for large-scale production of thermoplastic composites (Chapter 2).

This chapter describes the characterization of the different grades of BNNS and GNP studied, namely X-BNNS-SC, X-BNNS-T, Y-BNNS-L and X-GNP-SC, X-GNP-L, Y-GNP-L (Chapter 3). Specifically, the morphology and crystalline structure of BNNS/GNP grades was investigated by Scanning Electron Microscopy (SEM), X-Ray Diffraction (XRD) and Raman Spectroscopy. The surface chemistry was analysed by X-Ray Photoemission Spectroscopy (XPS) and Sessile (contact angle) measurements. The temperature of degradation was assessed by Thermo-gravimetric Analysis (TGA).

The grades X-BNNS-SC and X-GNP-SC were melt mixed with polypropylene (PP) and high density polyethylene (HDPE) at filler loading up to 5wt% by laboratory-scale extruder and test specimens prepared using injection moulding (Chapter 3). The composites were analysed by SEM, XRD, differential scanning calorimetry (DSC) to determine the effect of the filler inclusion on the morphology and crystalline structure of the polymer matrix. The rheology of the composites prepared was investigated by oscillatory rheology, to assess the extent of dispersion and distribution of the X-BNNS-SC and X-GNP-SC in PP/HDPE and if the formation of a 3D filler-filler network in the matrices was attained (*i.e.* rheological percolation). Thermal conductivity measurements (TC) were performed to determine whether the inclusion of the thermal conductive particles BNNS/GNP in PP/HDPE could form a thermal path throughout the polymer matrix. Tensile testing was performed to investigate the mechanical properties of the composites prepared.

PP was used as a model polymer to prepare composites with X-BNNS-SC, X-BNNS-T, Y-BNNS-L, X-GNP-SC, X-GNP-L and Y-GNP-L in the range of compositions, 0-10wt%

by 16mm co-rotating twin-screws extruder/injection moulding (Chapter 3). The composites were investigated by SEM, XRD, DSC, Oscillatory rheology, Tensile tests and TC.
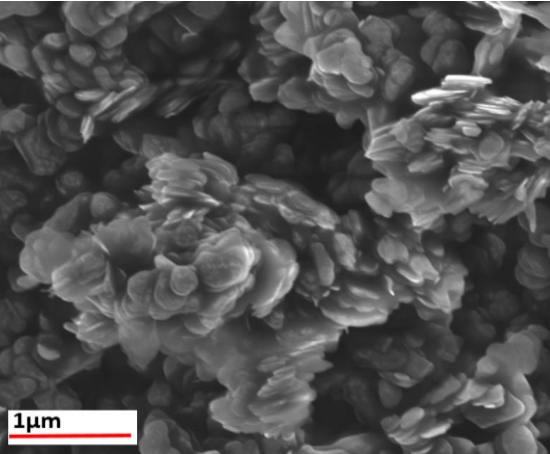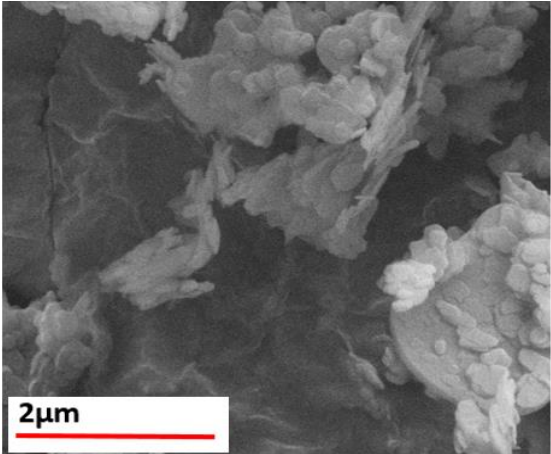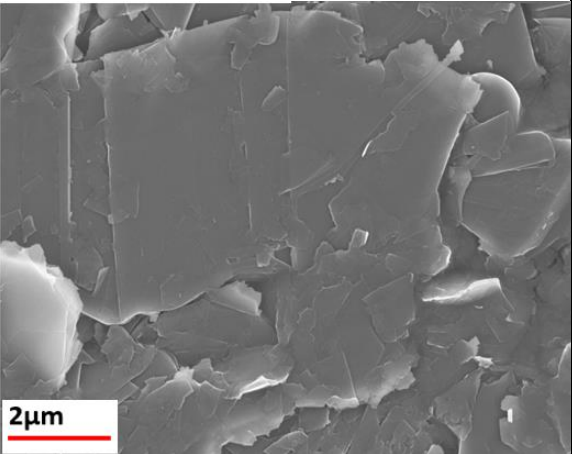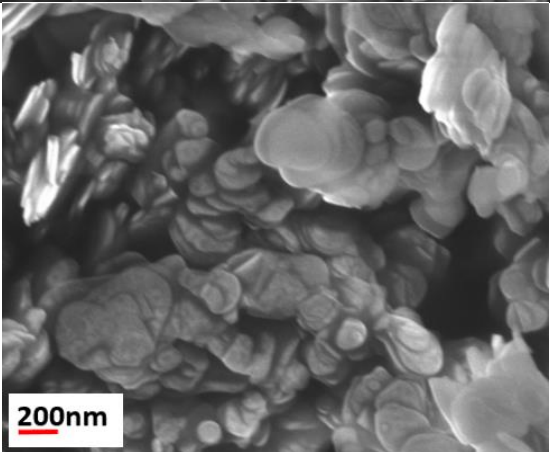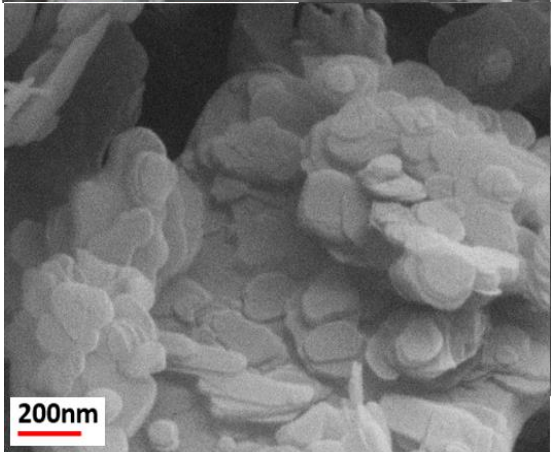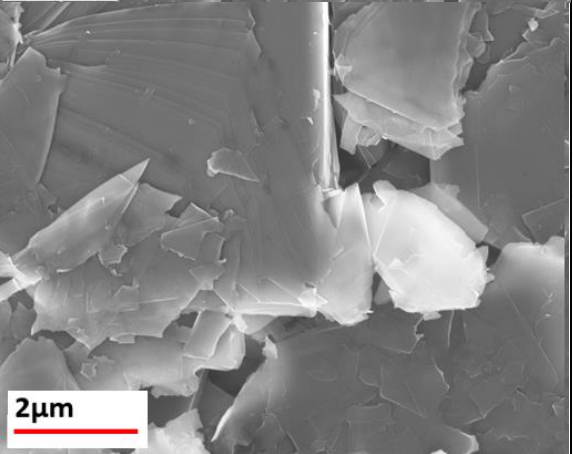
Composites of HDPE with X-BNNS-SC and X-GNP-SC were prepared by 16-mm co-rotating twin-screws extruder/injection moulding (Chapter 3) and characterized again by SEM, XRD, DSC, Oscillatory rheology and Tensile tests. Composites of HDPE with Y-BNNS-L (5wt%) were prepared as well and analysed by electro-rheology along with the composites of HDPE with X-BNNS-SC (5wt%), to assess the effect of the electrical impulses on the alignment and eventually on the rheological percolation of the polarizable BNNS particles with different lateral sizes (X-BNNS-SC= up to 200 nanometre (nm) length, Y-BNNS-L= up to 10 micrometre (µm) length, see next section).

The chapter also provide insights of the possible applications of TS BNNS and GNP as functional additives in thermoplastics for the manufacturing of masterbatches.

4.2- Characterization of X-BNNS-SC, X-BNNS-T, Y-BNNS-L, X-GNP-SC, X-GNP-L, Y-GNP-L

The following tables show concisely the results on the characterization of X-BNNS-SC, X-BNNS-T, Y-BNNS-L, X-GNP-SC, X-GNP-L and Y-GNP-L in term of morphology and crystalline structure, surface chemistry and thermal stability.

Table 4.1: Key outcomes from the characterization of Boron Nitride Nanosheets (BNNS) grades. X-BNNS-SC/X-BNNS-T/Y-BNNS-L= exfoliated materials; BN-X/ BN-Y= bulk materials, in terms of morphology, crystalline structure, surface chemistry and thermal stability.

Property	Technique	TS BNNS GRADES		
		X-BNNS-SC	X-BNNS-T	Y-BNNS-L
Morphology and Crystalline structure	SEM			

Property	Technique	X-BNNS-SC	X-BNNS-T	Y-BNNS-L
Morphology and crystalline structure	XRD (*)			
	Raman (**)			

$* \ d_{002} = \frac{\lambda}{2sin\theta}$ (interlayer distance, Bragg's law), $L_{002} = \frac{k\lambda}{\beta_{002}cos\theta_{002}}$ (thickness along the plane (002), Scherrer's equation). λ = X-Ray wavelength source (nm), θ = diffraction angle (rad) of the plane (002), β_{002} = FWHM of the peak (002), k=constant related to the shape of the crystallites with values between 0.89-0.94. In this case, the value of model spherical crystallites have been used (k=0.9). Ref.: [1-7]. ** Raman spectra references: [1, 8, 9]

Property	Technique	X-BNNS-SC	X-BNNS-T	Y-BNNS-L
Surface Chemistry	XPS (Core-level photoemission spectra*)	At %: B1s=20.32%; N1s=18.4%; C1s=48%; O1s=13.2%; Na1s=0.05%	At %: B1s=14%; N1s=50%; C1s=16%; O1s=20%	At %: B1s=14%; N1s=46%; C1s=18%; O1s=22%
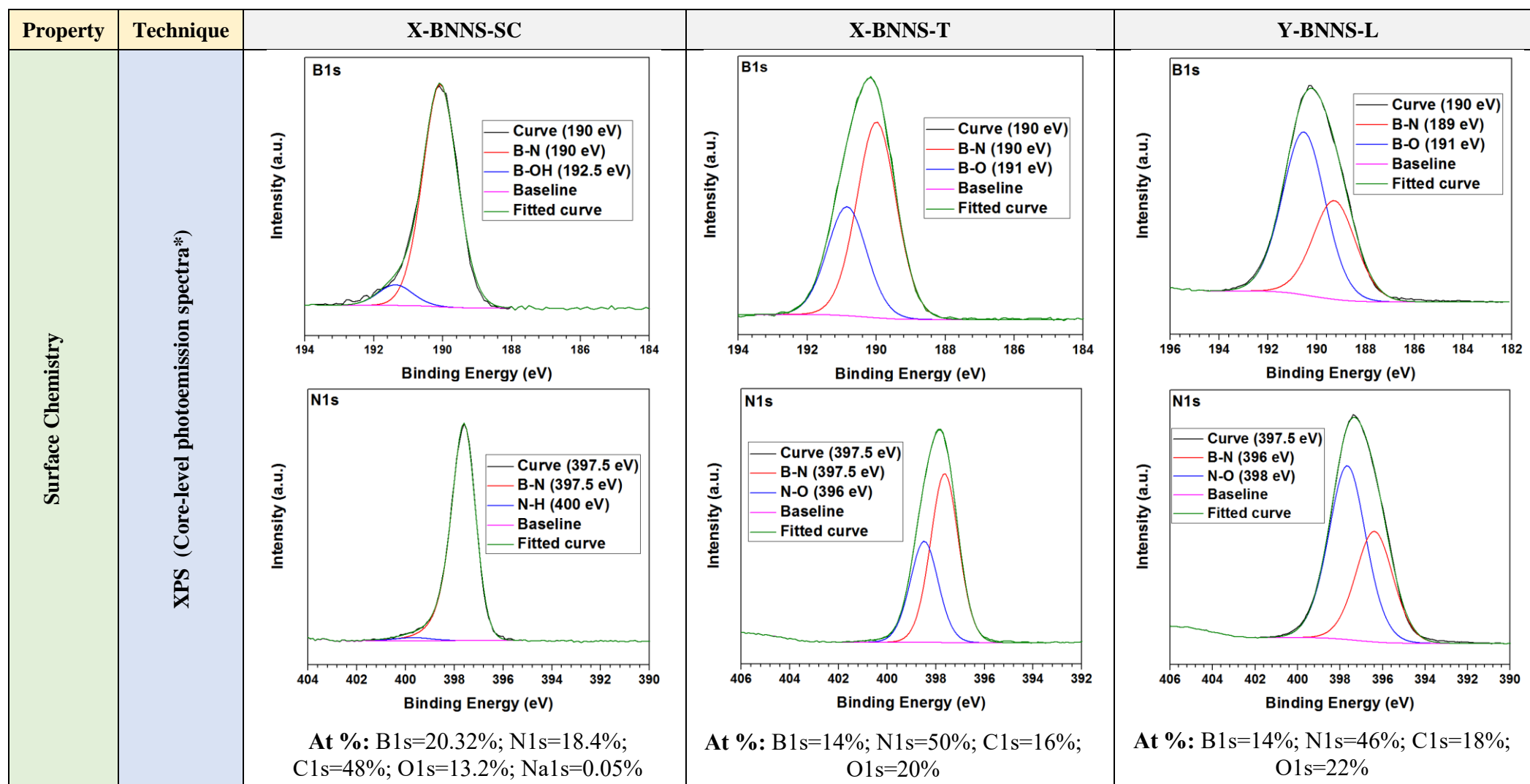
* Lorentzian/Gaussian combined profiles. Ref.: [1, 2, 10-12]. At(%)= atomic percentage as detected from the Survey spectra reported in the Appendix Part I.

Property	Technique	X-BNNS-SC	X-BNNS-T	Y-BNNS-L
Surface chemistry	Sessile tests	60°±3° at 0s 40°±2° at 10s	40°±3° at 0s 8°±2° at 10s	45°±4° at 0s 43°±2° at 10s
Thermal behaviour	TGA (*)	T_{onset}: 323°C T_{deg}: 367°C Weight loss at T_{onset}: 6wt% Weight loss at T_{deg}: 10wt%	T_{onset}: 323°C T_{deg}: 367°C Weight loss at T_{onset}: 0.01wt% Weight loss at T_{deg}: 0.03wt%	No degradation detected under the adopted conditions

* The TGA graphs are reported in the Appendix part I.

The SEM imaging of X-BNNS-SC, X-BNNS-T and X-BNNS-L revealed a distribution of flakes having different shapes and dimensions, particularly, round platelets of few nanometre (nm) lengths for X-BNNS-SC/X-BNNS-T and square platelets of a few micrometre (μm, up to 10μm) in length for Y-BNNS-L. The morphology of the bulk BN dominates the mechanism of fragmentation occurring during the HPH. Specifically, the BN-X is likely to exfoliate by edge fragmentation in presence of the surfactants SC and T, whereas the BN-Y probably exfoliates according to the bulk fragmentation mechanism in presence of the surfactant L [1, 13].

The crystalline structure of BN-X and BN-Y is retained in the X-BNNS-SC, X-BNNS-T and X-BNNS-L as evident from the sharp and intense peak in the XRD spectra at $2\theta=31°$, due to the crystallographic plane (002) typical of hexagonal boron nitride and confirmed by the interlayer distance $d_{002}=0.335$ (Bragg's law). The crystallite dimension L_{002} (Scherrer's equation) decreases from 30nm to 20nm when BN-X is exfoliated into X-BNNS-SC and X-BNNS-T, whereas L_{002} decreases from 40nm to 20nm when BN-Y is exfoliated into Y-BNNS-L, suggesting that during HPH BN-Y in the presence of L exfoliated more than BN-X did in presence of SC and T under the same processing conditions. It should be borne in mind that the L_{002} values are only indicative since the Scherrer's equation fails in the nm scale, due to the fact that the model equation does not take into account the poly-dispersity of nano-materials [1-7].
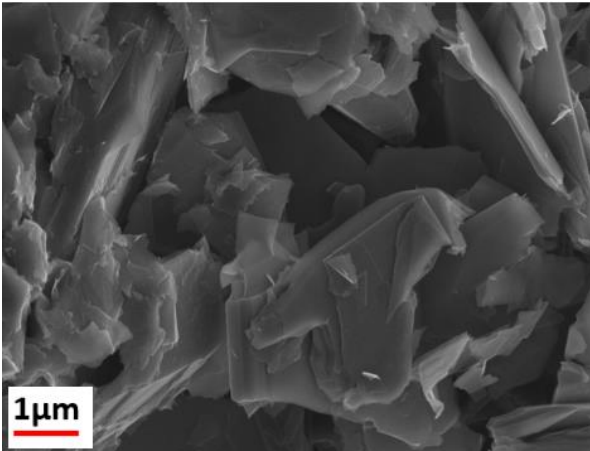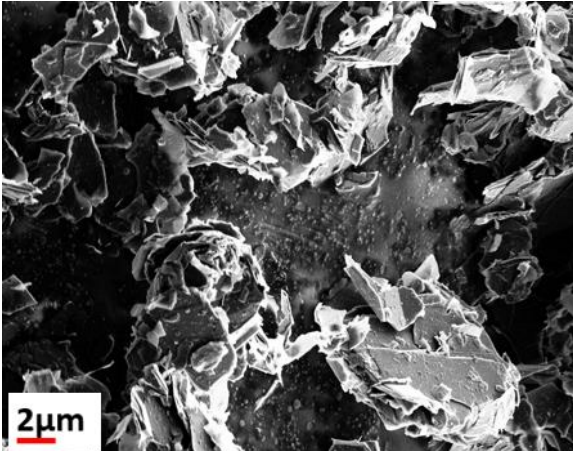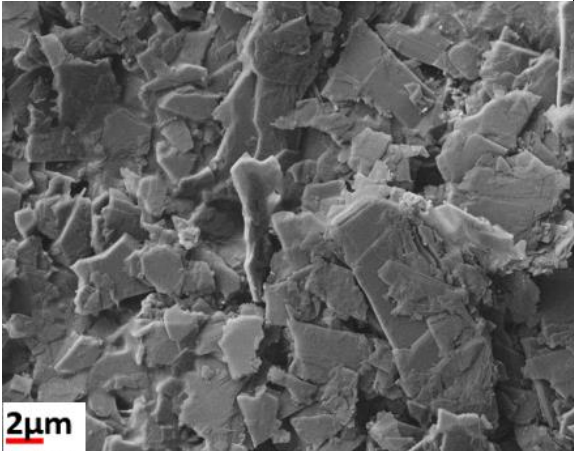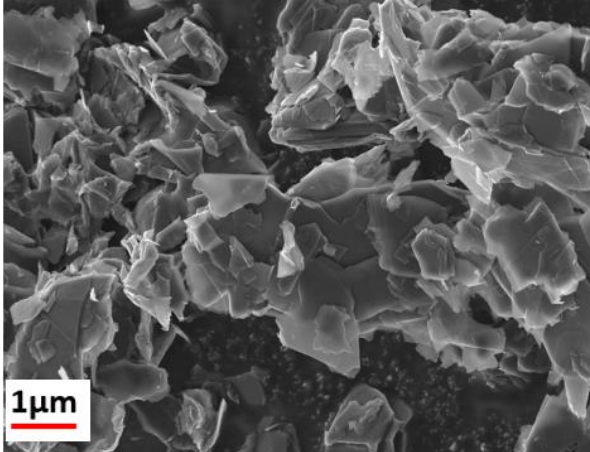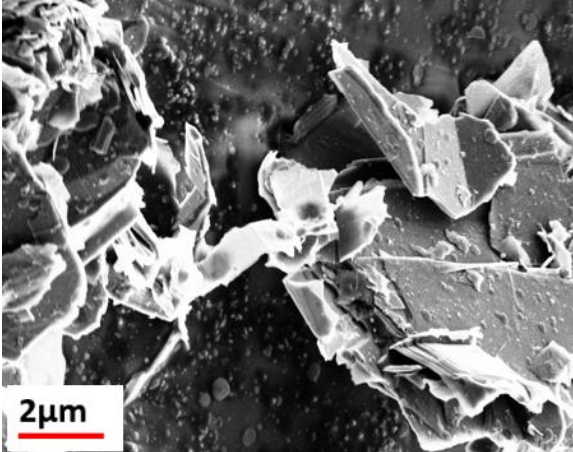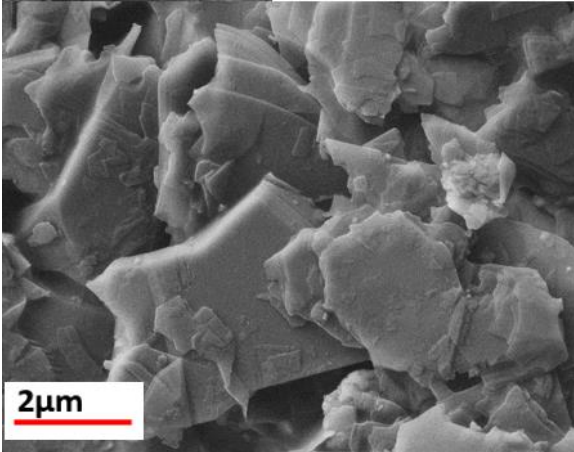
The Raman shift of the E_{2g} peak is 1360cm^{-1} for the BN-X and for the exfoliated materials X-BNNS-SC/X-BNNS-T and 1363cm^{-1} for the BN-Y and for Y-BNNS-L. The FWHM of the E_{2g} peak decreases from 15.5cm^{-1} to 11.7cm^{-1} and to 11.8cm^{-1} when BN-X is converted into thinner X-BNNS-SC and X-BNNS-T respectively, whereas the FWHM of the E_{2g} decreases from 26 cm^{-1} to 21.7cm^{-1} when BN-Y changed into Y-BNNS-L. These results confirmed that the HPH exfoliated to some extent bulk BN-X and BN-Y. Furthermore, the FWHM of the E_{2g} in BN-Y is higher than the FWHM of the E_{2g} in the BN-X, probably due to the presence of functionalities on the BN-Y [1, 8, 9]. This observation is of support to the industrial partner, since it highlights the crucial importance of the bulk material properties as key factors in determining the properties of the exfoliated products, in line with the SEM and XRD findings.

The surface chemistry analysis of the X-BNNS-SC, X-BNNS-T and Y-BNNS-L revealed impurities and/or functionalities on the platelets, confirmed by the presence of carbon and oxidised groups. Specifically, the B-O/N-H groups in the X-BNNS-SC and B-O/N-O

groups in the X-BNNS-T and Y-BNNS-L identified from the Lorentzian/Gaussian de-convolution of B1s and N1s peaks [1, 2, 10-12] suggests the hydrophilic characteristics of these grades of BNNS, and further confirmed from the sessile tests. The B:N ratio in X-BNNS-SC is 1:1 as expected in an hexagonal boron nitride structure, whereas the B:N ratio in X-BNNS-T and X-BNNS-L is 1:4 and 1:3, respectively. Probably, the morphology of BN-X and BN-Y - not reported as sensitive to the industrial partner- combined with the conditions adopted during the HPH and the chemistry of the surfactants T and L lead to unsaturation on the surface of X-BNNS-T and Y-BNNS-L, which are likely to take-up impurities from the atmosphere during the post-processing procedure adopted by the industrial partner and/or any procedure adopted before their use. Yet, this type of study is beyond this thesis.
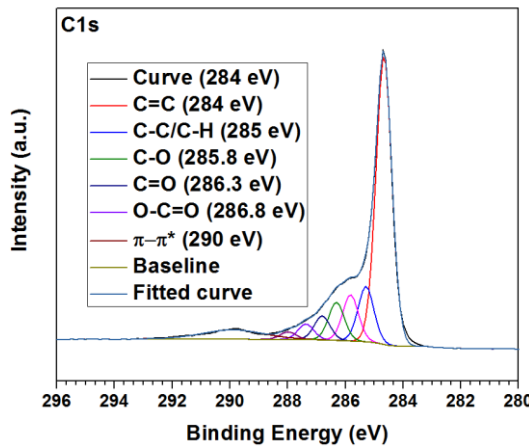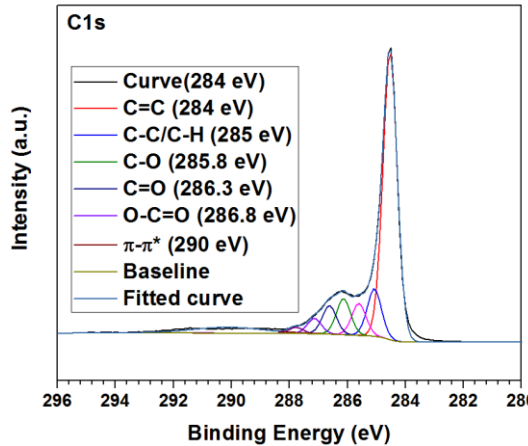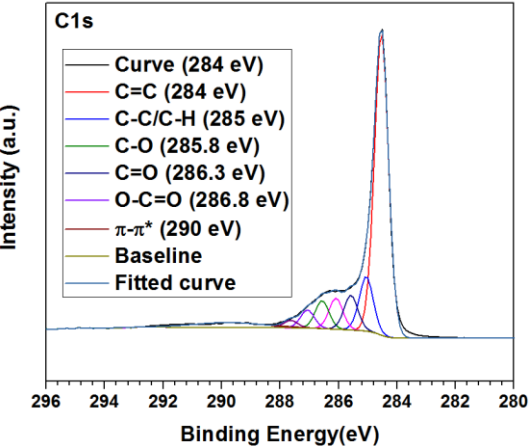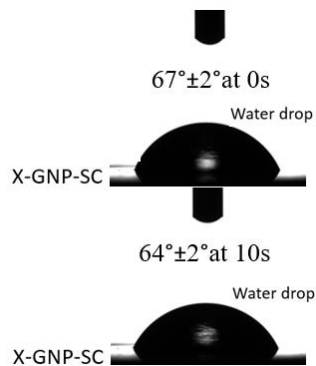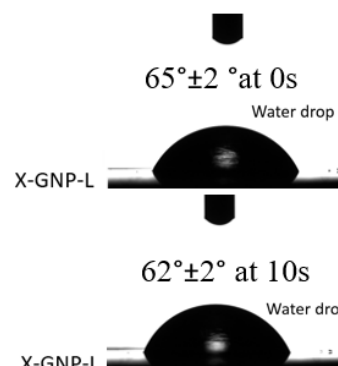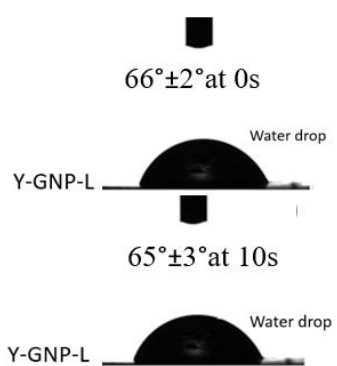
The X-BNNS-SC appear to be stable under oxidative conditions up to 323°C (T_{onset}) with a total weight loss of 10wt%. The weight loss registered below the T_{onset} (6 wt%) is probably due to the evaporation of water onto the surface of this BNNS and/or the evaporation/degradation of the surfactant SC. The X-BNNS-T starts to degrade at 323°C (T_{onset}) with a total weight loss of 0.03wt%. The weight loss of 0.01wt% registered below the T_{onset} is again probably due to the evaporation of water. The Y-BNNS-L appear to be stable under the oxidative conditions adopted up to 800°C. Although X-BNNS-T and X-BNNS-L have a relatively high content of oxidised groups (At% O1s =*ca* 20%, XPS), they appear more thermally stable than the X-BNNS-SC. Evidently, the type of surfactant affects the degradation mechanism when comparing these grades of BNNS under the same TGA experimental conditions. Particularly, the ionic surfactant SC, present in traces on the X-BNNS-SC is hygroscopic, thus, facilitating the accumulation of humidity on the surface of this BNNS, which could promote degradation (the TGA of the surfactant SC is reported in Appendix part I. The TGA of the surfactants T and L were performed but not reported as sensitive data to the industrial partner).

Table 4.2: Key outcomes from the characterization of Exfoliated Graphite Nanoplatelets (GNP) grades. X-GNP-SC/X-GNP-L/Y-GNP-L= exfoliated materials; graphite-X/graphite-Y= bulk materials, in terms of morphology, crystalline structure, surface chemistry and thermal stability.
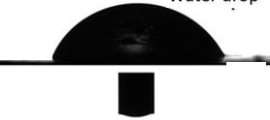
Property	Technique	TS GNP GRADES		
		X-GNP-SC	X-GNP-L	Y-GNP-L
Morphology and Crystalline structure	SEM			

Property	Technique	X-GNP-SC	X-GNP-L	Y-GNP-L
Morphology and crystalline structure	XRD (*)			
	Raman			

$* \; d_{002} = \frac{\lambda}{2 sin\theta}$ (interlayer distance, Bragg's law), $L_{002} = \frac{k\lambda}{\beta_{002} cos\theta_{002}}$ (thickness along the plane (002), Scherrer's equation). λ = X-Ray wavelength source (nm), θ = diffraction angle (rad) of the plane (002), β_{002} = FWHM of the peak (002), k=constant related to the shape of the crystallites with values between 0.89-0.94. In this case, the value of model spherical crystallites have been used (k=0.9). Ref.: [5, 6]. ** Raman spectra references [14-17].

Property	Technique	X-GNP-SC	X-GNP-L	Y-GNP-L
Surface Chemistry	XPS (Core-level photoemission spectra*)	**At %:** C1s=90.3%; O1s=9%; Na1s=0.7%	**At %:** C1s=80%; O1s=20%	**At %:** C1s=80%; O1s=20%
	Sessile tests	67°±2°at 0s / 64°±2°at 10s	65°±2 °at 0s / 62°±2° at 10s	66°±2°at 0s / 65°±3°at 10s

* Lorentzian/Gaussian combined profiles. Ref.: [18-20]. At(%)= atomic percentage from the Survey spectra reported in Appendix Part I.

Property	Technique	X-GNP-SC	X-GNP-L	Y-GNP-L
Thermal behaviour	TGA (*)	T_{onset}: 430°C T_{deg}: 630°C Weight loss at T_{onset}: 10wt% Weight loss at T_{deg}: 70wt%	T_{onset}: 550°C T_{deg}: 680°C Weight loss at T_{onset}: 1wt% Weight loss at T_{deg}: 3wt%	T_{onset}: 560°C T_{deg}: 680°C Weight loss at T_{onset}: 1.2wt% Weight loss at T_{deg}: 3wt%

* TGA graphs reported in Appendix Part I.

The SEM imaging of X-GNP-SC, X-GNP-L and Y-GNP-L revealed a distribution of flakes having irregular square-shaped platelets of few μm's in length. The morphology of the bulk graphite-X and graphite-Y dominate the mechanism of fragmentation occurring in the HPH, specifically, the graphite-X and graphite-Y are likely to exfoliate by bulk fragmentation [13, 21].

The crystalline structure of graphite-X and graphite-Y is retained in the X-GNP-SC, X-GNP-T and Y-GNP-L as evident from the sharp and intense peak in the XRD spectra at $2\theta=31°$- due to the crystallographic plane (002) and confirmed by the interlayer distance $d_{002}=0.335$ (Bragg's law). The crystallite dimension L_{002} (Scherrer's) decreases from 30nm to 20nm as the graphite-X and graphite-Y are exfoliated into thinner X-GNP-SC/X-GNP-L and Y-GNP-L respectively [5, 6].

The Raman spectra of graphite-X, graphite-Y and the X-GNP-SC, X-GNP-L and Y-GNP-L identified the D, $G(E_{2g})$, D′, G* and G′(2D) bands as indicated in the respective pictures in Table 4.2. The G band is the most intense due to the inelastic phonon-phonon scattering (first order Raman scattering), in particular, it refers to the doubly degenerate in-plane/out-of-plane vibrational modes of sp^2 hybridized carbon orbitals. The shift of the G band to lower Raman shifts when comparing graphite-X and graphite-Y with X-GNP-SC, X-GNP-L, Y-GNP-L indicates that the HPH partially exfoliated the bulk materials. In this case, the G band decreases from 1584 cm^{-1} and 1583 cm^{-1} for the graphite-X and graphite-Y respectively to 1580 cm^{-1}, 1581 cm^{-1} and 1581 cm^{-1} for the X-GNP-SC, X-GNP-L and Y-GNP-L respectively. The D and D′ bands in the exfoliated products are weak due to the low concentration of defects in the crystal lattice. The G′ (2D) band in X-GNP-SC, X-GNP-L and Y-GNP-L is slightly decentred denoting an exfoliated flake structure as further confirmed by the ratio $I_{G(2D)}/I_G$, which reduces from 0.45 (graphite-X) to 0.40 (X-GNP-SC/X-GNP-L) and from 0.42 (graphite-Y) to 0.40 (Y-GNP-L), suggesting that the bulk materials were exfoliated to some extent as a consequence of the shear stresses applied during HPH [14-17].

The XPS analysis of X-GNP-SC, X-GNP-L, Y-GNP-L identified the atomic species C1s, O1s at 284 eV and 532.5 eV. The presence of oxygen (and sodium where detected) is due to impurities from both the atmosphere and the surfactants (SC, L) used during the exfoliation process. The higher resolution core-level photoemission spectra of C1s show an asymmetric and broad peak for carbon for both the X-GNP-SC, X-GNP-L and Y-GNP-L, where the C1s spectra were fitted by six combined Lorentzian/Gaussian curves as indicated in the XPS images reported in Table 4.2. The shape of the C1s peak of X-GNP-L appears to be decoupled

compared with the C1s peak of X-GNP-SC and Y-GNP-L. The decoupling effect in X-GNP-L could be associated to the signal of two different carbon domains, namely the C1s from the X-GNP-L surface and the C1s from the surfactant L. This phenomenon is less prominent in X-GNP-SC/Y-GNP-L, which suggests that the C1s spectra resulted from one carbon domain, most likely the surface of X-GNP-SC/Y-GNP-L platelets interacting with the surfactants SC/L. Evidently, the combination of bulk-material morphology- again, not reported as sensitive data to the industrial partner- and surfactant determined the chemistry of the exfoliated materials post HPH. It is possible to speculate that the surfactants SC and L appear to interact with the graphite-X and graphite-Y respectively more than surfactant L did with graphite-X during HPH [18-20]. Probably, the mechanism of interactions between the surfactants and the bulk materials during HPH depends on both the morphology of the starting graphite, the chemical structure of the surfactants and perhaps the conditions adopted during the HPH. Yet, this type of study is beyond the objectives of this thesis.

The surface chemistry of X-GNP-SC/X-GNP-L/Y-GNP-L was further investigated by sessile tests, which revealed hydrophilic characteristics of the X-GNP-SC/X-GNP-L/Y-GNP-L surfaces, likely due to the oxidised groups present as different functionalities on the platelets and/or impurities from the surfactants (XPS).

X-GNP-SC started to degrade at 423°C (T_{onset}) with a total weight loss of 70 wt%. The weight loss registered at lower temperatures than the T_{onset} is probably due to the evaporation of water from the surface of this GNP and/or the evaporation/degradation of the surfactant SC. The X-GNP-L and Y-GNP-L appear to be stable under the oxidative conditions adopted up to 550°C (T_{onset}) with a total weight loss of 3wt%. As noticed with the BNNS grades, under the experimental conditions used, it is clear that the combination of graphite morphology and surfactant used affects the thermal stability of the exfoliated products. Again, the surfactant SC appears to promote the degradation of X-GNP-SC.

The following paragraph summarises concisely the properties (dimensions, crystallinity, surface chemistry, degradation) of the BNNS and GNP grades here examined:

➤ Lateral size (l): BNNS grades 200nm < l < 10µm; GNP grades 0.5µm < l < 5µm

➤ Aspect Ratio (AR, length/thickness from SEM): BNNS grades 5 < AR < 20; GNP grades 5 < AR < 10

➤ Crystallite dimensions (L): BNNS grades 20nm < L < 40; GNP grades 20nm < L < 30nm

➤ Oxidation (O): BNNS grades O =20 At (%); GNP grades 9 At% < O < 20 At (%)

➤ Hydrophilicity (contact angle γ): BNNS grades 40° < γ < 60°; GNP grades 60° < γ < 70°

➢ Degradation temperature (T): <u>BNNS grades</u> T ≥ 360°C; <u>GNP grades</u> T ≥ 400°C

4.3- Characterization of the composites of PP and HDPE with X-BNNS-SC and X-GNP-SC prepared by micro-processing.

X-BNNS-SC and X-GNP-SC were admixed with polypropylene (PP) and high-density polyethylene (HDPE) by laboratory scale extrusion and post-processed by micro-injection moulding. The as obtained composite materials were thoroughly characterized and the morphology, crystalline structure, rheological and mechanical properties determined.

4.3.1- Study of the morphology and crystalline structure of composites of PP and HDPE with X-BNNS-SC and X-GNP-SC.

SEM imaging was carried out on the composites to study the extent of the dispersion and distribution of X-BNNS-SC and X-GNP-SC in PP and HDPE. On one hand, the sate of dispersion of the filler in the matrix is related to the exfoliation of the layers of X-BNNS-SC/X-GNP-SC upon mixing with PP. On the other, the state of distribution of the fillers in the matrix is associated to the separation of the BNNS/GNP clusters (agglomerates of flakes) upon mixing with PP.

Figure 4.1 shows the representative SEM images of PP+X-BNNS-SC and PP+X-GNP-SC at a filler loading of 5wt%.
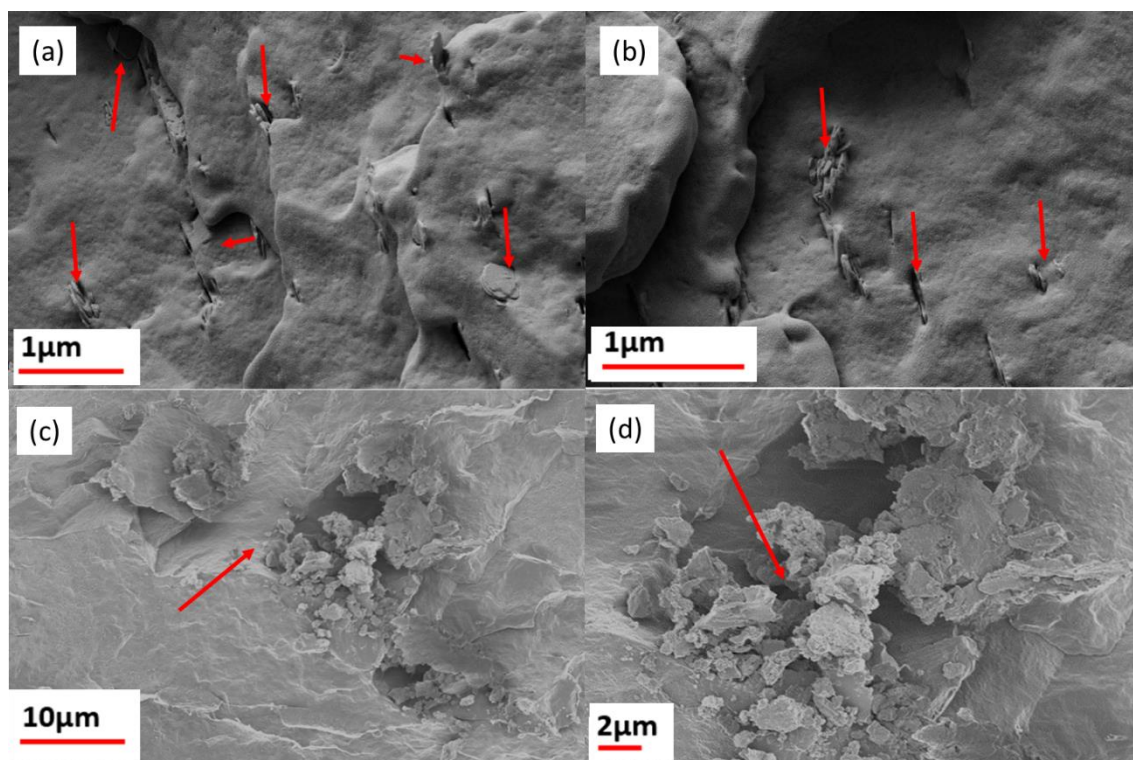
Figure 4.1: SEM images of PP composites with X-BNNS-SC (a) and (b) and X-GNP-SC (c) and (d) at 5wt% of filler. The magnification of the SEM images increases from left to right. X-BNNS-SC and X-GNP-SC agglomerate in PP. The red arrows point to the filler particles.

X-BNNS-SC and X-GNP-SC agglomerate when admixed in PP (Figure 4.1 a)-d)), probably caused by the strong particle-particle interactions which limited the distribution and dispersion of the two fillers in the matrix and/or by the limited efficiency of the processing adopted at imparting adequate shear forces to separate and distribute the flakes of the filler throughout the polymer matrix.

Figure 4.2 shows the SEM images obtained for the HDPE composites, with X-BNNS-SC and X-GNP-SC at 5wt%.
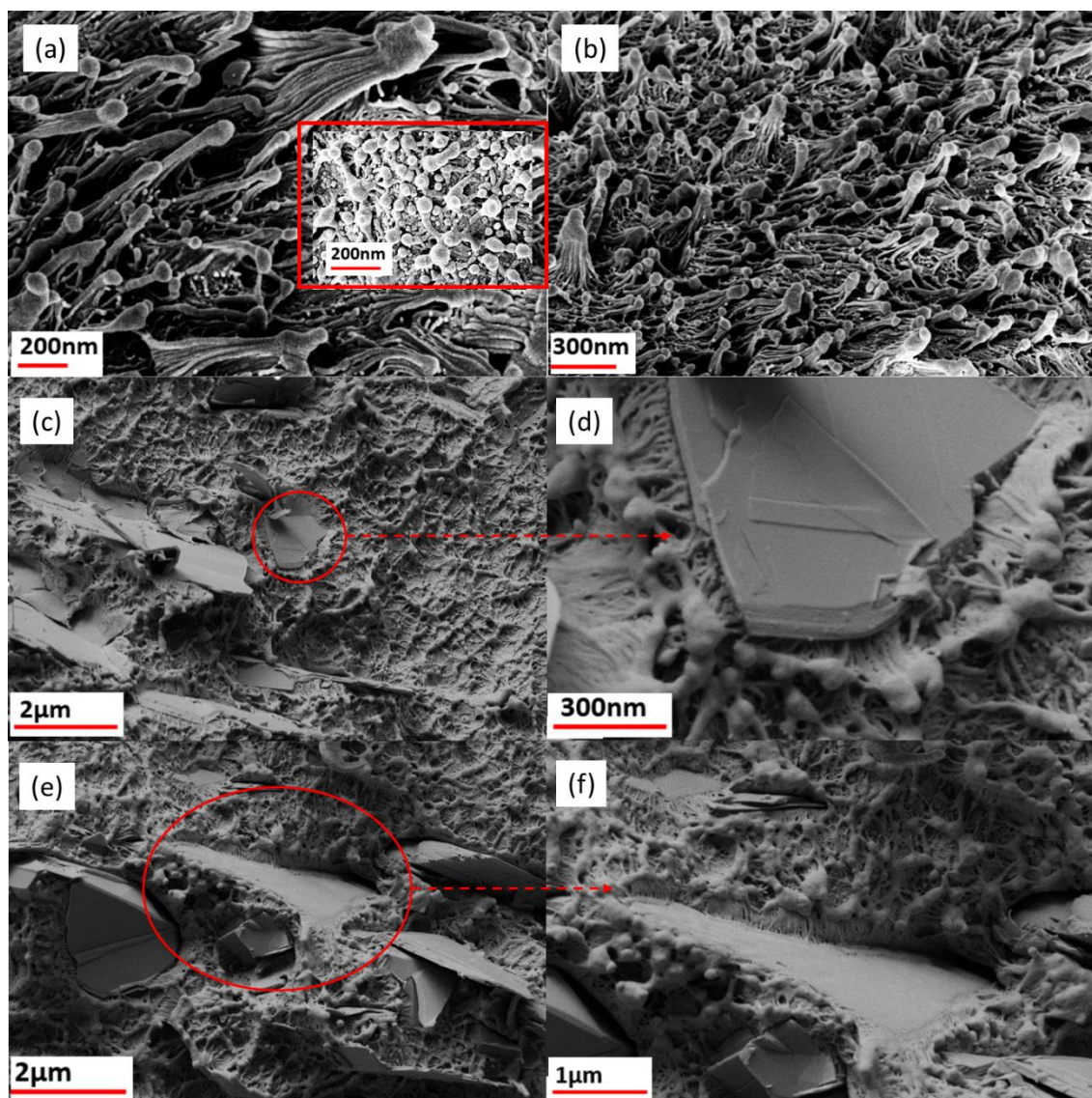
Figure 4.2: SEM images of composites of HDPE with X-BNNS-SC (a) and (b) and X-GNP-SC (c) – (f)) at 5wt% of filler. d) and f) are the magnified images of the areas encircled in red of c) and e), respectively. The magnification of the SEM images increases from left to right. HDPE retains a fibrillar morphology when adding X-BNNS-SC, as seen in the red square in (a). The X-BNNS-SC is not detectable in HDPE. The poor wettability of HDPE onto the X-GNP-SC favoured the formation of voids around the filler platelets.

Figure 4.2 a) and b) show the SEM images of HDPE+X-BNNS-SC at 5 wt% where HDPE shows a fibrillary morphology, which has been associated to the stretching of the HDPE chains along the injection direction during injection moulding. The insert in Figure 4.2 a) depicts the SEM images of the HDPE alone as a way of comparison. The specimen of HDPE+X-BNNS-SC at 5wt% was exhaustively scanned in different sections, yet, it was not possible to detect

filler particles, probably due to either the relative small dimensions of this grade of X-BNNS-SC (lateral size few nm) compared to the fibrils of the HDPE and/or to the inhomogeneity of the specimen characterized. Figure 4.2 c) –f) depict the SEM images of HDPE+ X-GNP-SC at 5wt%, where it is still possible to detect a fibril structure of HDPE. Voids formed around the irregular X-GNP-SC platelets, as evident from Figure 4.2 d) and f), which are the magnified images of Figure 2 c) and e) respectively (red encircled regions). The presence of the voids could be associated to the limited wetting of the HDPE onto the X-GNP-SC particles.

The crystalline structure of the composites was analysed by XRD. Figure 4.3 a) and b) show the XRD diffractograms of PP and composites of PP with X-BNNS-SC and X-GNP-SC, whereas Figure 4.3 c) and d) report the fraction of the β-form of the PP polymorph (K_β) within the composite samples as a function of filler loading. It was estimated from equation (4.1) [22, 23]:

$$K_\beta = \frac{H\beta}{H\beta + H\alpha_1 + H\alpha_2 + H\alpha_3} \quad (4.1)$$

where, H_β is the intensity of β (300) peak while $H\alpha_1$, $H\alpha_2$, $H\alpha_3$ are the intensities of α(100), α(040) and α(130) peaks respectively, as detected from the XRD patterns of PP and its composites with X-BNNS-SC and X-GNP-SC.
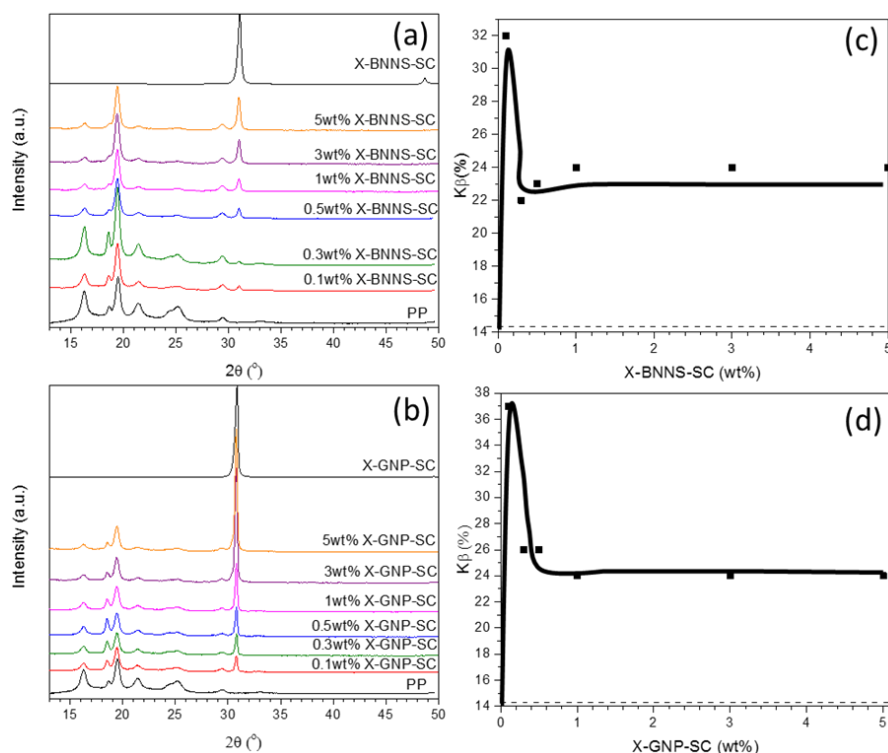
Figure 4.3: XRD of PP and composites of PP with X-BNNS-SC (a) and X-GNP-SC, (b) fraction of β-crystals of PP (K_β) in function of the X-BNNS-SC loading, (c) and X-GNP-loading (d)). The data are a replica of 3 measurements. The error on K_β falls on the first decimal cipher, not significant for this type of work.

The XRD patterns (Figure 4.3 a) and b)) show the most intense peaks for PP at 2θ = 16.5° α(100), 19.2° β(300), 20° α(040), 22° α(130) and X-BNNS-SC/X-GNP-SC at 2θ=31° (002). The diffraction angles of the registered peaks are shifted compared to the ones reported by other researchers since the X-ray source used in this work was Co ((Kα1 (λ) = 1.789 Å) [24-26]. The fraction of β-spherulites (K_β) increases from 14% (PP) to 32% and 37% for 0.1wt% of X-BNNS-SC and X-GNP-SC respectively, before decreasing and plateauing to 24% at filler content ≥ 0.3wt% (Figure 4.3 c) and d)). When the concentration of X-BNNS-SC/X-GNP-SC is ≤ 0.3wt%, the PP chains are free to arrange and orient onto the filler platelets and the number of PP chains able to orient in the β-conformation is high (increase in K_β). Yet, when the concentration of X-BNNS-SC/X-GNP-SC is ≥0.3wt%, the filler particles constrain the movement of PP chains, which limits the formation of more β-crystals (K_β tends to plateau) ([26] and references therein).

The K_β of the neat PP is 14% (Figure 4.3 c) and d), dashed line), which is due to both the pre-existent β-crystals in the neat as received polymer and the β-crystals formed during injection

86

moulding (induced crystallization) of the composites [22]. That is, the further increase in K_β after adding X-BNNS-SC and X-GNP-SC is solely due to the contribution of the filler [27].

The XRD diffractograms for HDPE and composites of HDPE with X-BNNS-SC and X-GNP-SC are shown in Figure 4.4.
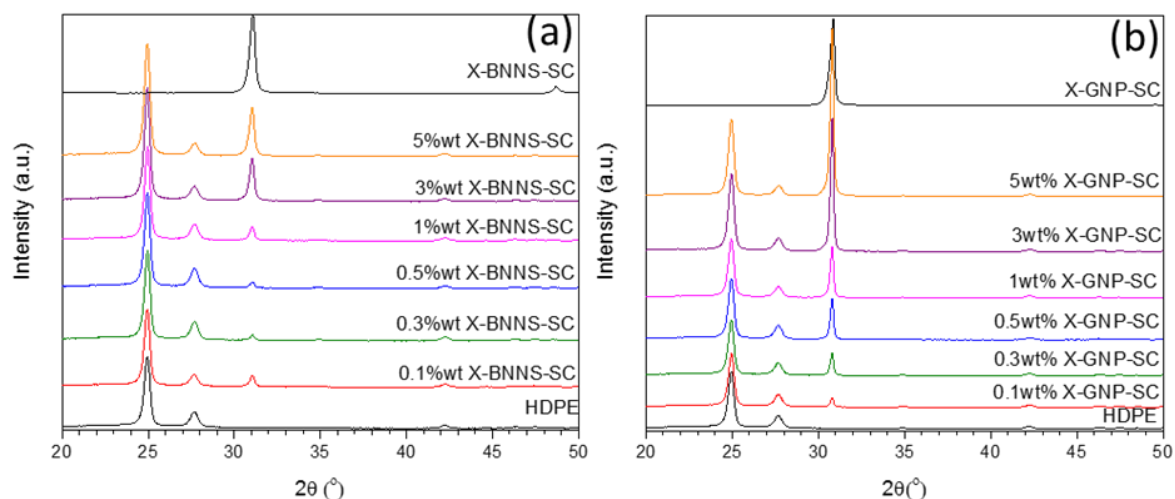
Figure 4.4: XRD spectra of HDPE and its composites with X-BNNS-SC (a)) and X-GNP-SC (b)). The data are a replica of 3 measurements.

The XRD patterns (Figure 4.4 a) and b)) depict the most intense peaks for HDPE at $2\theta = 25°$ (orthorhombic (100)), 27.7° (orthorhombic (200)), 35° (monoclinic (210)), 42.3° (orthorhombic (020)) and X-BNNS-SC/X-GNP-SC at $2\theta=31°$ (002). The registered peaks are shifted slightly compared to those reported previously due to the different X-ray source used [28, 29]. The presence of X-BNNS-SC and X-GNP-SC in HDPE is evident by the characteristic peak at $2\theta=31°$, which increases with increasing filler loading. Unlike the composites with PP, the addition of X-BNNS-SC and X-GNP-SC did not change the polymorphism of HDPE. The crystallinity (%) calculated for the neat HDPE was 50% and the addition of X-BNNS-SC/X-GNP-SC did not change the crystalline content. One possible explanation may be that it is known the crystallization kinetics of HDPE are very rapid but, the presence of X-BNNS-SC/X-GNP-SC even up to 5wt% did not affect the crystal content/morphology and nucleation/growth.

The DSC analysis was carried out to further investigate the crystallinity of the composites of PP and HDPE with X-BNNS-SC and X-GNP-SC. The thermograms registered during the DSC measurements are reported in Figure 4.5 and 4.6.
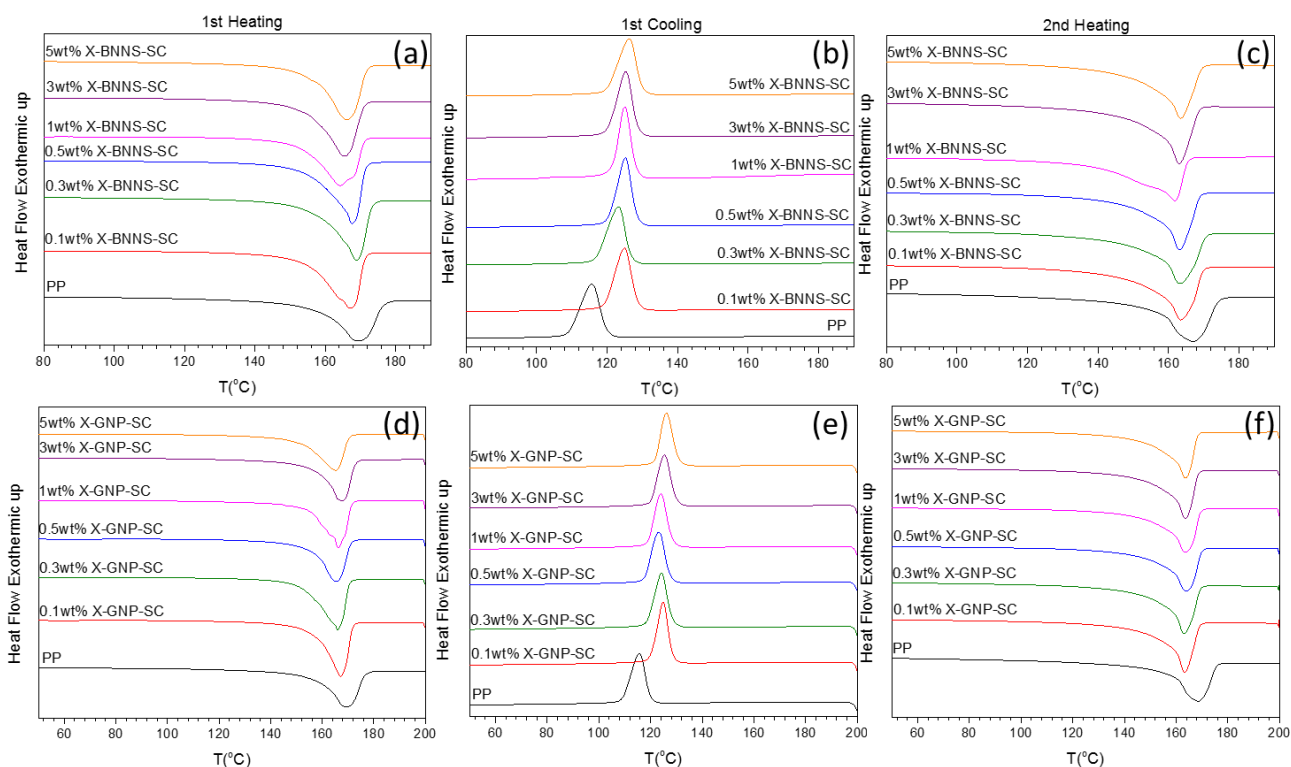
Figure 4.5: DSC thermograms of PP and its composites with X-BNNS-SC (a)-c)) and X-GNP-SC (d)-f)).

The first heating thermograms (Figure 4.5 a) and d)) show broad and asymmetric peaks, which confirm the coexistence of α-iPP and β-iPP crystals. The first cooling thermograms (Figure 4.5 b) and e)) show a shift toward higher temperatures upon filler incorporation. The major shift around 9°C is detected as low as 0.1wt% X-BNNS-SC and X-GNP-SC and remains constant for higher loadings of X-BNNS-SC whereas it continues increasing by *ca* 4°C more for a X-GNP-SC loading of 5wt%. These results prove the nucleating effect of X-BNNS-SC and X-GNP-SC for PP. The β-iPP form is totally absent for both X-BNNS-SC and X-GNP-SC based composites, probably due to the formation of the mainly α-form [27]. The second heating thermograms (Figure 4.5 c) and f)) show broad peaks after X-BNNS-SC and X-GNP-SC addition, yet more symmetric than the ones obtained in the first heating. The controlled cooling cycle realized during DSC measurements should have produced a material with a narrower crystallite distribution compared to the material cooled during injection molding, *i.e.* narrower peaks during second heating should be recorded. However, the melting peaks of the composites in the second heating thermograms are as broad as the ones in the first heating curves. The reason again may be associated with the β-α phase transition, which caused the superimposing

of the peaks related to the β-α recrystallization and/or β-spherulite melting and α-spherulite melting [22, 23, 27].

Table 4.3 summarizes the DSC results for the composites of PP with X-BNNS-SC and X-GNP-SC.

Table 4.3. Melting temperature (T_m), crystallization temperature (T_c), enthalpy of melting (ΔH_m), enthalpy of crystallization (ΔH_c) and crystallinity (X_c (%)) of PP and its composites with X-BNNS-SC and X-GNP-SC. The data reported were obtained from the DSC thermograms. The ΔH_c related to a theoretical PP crystal with infinite dimensions used to calculate the crystallinity is 207 J/g [30]. The results are a rapresentration of three measurements per each composition. The error calculated for T_m, T_c amd X_c (%) falls on the first decimal, which is not significant for the present study.

Sample	T_m(ºC)		T_c(ºC)	ΔH_m(J/g)		ΔH_c(J/g)	X_c(%)
	1st heating	2nd heating	1st cooling	1st heating	2nd heating	1st cooling	1st cooling
PP	168	170	116	88	102	97	47
0.1 wt% X-BNNS-SC	167	164	125	97	107	96	47
0.3 wt% X-BNNS-SC	169	163	123	97	106	97	47
0.5 wt% X-BNNS-SC	168	163	125	96	104	94	45
1 wt% X-BNNS-SC	164	162	125	95	106	93	45
3 wt% X-BNNS-SC	165	163	125	92	103	97	46
5 wt% X-BNNS-SC	166	163	126	94	103	96	44
0.1 wt% X-GNP-SC	167	163	125	96	101	97	47
0.3 wt% X-GNP-SC	166	163	124	97	106	99	47
0.5 wt% X-GNP-SC	165	164	123	86	103	95	45
1 wt% X-GNP-SC	166	164	124	94	106	97	46
3 wt% X-GNP-SC	168	164	130	86	101	94	44
5 wt% X-GNP-SC	165	164	130	94	98	90	41

From Table 4.3 it should be noted that the melting temperature T_m of PP during the first heating cycle does not particularly change when comparing neat PP to the composite with 5wt% X-BNNS-SC or X-GNP-SC, whereas during the second heating cycle the T_m decreases by *ca* 5°C when 5wt% of filler was added to PP. The shear forces imparted by the screws on the filler particles during the melt mixing with PP generated a distribution of X-BNNS-SC/X-GNP-SC aggregates with irregular shape and/or size, *i.e.* surface areas, which could have hindered the

crystallization of PP chains during injection moulding, especially at higher filler loadings, thus a larger fraction of PP amorphous phase formed and T_m was depressed ([27] and references therein). Conversely, the crystallization temperature T_c increases by 10°C and 14 °C when adding 5wt% of X-BNNS-SC and X-GNP-SC respectively, confirming the nucleating effect of X-BNNS-SC/X-GNP-SC in PP. The variation of melting enthalpy ΔH_m during the first heating of PP+X-BNNS-SC composites increases compared to the neat PP, probably due to a change of lamellar dimensions upon filler incorporation, whereas random values were detected for composites with X-GNP-SC. This may be due to the irregular shape of the X-GNP-SC flakes, which obstructs the crystallization of polymer chains, especially at high filler loadings [27, 31]. However, this difference is not evident during the second heating cycle perhaps due to the fact that the material experienced a previous controlled cooling step before the second heating cycle, thus, the internal stresses generated upon the fast crystallization during injection moulding are released, the polymer chains relax and the obstructing effect of the irregular shaped-flakes of X-GNP-SC is less dominant compared to the first heating cycle, therefore the polymer matrix displays the same behaviour with both the fillers [32-34]. Overall, $X_c(\%)$ decreases from 47% (PP) to 44% (5wt% X-BNNS-SC) and 41% (5wt% X-GNP-SC), probably due to the constraint imparted by the filler particles onto the PP chains during crystallization. Furthermore, the higher thermal conductivity of X-BNNS-SC and X-GNP-SC may locally produce faster heat transfer forcing the near neighbour PP chains to cool quicker than those further away during the cooling cycles, reducing the PP crystalline content [35]. In future work, the modulated DSC analysis coupled with the hot-stage polarised optical microscopy analysis both under isothermal and non-isothermal condition could be carried out to further assess the mechanisms of nucleation and growth of the PP crystallites upon inclusion of X-BNNS-SC/X-GNP-SC.
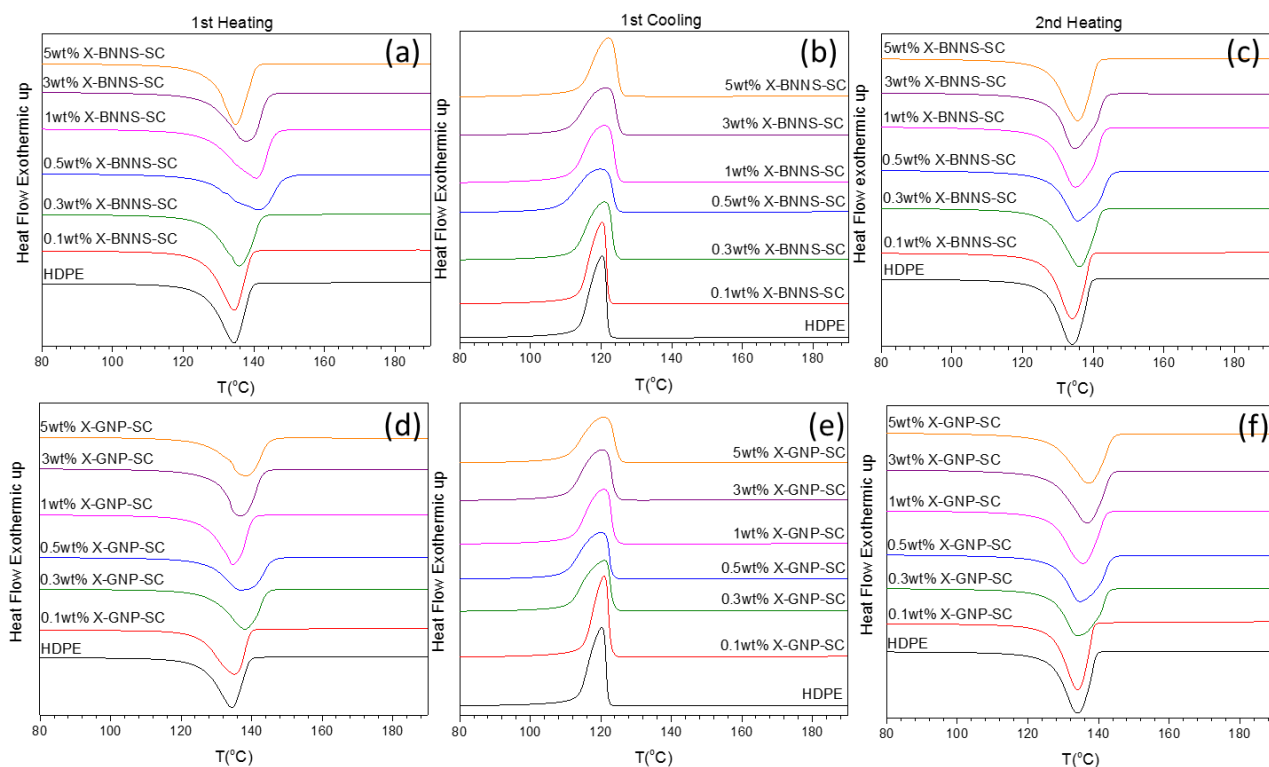
Figure 4.6: DSC thermograms of HDPE and its composites with X-BNNS-SC (a)-c)) and X-GNP-SC (d)-f)).

The melting peaks in the thermograms related to the first and second heating of the composites of HDPE+X-BNNS-SC (Figure 4.6 a) and c)) and HDPE+X-GNP-SC (Figure 4.6 d) and f)) show a broadening compared to the melting peak of the neat HDPE. Similarly, the cooling peaks in the first cooling thermograms of HDPE+X-BNNS-SC (Figure 4.6 b)) and HDPE+X-GNP-SC (Figure 4.6 e)) broaden compared to the peak for neat HDPE. These results suggest that a broader crystallite size distribution is realized upon addition of filler.

In Table 4.4, the main parameters determined from DSC analysis of the composites of HDPE with X-BNNS-SC and X-GNP-SC are reported.

Table 4.4. T_m, T_c, ΔH_m, ΔH_c and X_c (%) of HDPE and its composites with X-BNNS-SC and X-GNP-SC, obtained from the DSC thermograms. ΔH_c, related to a theoretical HDPE crystal with infinite dimensions, used to calculate the crystallinity was taken as 287 J/g [30]. The error calculated for T_m, T_c amd X_c (%) falls on the first decimal, which is not significant for the present study.

Samples	T_m(ºC)		T_c(ºC)	ΔH_m(J/g)		ΔH_c(J/g)	X_c(%)
	1st heating	2nd heating	1st cooling	1st heating	2nd heating	1st cooling	1st cooling
HDPE	134	134	120	177	205	202	69
0.1 wt% X-BNNS-SC	137	136	121	187	216	210	72
0.3 wt% X-BNNS-SC	136	136	121	187	223	219	75
0.5 wt% X-BNNS-SC	141	136	120	187	224	222	75
1 wt% X-BNNS-SC	141	135	121	187	224	222	78
3 wt% X-BNNS-SC	138	135	121	192	227	225	75
5 wt% X-BNNS-SC	133	136	122	194	220	217	70
0.1 wt% X-GNP-SC	135	134	121	184	212	202	69
0.3 wt% X-GNP-SC	138	134	121	184	216	208	71
0.5 wt% X-GNP-SC	137	135	120	175	213	210	71
1 wt% X-GNP-SC	135	135	121	192	219	215	73
3 wt% X-GNP-SC	136	135	120	193	230	230	76
5 wt% X-GNP-SC	136	136	121	179	221	222	72

From Table 4.4, it can be noted that both the melting temperature T_m and crystallization temperature T_c do not change when comparing neat HDPE to the composites with 5wt% of X-BNNS-SC/X-GNP-SC. The variation in melting enthalpy (ΔH_m) for HDPE+X-BNNS-SC and HDPE+X-GNP-SC calculated for the peak registered during the first and second heating cycles increases compared to neat HDPE, probably due to the crystallization of either larger or thicker HDPE lamellae upon filler incorporation. In addition, the ΔH_m calculated for the second heating cycle increases compared to the ΔH_m calculated for first heating cycle peaks for both sets of composites with X-BNNS-SC and X-GNP-SC, which could be caused by the formation of either larger or thicker lamellae formed during the first cooling cycle. The variation of crystallization enthalpy, ΔH_c follows the same trend as ΔH_m, *i.e.* the increase of ΔH_c upon filler incorporation could be associated with a change of HDPE crystallite size dimensions. X_c(%) increases from 69% (HDPE) to 75% when adding X-BNNS-SC up to 3wt% before decreasing to 70% at 5wt% of filler loading. The first increase could be associated with a better dispersion

and distribution of the small platelets of this BNNS in HDPE, providing higher surface area for crystallization of HDPE under the controlled conditions realised during the DSC experimental. The following decrease of X_c(%) at 5wt% of X-BNNS-SC could be caused by a combined effect of filler particle constraint onto the HDPE chains dynamics and/or aggregation of this BNNS at higher loadings, which reduced the surface areas available for the crystallization of HDPE. X_c(%) does not change when comparing HDPE with its composites with X-GNP-SC. Probably, the larger size of this GNP (few µm) compared to the X-BNNS-SC (few nm) constrained the HDPE chains more than the small X-BNNS-SC platelets. As already mentioned for the composites of PP, future hot-stage polarised microscopy could support to predict the mechanisms of nucleation and growth of the HDPE crystals in presence of X-BNNS-SC and X-GNP-SC.

4.3.2- Study of the rheological and mechanical properties of composites of PP and HDPE with X-BNNS-SC and X-GNP-SC.

Oscillatory rheology measurements were performed on composites of PP and HDPE with X-BNNS-SC and X-GNP-SC to assess the extent of filler dispersion and distribution in the matrix, see Figures 4.7 and 4.8.
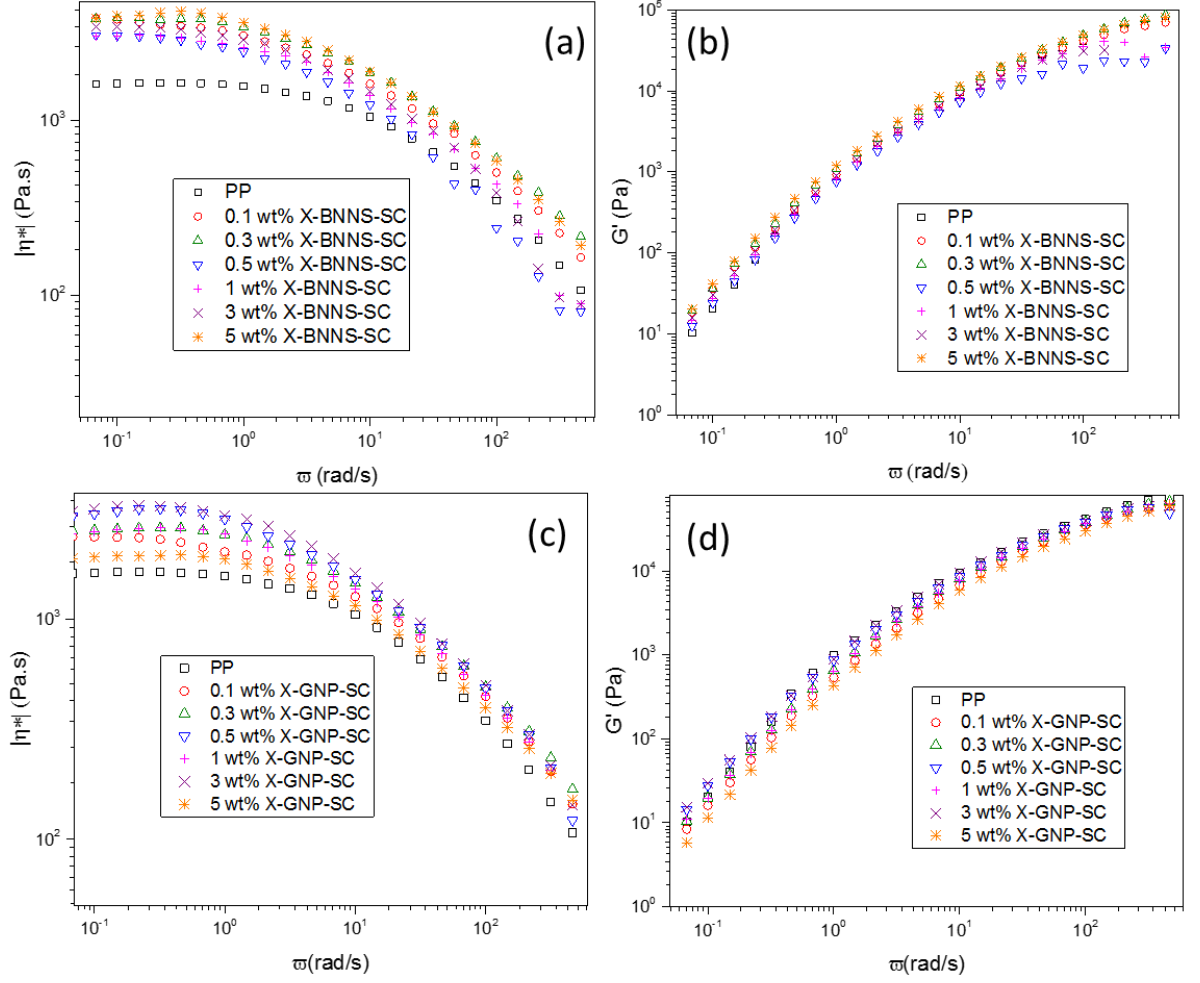
Figure 4.7: complex viscosity |η*| and storage modulus G′ as a function of angular frequency (ω) for PP and its composite with X-BNNS-SC (a)-(b) and X-GNP-SC (c)-(d).

The structure of polymers, in terms of chain arrangement, is altered when a 3D filler-filler network is formed. In particular, the storage modulus G′ tends to form a plateau with frequency when a percolated network is attained, whereas the viscosity tends to increase at low frequencies, since the material passes from displaying pseudo- 'fluid like' to a more pseudo- 'solid like' behaviour. The graphs in Figure 4.7 are reported in double logarithmic scale to better visualize the behaviour at low frequency. Indeed, at low frequencies, it is possible to study the structure at long-range between particles, thus detecting the eventual formation of a 3D network or rheological percolation [36]. The rheological profiles of the as prepared composites are not different when compared with neat PP. The complex viscosity |η*| is constant with the frequency at ω < 1 rad/s (Newtonian profile) both for PP and its composites with X-BNNS-SC and with X-GNP-SC, before linearly decreasing (power law) with frequency (Figure 4.7 a) and c)). An increase in viscosity of 1000 Pa.s at 5wt% filler was detected in the

Newtonian region, which was expected with such relatively high filler content. The storage modulus, G′(stiffness) increases with frequency and the trend does not change when comparing neat PP with both sets of composites with X-BNNS-SC and X-GNP-SC, that is, no percolation was detected (Figure 4.7 b) and f)). This could be associated to the strong particle-particle interactions during melt-mixing- partially caused by the presence of the surfactant SC- and the limited mixing efficiency of the adopted processing, which obstructed the optimal dispersion and distribution of the filler particles in PP during melt-mixing, thus preventing the formation of an interconnected 3D network of these BNNS/GNP grades in the matrix.
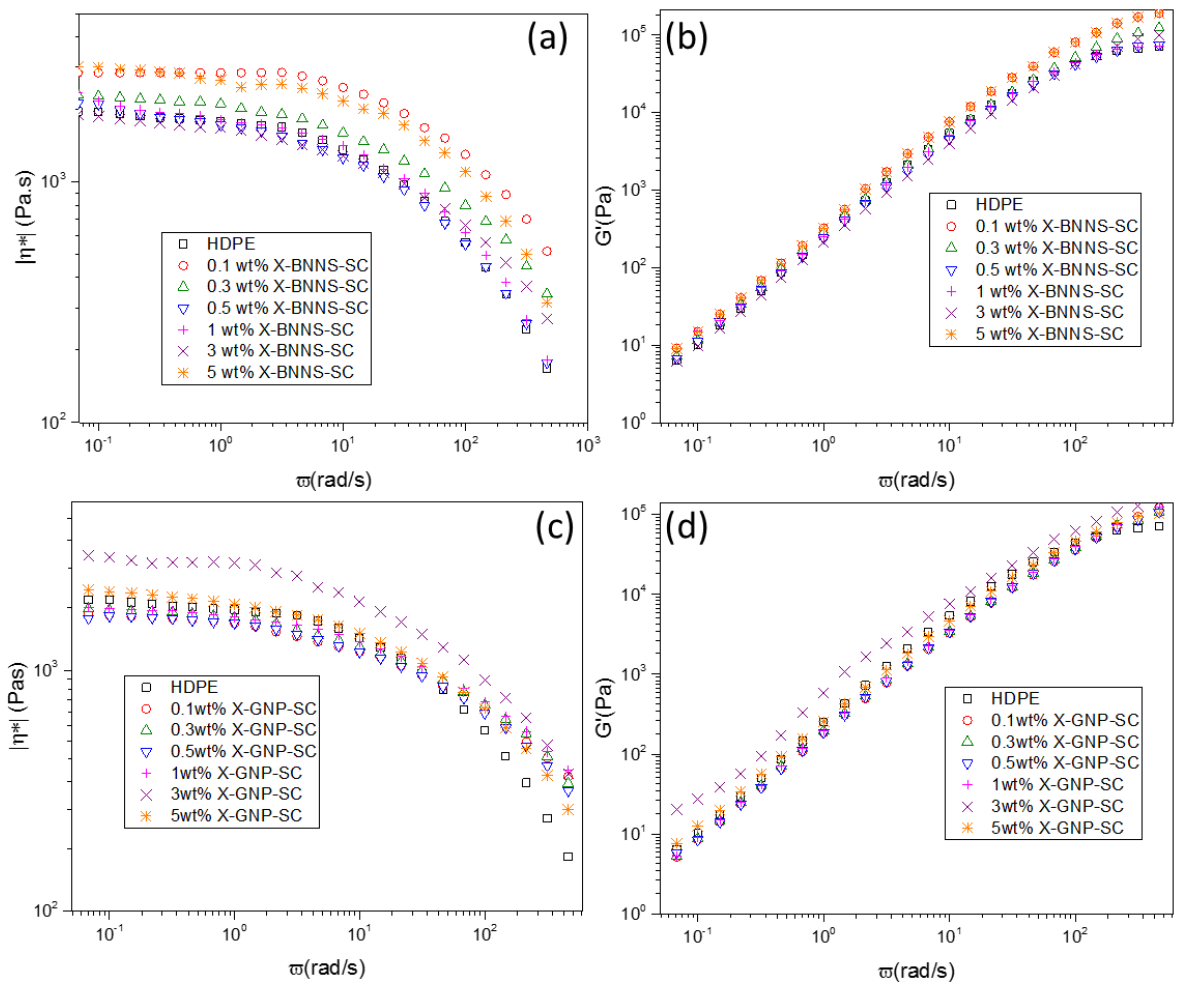
Figure 4.8: |η*| and G′ in function of ω for HDPE and its composite with X-BNNS-SC (a)-b)) and X-GNP-SC (c)-d)). The data are a replica of 3 measurements on a batch of 3 specimens per compositions.

The rheological profiles of the composites of HDPE with X-BNNS-SC and X-GNP-SC do not differ from the rheological profiles of the neat HDPE, suggesting that rheological percolation

was not attained. $|\eta^*|$ is constant with frequency at $\omega < 1$ rad/s (Newtonian profile) both for HDPE and its composites with X-BNNS-SC and with X-GNP-SC (Figure 4.8 a) and c)), before decreasing linearly with the frequency (power law). As already seen for the composites of PP with X-BNNS-SC and X-GNP-SC, $|\eta^*|$ increases to 1000 Pa.s at 5%wt of filler loading. No change in G´was detected (Figure 4.8 b) and d)), that is no rheological percolation was attained with the processing adopted and in the range of compositions explored. As already noticed for the composites of PP, the strong particle-particle interactions and the limited mixing efficiency under the adopted processing conditions could prevent the formation of a 3D network of X-BNNS-SC/X-GNP-SC in HDPE, thus no rheological percolation is detected.

The mechanical properties of the composites of PP and HDPE with X-BNNS-SC and X-GNP-SC were investigated by tensile tests. The representative stress-strain curves are reported in Figure 4.9 for the composites of PP and 4.10 for the composites of HDPE, along with the trends and values of the Young's modulus (E) and stress at yield (σ_y) in function of the X-BNNS-SC and X-GNP-SC loadings.
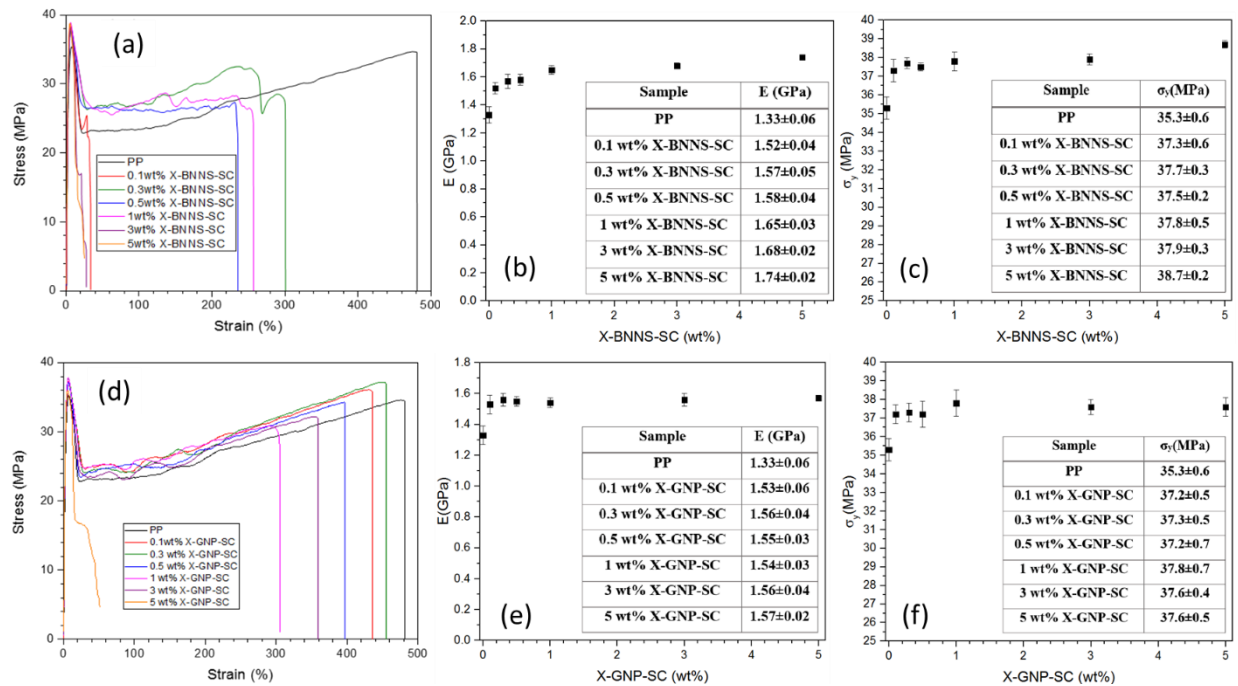
Figure 4.9: Representative stress-strain curves for PP and its composites with X-BNNS-SC (a)) and X-GNP-SC (d)). Young's modulus (E) in function of X-BNNS-SC loadings (b)) and X-GNP-loadings (e)). Stress at yield (σ_y) in function of X-BNNS-SC loading (c)) and X-GNP-loading (f)).

The stress-strain curves of PP and its composites with X-BNNS-SC and X-GNP-SC at different filler loadings are reported in Figure 4.9 a) and d) respectively. The presence of the filler particles appear to reduce the elongation at break of PP. Internal fractures occurred after yield, as evident from the noise detected in the plastic region, probably due to the dissipation of the internal stresses generated during the processing and/or by the presence of the filler particles acting as spots of stress accumulation. In addition, there could be some hydrophobic interactions between the cyclo-hexane rings of the surfactant SC (see Chapter 3) and PP, which could break as the polymer chains disentangle and stretch during the tensile tests. Further work should be addressed toward the study of the mechanism of interactions between the surfactant SC and PP by solid state ^{13}CNMR to confirm the mechanism of interactions between the BNNS/GNP and PP.

The inclusion of the X-BNNS-SC and X-GNP-SC resulted in an increase of the Young's Modulus (E) from 1.33±0.06 GPa for the neat PP to 1.74±0.02 GPa and 1.57±0.02 GPa at 5wt% of X-BNNS-SC and X-GNP SC respectively. The first major increase of E is detected at a filler content as low as 0.1 wt% before linearly increase with the X-BNNS-SC/X-GNP-SC content, as depicted in Figure 4.9 b) and e). The stress at yield (σ_y) follows the same trend as E as reported in Figure 4.9 c) and f), specifically σ_y increases from 35.3±0.6 MPa for the neat PP to 38.7±0.2 MPa and to 37.6±0.5 MPa at 5wt% of X-BNNS-SC and X-GNP-SC respectively. The increase of E and σ_y could be associated to a combination of factors including the intrinsic rigidity of the BNNS and GNP particles, the formation of entanglements of polymer chains around the filler particles and the change in polymorphism of PP upon filler incorporation. Indeed, as previously noticed in the XRD results (Figure 4.3), the addition of X-BNNS-SC and X-GNP-SC promoted the crystallization of the β-PP, which is known to be stiffer than the α-PP. Further study should be addressed toward the comprehension on the contribution of filler particle rigidity, polymer entanglements and polymer polymorphism onto the mechanical properties. By way of example, a modelling study on the melt-flow during melt-mixing, particularly during injection moulding, could support the research at understanding the extent of distribution and dispersion of the filler particles along the specimen being injected, the melt flow of the polymer and the crystallization dynamics as the polymer crystallizes in the dumbbell mould [37-42].
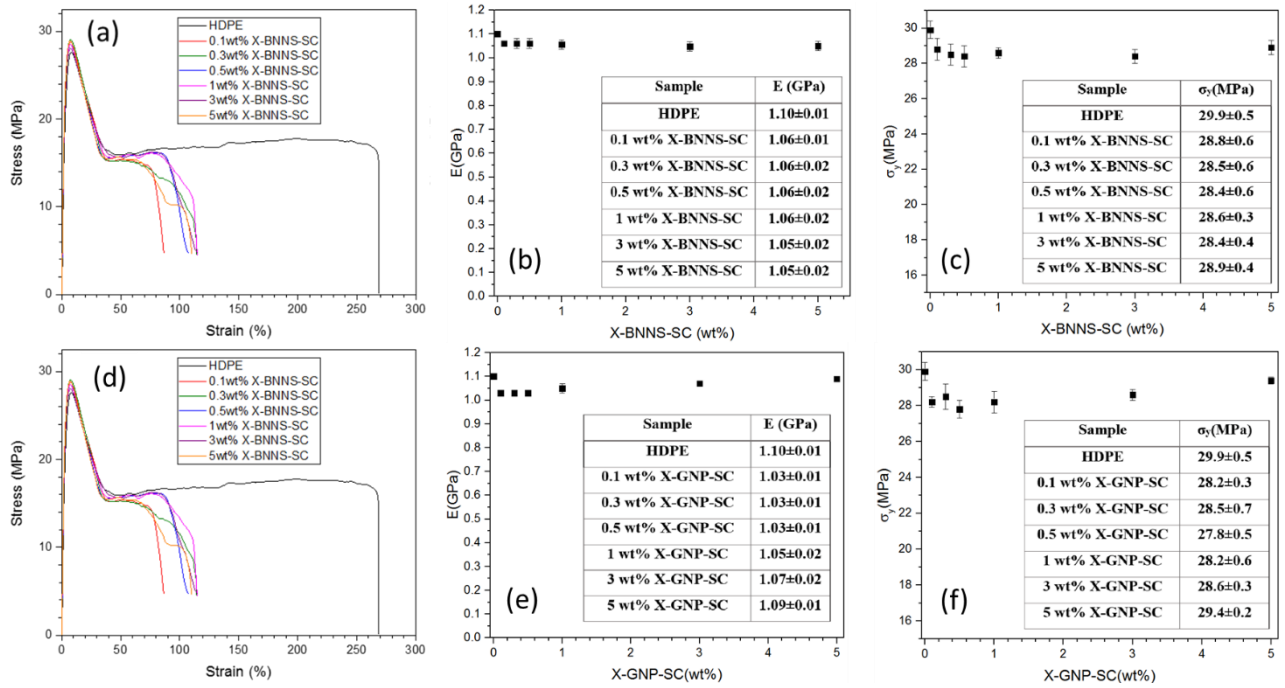
Figure 4.10: Representative stress-strain curves for PP and its composites with X-BNNS-SC (a)) and X-GNP-SC (d)). E in function of X-BNNS-SC loadings (b)) and X-GNP-loadings (e)). σ_y in function of X-BNNS-SC loading (c)) and X-GNP-loading (f)).

The stress-strain curves of HDPE and its composites with X-BNNS-SC and X-GNP-SC at different filler loadings are reported in Figure 4.10 a) and d) respectively. The presence of the filler particles appear to reduce the elongation at break as already noticed in PP. Again, the release of the internal stresses- generated during the processing and/or by the presence of the filler particles acting as spots of stress accumulation- could cause internal fractures manifested as a noise in the stress-strain curves after yield.

Both E and σ_y slightly decrease upon filler incorporation. The XRD confirmed that the addition of the filler did not change the crystallinity of the HDPE, therefore the reduction of E and σ_y is unlikely due to a decrease in the crystallinity of the polymer. Probably, the X-BNNS-SC and X-GNP-SC agglomerated during melt-mixing/injection moulding, perhaps due to the known rapid crystallization kinetics of HDPE, which could cause the exclusion of the X-BNNS-SC/X-GNP-SC from the crystalline domains and favour the agglomeration of the filler particles [37-42]. Again, a modelling study on the melt-flow of the composites during injection moulding could help to predict the mechanisms of distribution and dispersion of the filler particles in HDPE, as well as the dynamics of crystallization as the polymer flows in the mould, which ultimately affect the mechanical properties.

In the perspective of using TS BNNS and GNP composites in thermal conductive devices, thermal conductivity measurements were performed at TS (Chapter 3). The results are reported in the next section.

4.3.3- Thermal Conductivity (TC) of the composites of PP and HDPE with X-BNNS-SC and X-GNP-SC

Figure 4.11 shows the TC of PP and its composites with X-BNNS-SC (a)) and X-GNP-SC (b)) and for HDPE and, its composites with X-BNNS-SC (c)) and X-GNP-SC (d)).
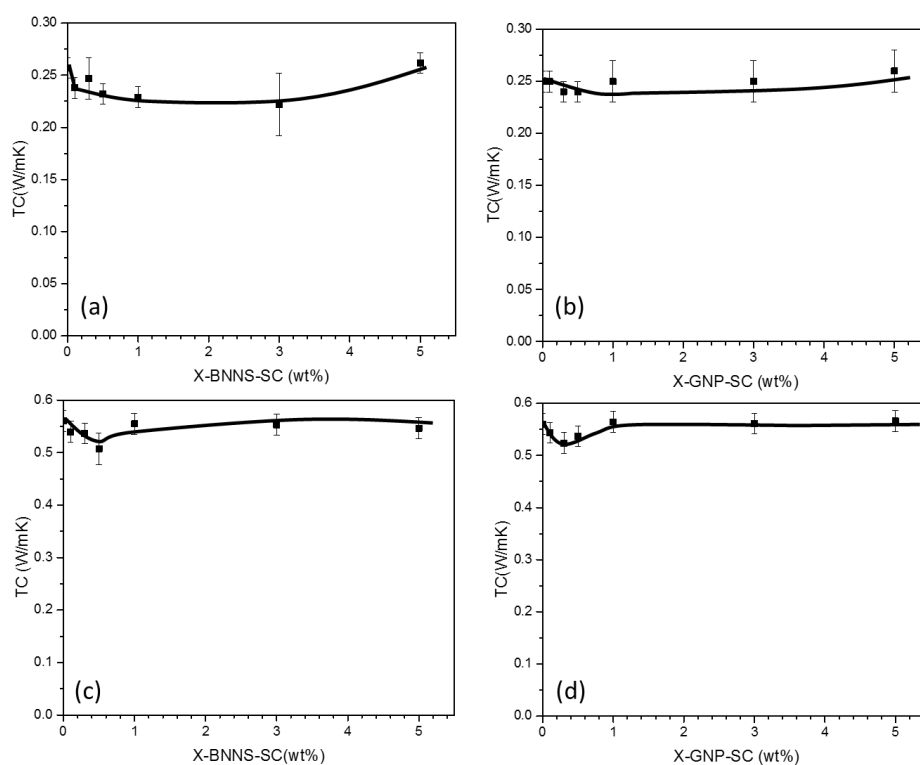
Figure 4.11: Thermal conductivity (TC) of PP and its composites with X-BNNS-SC and X-GNP (a) and b)) and HDPE and its composites with X-BNNS-SC and X-GNP-SC (c)-d)) as a function of filler loadings.

No difference in TC can be seen for both PP and HDPE composites. The irregular-shape flake of the filler and the particle-particle interactions preferred over the particle-polymer interactions contributed to the production of inhomogeneous composites during melt-mixing where a conductive 3D network of X-BNNS-SC/X-GNP-SC was not attained. In addition, the presence of the surfactant on the surface of the X-BNNS-SC/X-GNP-SC platelets, the

randomness of these BNNS/GNP flake distribution in the sample along the direction of the TC measurements (through thickness) could result in a high interfacial resistance *i.e.* phonon scattering, which depressed the thermal conduction [43] (and references therein).

The next section shows the results of the characterization of the composites with PP-model matrix- and the different grades of BNNS and GNP, namely X-BNNS-SC, X-BNNS-T, Y-BNNS-L, X-GNP-SC, X-GNP-L and Y-GNP-L (see section 4.2). The composites were prepared by 16mm co-rotating twin screw extruder and post processed by micro-injection moulding. The extruder used allowed for the setting of the temperature profile along the barrel and for the variation of the screw configuration, key parameters when processing functional composite materials. In one sense, the temperature profile defines the molten state of the polymer matrix in terms of viscosity (*i.e.* flowability), which in turn is a contributing factor with regard the distribution/dispersion of the filler. On other, the combination of the extensional flow realized along the helical elements and the shear forces achieved by the mixing elements along the screws in the parallel twin-screw extruder can assist the exfoliation of filler agglomerates, thus improving the mixing of the filler particles with the polymer matrix. Furthermore, the capacity of the equipment used is up to 500g/h, which better simulate the scale-up on industrial scale.

4.4- Characterization of the composites of PP with TS BNNS and GNP prepared by 16mm co-rotating twin-screws extruder and micro-injection moulding

4.4.1- Study of the morphology and crystalline structure of the composites of PP with X-BNNS-SC, X-BNNS-T, Y-BNNS-L

The morphology and crystalline structure of the composite of PP with the X-BNNS-SC, X-BNNS-T and Y-BNNS-L were investigated by SEM, XRD and DSC.
Figure 4.12 depicts the SEM images of the composites of PP and the examined grades of BNNS at 5wt% and 10wt% of filler loading.
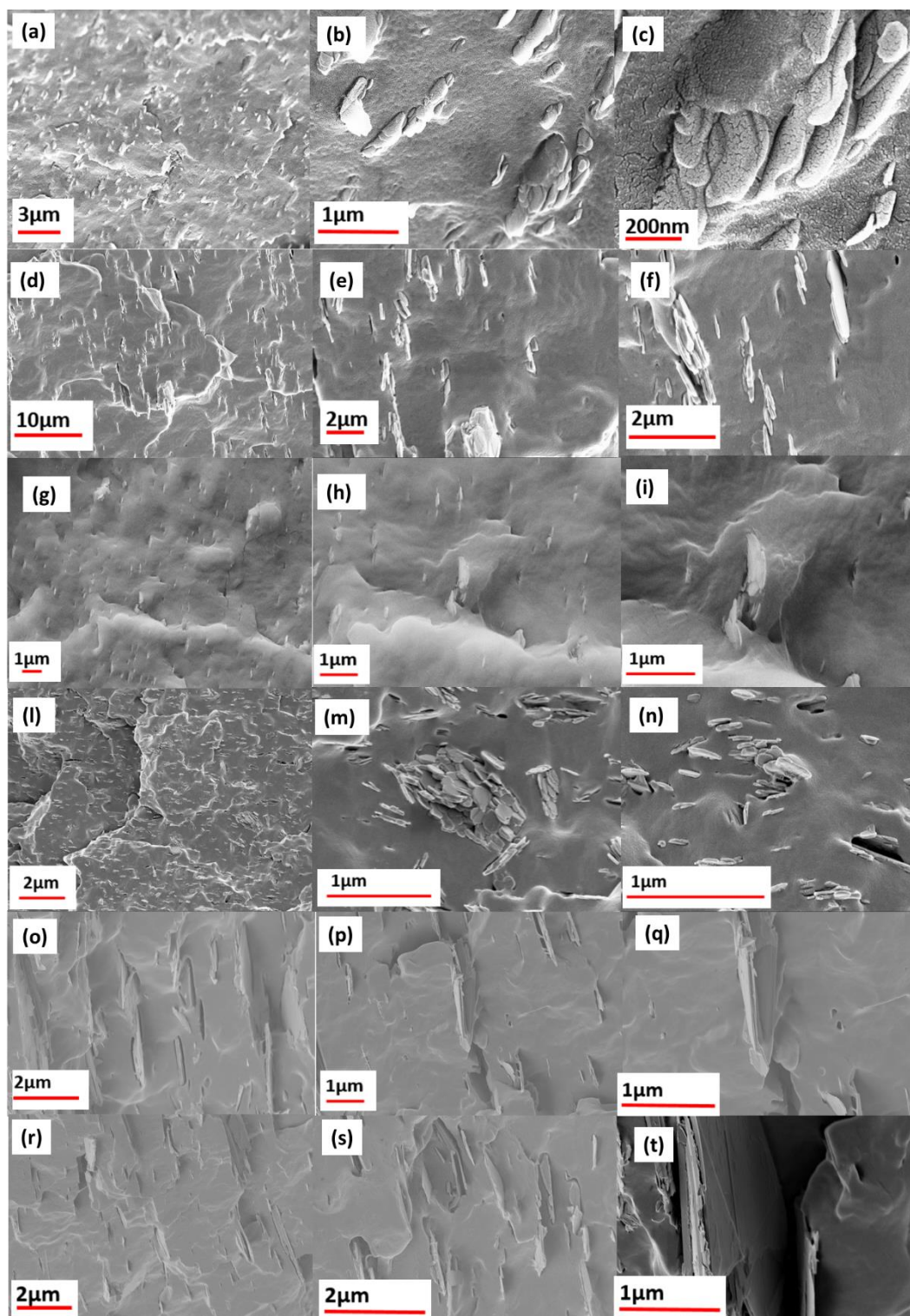
Figure 4.12: SEM images of the composites of PP with X-BNNS-SC at 5wt% (a)-c)) and 10wt% (d)-f)), X-BNNS-T at 5wt% (g)-i)) and 10wt% (l)-n)), Y-BNNS-L at 5wt% (o)-q)) and 10wt% (r)-t)). The magnification of the SEM images increases from left to right.

Good dispersion and distribution of the X-BNNS-SC in the polymer matrices was achieved at both 5wt% and 10wt% filler loading (Figure 4.12 a)-f)), when processed using the

16mm extruder (images examined across the length scales). The application of shear and some extensional flow in the parallel twin screw extruder was more effective at breaking down filler agglomerates during mixing with PP when compared with the laboratory scale extruder (Figure 4.1). The images a) and d) show an even distribution of X-BNNS-SC on the µm scale, but agglomerates are present on the nanometre scale (b, c).

The SEM images of PP+X-BNNS-T at 5wt% filler loading (Figure 4.12 g)-i)) show a relative homogeneous distribution of the X-BNNS-T in PP, particularly on the micrometre scale (g) whereas at 10wt% (Figure 4.12 l)-n)) large agglomerates of X-BNNS-T formed (dimension of agglomerate up to 1µm, image m)), probably due to the fact that the mixing conditions adopted did not exfoliate the platelets into thinner flakes when adding such relatively high quantities of this BNNS. In addition, the X-BNNS-T are highly hydrophilic (see sessile tests section 4.2.), which could lead to stronger particle-particle interactions when added in high amounts. The particle-particle interactions are preferred over polymer-particle interactions.

The SEM images of PP+Y-BNNS-L at 5wt% (Figure 4.12 o)-q)) and 10 wt% (Figure 4.12 r)-t)) of filler loadings show voids (as depicted in t)) around the Y-BNNS-L particles formed upon injection moulding, although a relative good distribution and dispersion of Y-BNNS-L in PP is attained on the micrometre scale (o, r). The presence of the voids could be caused by the limited wettability of the PP chains onto this BNNS particles, perhaps as a result of the hydrophilic irregular square-shaped of this BNNS, which prevented an intimate contact between the PP and the filler particles during crystallization.

Systematic SEM imaging should be carried out on a statistical number of samples along different sections of the specimens to assess accurately the effect of injection moulding and filler morphology/content onto the morphology of the resulting composites. In addition, it would be interesting to perform a modelling study on the melt flow of the PP composites, to better understand the state of dispersion, distribution and alignment of the filler particles in the matrix as PP crystallize during injection moulding.

The XRD data on the composites of PP with the different grades of BNNS are reported in Figure 4.13. Specifically, the XRD patterns are reported in Figure 4.13 a)-c) whereas the fraction of β-crystals (K_β), α-crystals (K_α) and total crystalline fraction (X_c(%)) of PP as a function of filler loadings for the three sets of composites with X-BNNS-SC, X-BNNS-T, Y-BNNS-L are reported in Figure 4.13 d)-f). The K_β was calculated using equation 4.1. X_c(%)

was calculated by integrating the XRD patterns in OriginPro. The K_{α} was calculated by subtracting the K_{β} values from the $X_c(\%)$ values, since the PP used crystallized only in the α and β forms.
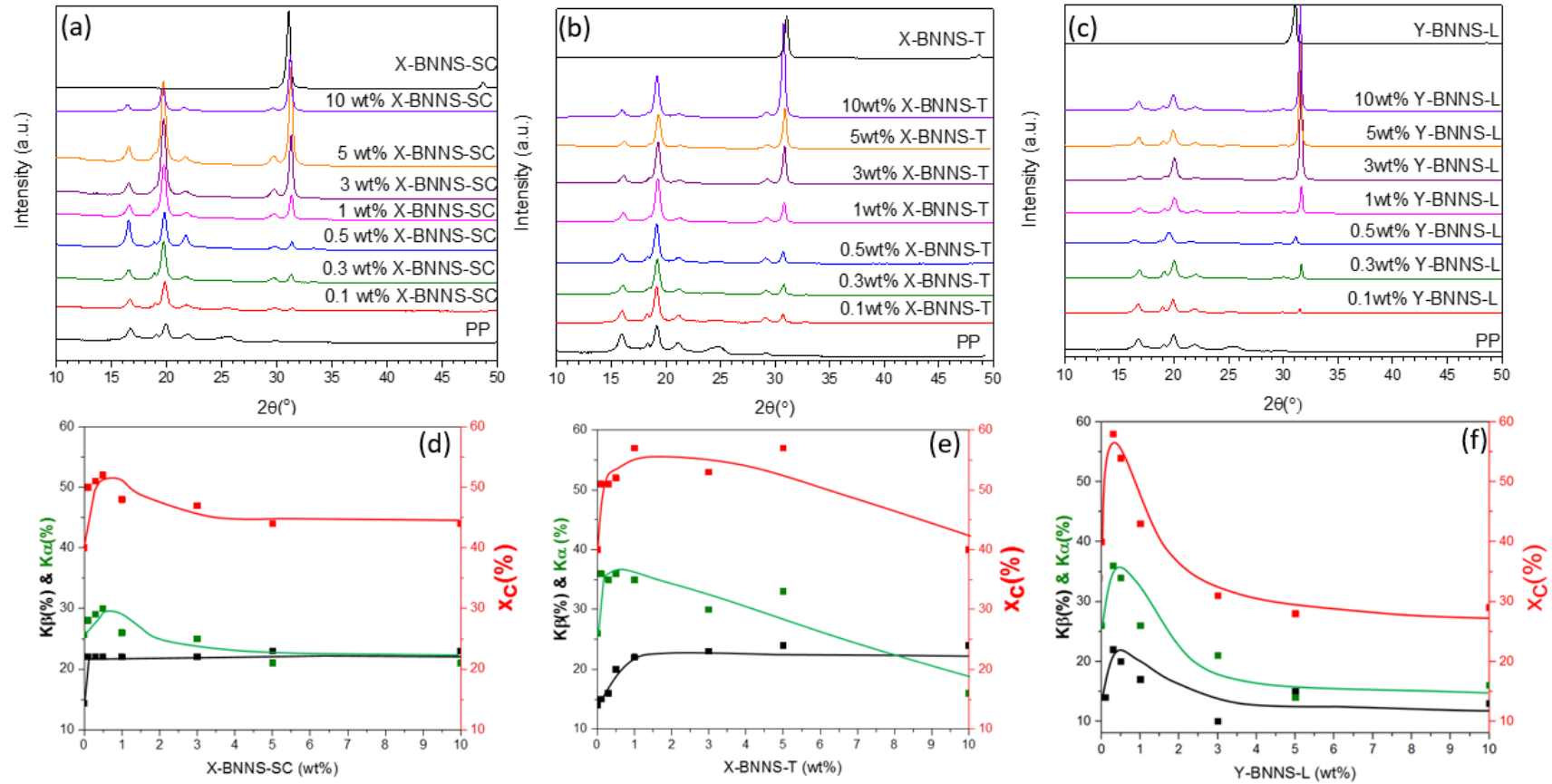
Figure 4.13: XRD patterns of PP and its composites with X-BNNS-SC (a)), X-BNNS-T (b)) and Y-BNNS-L (c)). Fraction of β-crystallites (K_β), fraction of α-crystallites (K_α) and total crystalline fraction ($X_c(\%)$) of PP in the composites with X-BNNS-SC (d)), X-BNNS-T (e)) and Y-BNNS-L (f)) in function of the filler loading. The results are from three replicates. The error calculated on the K_α, K_β, $X_c(\%)$ falls on the first decimal point, which is not significant for this type of study.

The XRD patterns reported in Figure 4.12 a)-c) showed the most intense peaks for PP at $2\theta = 16.5°$ $\alpha(100)$, $19.2°$ $\beta(300)$, $20°$ $\alpha(040)$, $22°$ $\alpha(130)$, and for the X-BNNS-SC/X-BNNS-T/X-BNNS-L at $2\theta = 31°$ (002). The intensity of the single peak in the X-BNNS-SC/X-BNNS-T/Y-BNNS-L patterns at $2\theta= 31°$ due to the crystallographic plane (002) increased with increasing filler loading, as expected, probably due to the agglomeration of filler particles at high loading [44].

The total crystalline content of β-crystals (K_β) of PP in the composites of X-BNNS-SC as a function of filler loading (Figure 4.12 d)) increased from 14% (PP, partially due to the pre-existent β-crystal in the material as received and partially derived from induced crystallization during injection moulding) up to 24% for X-BNNS-SC = 0.5 wt % and remained constant at higher X-BNNS-SC loadings, highlighting a β-nucleating effect of X-BNNS-SC for PP ([27] and references therein). Interesting insights can be made when further analysing the crystalline structures of the composites of PP with X-BNNS-SC in terms of total crystalline content of α-crystals (K_α) and the total crystallinity X_c(%) of PP in the composites as a function of X-BNNS-SC loading (Figure 4.12 d)). At X-BNNS-SC loadings up to 0.5wt%, K_α, K_β, X_c(%) increase whereas at higher filler loadings the trends in K_α, K_β, X_c(%) differ from each other. In particular, K_β remains constant at higher X-BNNS-SC whereas K_α and X_c(%) first decrease at a filler loading between 0.5wt% and 3wt% before plateauing at higher filler loadings. The X-BNNS-SC favoured the nucleation/growth of both the α-crystals and β-crystals when added in concentrations between 0.1wt% and 0.5wt%, resulting in the increase of the total crystal fraction X_c(%) compared with PP alone. At a concentration between 0.5wt% and 3wt%, X-BNNS-SC favoured the nucleation/growth of PP β-crystallites over the α-crystallites whereas at higher filler loadings there is no competition between the formation of α and β crystallites of PP.

From the trend in K_β for PP composites with X-BNNS-T (Figure 4.12 e)), it is clear that this grade of BNNS had a β-nucleating effect on the PP. Specifically, K_β calculated increased up to 24% for 0.5wt% X-BNNS-T and remained constant at higher filler loadings. There was no further β-nucleation above 0.5wt% of X-BNNS-T, probably because at higher filler loadings X-BNNS-T particles constrained the movement of PP chains and no more chains could align and orient onto the filler platelets, thus, limiting the formation of more β-crystals [26]. At X-BNNS-T loading up to 0.5wt %, K_α, K_β and X_c(%) increase (Figure 4.12 e)), suggesting that at low filler concentrations ($\leq$0.5wt%) X-BNNS-T facilitated the crystallization of both α and β

crystallites of PP, which results in an increase in the total crystalline fraction X_c(%) compared to the neat PP. At higher filler loadings (>0.5wt%) the trends in K_α, K_β and X_c(%) differ from each other. Indeed, K_β remains constant, whereas K_α and X_c(%) decrease with the increase of the filler content. This result suggest that X-BNNS-T favoured the formation of the β-crystallites of PP at the expense of the α-crystallites and the total crystallinity X_c(%) decreases.

The K_β increased from 14% (PP) up to 21%, at 0.5wt % of Y-BNNS-L (Figure 4.12 f)), before decreasing at *ca* 10% at 3wt% of Y-BNNS-L, where it remained constant at higher filler loadings. Clearly, this grade of BNNS favoured the β-crystals nucleation/growth at low filler content but the β-nucleating effect is depressed at Y-BNNS-L ≥0.5wt%. At a Y-BNNS-L loadings up to 0.5wt%, K_α, K_β, X_c(%) (Figure 4.12 f)) all increase, suggesting that at low filler concentrations (≤0.3wt%) Y-BNNS-L facilitated the crystallization of both α and β crystallites of PP, which resulted in an increase of the total crystalline fraction X_c(%) compared to the neat PP. Yet, at higher filler loadings K_α, K_β, X_c(%) decrease before plateauing at 3wt% of Y-BNNS-L, suggesting that the filler hindered the PP chains dynamic during crystallization, thus, obstructing the formation of either α or β crystallites.

The XRD results highlight the role of BNNS morphology and surface chemistry on the polymorphism of PP. The morphology of the different grades of BNNS depends mainly on the morphology of the bulk BN and the conditions adopted during the exfoliation thereof in the HPH by TS, whereas the surface chemistry is determined by the surfactant and liquid medium used during the exfoliation of the bulk materials.

The two grades of BNNS exfoliated from the bulk BN-X, namely X-BNNS-SC and X-BNNS-T, differ from each other by the presence of the surfactants SC and T respectively. The different trends of K_α, K_β, X_c(%) when comparing the two sets of composites of PP with X-BNNS-SC and X-BNNS-T could be a result of the different surface chemistry of the two BNNS. Indeed, the presence of functional groups on the surface of the filler particles (see XPS section 4.2) and the different chemical structures of the surfactants SC and T could affect the way the PP chains rearrange near the X-BNNS-SC and X-BNNS-T particles during crystallization. At low filler content (≤0.5wt%), K_α, K_β, X_c(%) increase for both set of composites but the K_β of the PP+X-BNNS-T appear to increase slower than K_β of the PP+X-BNNS-SC, whereas the K_α and X_c(%) of the composites with X-BNNS-T appear to increase faster than the composites with X-BNNS-SC (allowing for the error in the calculation). Probably, the X-BNNS-T particles obstructed the crystallization of the near PP chains in β-form more than the X-BNNS-SC did, perhaps due to the high concentration of oxidised groups onto the X-BNNS-T, which could

favour the particle-particle interactions, *i.e.* agglomeration, and less filler platelets are available for PP to crystallize on, thus favouring the more stable α-crystallites to nucleate/grow. At higher loadings (≥0.5wt%), K_α, X_c(%) decrease but K_β plateaus for the composites with X-BNNS-T, whereas K_α, K_β, X_c(%) all plateau for the composites with X-BNNS-SC. Probably, it becomes more difficult to distribute and disperse the filler in the matrix with the adopted processing procedure -due to different factors, including the viscosity of the system and the strong particle-particle interactions- therefore no further increase in K_β was noticed and K_β plateau for both sets of composites with X-BNNS-SC and X-BNNS-T.

The morphology of the bulk BN-Y determined the geometry of the resulting exfoliated Y-BNNS-L which showed large square platelets with lateral lengths up to 10 µm (SEM section 4.2). The geometry of the Y-BNNS-L reflects the trends obtained for K_α, K_β and X_c(%), which are completely different from the K_α, K_β, X_c(%) for X-BNNS-SC and X-BNNS-T. Specifically, the values of K_α, K_β, X_c(%) for the composites with Y-BNNS-L registered the first major increase at 0.1wt% before gradually decreasing, starting from a filler content as low as 0.3wt%. The large Y-BNNS-L platelets could hinder the PP chains dynamics during the crystallization of the polymer. As a consequence, K_α, K_β, X_c(%) depressed with the inclusion of more Y-BNNS-L particles.

In future work it would be interesting to carry out Small-Angle X-Ray scattering (SAXS) coupled with Wide-angle X-Ray diffraction (WAXD) measurements to assess the crystal geometry in which the PP chains arrange near and perhaps around the BNNS particles.

The DSC analysis was performed to further assess the nucleation effect and crystallinity of PP upon inclusion of X-BNNS-SC, X-BNNS-T and Y-BNNS-L. The results are summarised in Figure 4.14 and Table 4.5.
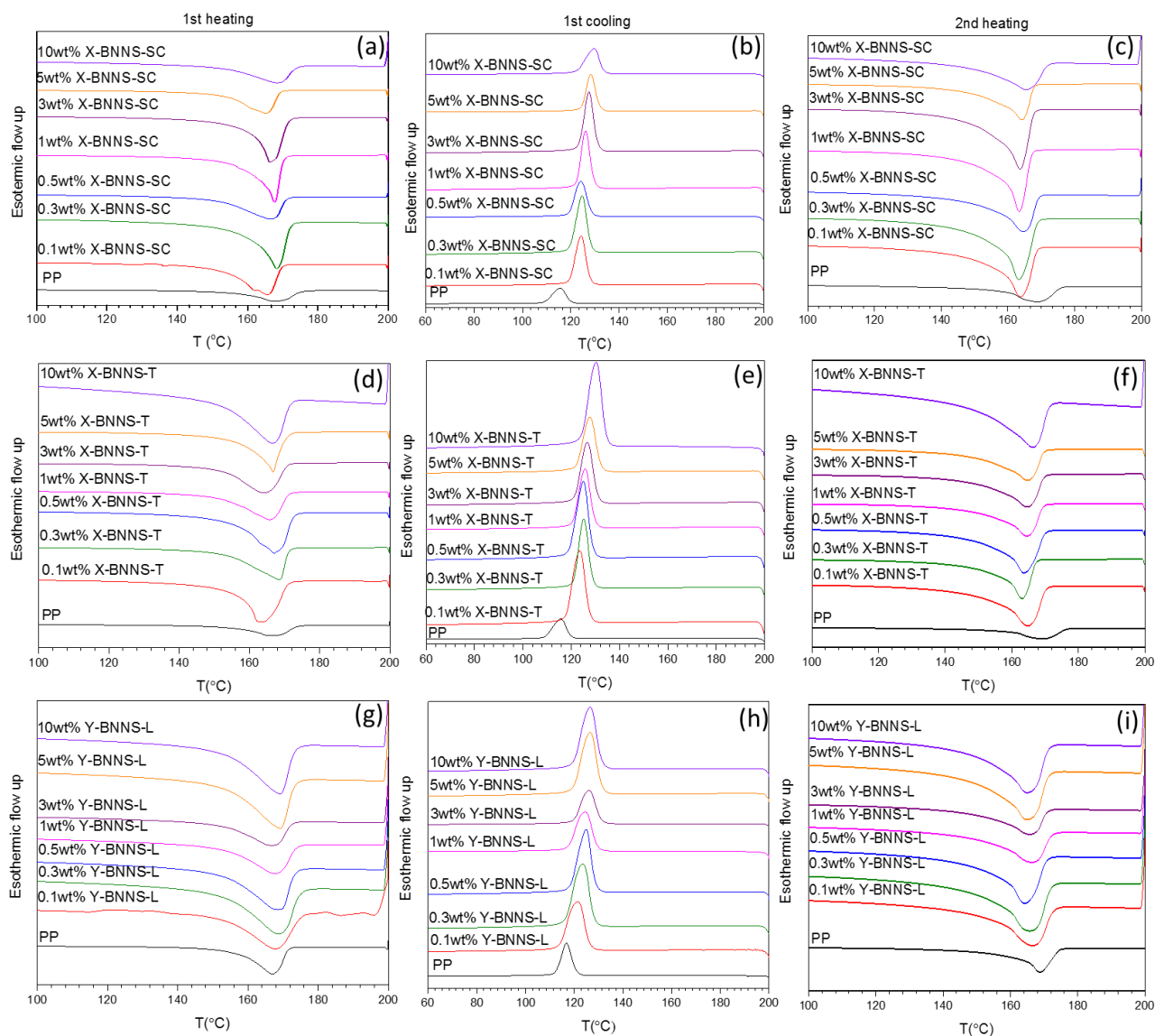
Figure 4.14: DSC thermograms for PP and its composites with X-BNNS-SC (a)-c)), X-BNNS-T (d)-f)) and Y-BNNS-L (g)-i)) at different filler loadings.

The first heating thermograms of the composites of PP with X-BNNS-SC (Figure 4.14 a)) show broad and asymmetric peaks confirming the coexistence of α-PP and β-PP crystals, as evident from the shoulder in the melting peaks at around 165.5 °C, for a X-BNNS-SC loading of 0.1wt%, 3wt% and 5wt%. These results suggest a change in PP polymorphism upon filler incorporation, as previously confirmed by XRD experiments. However, the β-PP polymorph content increased on going from the neat PP to the composites with 0.5 wt % X-BNNS-SC (XRD), but a similar trend was not visible in the DSC thermograms. The reason for this discrepancy could be associated with the β–α phase transition during the first heating step in the DSC experiment, which resulted in overlapping of the peaks related to the two polymorphic forms [27, 45, 46]. The first cooling thermograms (Figure 4.14 b)) show a shift toward higher temperatures upon X-BNNS-SC incorporation. In particular, T_c increased from 116 °C for the neat polymer to 126 °C for the composites with 5 wt% X-BNNS-SC, confirming the nucleating effect of this BNNS for PP, manifested as an increase in the T_c of PP, obtained for X-BNNS-SC loading as low as 0.1 wt %. Further increases in the loadings of X-BNNS-SC did not result in more nucleation or increased T_c, probably due to the X-BNNS-SC particles constraining the PP chains dynamics, thus delaying crystallization. The second heating thermograms (Figure 4.14 c)) show broad peaks after X-BNNS-SC addition, yet are more symmetric than those obtained during the first heating. The controlled cooling cycle realized during the DSC measurements should have produced a material with a narrower crystallite size distribution compared to the material cooled by injection moulding (*i.e.,* narrower peaks should have been recorded during the second heating cycle), perhaps due to an annealing effect. However, the melting peaks of the composites in the second heating thermograms are as broad as the ones in the first heating curves. This was because of the β–α phase transition, which caused superimposing of the peaks related to the β–α phase transition and α-spherulite melting [23, 46].

The first heating thermograms of the composites of PP with X-BNNS-T (Figure 4.14 d)) show broad and asymmetric peaks confirming the coexistence of α-PP and β-PP crystals, suggesting a change in PP polymorphism upon inclusion of X-BNNS-T, confirming the XRD results. However, the β-PP content increased from the neat PP to the composites with 0.5 wt% of X-BNNS-T from the XRD but a similar trend was not visible from the DSC thermograms. Again, the β–α phase transition occurring during the first heating step in the DSC experiment resulted in overlapping of the peaks associated with the two polymorphic forms ([27] and references therein). The first cooling thermograms (Figure 4.14 e)) show a shift toward higher temperatures upon X-BNNS-T incorporation. In particular, T_c increased from 116 °C for the

neat polymer to 130 °C for the composites with 10wt% of X-BNNS-T. As already noticed for the composites with X-BNNS-SC, the major leap of T_c occurred at a filler loading as low as 0.1wt% and the addition of more X-BNNS-T did not cause a further increase of T_c, probably due to the constraint of the filler particles onto the PP chains dynamics. The second heating thermograms (Figure 4.14 f)) show broad peaks after X-BNNS-T addition, yet are more symmetric than those obtained during the first heating, perhaps caused by the annealing phenomenon. The melting peaks of the composites in the second heating thermograms are as broad as the ones in the first heating curves, probably due to the β–α phase transition ([27] and references therein).

The first heating thermograms for the composites of PP with Y-BNNS-L (Figure 4.14 g)) show broad and asymmetric peaks, confirming again the coexistence of α-PP and β-PP crystals (XRD spectra). However, it is not possible to identify the peak related to the melting of the β-crystallites due to the β–α phase transition during the first heating step in the DSC experiment [27, 45, 46]. The first cooling thermograms (Figure 4.14 h)) show a shift toward higher temperatures upon filler incorporation, with T_c increasing from 116 °C (PP) to 126 °C at 10wt% of Y-BNNS-L, confirming the nucleating effect of this BNNS on PP. As already noticed for the composites with X-BNNS-SC and X-BNNS-T, the major leap is detected at a filler loading as low as 0.1wt% and the addition of more Y-BNNS-L caused small increase of T_c. Again, the constraint effect of the filler particles could limit the PP chains dynamics, thus, delaying the crystallization, manifested in small increase of the T_c at high filler loadings. The second heating thermograms (Figure 4.14h)) show broad peaks after the addition of the filler, which appear to be as broad as the ones in the first heating curves, probably due to the superimposing of the peaks related to the β–α phase transition and α-spherulite melting [23, 27].

Table 4.5: T_m, T_c, ΔH_m, ΔH_c and X_c (%) of PP and its composites with X-BNNS-SC and X-BNNS-T and Y-BNNS-L as obtained from the registered DSC thermograms during. The ΔH_c related to a theoretical PP crystal with infinite dimensions used to calculate the crystallinity is 207 J/g [30]. The error calculated for T_m, T_c amd X_c (%) falls on the first decimal, which is not significant for the present study.

Sample	T_m(ºC)		T_c(ºC)	ΔH_m(J/g)		ΔH_c(J/g)	X_c(%)
	1st heating	2nd heating	1st cooling	1st heating	2nd heating	1st cooling	1st cooling
PP	168	170	116	88	102	97	47
0.1 wt% X-BNNS-SC	165	164	124	83	106	100	48
0.3 wt% X-BNNS-SC	168	163	125	90	111	101	49
0.5 wt% X-BNNS-SC	164	163	125	94	118	94	45
1 wt% X-BNNS-SC	167	163	126	91	110	96	46
3 wt% X-BNNS-SC	166	164	128	86	108	98	46
5 wt% X-BNNS-SC	165	164	128	77	92	81	37
10wt% X-BNNS-SC	168	165	129	90	107	106	48
0.1 wt% X-BNNS-T	163	165	124	90	104	99	47
0.3 wt% X-BNNS-T	168	163	125	92	106	99	48
0.5 wt% X-BNNS-T	167	163	125	92	106	98	48
1 wt% X-BNNS-T	166	164	125	87	105	97	48
3 wt% X-BNNS-T	164	165	126	89	106	95	47
5 wt% X-BNNS-T	167	165	128	89	106	95	51
10wt% X-BNNS-T	166	166	130	88	108	97	57
0.1 wt% Y-BNNS-L	168	166	121	103	117	110	53
0.3 wt% Y-BNNS-L	168	166	124	103	117	110	55
0.5 wt% Y-BNNS-L	168	165	125	104	119	113	55
1 wt% Y-BNNS-L	168	166	125	105	120	112	55
3 wt% Y-BNNS-L	168	166	126	103	120	108	54
5 wt% Y-BNNS-L	170	165	127	106	115	107	54
10wt% Y-BNNS-L	170	166	126	105	115	108	54

In Table 4.5, it should be noted that the T_m of PP after the second heating cycle decreased by *ca* 5 °C when 5 wt % X-BNNS-SC were added. The addition of irregular shaped X-BNNS-SC platelets may have hindered the crystallization of PP chains, especially at higher filler loadings, thus a larger fraction of PP amorphous phase formed and T_m was depressed.

This phenomenon was evident from the change in crystalline content (X_c(%)), which increased from 47% (PP) to *ca* 50% when X-BNNS-SC were added at the 0.3wt % before decreasing to 37% when X-BNNS-SC were added at loadings up to 5 wt %. At X-BNNS-SC $\leq$ 0.5 wt%, PP chains were free to crystallize in defined geometries, which was more unlikely to happen at filler loadings >0.5 wt% due to the constraint on polymer chain mobility caused by the fillers particles [26, 27]. Furthermore, the BNNS particles are thermally conductive with values of up to 360 W/mK (at room temperature) reported [43, 47], in contrast, PP is a thermal insulator, thus, more efficient thermal dissipation was possible during the cooling cycle where the filler particles were present, forcing nearby neighbour PP chains to crystallize faster than those further away. This could have contributed to the formation of the amorphous phase. Yet, at 10wt% the crystallinity is again 48%, probably due to some agglomeration of X-BNNS-SC in PP, which imparted less constraint onto the long-distant PP chains, thus allowing more crystals of PP to nucleate and grow under the controlled conditions set for the DSC measurements. ΔH_m (second heating) and ΔH_c of the composites increased upon addition of up to 0.5 wt% of X-BNNS-SC to PP, but the T_m (second heating) decreased *i.e.,* either thicker/larger lamellae or more imperfect crystals of PP formed during the heating and cooling cycles in presence of the X-BNNS-SC. When 5wt% of filler were added, ΔH_m and ΔH_c decreased, probably due to the increase in the amorphous phase of PP (reduction of X_c(%)) ([27] and references therein).

The T_m of PP after the second heating cycle decreased by *ca* 3-5 °C when X-BNNS-T was included up to 10wt% whereas the crystalline fraction X_c(%) increases from 47% (PP) to 57% (10wt% X-BNNS-T). Differently from the composites of X-BNNS-SC, the small size of X-BNNS-T facilitated the crystallization of higher amount of small and/or imperfect PP crystals, manifested with the decrease of T_m but increase of X_c(%). One of the possible reasons of the differences in the X_c(%) for the two sets of composites with X-BNNS-SC and X-BNNS-T could be due to the tendency of X-BNNS-T to agglomerate more than X-BNNS-SC, thus imparting less constraint onto the PP chains than the X-BNNS-SC did, which ultimately facilitated the crystallization of PP, albeit small and/or imperfect crystals formed.

The T_c of the composites increases from 116°C (neat PP) to 130°C at 10wt% of X-BNNS-T, confirming the nucleating effect of the filler on the crystallization behaviour of PP as suggested earlier from XRD. ΔH_m and ΔH_c of the composites with X-BNNS-T increase compared to the neat PP, with ΔH_m increasing more (up to 6 units higher than PP) than ΔH_c (up to 2-3 units higher than PP), probably due to the formation of more but smaller/imperfect crystallites than in the PP alone.

The T_m of PP composites with Y-BNNS-L after the second heating cycle decreased by *ca* 3-4 °C at 10wt % of filler content, whereas $X_c(\%)$ increased from 47% (PP) to 54% (10wt% Y-BNNS-L). This result suggests that after the first cooling during the DSC a higher number of smaller crystallites formed, similarly to the composites with X-BNNS-T, yet, the mechanisms of crystallization are likely to be different. Specifically, the formation of small PP crystallites in the composites with Y-BNNS-L during the DSC measurements is more likely caused by the constraining derived from the large Y-BNNS-L uniformly distributed in PP, whereas the aggregation of the highly hydrophilic X-BNNS-T during melt-mixing probably caused the crystallization of the small crystallites during the DSC experiments. The T_c of the composites increases from 116°C (neat PP) to 126°C at 10wt% of Y-BNNS-L, confirming the nucleating effect of the filler on PP. Both ΔH_m and ΔH_c of the composites with Y-BNNS-L increased compared to PP, probably due to the increase of the crystal content.

It would be interesting for future work to assess the mechanisms of crystal nucleation and growth, particularly the mechanisms of β-nucleation, upon inclusion of these BNNS grades in PP by modulated DSC coupled with polarized hot-stage optical microscopy both under isothermal and non-isothermal conditions.

4.4.2- Study of the rheological and mechanical properties of the composites of PP with X-BNNS-SC, X-BNNS-T, Y-BNNS-L

The rheology of the composites of PP with X-BNNS-SC, X-BNNS-T and Y-BNNS-L was studied by Oscillatory rheology to further investigate the state of dispersion of the three grades of BNNS here studied in PP whereas the mechanical properties of the resulting composites were assessed by Tensile tests.
Figure 4.15 summarise the results on the rheological measurements performed.
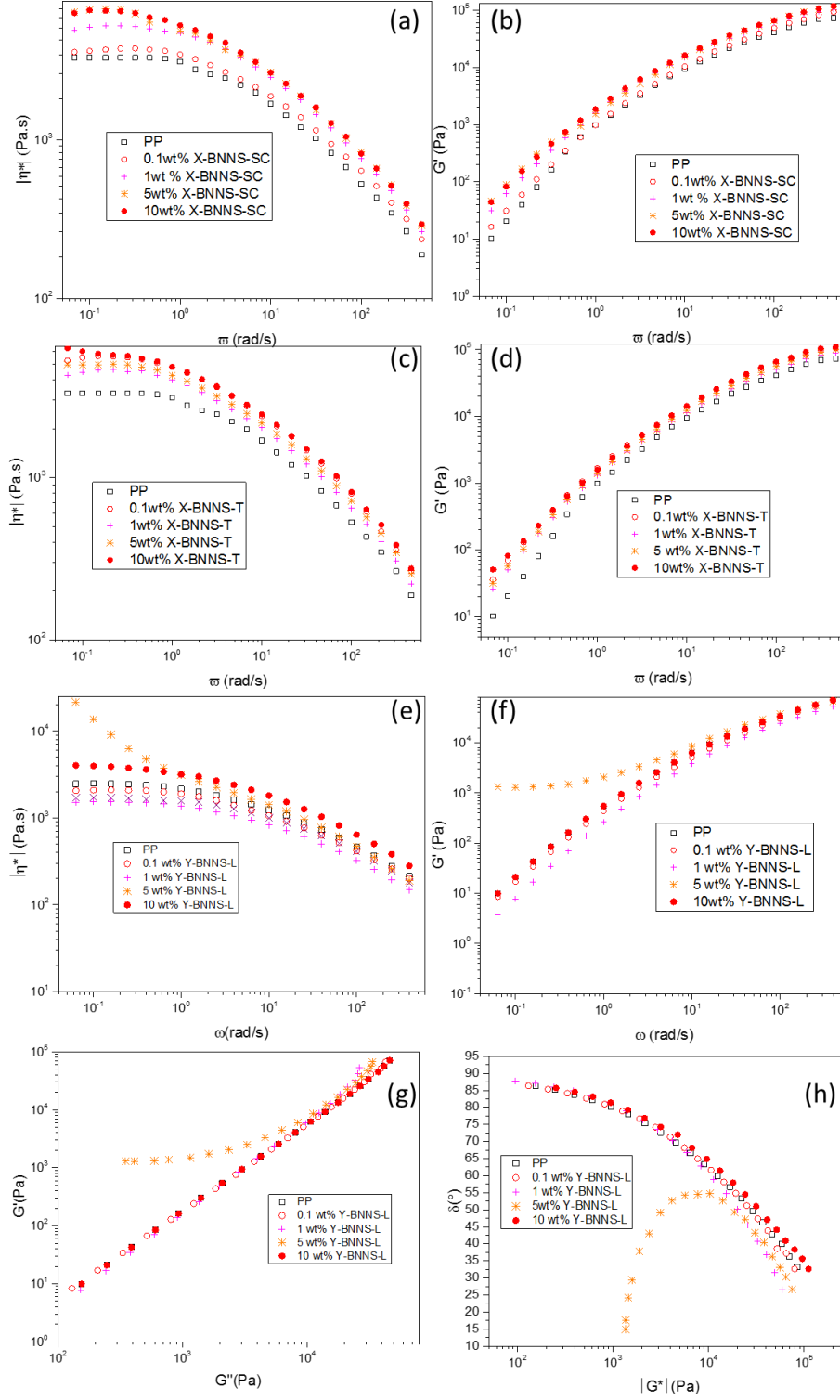
Figure 4.15: Complex viscosity (|η*|) and storage modulus (G′) as a function of the angular frequency (ω) for PP and its composites with X-BNNS-SC (a)-b)) and X-BNNS-T (c)-d)). |η*| and G′ in function of ω (e)-f)), Cole-Cole plot (g)) and Van-Gurp-Palmen plot (d)) for PP and its composites with Y-BNNS-L. The data are a replica of 3 measurements on a batch of 3 specimens per compositions.

No differences in the rheological profiles are evident when comparing PP with the composites with X-BNNS-SC. The complex viscosity $|\eta^*|$ is constant with frequency at $\omega < 1$ rad/s (Newtonian profile) both for PP and its composites with X-BNNS-SC, before linearly decreasing (power law) with frequency (Figure 4.15 a)). An increase in $|\eta^*|$ of 7000 Pa.s at 10 wt% filler was detected in the Newtonian region, which was expected for the composites with high filler content. The storage modulus, G′, increases with frequency and the trend does not change for PP and the composites with X-BNNS-SC, *i.e.* no percolation was detected (Figure 4.15 b)). Probably, the small BNNS platelets and/or agglomeration (strong particle-particle interactions in part caused by the presence of the surfactant SC) prevented the filler particles from percolating in PP.

No differences in the rheological behaviour was detected when comparing PP with its composites with X-BNNS-T. $|\eta^*|$ is constant with frequency at $\omega < 1$ rad/s (Newtonian profile) both for PP and PP+X-BNNS-T, before linearly decreasing (power law) with increasing frequency (Figure 4.15 c)). An increase in $|\eta^*|$ of 6000 Pa.s at 10wt% of filler was detected in the Newtonian region, as expected in composites with high filler content. G′ decreases at low frequencies both for PP and its composites with X-BNNS-T, that is, no rheological percolation was detected (Figure 4.15 d)). Again, the small size of this BNNS (few nm) along with the strong particle-particle interactions preferred over the particle polymer interactions (X-BNNS-T highly hydrophilic, sessile tests section 4.2) caused agglomeration of the filler upon inclusion in PP, thus preventing a 3D network from percolating.

Figure 4.15 e)-h) show the rheological profiles for the composites of PP with Y-BNNS-L at 0-10wt% in terms of $|\eta^*|$ vs ω (e)), G′ vs ω (f)), G′ vs G″ (g)) (Cole-Cole plot) and δ (phase angle) vs $|G^*|$ (h)) (Van-Gurp-Palmen plot). The rheological percolation at 5wt% for Y-BNNS-L is detected as there is a change from a Newtonian profile to a 'pseudo-plastic' profile at low frequency (Figure 4.15 e)), which indicates the passage from 'fluid-like' behaviour to a more 'solid-like' behaviour, symptomatic of the formation of a 3D network [36] of Y-BNNS-L in PP. The 3D network formed could be due to a combination of filler particle-particle connectivity and filler particle-polymer connectivity through the entanglement of the polymer chains [48] near the Y-BNNS-L platelets. The rheological percolation is confirmed by the plateauing of G′ at low frequency (Figure 4.15 f)) and the plateauing of G′ vs G″ typical of a material tending to a more solid-elastic behaviour (Figure 4.15 g)). The Van-Gurp-Palmen plot (Figure 4.15 h)) unequivocally depicts the rheological percolation at 5wt% of Y-BNNS-L, where the phase angle δ drastically diverges from that for neat PP as well as from that for the composites at lower filler loadings [49]. At $|G^*| > 10^4$ Pa the composites are stiff and more

elastic-(solid-like), thus, δ tends to zero (low values), whereas at $|G^*| < 10^4$ Pa the composites are more viscous- (liquid-like), thus, δ tends to 90°. Yet, at 5wt% of Y-BNNS-L the phase angle decreases up to 15° at $|G^*| < 10^4$ (1500 Pa precisely), indicating that the composite behaves as solid-like material *i.e.* a percolated structure is attained. Interestingly, the rheological percolation is not detected at 10wt% of Y-BNNS-L, probably due to the non-uniform distribution and dispersion of the filler at such high a concentration – it becomes more difficult to disperse and distribute the filler at high loadings. The processing conditions employed was not effective at forming a percolated network. It is possible to assert that at low filler content (<5wt%) the particle-particle and particle-polymer connectivity either was not achieved or was too weak to create a stable structure persistent for long times (low frequencies) and high temperatures (measurement temperature =200°C). At 5wt% of Y-BNNS-L, the particle-particle and particle-polymer connectivity is strong enough to persist for long times at high temperatures, thus, the rheological percolation is detected [48]. Clearly, the larger lateral size of this grade of BNNS facilitated the formation of an interconnected 3D network. At 10 wt% Y-BNNS-L, agglomerations obstructed the particle-particle and particle-polymer connectivity, therefore, no rheological percolation is detected. A schematic illustration of a physical interpretation of the structures realized at different Y-BNNS-L loadings is shown in Figure 4.16.

Cross section of disk specimens

Y-BNNS-L <5wt%

Y-BNNS-L = 5wt%

Y-BNNS-L = 10wt%

Schematic of the disk before rheology
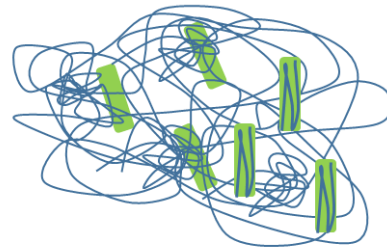
Y-BNNS-L evenly distributed. PP chains entangle around the filler particles and perhaps crystalize along the large platelets. The Y-BNNS-L aligned along the injection direction.
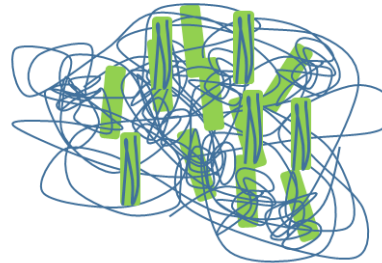
Y-BNNS-L evenly distributed, particle-particle and particle-polymer connectivity realized. PP entangle and/or crystallize onto the aligned Y-BNNS-L platelets.
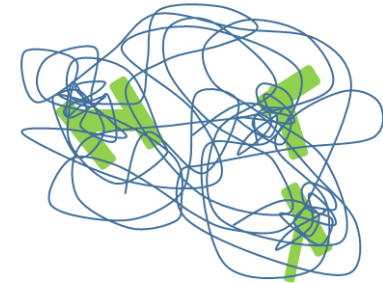
Y-BNNS-L agglomeration. Alignment obstructed by the agglomerates.

Schematic of the disk after rheology measurement- 200 °C, long times/ low frequency
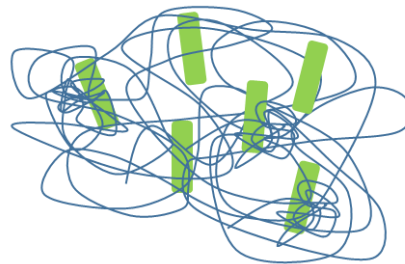
Polymer chains disentangled, particle-particle and particle-polymer connectivity not realized, i.e. no rheological percolation.
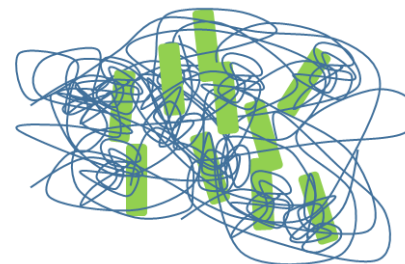
Polymer chains entanglements persistent. The crystalized PP chains along the platelets during injection melt and perhaps entangle around the Y-BNNS-L. Rheological percolation achieved by particle-particle and particle-polymer connectivity.
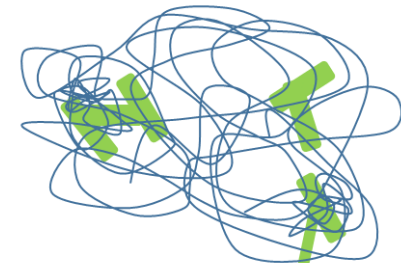
PP chains partially or totally disentangled, no particle-particle /particle-polymer connectivity, i.e. no rheological percolation.

PP chains entanglement   Flakes of Y-BNNS-L   PP chains crystallized near the Y-BNNS-L platelet

Figure 4.16: Schematic of PP+Y-BNNS-L hypothetical structures before and after the rheological measurements.

117

The composites of PP with X-BNNS-SC and X-BNNS-T show the same rheological profiles with no rheological percolation, whereas the composites with Y-BNNS-L percolated at a filler loading of 5wt%, yet the percolated structure is absent at 10wt% Y-BNNS-L. Clearly, the large particle size played a key role at determining the formation of a 3D network of Y-BNNS-L with respect to the smaller particles of the X-BNNS-SC and X-BNNS-T. In addition, the surfactant L could promote the distribution and perhaps dispersion of the Y-BNNS-L in PP. Further insights on the possible mechanisms of interactions between the surfactants SC, L and T are given in the tensile tests section.

At 10 wt% of Y-BNNS-L, the agglomeration of the filler due to a combined effect of particle-particle interactions and mixing conditions adopted, hindered the formation of rheological percolation for the three sets of composites, *i.e.* with X-BNNS-SC, X-BNNS-T and Y-BNNS-L.

Another aspect to consider is the secondary processing procedure, *i.e.* the injection moulding for the preparation of the disk-shape specimens used for the rheology measurements. The melt flow realised during injection moulding could force the PP chains to align along specific directions when cooling. This mechanism could lead to an exclusion phenomenon where the filler particles migrate toward the middle of the disk-shaped samples, thus producing specimens with a skin-core morphology, characterized by a rich-polymer phase skin and rich-particle phase core. In that case, the filler particles are forced to settle in a confined space, which could favour agglomeration, thus, preventing the formation of a 3D network (rheological percolation). This mechanism is more likely to occur with the small platelets of X-BNNS-SC and X-BNNS-T since they do not have enough inertia to resist polymer flow/crystallization, thus being dragged toward the middle of the disk-shaped mould as the polymer flows. On the contrary, the larger platelets of Y-BNNS-L could more easily oppose the PP flow during injection, overcoming the centripetal drag force in the mould. This generates samples where the Y-BNNS-L are likely to be more evenly distributed in PP throughout the disk shaped-samples compared to the X-BNNS-SC and X-BNNS-T composites. Although the injection-moulded samples of PP with X-BNNS-SC and X-BNNS-T did not show rheological percolation, it is not possible to exclude that the filler particles percolated in PP during extrusion. In other words it is possible that X-BNNS-SC/X-BNNS-T percolated during-melt mixing but the post-processing procedure (injection moulding) could have destroyed the particle-particle 3D network [50-54].

The disk shape test specimens used for rheology were used for XRD analysis. The two techniques appear to confirm that Y-BNNS-L were distributed and perhaps dispersed more

uniformly in PP than X-BNNS-SC/X-BNNS-T, probably due the combination of the large platelets and more optimal interactions between the Y-BNNS-L and PP. In the next paragraph the results on the mechanical properties are reported and described, along with a possible mechanisms of interactions between the filler particles/ surfactants and PP.

The Tensile tests were performed on a replica of six (6) specimens per compositions and representative stress-strain curves are reported in Figure 4.17 along with the values and trends of the Young's modulus (E) and stress at yield (σ_y) in function of the filler loading.
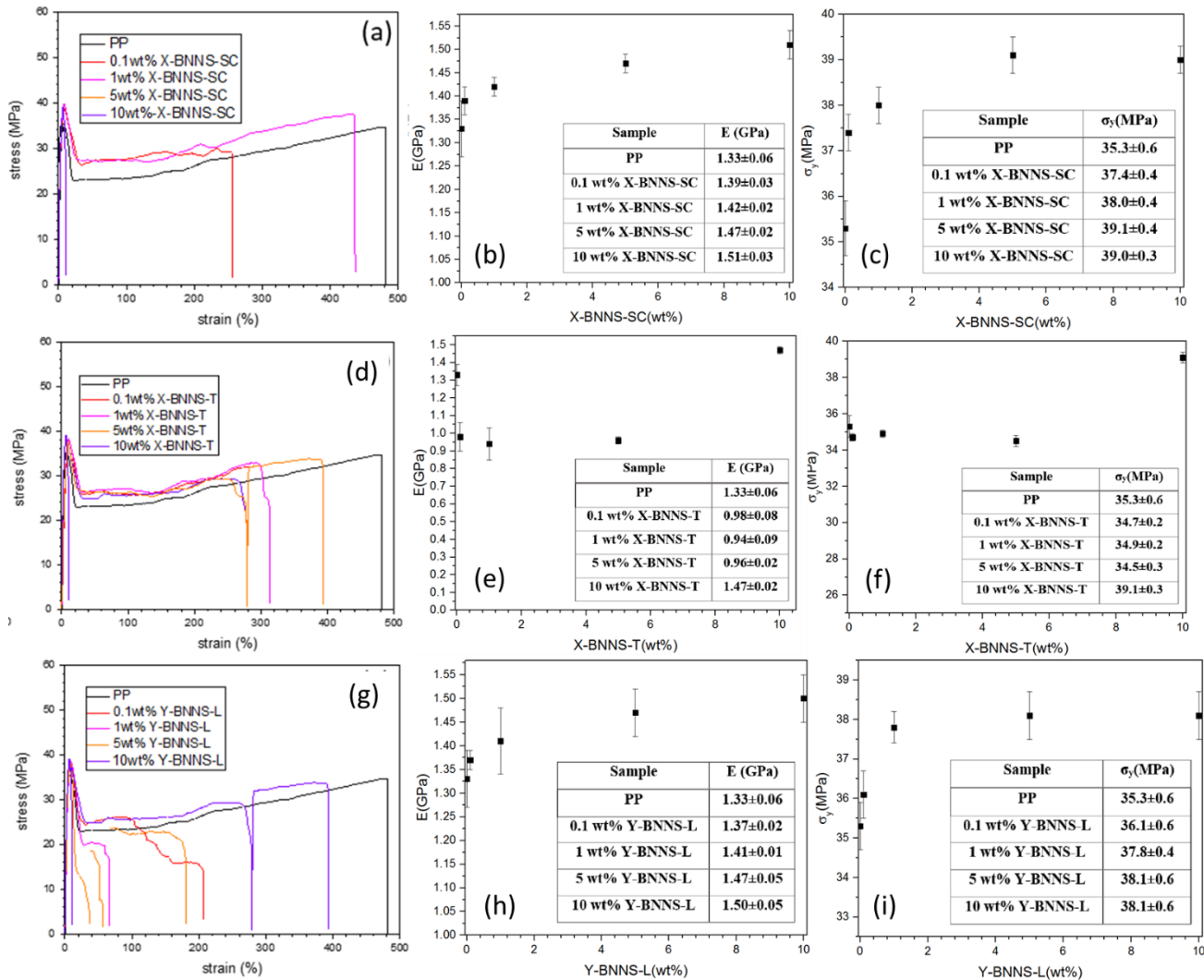
Figure 4.17: Stress-strain curves of PP and its composites with X-BNNS-SC (a)), X-BNNS-T (d)) and Y-BNNS-L (g)). G in function of the filler loading (b)-h)) and σ_y in function of the filler loading (c)-i)).

The stress-strain curves of PP and its composites with X-BNNS-SC at different filler loadings are reported in Figure 4.17 a). The presence of the filler particles appear to reduce the elongation at break of PP as already noticed for the counterpart composites prepared by laboratory scale extruder. The noise detected in the plastic region has been ascribed to the release of the internal stress generated during the processing and/or derived from the presence of the filler particles acting as spots of stress accumulation. Furthermore, as already explained for the composites prepared by laboratory scale extruder, there could be some hydrophobic interactions between the surfactant SC and PP, which could break during the tensile tests. [37-42].

The inclusion of the X-BNNS-SC resulted in an increase of the E from 1.33±0.06 GPa for the neat PP to 1.51±0.03 GPa at 10 wt% of filler (Figure 4.17 b)) and an increase of σ_y from 35.3±0.6 MPa for the neat PP to 38.7±0.2 MPa and 39.0±0.3 MPa at 10wt% of X-BNNS-SC (4.17 c)). The increase of E and σ_y could be associated the intrinsic rigidity of the BNNS, the formation of entanglements of polymer chains around the filler particles and the crystallization of β-PP upon inclusion of X-BNNS-SC, as observed in the XRD results (Figure 4.13) [37-42].

The stress-strain curves of PP and its composites with X-BNNS-T at different filler loadings are reported in Figure 4.17 c). The presence of the filler particles appear to reduce the elongation at break of PP. Again, the internal stress generated during the processing and/or derived from the presence of the filler particles acting as spots of stress accumulation are probably released by internal fractures, as evident from the noise detected in the plastic deformation region [37-42].

The inclusion of X-BNNS-T induced a decrease in E from 1.33±0.06 GPa for the neat PP to 0.96±0.02 GPa at 5wt% of filler loading, before increasing to 1.47±0.02 GPa at 10wt% of X-BNNS-T (Figure 4.17 d)). The same trend is observed for σ_y as depicted in Figure 4.17 e), where it is clear that the σ_y decreases from 35.3±0.6 MPa for the neat PP to 34.5±0.3 MPa at 5wt% of X-BNNS-T, before increasing to 39.1±0.3 MPa at 10wt% of filler loading. The decrease of E and σ_y at low filler content (≤5wt%) could be ascribed to the agglomeration of relative large clusters of X-BNNS-T [37-42]. The agglomeration could derive from the high hydrophilicity (see sessile tests section 4.2) of X-BNNS-T, thus limiting the distribution and dispersion of X-BNNS-T in PP.

The stress-strain curves of PP and its composites with Y-BNNS-L at different filler loadings are reported in Figure 4.17 g), where it is possible to note that the inclusion of Y-BNNS-L appear to reduce the elongation at break of PP as already noticed for the composites with X-BNNS-SC and X-BNNS-T. The noise detected in the plastic region can be again

ascribed to the release of the internal stress generated during the processing and/or derived from the presence of the filler particles acting as spots of stress accumulation [37-42].

The inclusion of the Y-BNNS-L caused an increase of the E from 1.33±0.06 GPa for the neat PP to 1.50±0.05 GPa at 10 wt% of filler (Figure 4.17 h)) and an increase of σ_y from 35.3±0.6 MPa for the neat PP to 38.1±0.6 MPa at 10wt% of Y-BNNS-L (4.17 i)). The increase of E and σ_y could derive from: i) the intrinsic rigidity and large dimensions of the Y-BNNS-L, ii) the formation of entanglements of polymer chains around the filler particles and the crystallization of β-PP upon inclusion of Y-BNNS-L, as previously noted in the XRD results (Figure 4.13) [37-42]. Yet, the XRD showed a decrease of both the β-crystal content and total crystal content with the addition of the Y-BNNS-L at high loadings (≥3wt), therefore the increase of E and σ_y at 5wt% and 10wt% of Y-BNNS-L is probably related to the high content of large and rigid Y-BNNS-L particles.

It is interesting to note how the mechanical properties of the composites of PP with X-BNNS-T are very different from the mechanical properties of the composites with X-BNNS-SC. The lateral dimension of the X-BNNS-SC and X-BNNS-T is comparable (few nm), therefore, the reason behind the differences in the mechanical properties could be ascribed to the different surface chemistry, particularly the surfactants used during the HPH process by our industrial partner to prepare X-BNNS-SC and X-BNNS-T. The surfactant SC (Chapter 3) is ionic and exposes cyclo-hexane rings to the PP when preparing the composites with X-BNNS-SC. The coexistence of X-BNNS-SC with PP is therefore favoured by the hydrophobic interactions between the cyclo-hexane rings of SC and the polymer chains. The surfactant T is amphiphilic and exposes the polyether-polyol tails to PP when admixing X-BNNS-T with the polymer, therefore facilitating the hydrophilic particle-particle interactions over the particle-polymer ones. The difference in the chemical structure of SC and T translated in a relative good distribution and perhaps dispersion of X-BNNS-SC in PP compared to the X-BNNS-T. This results are in line with the XRD study.

The mechanical properties of the composites of PP with X-BNNS-T and Y-BNNS-L are different. Certainly, the large lateral dimension of Y-BNNS-L (up to 10 µm) compared to the small X-BNNS-T platelets (lateral dimension few nm) play a key role at enhancing the stiffness of the PP. However, the fact that G and σ_y decreases when adding X-BNNS-T whereas G and σ_y increase when including Y-BNNS-L could indicate a different mechanism of interaction between the surfactant T and PP compared to the surfactant L. Both surfactants are amphiphilic with a polyether-polyol tails, however T shows an aromatic head with branched functionalities whereas the aromatic head of L does not contain such functionalities. The amphiphilic L could

"flip" when admixing the Y-BNNS-L in PP, thus exposing the aromatic head to PP and the polyether-polyol tails to the BNNS. In this way, the coexistence of Y-BNNS-L in PP could be favoured by the hydrophobic interaction between PP and the aromatic head of L - most likely between the π conjugated system of the aromatic ring and the CH_2 groups of PP [55] - , which lead to a relative good distribution and perhaps dispersion of the Y-BNNS-L in PP. The amphiphilic T could also potentially "flip" upon incorporation of X-BNNS-T in PP, however, the steric hindrance of the branched functionalities on the aromatic head make "flipping" less probable. As a consequence, the dangling polyether-polyol chains are more likely to expose to the hydrophobic PP, thus facilitating the particle-particle interactions over the particle-polymer interactions, that is, the X-BNNS-T is prone to agglomerate when admixed in PP. This results are in line with the XRD and rheology results.

The mechanism of interactions between the surfactants SC, T and L with PP should be carried out in future work to better understand the mechanisms of interactions between the filler particles and the PP. For that purpose, the $^{13}CNMR$ analysis could be used. In addition, a modelling study on the melt-flow during injection moulding could predict the mechanism of distribution and dispersion of the filler particles, the melt flow of the polymer and the crystallization dynamics as the polymer crystallizes in moulds of different shapes and dimensions during injection moulding, thus supporting the understanding on how the inclusion of X-BNNS-SC, X-BNNS-T and Y-BNNS-L affect the properties of PP.

The variability of the properties of the composites with the type of processing, particularly the influence of post-processing, has been seldom reported in the literature (see Chapter 2). Yet, this information is crucial when addressing the properties of the final composites and optimizing production on an industrial scale.

The detection of the rheological percolation with the Y-BNNS-L is a promising result in the manufacturing of these functional composites *e.g.* thermal conductive materials where the Y-BNNS-L percolate in a conductive path.

4.4.3- Thermal conductivity measurements of the composites of PP with Y-BNNS-L

Thermal conductivity measurements were performed on the PP+Y-BNNS-L (5wt%), since a percolated structure was detected by rheology and so it is possible a phonon-path for the thermal conduction formed. The results are shown in Table 4.9 for the composites with 0.1wt%, 1wt% and 10wt% Y-BNNS-L.

Table 4.6: Thermal conductivity (TC) of PP and its composites with Y-BNNS-L. The results are an average taken from six (6) replicates.

Sample	TC (W/mK)
PP	0.25±0.01
0.1wt% Y-BNNS-L	0.27±0.01
1 wt% Y-BNNS-L	0.28±0.01
5wt% Y-BNNS-L	0.28±0.01
10wt% Y-BNNS-L	0.28±0.01

The TC values of the composites with Y-BNNS-L increase a little compared to the neat PP. The TC of the composites at 5wt% of Y-BNNS-L, which showed rheological percolation, is the same as for the composites at 0.1wt%, 1wt% and 10wt% of Y-BNNS-L. The very modest improvement in TC may be due to. (i)- The samples used for the TC measurements were different from the samples used for the rheology measurements, *i.e.* the morphology of the two types of samples may not be the same as a result of different melt flow during injection moulding. Therefore, there may be no rheological percolated network for the TC specimens and no particle-particle connectivity achieved, *i.e.* no thermal path for conduction was realised. (ii)- The presence of polymer-polymer connectivity surrounding the filler network will depress the TC as the polymer chains are insulators and facilitate phonon-scattering. (iii)- The irregular-shaped Y-BNNS-L flakes combined with its surface chemistry (*e.g.* presence of the surfactant L) could increase the interfacial thermal resistance through phonon-scattering, hence, the depression of the thermal conduction. (iv)- The Y-BNNS-L could randomly distribute during injection moulding, thus lowering the TC. (v)- The way the TC measurements were performed could affect the TC results. The MTPS instrument (see Chapter 3) averages the TC measurements along the different directions of the samples, that is, even if the Y-BNNS-L managed to align along the injection moulding direction and facilitated TC in that specific direction, the phonon scattering occurring along the transversal directions to the injection direction will depress the resulting TC ([43] and references therein).

The TC measurements appear to confirm that although the use of large particles of functional filler is crucial, it is not sufficient alone at improving thermal conduction properties (*e.g.* thermal conductivity) of the final composites. The optimization of the interfacial interactions between the filler and the polymer along with optimal processing conditions and

filler alignment is fundamental to manufacturing composites with enhanced properties (thermal, mechanical). Furthermore, it is important to recognize the limitation of the instruments used for the characterization of the samples, since the behaviour of the material in question as observed by certain techniques could not necessary reflect the real structure of the samples.

4.4.4- Study of the morphology and crystalline structure of the composites of PP with X-GNP-SC, X-GNP-L, Y-GNP-L

      SEM imaging and XRD and DSC analysis were performed to study the morphology and crystalline structure of the composites of PP with the different GNP grades.
The SEM images of the composites of PP with the three grades of GNP examined are reported in Figure 4.18.
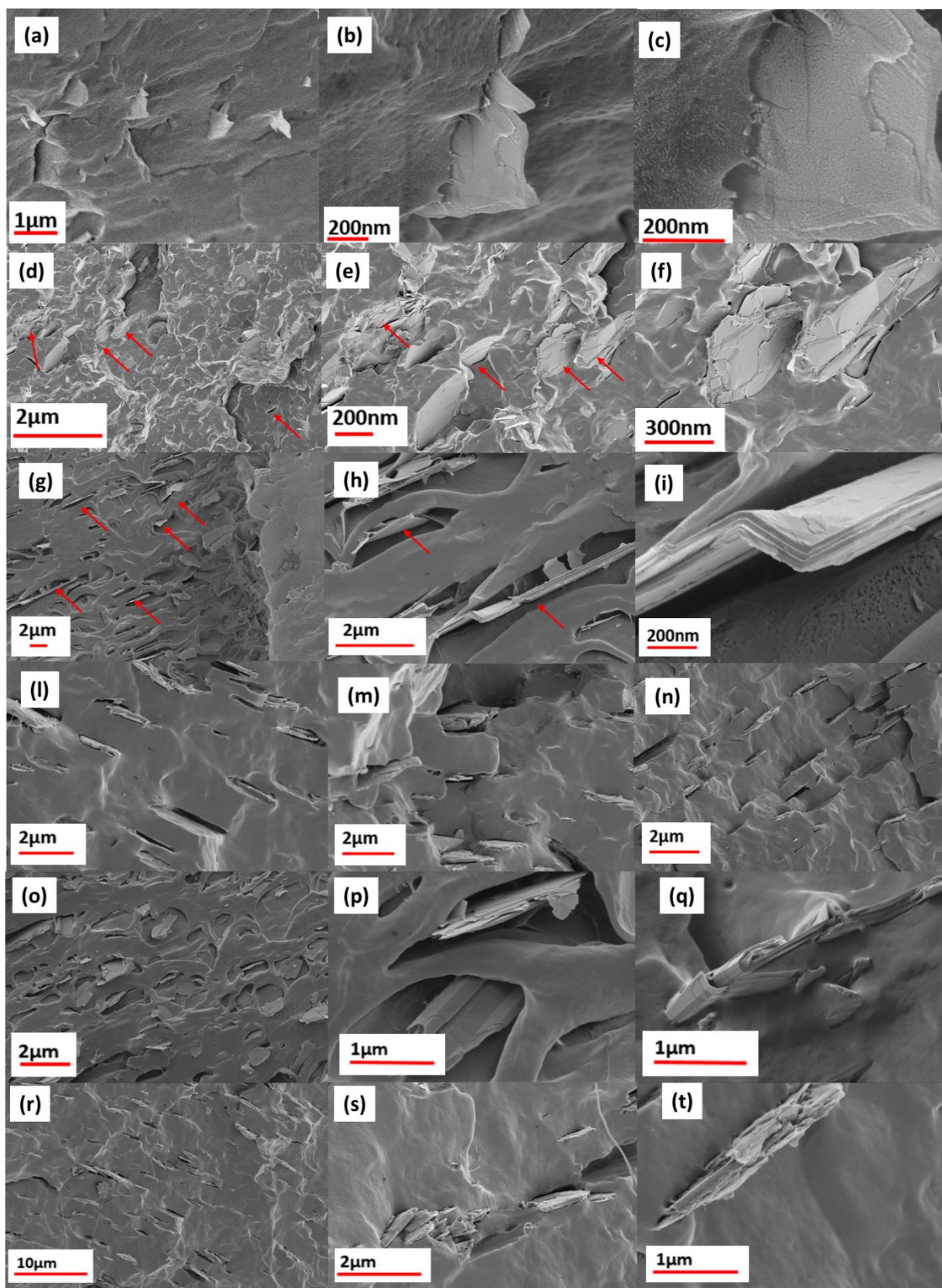
Figure 4.18: SEM images of the composites of PP with X-GNP-SC at 5wt% (a)-c)) and 10wt% (d)-f)), X-GNP-L at 5wt% (g)-i)) and 10wt% (l)-n)), Y-GNP-L at 5wt% (o)-q)) and 10wt% (r)-t)). The magnification increases from left to right. The red arrows point to the GNP particles.

X-GNP-SC is uniformly distributed in PP (particles evenly separated as depicted in Figure 4.18 a)-c)), probably due to the application of shear and some extensional flow in the parallel twin screw extruder, which enabled the break-up of large filler aggregates into smaller and perhaps thinner flakes when admixed in the polymer melt. In addition, as already noticed in the composites of PP with X-BNNS-SC, the surfactant SC could favour to some extent the wetting of the X-GNP-SC with PP, thus facilitating the distribution of this GNP. Yet, some large agglomerates of non-uniform particles are present on addition of X-GNP-SC at 10wt% (red arrows Figure 4.18 d)-f)). Clearly, at high filler loading (up to 10 wt%) the distribution and dispersion of the X-GNP-SC becomes more challenging with the processing methods used.

The SEM images of PP+X-GNP-L at 5wt% and 10wt% (Figure 4.18 g)-n)) show a good distribution of the filler in the matrix (as indicated by the red arrows in pictures g-h), yet large voids formed upon mixing (h, i, m), probably due to the poor wetting between PP and X-GNP-L, in part due to the irregular square-shape flakes of this filler (i), thus favouring the formation of voids upon cooling as PP chains crystallize. Yet, the relative good distribution of this GNP let us speculate that there could be some interactions between the filler particles and PP. As already noticed for the composites with Y-BNNS-L, the surfactant L could perhaps interact to some extent with the PP, thus limiting the particle-particle interactions, resulting in a more uniform distribution.

The SEM images of PP+Y-GNP-L at 5 wt% (Figure 4.18 o)-q)) and 10 wt% (Figure 4.18 r)-t)) show a good distribution of the filler in the matrix (o, r), yet large voids are obvious (p), due to the limited wetting between PP and Y-GNP-L, probably caused by the irregular-shape platelets of this GNP (s, t). However, the relative good distribution of the filler in the matrix could be symptomatic of the partial interactions between Y-GNP-L and PP, perhaps through the surfactant-polymer interactions, as seen for the composites with Y-BNNS-L.

The results from the XRD analysis on the composites of PP with the different grades of GNP are reported in Figure 4.19. Specifically, the XRD pattern are reported in Figure 4.19 a)-c) whereas the K_β, K_α and X_c(%) trends of PP in function of the filler loadings for the three sets of composites with X-BNNS-SC, X-BNNS-T, Y-BNNS-L are reported in Figure 4.19 d)-f). The K_β was calculated according to equation 4.1. X_c(%) whereas the K_α and X_c(%) values, were calculated as described for the composites of BNNS (XRD results section 4.4.3).
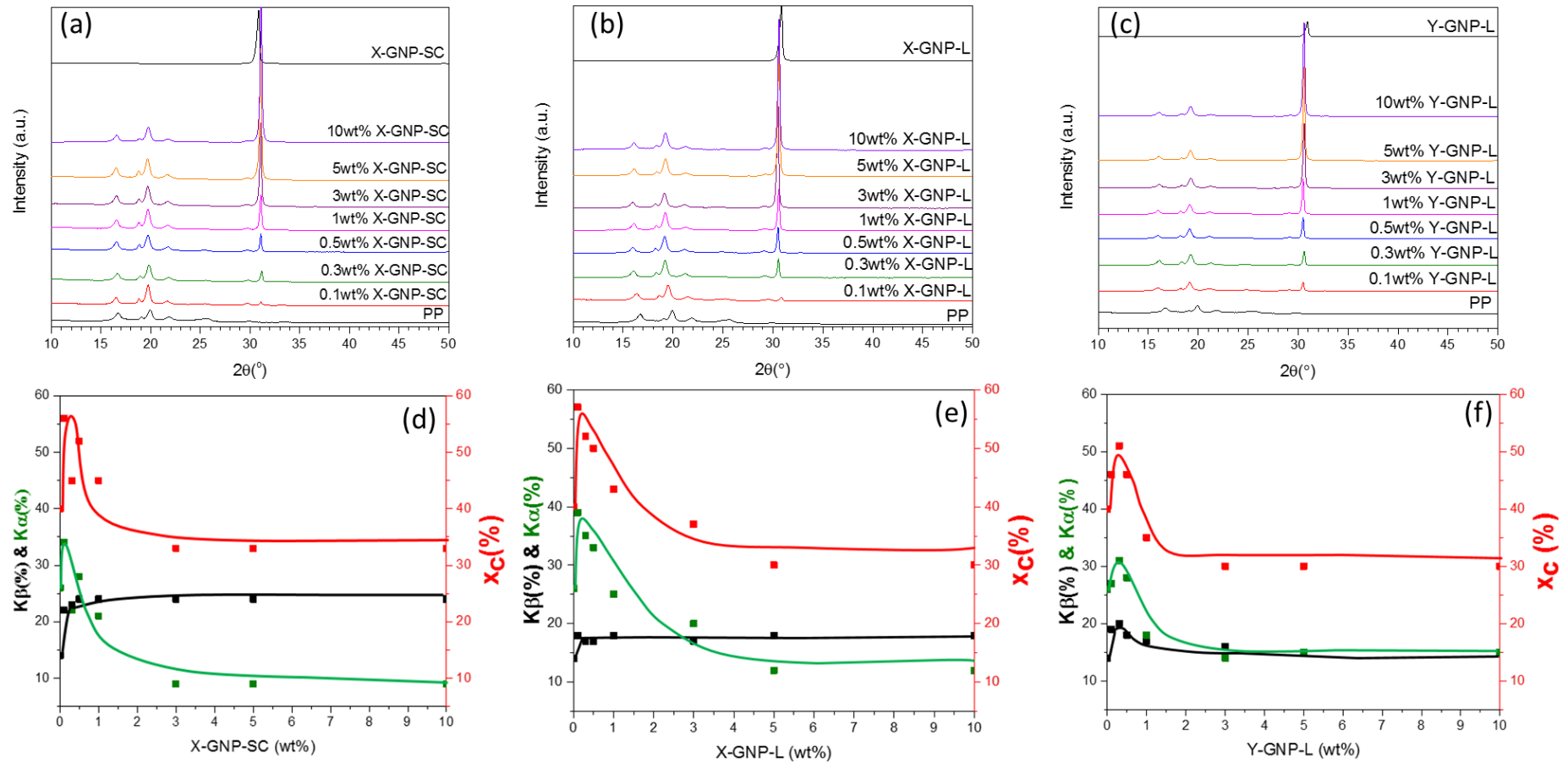
Figure 4.19: XRD patterns of PP and its composites with X-GNP-SC (a)), X-GNP-L (b)) and Y-GNP-L (c)). K_β, K_α and X_c(%) of PP in the composites with X-GNP-SC (d)), X-GNP-L (e)) and Y-GNP-L (f)) in function of the filler loading. The results are a replica of 3 measurements per sample on a batch of three disks per compositions. The error calculated on the K_α, K_β, X_c(%) falls on the first decimal cipher , which is not significant for this type of study.

The XRD patterns reported in Figure 4.19 a)-c) show the most intense peaks for PP at $2\theta =$ 16.5° α(100), 19.2° β(300), 20° α(040), 22° α(130), and for the X-GNP-SC/X-GNP-L/Y-GNP-L at $2\theta = 31°$ (002) [26, 56]. The intensity of the peak related to the crystallographic plane (002) of the fillers in the composites with PP increased with increasing filler loading, as expected, probably due to the agglomeration of these GNP particles at high loading as reported by Tajaddod *et al.* [44].

The plot of K_β as a function of the filler content in the composites (Figure 4.19 d)-f), black curves) increased from 14% (PP, partially due to the pre-existent β-crystal in the material as received and partially derived from induced crystallization during injection moulding) to 24% at 0.5wt% of X-GNP-SC and to 18% at 0.5wt % of X-GNP-L and Y-GNP-L. The K_β remained constant at 24% and 18% when adding more X-GNP-SC and X-GNP-L respectively, whereas K_β first decreased to *ca* 15% at 3wt% of Y-GNP-L before plateauing at higher filler loadings. Clearly, after a critical concentrations of these grades of GNP there was no further β-nucleation, probably due to either a constraint effect of the filler particles onto the PP chains, which limited the alignment thereof in the β-conformation, or to a competition effect with the crystallization of α-form of PP.

For a X-GNP-SC/X-GNP-L/Y-GNP-L loading up to 0.5wt %, K_α, X_c(%) of the composites increased compared to the PP, suggesting that at low filler concentrations (≤0.5wt%) these GNP facilitated the crystallization of both α and β crystallites of PP, resulting in an increase of the total crystalline fraction X_c(%) compared to PP alone. The three fillers act as β-nucleating agents for PP without obstructing the formation of the α-crystallites. Specifically, the K_α increased from 25% (PP) up to 35%, 40% and 30% when adding 0.5wt% of X-GNP-SC, X-GNP-L and Y-GNP-L respectively, suggesting that the X-GNP-L facilitated the crystallization of the α-form more than the X-GNP-SC and Y-GNP-L did. Probably, the more irregular-shaped flakes of the X-GNP-L limited the alignment of the PP in β-form, thus facilitating the crystallization of the more stable α-crystals.

At higher filler loadings (≥0.5wt%), K_α, X_c(%) of the composites decrease before plateauing at 3wt% of X-GNP-SC/X-GNP-L/Y-GNP-L and the same trend was observed for the K_β. The three fillers hindered the PP chains dynamics during crystallization, thus, obstructing the formation of further α and/or β crystallites, therefore the K_α, K_β, X_c(%) tend to be constant at higher loadings of these GNP.

The fact that K_α, K_β, X_c(%) all tend to plateau (no increase) could be also due to the mixing efficiency of the adopted manufacturing process. Indeed, the mixing of the GNP particles in

PP becomes more challenging at higher loadings up to 10wt%- as already noticed for the composites of PP with the BNNS grades- thus, limit the crystallization of more PP chains onto the GNP platelets.

The XRD results of the composites of PP with X-GNP-SC, X-GNP-L and Y-GNP-L reveal the importance of the filler geometry and surface chemistry (particularly the surfactant) onto the crystallization of PP in the composites, more evident by a direct comparison of the K_α, K_β, X_c(%) trends for the composites of PP with X-GNP-L and Y-GNP-L. These two grades of GNP were exfoliated in the presence of the surfactant L and differ from each other by the starting graphite used during HPH. At low filler content (<1 wt%) the X-GNP-L appear to favour the crystallization of PP (either α or β form) more than Y-GNP-L did, whereas at higher filler loadings (>1 wt%) the two filler affect the crystallization of PP similarly. Probably, at low filler content, the more irregular shape of X-GNP-L imparted lesser constraint onto the PP chains than Y-GNP-L- particularly on those further away from the filler particles- and the geometry of the GNP platelets is more dominant at determining the crystallization of PP. Yet, at higher filler loadings, the agglomeration of the filler particles is more dominant at affecting the crystallization of PP, thus the two sets of composites of PP with X-GNP-L and Y-GNP-L present similar crystalline profiles. As already mentioned for the composites with the BNNS, it would be interested for future work to combine the WAXD analysis to the SAXS measurements to assess the crystalline geometry and chain arrangement of the PP near and perhaps around the GNP particles.

Further investigation on the nucleating effect and polymorphism of PP by X-GNP-SC, X-GNP-L and Y-GNP-L inclusion was carried out by DSC analysis. The results are reported in Figure 4.20 and Table 4.8.
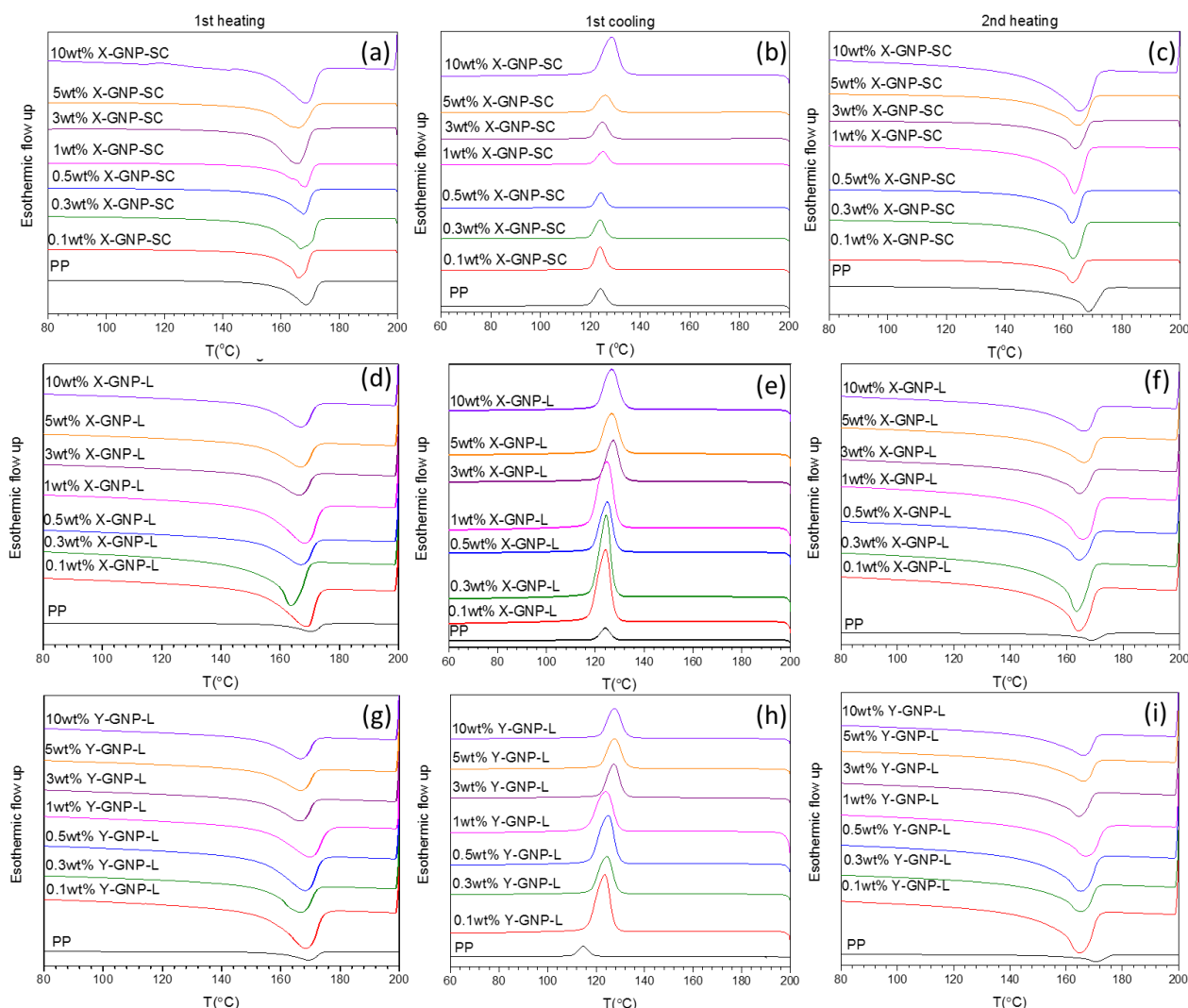
Figure 4.20: DSC thermograms of PP and its composites with X-GNP-SC (a)-c)), X-GNP-L (d)-f)) and Y-GNP-L (g-i)) at different filler loadings.

The first heating thermograms (Figure 4.20 a)) of the composites of PP with X-GNP-SC show broad and asymmetric peaks confirming the coexistence of α-PP and β-PP crystals. The first cooling thermograms (Figure 4.20 b)) show a shift toward higher temperatures upon X-GNP-SC incorporation. In particular, T_c increased from 116 °C for the neat PP to 128 °C for the composites with 10 wt% X-GNP-SC. The biggest increase in the T_c of PP was registered at X-GNP-SC loading as low as 0.1 wt % and the addition of further amounts of X-GNP-SC did not result in more nucleation, and little increases of T_c were registered. This could be associated with the even distribution of X-GNP-SC throughout the PP matrix, which constrained PP chains in a confined space delimited by filler particles, thus delaying crystallization with no further increase in T_c. The second heating thermograms (Figure 4.20 c)) show broad peaks after X-GNP-SC addition, yet the peaks are more symmetric than those obtained during the first

heating. One of the possible reasons may lay in the annealing effect as already noticed in the composites of PP with X-BNNS-SC. The melting peaks in the second heating thermograms are as broad as the ones in the first heating curves, probably due to the β–α phase transition, which caused superimposing of the peaks related to the β–α phase transition and α-spherulite melting [23, 46].

The first heating thermograms (Figure 4.20 d)) of the composites of PP with X-GNP-L show broad and asymmetric peaks confirming the coexistence of α-PP and β-PP crystals, suggesting a change in PP polymorphism upon inclusion of X-GNP-L. The first cooling thermograms (Figure 4.20 e)) show a shift toward higher temperatures upon X-GNP-L incorporation. In particular, T_c increased from 116 °C (PP) to 130 °C for the composites with 10wt% of X-GNP-L. The second heating thermograms (Figure 4.20 f)) show broad peaks after X-GNP-L addition, yet they are more symmetric than those obtained during the first heating. The controlled cooling cycle realized during the DSC measurements produced a material with a narrower crystallite size distribution compared to the material cooled by injection moulding (annealing effect). However, the melting peaks of the composites in the second heating thermograms are as broad as the ones in the first heating curves, probably as a results of the β–α phase transition ([27] and references therein).

The first heating thermograms (Figure 4.20 g)) of the composites of PP with Y-GNP-L show broad and asymmetric peaks, confirming the coexistence of α-PP and β-PP crystals. However, it is not possible to identify the peak related to the melting of the β-crystallites due to the β–α phase transition during the first heating step in the DSC experiment, which resulted in overlapping of the peaks associated with the two polymorphic forms [27, 45, 46]. The first cooling thermograms (Figure 4.30 h)) show a shift of the cooling peak toward higher temperatures upon filler incorporation. In particular, T_c increased from 116 °C (PP) to 128 °C, at 10 wt% of Y-BNNS-L. The second heating thermograms (Figure 4.20 i)) show broad peaks after the addition of the filler, which appear to be as broad as the ones in the first heating curves, probably due to the superimposing of the peaks related to the β–α phase transition and α-spherulite melting [23, 27].

Table 4.7: T_m, T_c, ΔH_m, ΔH_c, X_c (%) of PP and its composites with X-GNP-SC and X-GNP-L and Y-GNP-L as detected by the DSC thermograms. The ΔH_c related to a theoretical PP crystal with infinite dimensions used to calculate the crystallinity is 207 J/g [30]. The results are a representation of three measurements per each composition. The error calculated for T_m, T_c amd X_c (%) falls on the first decimal, which is not significant for the present study.

Sample	T_m(ºC)		T_c(ºC)	ΔH_m(J/g)		ΔH_c(J/g)	X_c(%)
	1st heating	2nd heating	1st cooling	1st heating	2nd heating	1st cooling	1st cooling
PP	168	170	116	88	102	97	47
0.1 wt% X-GNP-SC	166	163	124	92	109	100	48
0.3 wt% X-GNP-SC	166	163	124	95	111	103	50
0.5 wt% X-GNP-SC	168	163	124	92	110	102	49
1 wt% X-GNP-SC	168	164	125	89	109	99	47
3 wt% X-GNP-SC	166	164	125	85	105	94	44
5 wt% X-GNP-SC	166	165	126	89	102	93	44
10wt% X-GNP-SC	168	165	128	93	108	109	48
0.1 wt% X-GNP-L	169	164	124	122	117	138	67
0.3 wt% X-GNP-L	164	164	124	116	115	124	60
0.5 wt% X-GNP-L	167	164	125	95	117	119	58
1 wt% X-GNP-L	168	166	125	94	115	120	58
3 wt% X-GNP-L	166	166	127	88	109	115	58
5 wt% X-GNP-L	166	166	127	88	109	115	58
10wt% X-GNP-L	166	166	127	89	108	116	59
0.1 wt% Y-GNP-L	168	165	124	92	112	108	52
0.3 wt% Y-GNP-L	166	165	124	81	113	125	60
0.5 wt% Y-GNP-L	168	165	125	94	115	116	56
1 wt% Y-GNP-L	169	167	124	83	110	101	49
3 wt% Y-GNP-L	166	164	128	91	111	114	57
5 wt% Y-GNP-L	166	166	127	91	110	127	64
10wt% Y-GNP-L	167	167	128	90	110	127	63

The T_m of PP in the composites with X-GNP-SC after the second heating cycle decreased by *ca* 5 °C when 10wt % X-GNP-SC were added. The addition of irregular shaped X-GNP-SC platelets may have hindered the crystallization of PP chains, thus either a larger fraction of PP amorphous phase or imperfect/small PP crystals formed upon cooling and T_m was depressed.

This phenomenon can be better explained by analysing the trend of the total crystalline fraction (X_c%). X_c(%) increased from 47% (PP) to 50% when X-GNP-SC were added at loadings up to 0.5wt%, then X_c(%) decreased at loadings between 0.5wt% and 5wt% before increasing again to 50% when 10wt% of X-GNP-was included in PP. At X-GNP-SC ≤ 0.5 wt%, the PP chains were free to crystallize in defined geometries, thus more but probably smaller/imperfect crystals of PP formed compared to the polymer alone. At higher filler loadings, between 0.5wt% and 5wt%, the constraint effect of the X-GNP-SC particles on the polymer chain mobility lead to a reduction of the crystallinity [26, 27]. Furthermore, GNP particles are thermally conductive with values of up to 7000 W/mK (at room temperature) [43, 47] whereas PP is a thermal insulator, thus, more efficient thermal dissipation was possible during the cooling cycle where X-GNP-SC particles were present, forcing nearby neighbour PP chains to crystallize faster than those further away. This may have contributed to the formation of the amorphous phase. Yet, this explanation seem to contrast the results obtained at 10wt% X-GNP-SC, where an increase in the crystallinity was registered. Probably, at such high concentration, the X-GNP-SC could agglomerate more, thus imparting less constraint onto the long-distant PP chains, which manifested as an increase in the crystallinity. Yet, the T_m of the composites at 10wt% of X-GNP-SC decreased, which let us speculate that the increase in the crystallinity was probably due to the formation of a higher amount of small crystallites compared to PP. ΔH_m and ΔH_c of the composites follow the same trend as X_c(%), *i.e.* ΔH_m and ΔH_c first increase when adding the X-GNP-SC at 0.5wt%, then ΔH_m and ΔH_c decrease when adding the filler up to 5wt% before increasing again at 10wt% of X-GNP-SC. The change in the crystalline amounts and/or dimensions upon filler incorporation reflect the change of the ΔH_m and ΔH_c.

The T_m of PP in the composites with X-GNP-L after the second heating cycle decreased by *ca* 3-5 °C at 10wt % of X-GNP-L whereas X_c(%) first increases from 47% (PP) to 67% at 0.3wt% of filler loadings, before decreasing to 59% when adding 10wt% of X-GNP-L. This result suggests that after the first cooling during the DSC a higher number of smaller and/or more imperfect crystallites formed when comparing the composites of X-GNP-L with the neat PP. Probably, the irregular shape of this GNP favoured the crystallization of small and/or imperfect crystals of PP under the controlled conditions adopted during the DSC. The trend of X_c(%) is probably due to a diverse constraint effect of the X-GNP-L onto the PP chains when adding the filler in higher amounts, probably due to different levels of nano-filler dispersion and distribution. ΔH_m and ΔH_c of the composites with X-GNP-L follow the same trend as T_m and X_c(%). Again, the change in the crystalline amounts and/or dimensions upon filler

incorporation reflect the change of the ΔH_m and ΔH_c, as a result of the diverse constraint effect of the polydispersed nano-foller particles onto the PP chains dynamics.

The T_m of PP in the composites with Y-GNP-L after the second heating cycle decreased by *ca* 3-4 °C at a 10wt % of Y-GNP-L, probably due to the formation of smaller and/or more imperfect crystals of PP when adding Y-GNP-L. $X_c(\%)$ increases when comparing the PP with the composites of Y-GNP-L, yet it is not possible to identify a specific trend, probably due to a diverse state of distribution and dispersion of this grades of GNP, which imparted a different constraint effect onto PP chains, resulting in the formation of a distribution of imperfect crystals of PP. ΔH_m and ΔH_c increase compared to the neat PP but it is not possible to identify a trend, which can probably be associated to the correspondent change in the crystalline fraction.

The DSC results appear to confirm the crucial role of the GNP geometry and state of dispersion onto the properties- crystallinity and nucleation effect- of the composites with PP, as already noticed for the composites with the BNNS. It seems that the Y-GNP-L present a more diverse state of distribution and perhaps dispersion in the PP compared to the grades X-GNP-SC and X-GNP-L, probably caused by the combined effect of the morphology derived from the starting graphite-Y and the surface chemistry (*i.e.* surfactant L and surface functionalities).

In future work, the modulated DSC and polarised hot-stage microscopy could support the understanding on the mechanisms of nucleation, particularly the β-nucleation, of PP upon incorporation of the GNP particles.

4.4.5- Study of the rheological and mechanical properties of the composites of PP with X-GNP-SC, X-GNP-L, Y-GNP-L

Further analysis on the state of distribution and dispersion of the TS GNP grades was performed by Oscillatory rheology whereas the Tensile tests were performed to determine the mechanical properties of the composites prepared.

The results from the rheological study are reported in Figure 4.21.
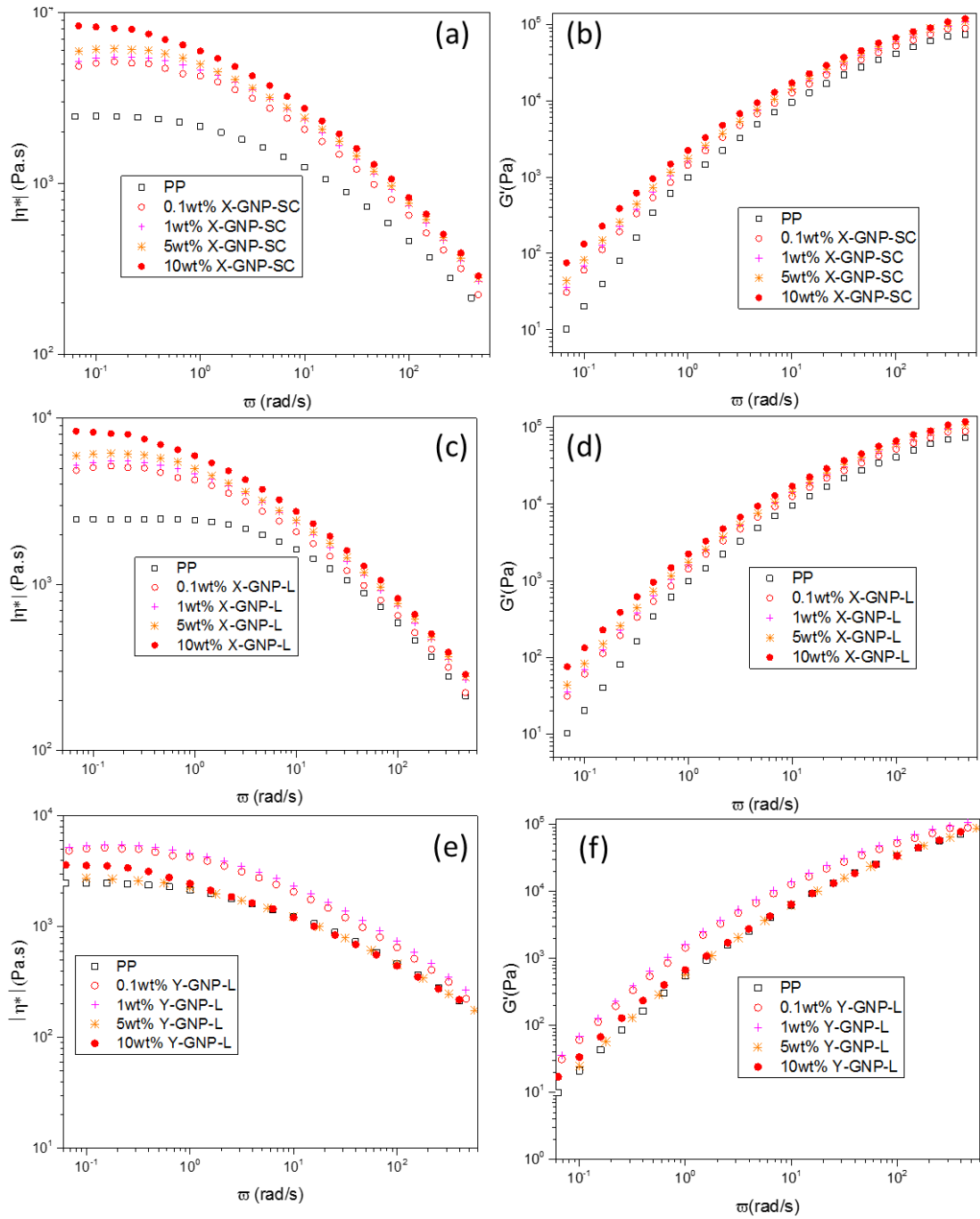
Figure 4.21: |η*| and G′ as a function ω for PP and its composites with X-GNP-SC (a)-b)), X-GNP-L (c)-d)) and Y-GNP-L (e)-f)). The data are a replica of 3 measurements on a batch of 3 specimens per compositions.

No difference in the rheological profiles were detected when comparing the neat PP with the three sets of composites of X-GNP-SC, X-GNP-L, Y-GNP-L. The complex viscosity |η*| is constant with the frequency at ω < 1 rad/s (Newtonian profile) both for PP and its composites, before linearly decreasing (power law) with frequency (Figure 4.21 a), c), e)). An increase in

|η*| of 8000 Pa.s at 10wt% of filler was detected in the Newtonian region, which was expected in composites with high filler content. The storage modulus G′ increases with frequency and the trend does not change when comparing the composites of these grades of GNP with PP and no rheological percolation was detected (Figure 4.20 b), d), f)). Probably, the irregular shaped-flakes of these GNP, the surface chemistry - presence of the surfactants SC and L - and the melt flow during the injection of the composites all prevented the filler particles from percolating in a 3D interconnecting structure, thus no rheological percolation was attained. Further insights on the mechanisms of interactions between PP and the surfactants SC and L present on the GNP particles are given in the tensile tests section.

The rheology of the composites of PP with X-GNP-SC, X-GNP-L, Y-GNP-L, confirm the complexity of the particles dimensions, surface chemistry and processing optimization to manufacturing homogeneous and functional composites. As already noticed for the composites of PP with the BNNS grades, a melt-flow modelling study could help to predict the state of distribution and dispersion of the examined GNP particles in PP during injection moulding.

The mechanical properties of the composites with PP and X-GNP-SC, X-GNP-L, Y-GNP-L (replica of 6 specimens per composition) were analysed and the results are reported in Figure 4.22.
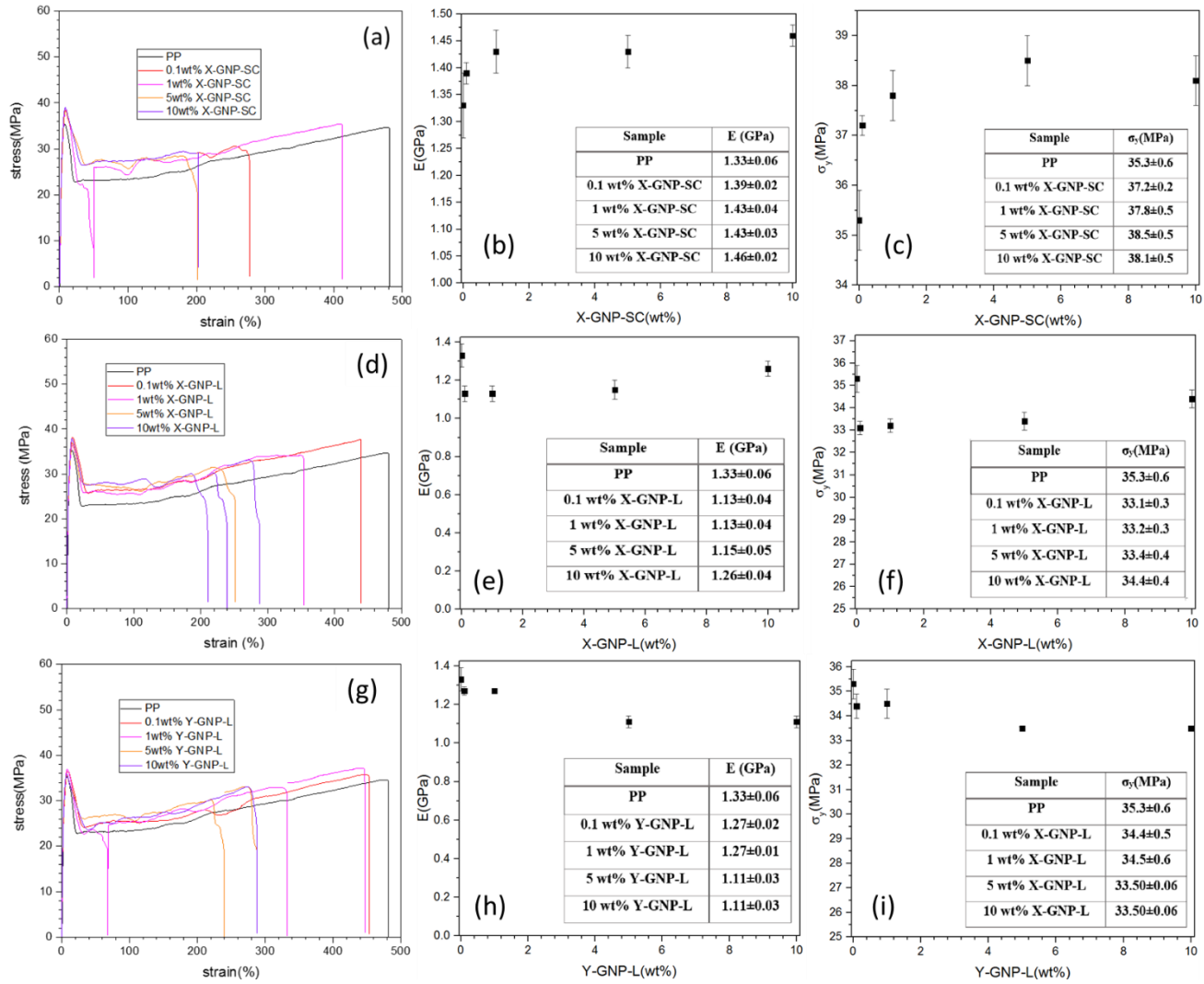
Figure 4.22: Stress-strain curves of PP and its composites with X-GNP-SC (a)), X-GNP-L (d)) and Y-GNP-L (g)). G in function of the filler loading (b-h)) and σ_y in function of the filler loading (c-i)).

The stress-strain curves of PP and its composites with X-GNP-SC, X-GNP-L and Y-GNP-L at different filler loadings are reported in Figure 4.22 a)-g). The addition of the GNP reduced the elongation at break of PP and probably acted as spots of stress accumulation, released by giving internal fractures, as evident from the noise detected in the plastic deformation region [37-42]. Both E and σ_y increase upon inclusion of X-GNP-SC in PP. E increases from 1.33±0.06 GPa for the neat PP to 1.46±0.02 GPa for the composite with 10wt% of X-GNP-SC, whereas σ_y increases from 35.3±0.6 MPa for the neat PP to 38.1±0.5 MPa at 10wt% of filler loading. As already noticed for the counterpart composites prepared by laboratory scale extruder, the increase of E and σ_y could derive by the formation of entanglements of PP around the GNP

particles, the intrinsic rigidity of GNP and the crystallization of the β-PP crystals upon filler incorporation- as reported in the XRD analysis [37-42].

The mechanical properties of the composites of PP+X-GNP-L and PP+Y-GNP-L display similar trends. E decreases from 1.33±0.06 GPa for the neat PP to 1.26±0.04 GPa at 10wt% of X-GNP-L and to 1.11±0.03 GPa at 10wt% of Y-GNP-L. σ_y decreases from 35.3±0.6 MPa for the neat PP to 34.4±0.4 MPa at 10wt% of X-GNP-L and to 33.50±0.06 MPa at 10wt% of Y-GNP-L. The trends of E and σ_y could be ascribed to the agglomeration of the X-GNP-L and Y-GNP-L upon incorporation in PP [37-42].

The three GNP grades here studied show similar lateral dimensions (few µm), yet the mechanical properties of the composites of PP with X-GNP-SC are different from the mechanical properties registered for the composites of PP with X-GNP-L and Y-GNP-L. As already noticed for the composites with the BNNS grades, the difference in the mechanical properties of the composites could be ascribed to the mechanism of interactions between the surfactants present in traces on the surface of the nanoparticles examined and PP.

SC appear to favour the coexistence of the X-GNP-SC in PP, perhaps through the hydrophobic interactions between the cyclo-hexane rings of SC with the polymer chains. The amphiphilic surfactant L contains an aromatic head interacting with GNP and a polyether-polyol tail exposing out of the GNP flakes. As anticipated for the composites with Y-BNNS-L, the surfactant L could ideally "flip" when admixing the X-GNP-L/Y-GNP-L in the polymer, to exposing the aromatic head to the hydrophobic PP and the polyether-polyols tails to the GNP. However, this mechanism is unlikely to occur in the composites with the GNP, since the stable aromatic structure of GNP could repulse the polyether-polyol tail of L, which is therefore exposed to the polymer matrix. This type of arrangement, would promote the particle-particle interactions over the particle-polymer interaction, thus, causing the agglomeration of the filler particles when X-GNP-L/Y-GNP-L are admixed in PP, which could justify the decrease of E and σ_y of the composites compared to the neat PP. These results are in line with the XRD, DSC and rheology findings.

As explained for the composites with the BNNS grades, future work should focus on the study on the mechanisms of interactions between the surfactants SC and L with PP by way of ^{13}CNMR. In addition, a modelling study on the melt-flow of the PP composites during injection moulding could support the research to understanding the mechanisms and the state of distribution and dispersion of the GNP in PP as the polymer crystallizes in the moulds of different shapes and dimensions.

4.5- Characterization of composites of HDPE with X-BNNS-SC, Y-BNNS-L, X-GNP-SC prepared by 16mm co-rotating twin-screws extruder and micro-injection moulding.

Composites of HDPE with X-BNNS-SC (lateral size few nm) and X-GNP-SC (lateral few μm) were prepared with a filler loading in the range 0-5wt% and the morphology, crystalline structure, rheological and mechanical properties determined.

A stand-alone study was carried out on the electro-rheological properties of the composites of HDPE+Y-BNNS-L (5wt%) (lateral size up to 10 of μm) and HDPE+X-BNNS-SC (5wt%), to assess the effect of two grades of BNNS presenting two different lateral sizes onto the rheological properties of HDPE. The electro-rheology measurements were performed at the University of Huelva (Spain) as part of the International Placement (Chapter 3).

4.5.1- Study of the morphology, crystalline structure, rheological and mechanical properties of the composites of HDPE with X-BNNS-SC and X-GNP-SC.

The composites of HDPE with X-BNNS-SC and X-GNP-SC were characterized in terms of morphology, crystalline structure (SEM, XRD, DSC), rheological and mechanical properties (oscillatory rheology and tensile tests), to assess the effect of the filler on the polymorphism of HDPE, which was previously noticed in PP, and the extent of distribution and dispersion of the fillers in the matrix.

Figure 4.23 depicts the SEM images of the composites of HDPE at 5wt% of filler loading.
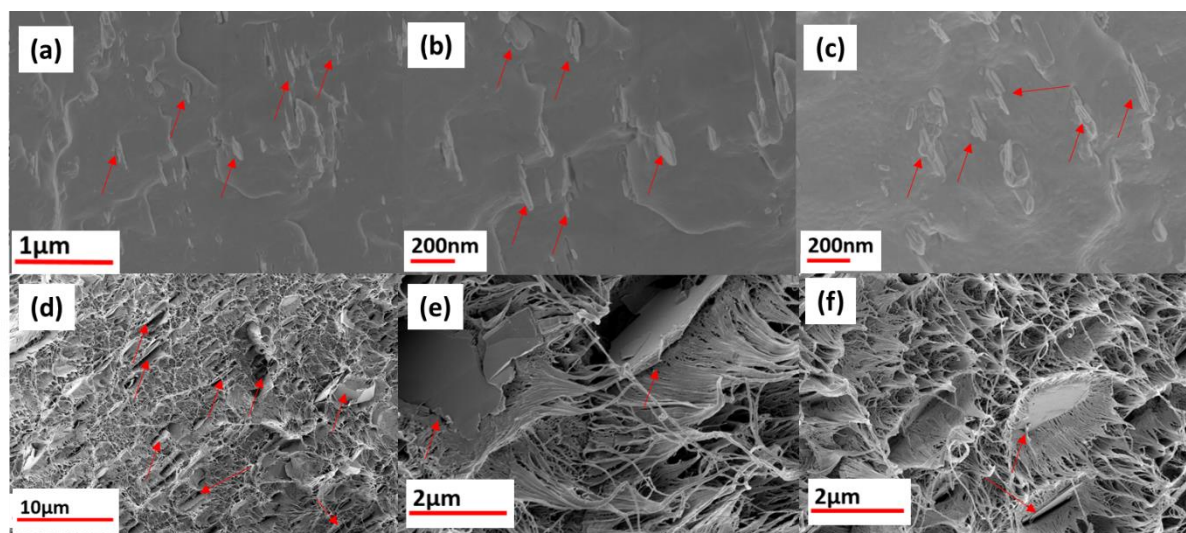
Figure 4.23: SEM images of HDPE+X-BNNS-SC (a)-c)) and HDPE+X-GNP-SC (d)-f)). The magnification increases from left to right. X-BNNS-SC and X-GNP-SC dispersed to some extent in HDPE. The poor wettability of HDPE onto X-GNP-SC favoured the formation of voids around the filler platelets. The red arrows point to X-BNNS-SC and X-GNP-SC particles.

Good dispersion and distribution of the X-BNNS-SC and X-GNP-SC in the polymer matrices was achieved. The composites of HDPE with X-BNNS-SC present a smooth surface with relatively small voids around the BNNS particles. However, the composites of HDPE with X-GNP-SC appear to present large interfaces (voids), probably due to the known rapid crystallization kinetics of HDPE, which could cause the exclusion of X-GNP-SC particles from the crystal domains by creating large interfaces. This phenomenon is not evident in the composites of HDPE with X-BNNS-SC, probably due to the smaller particle length (few nm) and round-shape platelets this BNNS.

The crystalline structure of the composites of HDPE with X-BNS-SC and X-GNP-SC at different filler loadings was investigated by XRD. The results are reported in Figure 4.24.
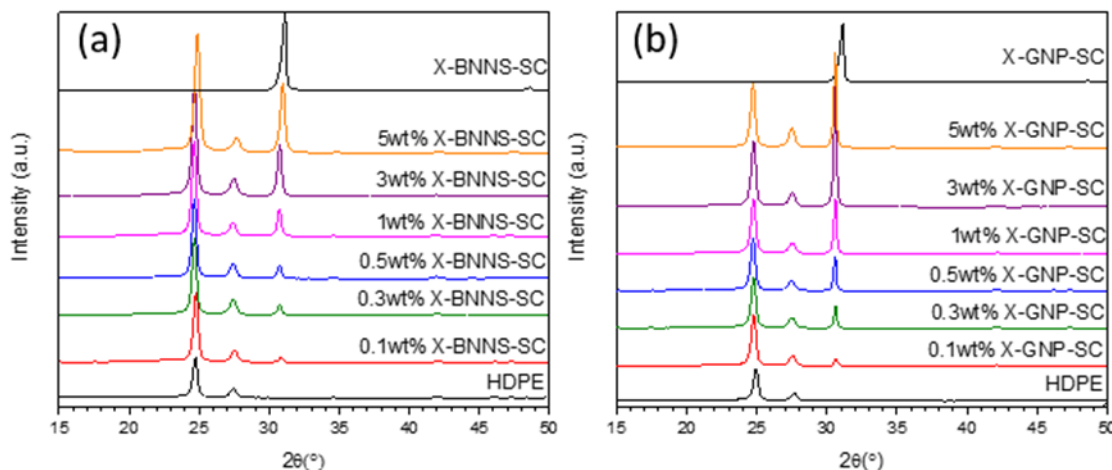
Figure 4.24: XRD patterns of HDPE and its composites with X-BNNS-SC (a)) and X-GNP-SC (b)). The data are a replica of 3 measurements on a batch of 3 specimens per compositions.

The XRD patterns (Figure 4.24) show the most intense peaks for HDPE at $2\theta = 25°$ (orthorhombic (100)), 27.7° (orthorhombic (200)), 35° (monocline(210)), 42.3° (orthorhombic (020)) and X-BNNS-SC/X-GNP-SC at $2\theta=31°$ (002). As already noticed for the composites of PP, the registered peaks may be shifted compared to the ones reported due to the different X-ray source used in this work [28, 29]. The presence of X-BNNS-SC and X-GNP-SC in HDPE is evident by the characteristic peak at $2\theta=31°$, which increases with increasing filler loading. Unlike the composites with PP, the addition of X-BNNS-SC and X-GNP-SC did not change the polymorphism of HDPE. The crystalline content (%) of HDPE is 50% and the addition of the filler particles did not induce any change in the content of crystalline fraction. This may be associated with the rapid crystallization kinetics of HDPE, thus the presence of X-BNNS-SC/X-GNP-SC even up to 5wt% did not affect crystal content, nucleation/growth.

Further analysis on the effect of the X-BNNS-SC and X-GNP-SC particle onto the crystallinity of HDPE was carried out using DSC. The results are reported in Figure 4.25 and Table 4.9.
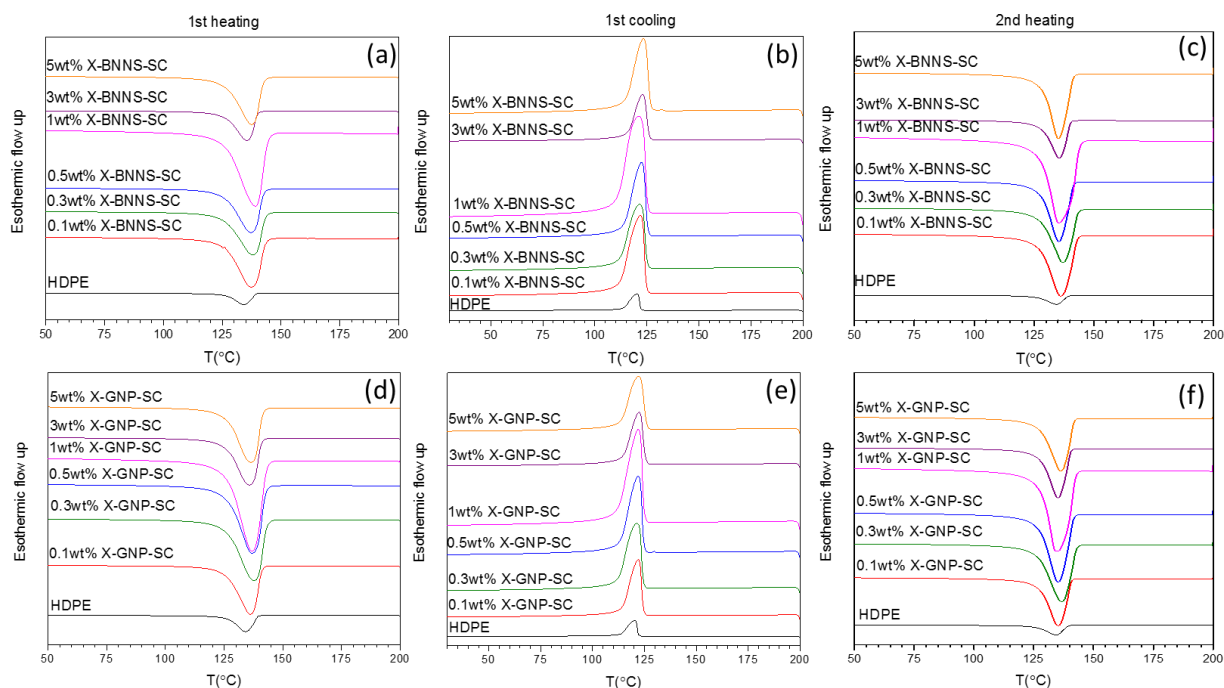
Figure 4.25: DSC thermograms of HDPE and its composites with X-BNNS-SC (a)-c)) and X-GNP-SC (d)-f)) at different filler loadings.

Both the heating and cooling thermograms of the composites of HDPE with X-BNNS-SC show a slight broadening of the melting peak when comparing the neat HDPE to the composites with X-BNNS-SC. This is due to a broader crystallite size distribution upon filler incorporation. However, the peak broadening does not follow a specific trend when comparing one composition to another, probably due to the poor distribution/particles aggregation of the filler in the matrix, which produced inhomogeneous materials.

The thermograms related to the composites of HDPE with X-GNP-SC show the same trends as the thermograms related to the composites HDPE+X-BNNS-SC. The peaks in both the heating and cooling thermograms of the as prepared composites appear slightly broader than the heating/cooling peaks of the neat HDPE, probably due to a broadening in the crystallites size upon X-GNP-incorporation. The broadening does not follow a trend, which is likely caused by the inhomogeneity of the samples.

It is interesting to note that neither X-BNNS-SC nor X-GNP-SC have a nucleating effect on HDPE (no change in T_c). The kinetics of crystallization of HDPE is much more rapid than PP, that is, HDPE crystallization is less sensitive to the effect of X-BNNS-SC/X-GNP-SC loadings [57].

Table 4.8: T_m, T_c, ΔH_m, ΔH_c and X_c (%) of HDPE and its composites with X-BNNS-SC and X-GNP-SC as obtained from the DSC thermograms. The ΔH_c related to a theoretical HDPE crystal with infinite dimensions used to calculate the crystallinity is 287 J/g [30]. The results are a representation of three measurements per each composition. The error calculated for T_m, T_c amd X_c (%) falls on the first decimal, which is not significant for the present study.

Samples	$T_m(^oC)$		$T_c(^oC)$	$\Delta H_m(J/g)$		$\Delta H_c(J/g)$	$X_c(\%)$
	1st heating	*2nd heating*	*1st cooling*	*1st heating*	*2nd heating*	*1st cooling*	*1st cooling*
HDPE	134	134	120	177	205	202	69
0.1 wt% X-BNNS-SC	137	136	122	203	251	247	86
0.3 wt% X-BNNS-SC	138	137	122	201	245	244	85
0.5 wt% X-BNNS-SC	137	135	122	196	240	236	83
1 wt% X-BNNS-SC	139	135	121	203	246	244	86
3 wt% X-BNNS-SC	135	135	123	197	243	238	85
5 wt% X-BNNS-SC	137	135	123	193	232	229	84
0.1 wt% X-GNP-SC	136	135	122	205	254	247	86
0.3 wt% X-GNP-SC	138	137	122	194	241	238	83
0.5 wt% X-GNP-SC	137	135	122	202	243	239	84
1 wt% X-GNP-SC	137	134	122	202	248	246	86
3 wt% X-GNP-SC	136	135	122	191	238	231	83
5 wt% X-GNP-SC	136	136	122	189	233	227	83

From Table 4.12 it is possible to note that both the melting temperature T_m and crystallization temperature T_c do not change when comparing the neat HDPE to the composite with 5wt% of X-BNNS-SC/X-GNP-SC in both the first and second heating cycles. The variation of melting enthalpy ΔH_m increases when comparing the first heating with the second heating cycle for both the composites with X-BNNS-SC and with X-GNP-SC. Similarly, ΔH_m increases when comparing the HDPE alone with the composites of X-BNNS-SC and with X-GNP-SC, *i.e.* either larger or thicker lamellae formed during the first cooling cycle. The variation of crystallization enthalpy ΔH_c follows the same trend as ΔH_m and reflects the change in the dimensions of the crystallites lamellae. The X_c(%) increases from 69% (HDPE) up to 83% (5wt% X-BNNS-SC) and 83% (5wt% X-GNP-SC). Clearly, under the controlled cooling/heating conditions realised during the DSC measurements, the filler particles favoured the crystallization of HDPE. One of the possible reasons could be ascribed to the fact that the slow cooling during the DSC facilitated the crystallization of the polymer chains around the

filler particles. As already noticed with the composites of PP, for future work it would be interesting to investigate the composites of HDPE by hot-stage polarised optical microscopy both under isothermal and non-isothermal conditions, to assess the mechanism of nucleation and growth of the polymer crystallites in presence of the filler particles.

The extent of distribution and dispersion of the X-BNNS-SC and X-GNP-SC in HDPE was again assessed by Oscillatory rheology (Figure 4.26) whereas the mechanical properties were investigated by Tensile tests (Figure 4.27).
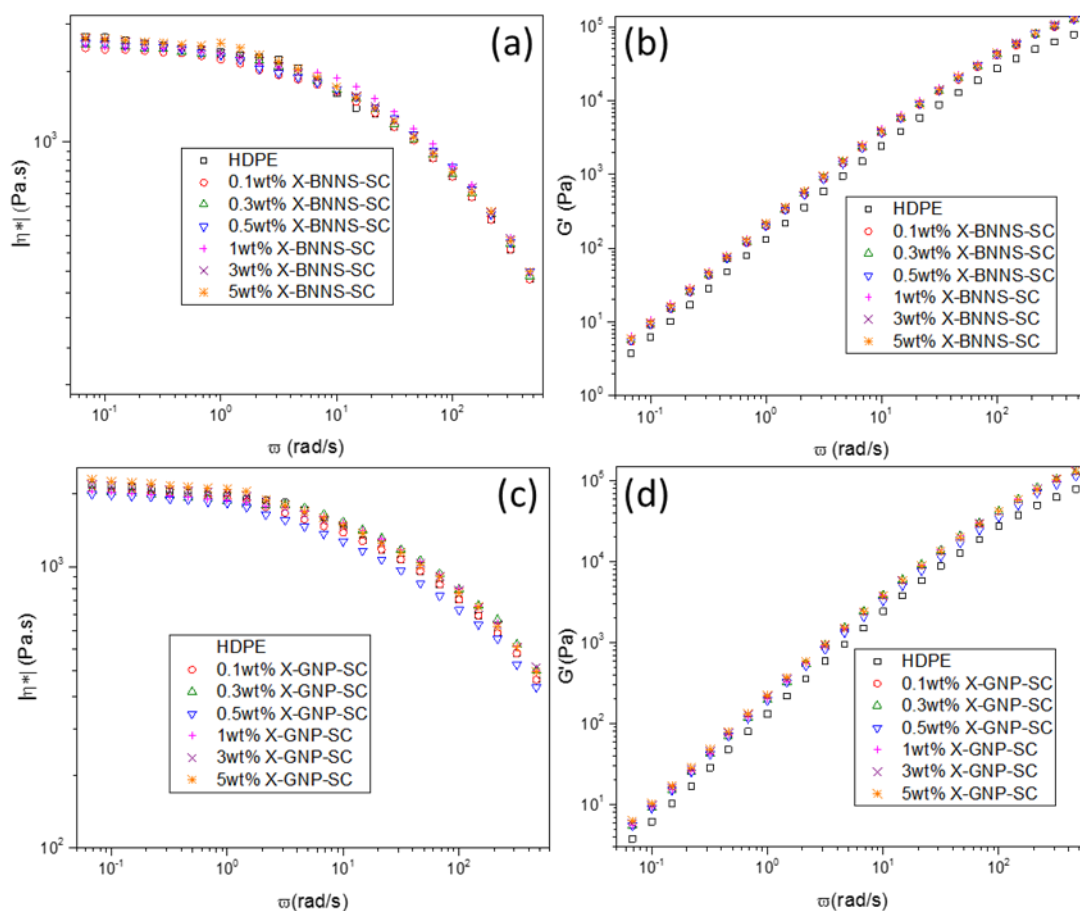
Figure 4.26: $|\eta^*|$ and G' as a function ω for HDPE and its composites with X-BNNS-SC (a)-b)) and X-GNP-SC (c)-d)). The data are a replica of 3 measurements on a batch of 3 specimens per compositions.

No difference in the rheological profiles between the neat HDPE and the composites with X-BNNS-SC and X-GNP-SC is visible, that is no rheological percolation was attained. In fact, the viscosity is constant with the frequency at $\omega < 1$ rad/s (Newtonian profile) both for HDPE and its composites with X-BNNS-SC and with X-GNP-SC (Figure 4.26 a), c)). Then, the

144

viscosity decreases linearly with frequency (power law). As already reported for the PP composites, the viscosity also increases, but to 1000 Pa.s at 5%wt filler loading. No change in G´ was observed (Figure 4.26 b), d)) that is, the rheological percolation was not realized using the adopted mixing procedure in the range of compositions explored. Probably, the agglomeration of the filler particles - due to both the strong particle-particle interactions and the aggregation/exclusion from the polymer domains during the crystallization of the HDPE - prevented a 3D network of X-BNNS-SC/X-GNP-SC from percolating.

The representative stress-strain curves from the tensile testing of HDPE composites with X-BNNS-SC and X-GNP-SC (0-5wt%) are reported in Figure 4.27, along with the trends and values of G and σ_y in function of the filler loading.
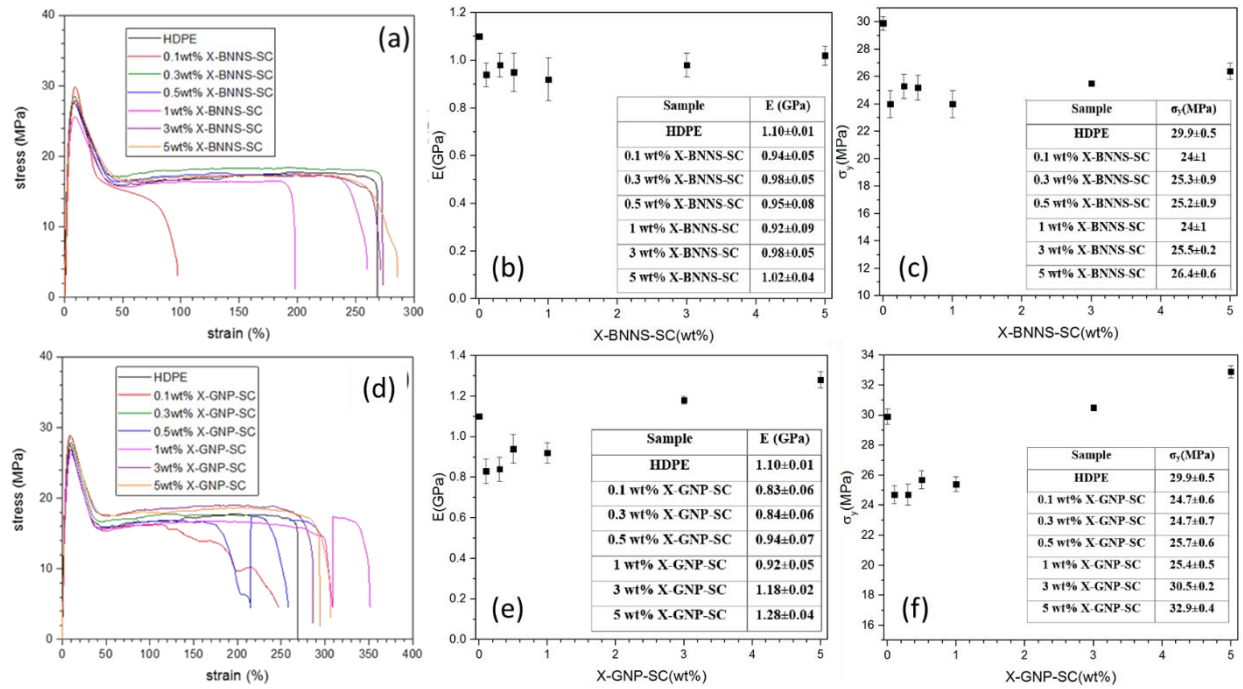
Figure 4.27: Stress strain curves of HDPE and its composites with X-BNNS-SC (a)) and X-GNP-SC (b)), at different filler loadings. The curve are a results of 6 replica per set of compositions. G in function of X-BNNS-SC content (b)) and X-GNP-SC content (e)). σ_y in function of X-BNNS-SC loading (c)) and X-GNP-SC loading (f)).

The stress-strain curve (Figure 4.27 a), d)) of the HDPE and its composites with X-BNNS-SC and X-GNP-SC show a reduction of the elongation at break upon filler incorporation along with internal fractures, manifested as a noise in the plastic deformation region. The release of the stress accumulated during the processing and perhaps aggregation of the filler particles could explain the internal fractures [37-42].

The addition of X-BNNS-SC/X-GNP-SC up to 5wt% caused a decrease in the values of E and σ_y compared to the neat HDPE, probably due to the agglomeration of the filler particles as a result of the strong particle-particle interactions over the particle-polymer interactions and/or the rapid kinetics of crystallization of HDPE during injection moulding, which could exclude the filler particles from the polymer domains, thus favouring the aggregation of relative large clusters of X-BNNS-SC/X-GNP-SC. The addition of 10wt% of the fillers in HDPE increased both E and σ_y, probably as a result of the presence of a high amounts of agglomerates of rigid filler particles [37-42].

As already noticed for the composites of PP, a modelling study on the melt-flow during injection moulding could support the understanding of the state of filler distribution and dispersion during the crystallization of HDPE in the dumbbell, thus the resulting mechanical properties.

4.5.2- Study of the electro-rheological properties of the composites of HDPE with Y-BNNS-L (5wt%) and X-BNNS-SC (5wt%)

The rheological measurements on the composites of PP with Y-BNNS-L showed a percolated structure at 5wt% filler loading. However, the addition of 5wt% of Y-BNNS-L in HDPE did not show rheological percolation (the results on the rheological measurements of HDPE+Y-BNNS-L are reported in Appendix Part I), which confirmed that the properties of the polymer matrix (*e.g.* viscosity and crystallization mechanisms) play a dominant role in achieving rheological percolation. In particular, the fast crystallization kinetics and high melt viscosity of this grade of HDPE could prevent the alignment and interconnection of the Y-BNNS-L particles under the applied processing conditions. To verify this hypothesis, electro-rheology measurements were performed on the HDPE+Y-BNNS-L (5wt%) and HDPE+X-BNNS-SC (5wt%) composites, for comparison (lateral dimension X-BNNS-SC= few nm, lateral dimension Y-BNNS-L= up to 10µm). The electrical stimulus during the electro-rheology measurements should orientate the polarizable particles of these two grades of BNNS along a specific direction, thus facilitating the formation of a 3D network [58-63] (see Chapter 3). Due to the limitations of the heating device on the instrument used, only the composites of HDPE were studied.

Preliminary measurements were performed to detect the minimum voltage needed to initiate a change in sample structure and, was determined to be a voltage of 1500V. The following measurement cycle was developed: i) a frequency sweep with no voltage applied

(FS1), ii) a frequency sweep at 1500V (FS2@1500V) and iii) a frequency sweep with no voltage applied (FS3). FS1 was performed as a reference whereas FS3 was performed to explore the reversibility of any structural changes that occurred after ii).

The variation in $|\eta^*|$ and G′ as a function of ω and the Van-Gurp-Palmen plot (phase angle δ vs complex modulus $|G^*|$) for HDPE+X-BNNS-SC (5wt%) and HDPE+Y-BNNS-L (5wt%) were constructed from electro-rheology measurements, see Figure 4.27.
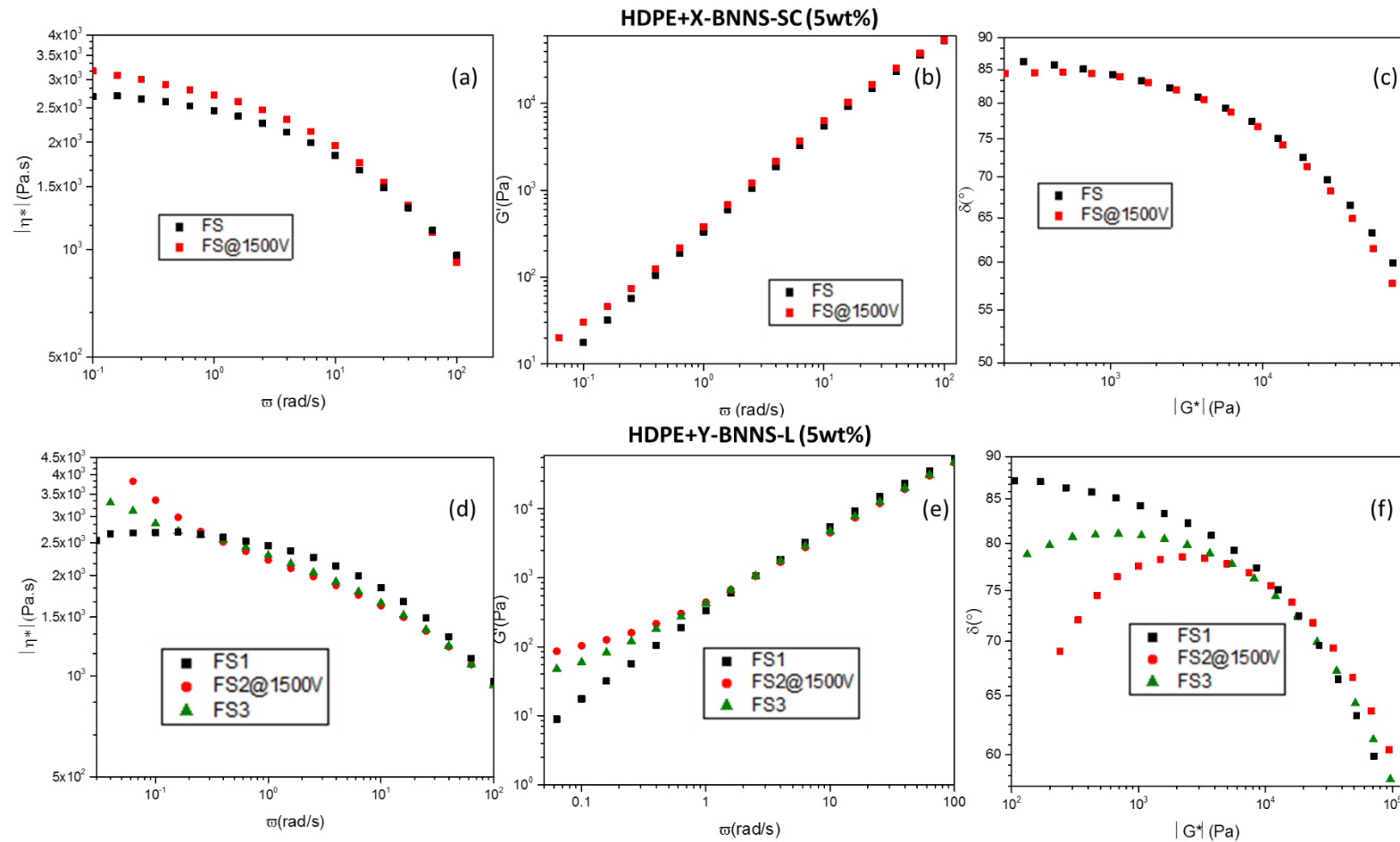
Figure 4.28: |η*| and G′ in function ω (a), b)) and Van-Gurp-Palmer plot (c)) obtained for HDPE+X-BNNS-SC 5 wt%. |η*| and G′ in function ω (d), e)) and Van-Gurp-Palmer plot (f)) for HDPE+Y-BNNS-L (5 wt%). FS1= Frequency Sweep with no current; FS2@1500V= Frequency Sweep at 1500V; FS3= Frequency Sweep with no current after FS2.

HDPE+X-BNNS-SC (5wt%) did not show any change in rheological profile after the application of the electrical impulse (Figure 4.27 a)-c)), whereas HDPE+Y-BNNS-L (5wt%) appeared to percolate upon electrical impulsion (FS2@1500V), evident from the plateau in $|\eta^*|$ and G′ at low frequencies (Figure 4.27 d), e)), and the divergence of δ in the Van-Gurp-Palmen plot (Figure 4.27 f)). Yet, the percolated structure is not stable (FS3) and the rheological behaviour of HDPE+Y-BNNS-L partially reverses to a non-percolated structure (FS1) when the electrical impulse is removed. This behaviour may be associated with the fact that polymer/polymer and polymer/filler interactions attained upon orientation of Y-BNNS-L particles under the electrical impulse are relatively weak and the percolated structure partially reverses to a non-percolated structure once the electrical impulse was removed.

The electro-rheological results presented prove that under a critical platelet length, the geometrical structure of the filler is more dominant in determining rheological percolation as is the case for the X-BNNS-SC composites. Whereas at the critical platelet length or above the properties of the matrix and/or the processing conditions employed determine the formation of a 3D network, as seen for Y-BNNS-L composites. In addition, the electro-rheology measurements proved it is possible to manipulate the structure of HDPE+Y-BNNS-L (5wt%) reversibly.

Further electro-rheology measurements should be carried out at different voltages to explore the effect of current on the reversibility of the formation of percolated structures and examine the relationship between filler platelet length and applied current (energy).

4.6- Summary of the experimental and possible applications of TS BNNS/GNP for the masterbatch production

The X-BNNS-SC, X-BNNS-T, Y-BNNS-L display a distribution of flake shapes and dimensions. X-BNNS-SC and X-BNNS-T platelets are round and a few nm in length whereas the Y-BNNS-L are square platelets of up to 10 of µm in length. Examination of X-GNP-SC, X-GNP-L and Y-GNP-L revealed a distribution of flakes, having irregular square-shaped platelets of few µm in length. The HPH process produced exfoliated BNNS/GNP with low defect concentration in the crystal lattice. The use of the solvent (water) and the surfactants SC, T and L during HPH introduced functionalities onto the surface of the filler particles (*e.g.* oxidised groups) which resulted in the production of hydrophilic BNNS/GNP. The X-BNNS-SC, X-BNNS-T, Y-BNNS-L, X-GNP-SC, X-GNP-L and Y-GNP-L are thermally stable under the oxidative conditions ($T_{deg} > 300°C$ @ air rate 15mL/min).

TS BNNS and GNP promoted the β-crystallization of PP, particularly at low filler contents (up to 0.5wt%). At higher loadings (>0.5wt%) the combination of particles length and/or particle aggregation limit the β-nucleating effect of the filler in PP. In addition, the examined BNNS/GNP show a nucleating effect in PP, manifested by an increase of the T_c up to 10-15°C compared to the neat polymer. This aspect is helpful when scaling up the manufacturing of PP composites with the BNNS/GNP here explored, since the increase in T_c could reflect into a reduction of the injection moulding temperature cycles, *i.e.* less energy consumption, which translates into a more sustainable processing with a reduction of both the environmental impact and costs.

The traces of the surfactant present on the surfaces of the BNNS and GNP grades examined affected the state of distribution and dispersion in the polymer matrix, thus the mechanical properties. It was found that the surfactant SC and L facilitated the distribution and perhaps the dispersion in PP of BNNS more than the surfactant T, manifested by an increase of the Young's modulus up to 20% when including the X-BNNS-SC and Y-BNNS-L in PP, whereas a decrease of *ca* 20% was registered when X-BNNS-T was added in PP. The surfactant SC also facilitated the distribution and the dispersion to some extent of the GNP particles, manifested again by an increase of the Young's modulus up to 20% compared to PP. However, the surfactant L appeared to favour the GNP particle-particle interactions - thus agglomeration-upon inclusion of X-GNP-L and Y-GNP-L in PP, which caused a decrease of the Young's modulus by *ca* 20%. It should be borne in mind that the intrinsic rigidity of the BNNS/GNP particles and the change in PP polymorphism (β-crystallization) upon filler incorporation could have contributed to the increase of the Young's modulus for the composites with X-BNNS-SC, Y-BNNS-L and X-GNP-SC.

The addition of X-BNNS-SC and X-GNP-SC in HDPE did not change the polymorphism or crystalline content (as determined by XRD) of the matrix. In addition, a reduction in the Young's modulus of *ca* 20% was detected upon filler incorporation. The results were ascribed to the agglomeration of the filler particles, probably caused by the high viscosity and perhaps the known rapid crystallization kinetics of HDPE during injection moulding, which could cause the exclusion and agglomeration of the filler particles as the molten composites flowed into the mould.

Fillers with large particles, such as the Y-BNNS-L (lateral length up to 10µm), facilitated the formation of a 3D network in the PP, yet, the type of mould used during injection

moulding could prevent the filler particles from percolating. Indeed, the shape and dimension of the moulds used could force the BNNS/GNP particles to settle/aggregate as the polymer chains cool down and crystallize. Furthermore, high viscous polymers with rapid kinetics of crystallization, such as HDPE, could obstruct the percolation of the BNNS/GNP into a 3D network. The application of an external electrical field may help the filler particles to align and overcome the inertia of the polymer chains in the molten state, thus, percolating in an interconnected particle-particle and/or particle-polymer structure, as detected in the case of the composites of HDPE with Y-BNNS-L at 5wt% of filler loading.

Table 4.9, the properties of the composites of PP with the BNNS and GNP (5wt%) are compared against the data reported in the literature and theoretical models (where possible) to benchmark the results obtained and described throughout the chapter.

Table 4.9: increment of crystallization temperature (T_c), increment of crystallinity content (X_c), Young's modulus (E) and thermal conductivity (TC) of the composites of PP with BNNS and GNP (5wt%, i.e. 2v%)) as reported in this work (reference, R) compared to benchmark data (benchmark, B).

Material	Property							
	T_c increment (%)		X_c increment (%)		E (GPa)		TC (W/mK)	
	R	B	R	B	R	B	R	B
BNNS (2v%)	≤ 9	NA	≤ 16	NA	≤ 1.50	≤ 10	none	≤ 40
GNP (2v%)	≤ 9	≤ 14	≤ 30	≤ 10	≤ 1.26	≤ 500	none	≤ 160

T_c and X_c were benchmarked against the data reported in the literature. E and TC were benchmarked against the rules of mixture (RoM) and parallel conductor model (PCM) respectively.

RoM: $E_c = \eta_l * \eta_0 * FVF * E_F + (1-FVF) * E_M$ [64]; where E_c is the Young's modulus of the composites, η_l is the length efficiency factor (aspect ratio), η_0 is the Krenchel orientation factor, FVF is the volume fraction of GNP/BNNS, (1-FVF) is the volume fraction of PP, E_F is the Young's modulus of BNNS/GNP (theoretical values as reported in the literature, see Chapter 2 Table 2.1) and E_M is the Young's modulus of PP (from tensile tests data). η_l has been

estimated as 50 (average aspect ratio of BNNS/GNP particles), whereas a value of 8/15 has been considered for η_0 since it is more likely that the BNNS and GNP are randomly distributed in PP (see SEM, DSC). The FVF was calculated by converting the FMF on a basis of 100g of composites (m) and considering the density of exfoliated graphite (*ca* 2.2 g/cm^3) and exfoliated boron nitride (*ca* 2.1 g/cm^3) for GNP and BNNS respectively. FVF= (FMF*m/ρ_F)/(FMF*m/ρ_F)+((1-FMF)*m/ρ_M), where ρ_F and ρ_M are the density of the fillers and PP respectively.

PCM: TC$_c$= FVF* TC$_F$ + (1-FVF)* TC$_M$, where TC$_c$ is the thermal conductivity of the composites, TC$_F$ and TC$_M$ are the thermal conductivity of the filler and the matrix respectively. For the TC of GNP and BNNS, the theoretical values as reported in the literature (see Table Chapter 2-2.1) were considered, whereas the TC of PP was taken from the experimental data.

The increment in the crystallization temperature (T$_c$) for the composites of PP with BNNS and GNP (5 wt%) was registered as high as 9% compared to the neat PP. There are no benchmark data for the BNNS composites (at the time of writing) whereas the benchmark data (as collected from the literature, see Chapter 2- references [184], [186]) for the composites with GNP show an increase of T$_c$ of 14% upon filler incorporation. This discrepancy could be associated to the higher aspect ratio of the GNP grade used by the benchmark data.

The crystallinity content (X$_c$, DSC) increased up to 16% and 30% when BNNS and GNP were added to PP respectively. No benchmark data are available for the BNNS composites (at the time of writing) whereas a benchmark value of 10% was reported for the composites with GNP (see Chapter 2- reference [226]). The difference between the increment reported in this work and the one from the benchmark data could be associated to the higher content of GNP used in the present work (5wt%, *ca* 2v%).

The Young's modulus (E) of the composites of PP with BNNS and GNP (5wt%) was registered as high as 1.50 GPa and 1.26 GPa respectively. The RoM used assumes a perfect bonding between the filler and the matrix, BNNS/GNP particles randomly distributed/dispersed in PP and low aspect ratio of the BNNS/GNP (AR ≤ 50). It appears that the low AR of the BNNS/GNP along with the limited adhesion between the filler particles and PP depress the mechanical properties of one order of magnitude for BNNS and two orders of magnitude for GNP composites.

The thermal conductivity (TC) of PP with BNNS and GNP showed no change compared to the neat polymer, whereas an increase of up to 40 W/mK and 160 W/mK was predicted by the

parallel conductors model. The results could be ascribed to the fact that the aspect ratio of BNNS and GNP here examined is relatively low (AR <50), therefore phonon scattering occurs upon application of thermal stimuli, which lower the TC. Furthermore, the random distribution/dispersion of the anisotropic BNNS/GNP in PP along with the presence of functionalities (oxidised groups) onto the filler particles could increase the interfacial thermal resistance, thus lowering the thermal conduction.

The utilisation of a combination of complementary characterisation techniques is crucial for a comprehensive understanding of the behaviour of composites of BNNS and GNP with polymer matrices, thus addressing the properties of the final composites (*e.g.* thermal, mechanical, rheological), which in turn determine the applications. The information provided in this thesis could help TS to customise the BNNS/GNP grades to match the structure of the polymer matrix (backbone chemistry, crystallinity, morphology), thus breakthrough the masterbatch production market. The next section provides some insights into the possible applications of TS BNNS/GNP grades as functional additives for the manufacturing of polymer masterbatches. The comments reported are based on the information available in the literature and partially on the knowledge acquired from the clients/competitor analysis that the author performed during a secondment at TS (the complete client/competitor analysis is not reported as it contains sensitive data in use by the industrial partner, TS).

4.6.1- Proposals to customise TS BNNS/GNP as functional additives in thermoplastic-based masterbatches

Masterbatches have been exploited for years in the pigments and wide plastics industries, particularly for packaging applications. With the growth of interest in nanocomposites, masterbatch technology could find applications in new industrial fields including aerospace, transportation and construction. A masterbatch of polymer-based composites with a solid functional additive (filler) is a concentrated mixture where the filler loading can reach values up to 30-40 wt%. Yet, for industrial applications the typical concentrations varies between 10-20 wt%, since higher loadings make melt processing more difficult, due to the increase of viscosity and hardness of the masterbatch being manufactured. The preparation of masterbatches with nanoparticles such as BNNS and GNP is practical, cost-effective and sustainable. Masterbatches allow for the storage of the nanomaterials as a pre-formulation, which can be further diluted with polymer to the desired concentrations in a

second step. In addition, the use of masterbatches provides for better control over composition when manufacturing the end-composites, since the direct addition of nanoparticles in small amounts (up to 1wt%)- typical of real applications- requires accurate scaling systems, additional costs to processing. Furthermore, potential clients working with polymer composites do not always possess facilities adequate to handle nanoparticles, thus, arousing health and safety issues. Yet, the production of masterbatches by expert producers could support and facilitate the distribution of nanoparticles as masterbatches from the manufacturers to the clients [65-68].

One of the possible routes for TS to benefit from the masterbatch technology is the customisation of the BNNS/GNP grades. Specifically, the embodiment of different classes (*i.e.* chemical structures) of surfactants during the HPH process could tailor the surface chemistry of the resulting BNNS/GNP, thus their applications in polymers. With this approach, the surfactant becomes a functional additive to the BNNS/GNP-polymer system and assumes the role of a coupling agent [69] between the filler particles and the polymer matrix.

Among the wide range of surfactants available on the market, the use of block-copolymers as surfactants may be a valid strategy for the modification of the BNNS/GNP as functional additives in polymers. Block copolymers are copolymers where the backbone is a repetition of monomers alternated as clusters (blocks). The study of the different classes of block-copolymers is beyond this project, yet the aim of this section is to propose ideas and opportunities for the manufacture of composites of thermoplastics with TS BNNS/GNP. By way of example, block-copolymers having aromatic units alternated by polyolefin units could be used to prepare BNNS/GNP for polyolefins. Indeed, the aromatic block would interact with the basal planes of the BNNS/GNP through π-π* interactions, whereas the polyolefin block would ideally co-crystallize with matrix [70-72], thus linking the filler particles and the polymer together. The optimization of the BNNS/GNP particle-polymer interactions, would improve the state of distribution and dispersion of the filler in the matrix, which translates into the manufacturing of uniform composites. Furthermore, the improvement of the interfacial interactions particles-polymer would enhance the stress-transfer from the polymer to the filler throughout the composites. In addition, the ideal co-crystallization of the polyolefin block exposing out of the BNNS/GNP particles with the polymer matrix would facilitate the growth of crystalline domains around the filler platelets, which could improve the thermal conduction ([43] and references therein).

The customization of the BNNS/GNP properties (particularly the surface chemistry) would lead to the manufacturing of a variety of masterbatches not limited to the polyolefins. It

would be interesting to manufacture BNNS/GNP prepared with block-copolymer surfactants showing the aromatic units alternated by polyether, polyester or polyamide blocks. The as prepared BNNS/GNP could be ideally embedded in a whole set of thermoplastics including polyamides (PA6, PA6,6, PA11), polyesters (PET, PBT, PCL), polyetherketons (PEH, PEEK). In those case, the interactions between the surfactants and the matrix would probably occur by hydrogen-bonds and/or polar-polar interactions [73-76].

The interactions between the polymer matrix and the filler particles through the surfactant could facilitate the control over the alignment and orientation of the filler particles into a 3D network, ideally acting as thermal (or electrical, GNP) conductive path. The electro-rheology results explained in this chapter revealed that the application of electrical stimuli could align the polarizable particles of Y-BNNS-L in HDPE with the possibility to reversibly control the rheology of the HDPE+Y-BNNS-L composites. The use of surfactants linking polymer chains and BNNS together could favour the control over the orientation of the BNNS in the HDPE, which could be useful in the production of masterbatches for soft-electronics were the 3D network of BNNS in the matrix is triggered on-demand.

The manufacturing of masterbatches of thermoplastics with BNNS/GNP is not exempt from challenges. A masterbatch contains high amounts of nanoparticles, thus, entailing concerns on the health and safety. To minimize the handling of nanoparticles, it would be interesting to use BNNS/GNP as concentrated-water dispersions, to be added in the polymer matrix during extrusion. With the use of BNNS/GNP-concentrated water dispersions there would be no need to handle the solid nanoparticles during the manufacturing of the masterbatches [77]. Furthermore, the solvent used during the HPH by TS is water. The preparation of BNNS/GNP-concentrated water dispersions would limit the evaporation step during the HPH, thus optimizing the exfoliation process. Certainly, different issues are related to the approach described. By way of example, the melt mixing of polymers at high temperatures in presence of water could degrade the matrix. To prevent this phenomenon, it may be helpful to use low melting temperature polymers (e.g. LDPE, PEG) and/or adding thermal/oxidising stabilisers in the BNNS/GNP-concentrated water dispersions.

The proposals of using block-copolymers to design the surface chemistry of TS BNNS/GNP are innovative and practical, yet a thorough study is required to investigate their role as surfactants/compatibilizer for composites of polymers with BNNS/GNP.

References

[1] Guerra V CW, Sloan J, Degirmenci V, Presvytis D, McNally T 2018 *Nanoscale* **10** 19469-77.

[2] Nazarov AS, Demin VN, Grayfer ED, Bulavchenko AI, Arymbaeva AT, Shin HJ, Choi JY, Fedorov VE 2012 *Chem. Asian J.* **7** 554-60.

[3] Kostoglou N, Polychronopoulou K, Rebholz C 2015 *Vacuum* **112** 42-5.

[4] Kostoglou N*, et al.* 2016 *Mater. Des.* **110** 540-8.

[5] Lesiak B, Stobinski L, Malolepszy A, Mazurkiewicz M, Kover L, Toth J 2014 *J. Electron. Spectrosc. Relat. Phenom.* **193** 92-9.

[6] Li YM, Tang LH, Li JH 2009 *Electrochem. Commun.* **11** 846-9.

[7] Jensen H, Pedersen JH, Jorgensen JE, Pedersen JS, Joensen KD, Iversen SB, Sogaard EG 2006 *Journal of Experimental Nanoscience* **1** 355-73.

[8] Sajjad M, Morell G, Feng P 2013 *ACS Appl. Mater. Interfaces* **5** 5051-6.

[9] Chubarov M, Pedersen H, Hogberg H, Filippov S, Engelbrecht JAA, O'Connel J, Henry A 2014 *Physica B Condens. Matter* **439** 29-34.

[10] Song L*, et al.* 2010 *Nano Lett.* **10** 3209-15.

[11] Dean JA. *Lange's Handbook of Chemistry*. fourteeth ed. New York: McGraw-Hill, Inc. 1999.

[12] Achour H, Achour A, Solaymani S, Islam M, Vizireanu S, Arman A, Ahmadpourian A, Dinescu G 2017 *Diamond Relat. Mater.* **77** 110-5.

[13] Liscio A, Kouroupis-Agalou K, Betriu XD, Kovtun A, Treossi E, Pugno NM, De Luca G, Giorgini L, Palermo V 2017 *2d Materials* **4**.

[14] Malard LM, Pimenta MA, Dresselhaus G, Dresselhaus MS 2009 *Physics Reports-Review Section of Physics Letters* **473** 51-87.

[15] Shimada T*, et al.* 2005 *Carbon* **43** 1049-54.

[16] Mafra DL, Samsonidze G, Malard LM, Elias DC, Brant JC, Plentz F, Alves ES, Pimenta MA 2007 *Phys. Rev* **76** 233407/1-4.

[17] Allen MJ, Tung VC, Kaner RB 2010 *Chem. Rev.* **110** 132-45.

[18] Greczynski G, Hultman L 2020 *Prog. Mater Sci.* **107**.

[19] Stobinski L, Lesiak B, Malolepszy A, Mazurkiewicz M, Mierzwa B, Zemek J, Jiricek P, Bieloshapka I 2014 *J. Electron. Spectrosc. Relat. Phenom.* **195** 145-54.

[20] Shtein M, Nadiv R, Buzaglo M, Kahil K, Regev O 2015 *Chem. Mater.* **27** 2100-6.

[21] Guerra V, Wan CY, Degirmenci V, Sloan J, Presvytis D, Watson M, McNally T 2019 *J. Mater. Chem. C* **7** 6383-90.

[22] Varga J 2002 *J Macromol Sci Polymer B* **B41** 1121-71.

[23] Papageorgiou DG, Chrissafis K, Bikiaris DN 2015 *Polym Rev* **55** 596-629.

[24] Yang HS, Kiziltas A, Gardner DJ 2013 *J. Therm. Anal. Calorim.* **113** 673-82.

[25] Cho D, Zhou HJ, Cho Y, Audus D, Joo YL 2010 *Polymer* **51** 6005-12.

[26] Kalaitzidou K, Fukushima H, Askeland P, Drzal LT 2008 *J Mater Sci* **43** 2895-907.

[27] Guerra V, Wan C, McNally T 2019 *Journal of Composites Science* **3** 38.

[28] Kolanthai E, Bose S, Bhagyashree KS, Bhat SV, Asokan K, Kanjilal D, Chatterjee K 2015 *PCCP* **17** 22900-10.

[29] Lin YJ, Du WC, Tu DM, Zhong W, Du QG 2005 *Polym. Int.* **54** 465-70.

[30] Jose S, Aprem AS, Francis B, Chandy MC, Werner P, Alstaedt V, Thomas S 2004 *Eur. Polym. J.* **40** 2105-15.

[31] Preobrajenski AB, Ng ML, Vinogradov AS, Martensson N 2008 *Phys Rev B* **78** 073401/1-4.

[32] Preobrajenski AB, Ng ML, Vinogradov AS, Martensson N 2008 *Phys. Rev* **78**.

[33] Li T, Zhang Z 2010 *Journal of Physics D-Applied Physics* **43**.

[34] Stankovich S, Dikin DA, Dommett GHB, Kohlhaas KM, Zimney EJ, Stach EA, Piner RD, Nguyen ST, Ruoff RS 2006 *Nature* **442** 282-6.

[35] Suplicz A, Szabo F, Kovacs JG 2013 *Thermochim. Acta* **574** 145-50.

[36] Chin SJ, Vempati S, Dawson P, Knite M, Linarts A, Ozols K, McNally T 2015 *Polymer* **58** 209-21.

[37] Liang JZ, Du Q, Tsui GCP, Tang CY 2016 *Compos Part B Eng* **95** 166-71.

[38] Gietl H, Riesch J, Coenen JW, Hoschen T, Linsmeier C, Neu R 2017 *Fusion Eng. Des.* **124** 396-400.

[39] da Silva ALN, Rocha MCG, Moraes MAR, Valente CAR, Coutinho FMB 2002 *Polym. Test.* **21** 57-60.

[40] Qiu F, Hao YB, Li XY, Wang B, Wang M 2015 *Compos Part B Eng* **71** 175-83.

[41] Valles C, Abdelkader AM, Young RJ, Kinloch IA 2014 *Faraday Discuss.* **173** 379-90.

[42] Ahmad SR, Xue CZ, Young RJ 2017 *Materials Science and Engineering B-Advanced Functional Solid-State Materials* **216** 2-9.

[43] Guerra V, Wan CY, McNally T 2019 *Prog. Mater Sci.* **100** 170-86.

[44] Tajaddod N, Song K, Green EC, Zhang YY, Minus ML 2016 *Macromolecular Materials and Engineering* **301** 315-27.

[45] Dai J, Shen Y, Yang JH, Huang T, Zhang N, Wang Y 2014 *Colloid. Polym. Sci.* **292** 923-33.

[46] Juhasz P, Varga J, Belina K, Belina G 2002 *J Macromol Sci B* **B41** 1173-89.

[47] Pop E, Varshney V, Roy AK 2012 *MRS Bull.* **37** 1273-81.

[48] Potschke P, Abdel-Goad M, Alig I, Dudkin S, Lellinger D 2004 *Polymer* **45** 8863-70.

[49] Meincke O, Kaempfer D, Weickmann H, Friedrich C, Vathauer M, Warth H 2004 *Polymer* **45** 739-48.

[50] Heldele R, Rath S, Merz L, Butzbach R, Hagelstein M, Hausselt J 2006 *Nuclear Instruments & Methods in Physics Research Section B-Beam Interactions with Materials and Atoms* **246** 211-6.

[51] Phillips RJ, Armstrong RC, Brown RA, Graham AL, Abbott JR 1992 *Physics of Fluids a-Fluid Dynamics* **4** 30-40.

[52] D. Leighton AA 1987 *J. Fluid Mech.* **181** 415.

[53] Leighton D, Acrivos A 1987 *J. Fluid Mech.* **177** 109-31.

[54] Mills P, Snabre P 1995 *J. Phys. II* **5** 1597-608.

[55] Yamate T, Fujiwara T, Yamaguchi T, Suzuki H, Akazome M 2018 *Polymer Chemistry* **9**.

[56] Yi QF, Wen XF, Dong JY, Han CC 2008 *Polymer* **49** 5053-63.

[57] Eder M, Wlochowicz A 1983 *Polymer* **24** 1593-5.

[58] Choi HJ, Jhon MS 2009 *Soft Matter* **5** 1562-7.

[59] Block H, Kelly JP 1988 *Journal of Physics D-Applied Physics* **21** 1661-77.

[60] Akhavan J 2007 *Proceedings of the Institution of Mechanical Engineers Part G-Journal of Aerospace Engineering* **221** 577-87.

[61] Deinega YF, Vinogradov GV 1984 *Rheol. Acta* **23** 636-51.

[62] Lee S, Yoon CM, Hong JY, Jang J 2014 *J. Mater. Chem. C* **2** 6010-6.

[63] Dong YZ, Kwon SH, Choi HJ, Puthiaraj P, Ahn WS 2018 *Acs Omega* **3** 17246-53.

[64] Li ZL, Young RJ, Wilson NR, Kinloch IA, Valles C, Li Z 2016 *Compos. Sci. Technol.* **123** 125-33.

[65] Shah RK, Paul DR 2004 *Polymer* **45** 2991-3000.

[66] Pokharel P, Lee DS 2014 *Chem. Eng. J.* **253** 356-65.

[67] Simon DA*, et al.* 2017 *Mater. Des.* **134** 103-10.

[68] . Cea. POLYMER -G RAPHENE NANOCOMPOSITES. 2017;9 , 790 , 334 B2.

[69] Zhuo Q, et al. Thermally Conductive Thermoplastic. 2000;6,162,849

[70] Cherukuvada S, Kaur R, Row TNG 2016 *Crystengcomm* **18** 8528-55.

[71] Fonseca CA, Harrison IR 1998 *Thermochim. Acta* **313** 37-41.

[72] Cho KW, Li FK, Choi J 1999 *Polymer* **40** 1719-29.

[73] Hsieh TT, Tiu C, Simon GP 2001 *Polymer* **42** 1931-9.

[74] Moacanin J CE 1966 *Journal of Polymer Science Part C: Polymer Symposia* **14** 313-22.

[75] Lu XJ, Wang YS, Wu XW 1994 *Polymer* **35** 2315-20.

[76] Zagar E, Grdadolnik J 2003 *J. Mol. Struct.* **658** 143-52.

[77] Cv G. Method Of Making Masterbatches Of Liquid Additives And, In Particular, Antimicrobial. 2001;Us 6,284,814 B1.

CHAPTER 5: CONCLUSIONS AND FUTURE PERSPECTIVES

Composites of thermoplastic polymers with boron nitride nanosheets (BNNS) and exfoliated graphite nanoplatelets (GNP) are increasingly sought after as, light, functional and sustainable materials for exploitation in a variety of applications including automotive, aerospace, electronics and energy.

The addition of BNNS and GNP (fillers) into polymers can enhance the properties of the polymer matrix (*e.g.* thermal, electrical (GNP only), mechanical, and rheological) if effective dispersion and distribution of the filler in the polymer phase is attained and interfacial interactions between BNNS/GNP platelets and the polymer realized. Indeed, when the BNNS and GNP are uniformly distributed and dispersed in the polymer matrix, ideally as a 3D interconnected particle-particle network and the interfacial energy with the polymer chains is minimized, it is possible to improve significantly the thermal and electrical conductivity and mechanical properties of the polymer matrix of interest. Yet, there is little literature available on the manufacturing of thermoplastic-based composites with BNNS/GNP using industrial relevant manufacturing technologies, *e.g.* extrusion and injection moulding, limiting the exploitation of these functional composites on a large scale.

In this thesis, composites of isotactic polypropylene (PP) and high-density polyethylene (HDPE) with BNNS and GNP were manufactured by melt-mixing and the morphology, crystalline structure, rheological and mechanical properties of the resultant composites studied using a range of techniques. The nano-fillers were provided by the industrial partner Thomas Swan & Co. Ltd (TS) and prepared using a proprietary high pressure homogenisation process (HPH, Chapter 1). Various grades of BNNS and GNP were utilised, which differed from each other depending on the type of bulk starting materials (hexagonal boron nitride for the BNNS grades and graphite for the GNP grades) and the surfactant used during HPH. It was found that the morphology of the bulk starting materials defined the geometry of the exfoliated BNNS and GNP whereas the solvent (water) and the surfactants fed into the HPH process determined the surface chemistry of the fillers. The BNNS and GNP studied had flake-like morphology characterized by a distribution of irregular-shaped platelets with lateral dimensions ranging from 100-200 nanometre (nm) up to 10 micrometre (µm). The BNNS and GNP obtained were highly crystalline with a low defect concentration in the crystal lattice. Some functionalities (oxidised groups) were detected on the surface of the platelets, in part derived from the surfactants present in trace amounts on the surface of the platelets, which imparted hydrophilic

characteristics to the nanoparticles. The BNNS and GNP grades were stable under oxidative conditions up to 300-400°C.

The 16mm co-rotating twin-screws extruder and micro-injection moulding (Chapter 3) processes adopted to manufacture the composites of PP and HDPE with the BNNS and GNP at loadings up to 10 wt% allowed for the preparation of composite materials with different levels of filler particles dispersion and distribution. Some aggregation of the BNNS/GNP flakes occurred upon mixing as a result of strong particle-particle interactions preferred over the particle-polymer interactions. The presence of oxygen containing groups on the surface of the nanoparticles along with traces of surfactant (*i.e.* sodium cholate (SC), T and L) played a key role in determining the state of BNNS/GNP dispersion and distribution in PP. Specifically, it was found that when the surfactant T was present on the surface of X-BNNS-T it was less effective. This behaviour was associated with the different chemical structures of the three surfactants, which in turn determined the mechanism of interactions with the host polymer. It was proposed that the cyclo-hexane rings of the SC interacted with the non-polar PP, whereas the polyether-polyol backbone of surfactant T promoted particle-particle interactions, resulting in agglomeration of X-BNNS-T upon mixing with PP. The backbone of surfactant L has also a polyether-polyol structure, yet it appeared that the Y-BNNS-L was better distributed and dispersed in PP than was observed for X-BNNS-T. The reason was ascribed to the different head structures of the surfactants T and L. Both surfactants are amphiphilic with aromatic heads, yet the aromatic ring in T contains branched functional groups whereas the aromatic head of L does not contain such functionality. The surfactant L could "flip" as Y-BNNS-L was added to PP, thus exposing the aromatic head to PP, which could promote non-polar interactions with the polymer chains - most likely between the π-conjugated system of the aromatic head of L and the CH_2 groups of PP - therefore, facilitating the distribution and perhaps some dispersion of Y-BNNS-L in PP. On the other hand, the branched functionalities on the aromatic head of T make "flipping" less probable, therefore it is more likely that the surfactant exposed the polyether-polyol tail when admixing X-BNNS-T into PP, thus aggregation of the nanoparticles is more likely.

The inclusion of SC assisted the distribution and perhaps dispersion of X-GNP-SC in PP more than the surfactant L (X-GNP-L/Y-GNP-L). It was proposed that for surfactant L the polyether-polyol tails are exposed to the GNP platelets while attempting to "flip" upon inclusion in PP. However, the relatively stable GNP aromatic structure repulsed the polyether-polyol tail of surfactant L, thus making "flipping" less probable. As a consequence, the polyether-polyol tails of L exposed to PP and resulted in filler agglomeration.

The interactions between BNNS/GNP and PP, perhaps through the surfactant, the extent of filler distribution and dispersion in the polymer - in part related to the mixing efficiency during extrusion, the melt flow during injection moulding, filler-polymer interactions and the lateral dimensions of the platelets - altered the polymorphism and nucleation behaviour of PP. It was found that at low filler content ($\leq$ 0.5wt%) the inclusion of X-BNNS-SC and X-BNNS-Y favoured β-PP crystallization more than X-BNNS-T, perhaps as a result of the limited interactions between X-BNNS-T and PP. At higher filler content ($\geq$ 0.5wt%), the combination of filler agglomeration and lateral size, particularly for the large platelets of Y-BNNS-L (up to 10 µm), hindered polymer chain dynamics and thus the crystallization of β-PP (XRD).

The addition of X-GNP-SC, X-GNP-L and Y-GNP-L promoted the β-crystallization of PP, yet X-GNP-SC appeared to facilitate the crystallization of β-PP more than X-GNP-L and Y-GNP-L. Again, the reason of this discrepancy was associated to the more effective interactions between PP and X-GNP-SC- probably due to the surfactant SC- compared to X-GNP-L and Y-GNP-L (XRD).

The BNNS/GNP particles acted as nucleating agents in PP, manifested by an increase in the crystallization temperature T_c up to 10-15˚C compared to PP as determined by DSC. This aspect is helpful in perspective of manufacturing composites of PP with BNNS/GNP on large scale, since the increase of T_c could result into a reduction of the injection moulding cycle (less energy consumption, *i.e.* more sustainable process).

The lateral dimensions of the filler particles in combination with effective mixing determine if percolation, *i.e.* formation of an interconnected 3D particle-particle network in the PP matrix, occurs. The addition of 5wt% Y-BNNS-L (lateral size up to 10 µm) in PP did achieve rheological percolation. However, the formation of a 3D network of filler particles in the polymer does not translate to an increase in composite thermal conductivity. Indeed, orientation of filler particles as well as interfacial interactions with the polymer played a role in obtaining limited increases in thermal conduction. Specifically, the random distribution and/or large thermally resistant interfaces cause phonon scattering and lower the thermal conductivity (TC). For that reason, no improvement in the TC was detected when comparing the composites PP+Y-BNNS-L with the polymer alone.

The state of distribution and dispersion of the filler particles in PP, the intrinsic rigidity of the BNNS/GNP and the change of the polymorphism of PP upon inclusion of the fillers examined determined the mechanical properties of the prepared composites. The addition of X-BNNS-SC, Y-BNNS-L and X-GNP-SC in PP determined an increase in the Young's modulus of PP

by 20%, whereas a decrease in the Young's modulus of PP by *ca* 20% was registered when X-BNNS-T, X-GNP-L and Y-GNP-L were added in PP.

The viscosity and crystallization mechanisms of the polymer matrix also play a fundamental role in the distribution and dispersion of the nanoparticles upon mixing. The high melt viscosity and the rapid crystallization kinetics of HDPE probably caused the exclusion and agglomeration of the filler particles as the polymer crystallized during injection moulding. The exclusion of the filler particles into aggregates upon crystallization of HDPE did not change the crystalline content and polymorphism of HDPE - as determined by XRD - but affected the mechanical properties of the final composites. Indeed, a decrease of *ca* 20% of the Young's modulus of HDPE upon inclusion of the X-BNNS-SC and X-GNP-SC was registered. The exclusion and the agglomerations of the filler particles in HDPE also obstructed the rheological percolation. However, it was proved that the addition of a filler with large platelets- such as the Y-BNNS-L (lateral size up to 10 μm) - and the application of electrical impulses could promote the rheological percolation, as noticed by the electro-rheology measurements. Probably, the application of an external electrical field aligned the large Y-BNNS-L particles in the molten HDPE, thus favouring the particle-particle and/or particle-polymer connectivity.

5.1- Experimental proposal for future study

The outputs and 'know-how' acquired during the work described in this thesis has supported TS in their understanding on the requirements for effective dispersion and distribution of their 2D materials in polymers. In particular, the effect of BNNS/GNP addition on the morphology, rheology, and mechanical properties of PP and HDPE is now better understood.

In order to achieve optimum property enhancements of the polymer matrix of interest on addition of BNNS or GNP, future work should address the following aspects:

i. The mechanism(s) of interaction between SC, T, L, and other surfactants present in traces amounts in BNNS/GNP with the PP require further study. For that purpose, solid state ^{13}C Nuclear Magnetic Resonance (^{13}C NMR) and Electron Energy Loss spectroscopy (EELS) could be used.

ii. The state of nano-filler dispersion and distribution in PP and HDPE during melt mixing, particularly during injection moulding. For that purpose, capillary rheology (high shear) coupled with a modelling study on the melt flow of the composites during injection

moulding could help inform the mechanism of distribution and dispersion of BNNS/GNP in the polymer matrix.

iii. Polymorphism and crystallization behaviour of PP upon inclusion of BNNS or GNP by using simultaneous Wide-Angle X-Ray Scattering (WAXS) to Small-Angle X-Ray Scattering (SAXS), Modulated Differential Scanning Calorimetry (DSC) and polarized hot-stage optical microscopy under both isothermal and non-isothermal conditions. The aim is to understand the way the PP chains arrange, nucleate and crystallize near or on the BNNS/GNP particles, thus determining the crystalline structures, which affect the properties of the final composites *e.g.* mechanical, thermal and electrical (GNP composites only) properties.

iv. Kinetics of HDPE crystallization in the presence of BNNS/GNP by DSC and optical microscopy. It would be interesting to explore methods to slow the kinetics of crystallization of HDPE. By way of example, the introduction of co-monomer units of PP in the HDPE backbone could delay crystallization.

v. Study composites of BNNS/GNP with more polar polymers than PP and HDPE, *e.g.* PET, PA6, PA11, to assess the effect of the surfactants (SC, T, L) on filler dispersion in alternative polymers.

vi. The addition of processing aids during melt-mixing to vary the melt viscosity of HDPE or PP thus varying the shear stresses acting on the 2D materials during melt mixing. By way of example, it would be interesting to synthetize *ad-hoc* block copolymers with monomers of polyether-polyol alternated to monomers of i-PP. By doing so, the polyether-polyol segments would interact with the tails of the surfactant T and L by polar-polar interactions, whereas the i-PP segment would interact with the PP matrix - ideally co-crystallize - thus promoting the interfacial interactions between the X-BNNS-T, Y-BNNS-L, X-GNP-L, Y-GNP-L with PP. The optimization of the interfacial bonds between the filler particles and PP would improve dispersion and the stress-transfer between filler and polymer.

vii. Optimization of the extrusion process. It would be interesting for future work to perform a systematic study on the extrusion process to obtain the optimal conditions for the manufacturing of composites of PP/HDPE with BNNS/GNP, including varying the screw configuration, screw speed, temperature profiles and feeding protocol. It is been reported in the literature that the narrower the width of the kneading elements, the more efficient the distributive mixing, whereas the wider the kneading mixing elements the better the dispersive mixing. Therefore, a combination of kneading elements of

different widths could optimise the state of BNNS/GNP dispersion and distribution in the polymer, without degrading the lateral dimensions of the platelets. The screw speed determines the residence time of the material in the extruder. If the screw speed is too high, the composite being processed may not have enough time to be evenly mixed. If the polymer is shear sensitive, then degradation may occur. Therefore, for a given screw configuration and temperature profile, a numerical/modelling analysis could predict the optimal screw speed to maximise output of a uniform mixed composite material. It would be also interesting to observe the effect of higher L/D ratios on the state of filler distribution and dispersion (L/D=40 for the extruder used in this work). It is been reported in the literature that high L/D ratios (longer flight length) generate more shear heat with increased residence time, which could improve the homogeneity of the composites.

The optimization of the temperature profile could be attained through a "progressive temperature set-up" study. This approach consists of leaving the temperature profiles as set in Chapter 3 but changing the temperature of one zone of the extruder at a time (*e.g.* in increments/decrement of 10°C), starting from the zone 1. The output is then measured and the optimal temperature per each zone would be that resulting in maximum output. The feeding protocol can also play a crucial role in optimising the extrusion process. Volumetric feeders guarantee better control and avoid the build-up of material at the extruder feeding zone. However, when mixing powders of different dimensions and density (*i.e.* polymer and filler powders), the composition inside the feeder may be non-uniform as the feeder feeds the extruder. One possible solution to this problem is the insertion of a screw inside the feeder coupled to an external ultrasonic vibrating plate, which constantly mixes the powder along and across the feeder from the upper side to the throat of the extruder.

Critically, the optimization of the extrusion process needs to be coupled with the optimization of the injection moulding process (see point ii) in order to improve the entire processability of the composites.

APPENDIX

PART I

AI.I- Additional experimental results of TS BNNS and GNP grades characterization

X-ray photoemission spectroscopy (XPS) survey spectra of TS BNNS and GNP
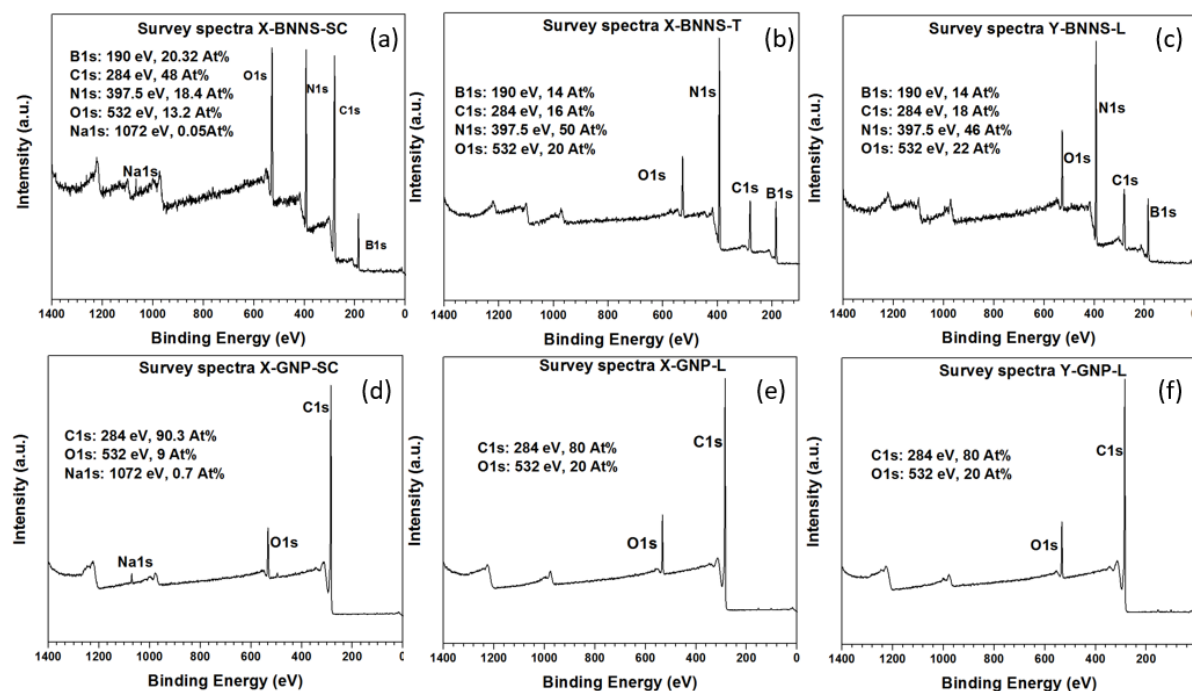
Appendix 1: XPS survey spectra of X-BNNS-SC (a)), X-BNNS-T (b)), Y-BNNS-L (c)), X-GNP-SC (d)), X-GNP-L (e)), Y-GNP-L (f)). The Binding Energy and the Atomic percentage (At%) of each atom detected are also reported.

Thermo-gravimetric analysis (TGA) graphs of TS BNNS and GNP grades
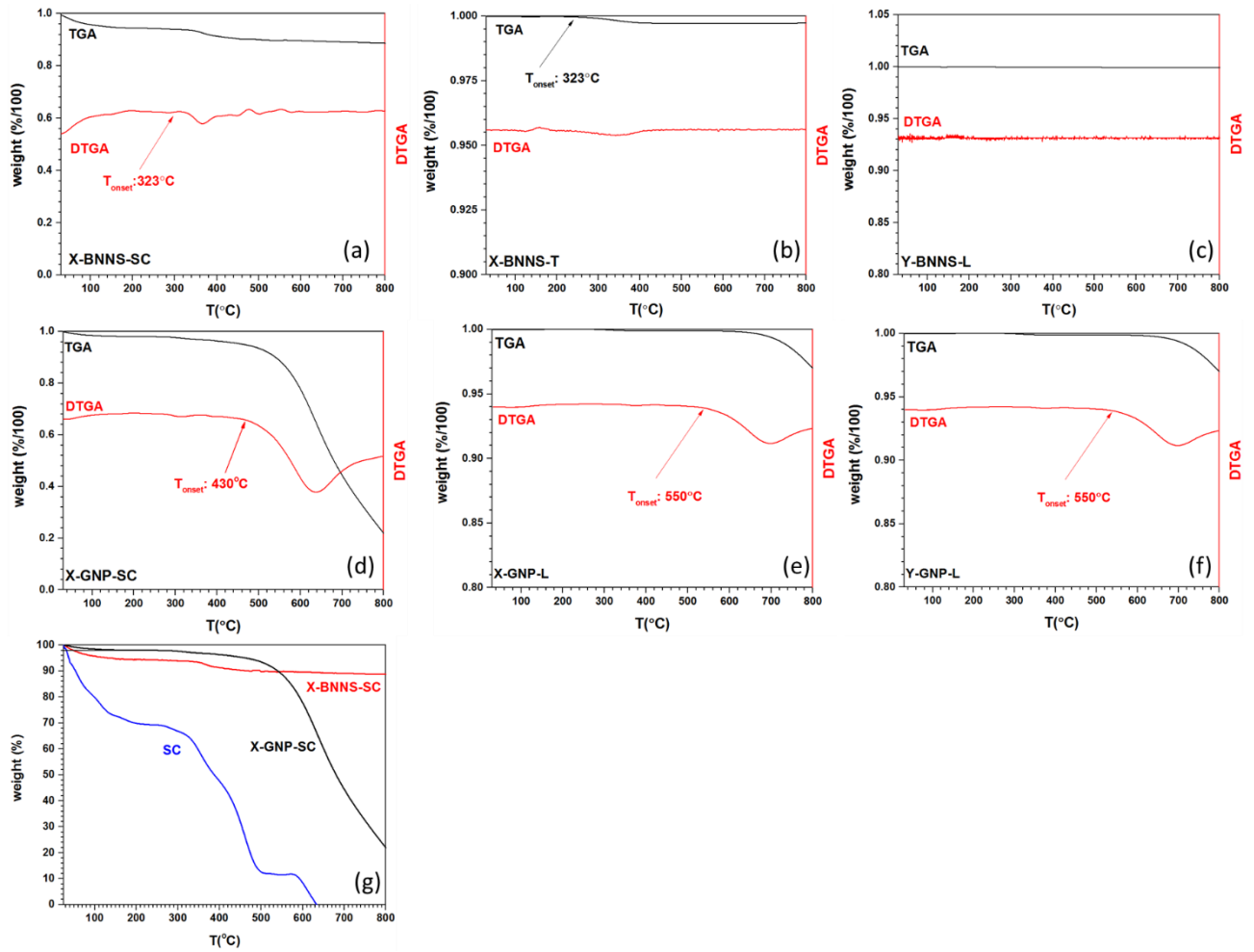
Appendix 2: weight (%/100) and 1st derivative of weight (DTGA) profiles in function of the temperature (T(°C)) for X-BNNS-SC (a)), X-BNNS-T (b)), Y-BNNS-L(c)), X-GNP-SC (d)), X-GNP-L (e)), Y-GNP-L (f)). The temperature of onset-degradation (T$_{onset}$) are also indicated. (g) depicts the TGA curves of the surfactant SC along with the TGA curves of the X-BNNS-SC and X-GNP-SC.

AI.II- Rheological profiles of composites of HDPE with Y-BNNS-L by oscillatory rheology
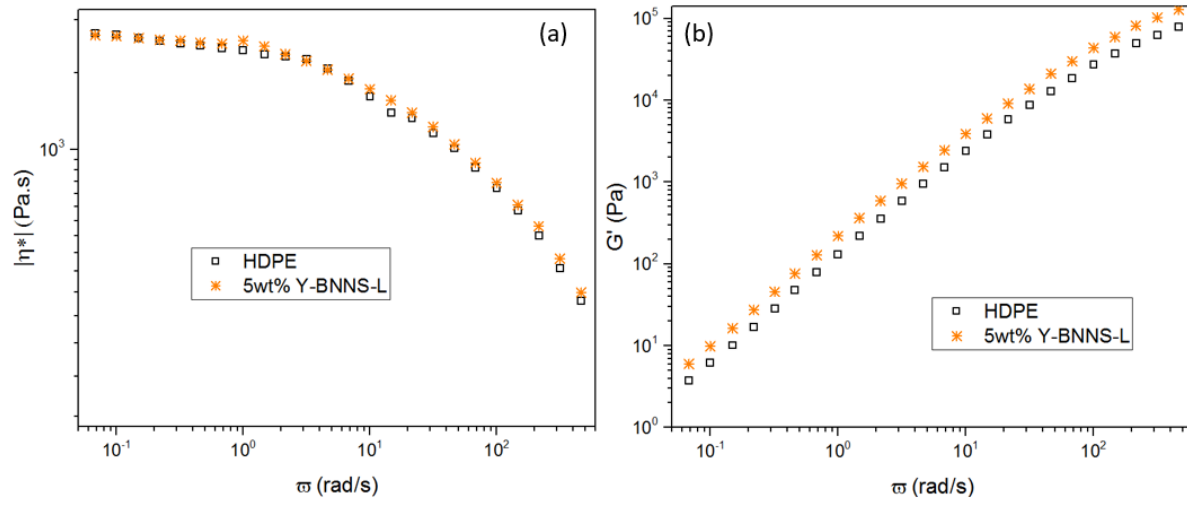
Appendix 3: Complex viscosity ($|\eta^*|$) and Storage modulus (G′) in function of the angular frequency (ω) for the HDPE and its composites with Y-BNNS-L (5wt%).

PART II

AII.I- Published and submitted papers

V. Guerra, C. Wan, T. McNally, Thermal conductivity of 2D nano-structured boron nitride (BN) and its composites with polymers, Progress in Material Science, 2019, 100, 170-186. https://doi.org/10.1016/j.pmatsci.2018.10.002

V. Guerra, C. Wan, J. Sloan, V. Degirmenci, D. Presvytis, T. McNally, 2D Boron Nitride Nanosheets (BNNS) Prepared by High-Pressure-Homogenisation: Structure and Morphology, Nanoscale, 2018, 10, 19469-19477. https://doi.org/10.1039/c8nr06429f

V. Guerra, C. Wan, J. Sloan, V. Degirmenci, D. Presvytis, T. McNally, Characterisation of graphite nanoplatelets (GNP) prepared at scale by high-pressure homogenisation, Journal of Material Chemistry C, 2019, 7, 6383-6390. https://doi.org/10.1039/c9tc01361fj

V. Guerra, C. Wan, T. McNally, Nucleation of the β-polymorph in Composites of Poly(propylene) and Graphene Nanoplatelets, Journal of Composites Science, 2019, 3, 2-11 https://doi.org/10.3390/jcsc3020038

V. Guerra, C. Wan, T. McNally, Fused Deposition Modelling (FDM) of Composites of graphene Nanoplatelets (GNP) and polymers for high thermal conductivity: a mini-review, Functional Composites Materials, 2020, 1, 1-11. https://doi.org/10.1186/s42252-020-00005-x

V. Guerra, T. McNally, Surface Cleaning of 2D Materials: Boron Nitride Nanosheets (BNNS) and Exfoliated Graphite Nanoplatelets (GNP). Submitted to Advanced Materials Interfaces.

AII.II- Conferences presentation

WMG PhD/EngD annual conference, University of Warwick, 30th June 2017, Poster title: Composites Of Poly(Propylene) (PP) With Boron Nitride Nanosheets (BNNS) For Innovative Electronic Devices. Authors: **V. Guerra**, C. Wan, T. McNally.

SMMCDT EngD annual conference, University of Warwick, 20th March 2018. Poster title: Composites Of Poly(Propylene) (PP) With Boron Nitride Nanosheets (BNNS) For high thermal conductive materials. Authors: **V. Guerra**, C. Wan, T. McNally

CNPComp Conference in London, Queen Mary University, 16-19 July 2019. Presentation title: Characterisation of Graphene Nanoplatelets (GNP) Prepared by High Pressure Homogenisation: Structure and Morphology. Authors: **V. Guerra**, C. Wan, T. McNally

37th Australasian conference, Australia, Queensland, Sunshine Coast, Novotel Twin Waters, 10-13 November 2019. Presentation title: Rheological Percolation in Composites of Boron Nitride Nanosheets (BNNS) and polypropylene (PP). Authors: **V. Guerra**, C. Wan, T. McNally.
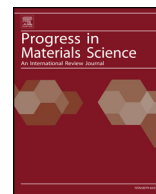
Thermal conductivity of 2D nano-structured boron nitride (BN) and its composites with polymers

Valentina Guerra, Chaoying Wan, Tony McNally[*]

International Institute for Nanocomposite Manufacturing (IINM), WMG, University of Warwick, CV4 7AL, UK

ABSTRACT

High thermal conductivity, structural stability, good mechanical and anti-oxidant properties makes hexagonal boron nitride (h-BN) a promising functional filler for polymers to produce composite materials where excellent thermal management is required, such as in electronic devices. Theoretical studies have revealed that two dimensional (2D) BN has higher thermal conductivity (up to 400 $Wm^{-1} K^{-1}$, in-plane) than bulk h-BN due to a reduction in phonon-phonon scattering when scaling down the thickness of the material. For this reason, 2D boron nitride nanosheets (BNNS) are gaining intense interest since they could be utilised in the design of composite materials with excellent efficiency to dissipate heat. Various methods have been explored to produce 2D BNNS including mechanical and chemical exfoliation of pristine bulk BN, chemical reaction, chemical vapour deposition (CVD) and electron irradiation. To facilitate the dispersion of BNNS in polymers, different functionalization strategies have been applied for surface-treatment of BNNS. In this review, the different synthesis approaches adopted for BNNS are compared and the effects of BNNS dispersion on the thermal conduction of polymers are discussed. The factors influencing the mechanism of thermal conduction such as materials crystallinity, filler geometry, filler surface functionalization and alignment, filler/matrix interface and processing conditions are discussed. Some perspectives and future directions on how to generate high thermally conductive composites of BNNS and polymer are proposed.

---

[*] Corresponding author.
E-mail address: ███████████████ (T. McNally).

2D boron nitride nanosheets (BNNS) prepared by high-pressure homogenisation: structure and morphology

Valentina Guerra,[a] Chaoying Wan, [ID][a] Volkan Degirmenci, [ID][b] Jeremy Sloan, [ID][c] Dimitris Presvytis[d] and Tony McNally [ID] *[a]

2D Boron Nitride Nano-sheets (BNNS) were prepared using a high-pressure homogenisation process to exfoliate bulk hexagonal boron nitride (h-BN). The effectiveness of this process was studied by characterising bulk h-BN and BNNS post-processing using numerous techniques. The BNNS produced was composed of a mixture of sheets having lengths on the nanometre (nm) scale, but lateral thicknesses on the micron (μm) length scale. The product was a macro-porous material containing slit-like pores with a surface area of 170 $m^2 g^{-1}$. It had a polycrystalline structure with d_{002} = 0.335 nm and L_{002} = 2 nm. From the sharp E_{2g} peak in the Raman spectrum at 1360 cm^{-1} (FWHM = 12.5 cm^{-1}), the sheets had a low defect density and were highly exfoliated. X-Ray photoelectron spectroscopy (XPS) studies detected B−OH and N−H groups on the BNNS surface and the presence of residual surfactant. Contact angle measurements (60° ± 3° (0 s); 40° ± 2° (10 s)) confirmed a hydrophilic surface. The BNNS was thermally stable under oxidative conditions up to 323 °C.

[a]*International Institute for Nanocomposite Manufacturing (IINM), WMG, University of Warwick, CV4 7AL, UK. E-mail:*
[b]*School of Engineering, University of Warwick, CV4 7AL, UK*
[c]*Department of Physics, University of Warwick, CV4 7AL, UK*
[d]*Thomas Swan & Co. Ltd, Consett, County Durham, DH87ND, UK*

Check for updates

Characterisation of graphite nanoplatelets (GNP) prepared at scale by high-pressure homogenisation

Valentina Guerra,[a] Chaoying Wan, [ID][a] Volkan Degirmenci, [ID][b] Jeremy Sloan,[c] Dimitris Presvytis,[d] Michael Watson[d] and Tony McNally [ID] ⋆[a]

Graphite nanoplatelets (GNP) were prepared by a high-pressure homogenisation process (HPHP) *via* exfoliation of bulk graphite, yielding GNP in the form of square shaped platelets with lateral dimensions on the micrometre (μm) scale and thicknesses on the nanometre (nm) scale (<200 nm). The platelets have a polycrystalline structure with d_{002} = 0.335 nm and L_{002} = 2 nm, with a low crystalline defect concentration confirmed by weak D and D′ bands in the Raman spectra. The shift in the G band from 1587 cm^{-1} (graphene) to 1580 cm^{-1} (GNP) and the asymmetric G′ band combined with a decrease in $I_{G'}/I_G$ from 0.45 for the bulk graphite to 0.40 for the GNP confirmed a partially exfoliated structure. X-ray photoelectron spectroscopy (XPS) confirmed the presence of impurities on the GNP surface due to the surfactant used during the exfoliation process. Contact angle measurements (67° ± 2° (0 s), 64° ± 2° (10 s)) suggested the surface of the GNP was hydrophilic. The as produced GNP is a macro-porous material with sheet-like particles having non-uniform shape and size and a BET surface area of *ca.* 94 m^2 g^{-1}. The GNP is thermally stable under oxidative conditions up to 430 °C. The HPHP process is readily scalable and provides a cost effective route for the production of GNP.

[a] *International Institute for Nanocomposite Manufacturing (IINM), WMG, UK.*
 E-mail: ▮▮▮▮▮▮▮; Tel: ▮▮▮▮▮▮
[b] *School of Engineering and, University of Warwick, CV4 7AL, UK*
[c] *Department of Physics, University of Warwick, CV4 7AL, UK*
[d] *Thomas Swan & Co. Ltd, Consett, County Durham, DH87ND, UK*

This journal is © The Royal Society of Chemistry 2019

J. Mater. Chem. C, 2019, **7**, 6383–6390 | 6383

Article

Nucleation of the β-polymorph in Composites of Poly(propylene) and Graphene Nanoplatelets

Valentina Guerra, Chaoying Wan[ID] and Tony McNally *

International Institute for Nanocomposites Manufacturing (IINM), WMG, University of Warwick,
Coventry CV4 7AL, UK; ▮▮▮▮▮▮▮▮▮▮▮▮▮ (V.G.); ▮▮▮▮▮▮▮▮▮▮▮▮▮▮ (C.W.)
* Correspondence: ▮▮▮▮▮▮▮▮▮▮; Tel.: ▮▮▮▮▮▮▮▮▮▮

check for updates

Abstract: The effects of graphene nanoplatelets (GNPs) on the nucleation of the β-polymorph of polypropylene (PP) were studied when melt-mixed at loadings of 0.1–5 wt % using a laboratory scale twin-screw (conical) extruder and a twin-screw (parallel) extruder with $L/D = 40$. At low GNP loadings (i.e., ≤0.3 wt %), the mixing efficiency of the extruder used correlated with the β-nucleating activity of GNPs for PP. GNP agglomeration at low loadings (<0.5 wt %) resulted in an increase in the β-phase fraction (K_β) of PP, as determined from X-ray diffraction measurements, up to 37% at 0.1 wt % GNPs for composites prepared using a laboratory scale twin-screw (conical) extruder. The level of GNP dispersion and distribution was better when the composites were prepared using a 16-mm twin-screw (parallel) extruder, giving a K_β increase of 24% upon addition of 0.1 wt % GNPs to PP. For GNP loadings >0.5 wt %, the level of GNP dispersion in PP did not influence the growth of β-crystals, where K_β reached a value of 24%, regardless of the type of extruder used. From differential scanning calorimetry (DSC) measurements, the addition of GNPs to PP increased the crystallization temperature (T_c) of PP by 14 °C and 10 °C for the laboratory scale extruder and 16-mm extruder, respectively, confirming the nucleation of PP by GNPs. The degree of crystallinity (X_c%) of PP increased slightly at low GNP additions (≤0.3 wt %), but then decreased with increasing GNP content.

Keywords: poly(propylene); graphene nanoplatelets (GNPs); nucleation; β-polymorph

1. Introduction

The microstructure of polymer polymorphs, in terms of crystalline content, crystallite type, and size (i.e., packing geometries) formed upon cooling, is widely influenced by processing conditions as well as the presence of additives [1]. Isotactic polypropylene (PP) (i-PP) is a polymorph thermoplastic polymer with chains arranged in a helical conformation. The polymorphism of i-PP is derived from the different crystalline geometries (unit cells) in which the helices pack, namely monoclinic (α), trigonal (β), and triclinic (γ). A metastable smectic (δ) phase consisting of helices with a highly disordered arrangement can be obtained by quenching molten i-PP below 0 °C [2,3]. The α-form is the most common and stable polymorphic phase of i-PP. However, with increasing requirements and demand for lightweight materials, there has been significant interest regarding the β-polymorph of i-PP, which has a higher impact strength and toughness than the α-polymorph of i-PP [4–6]. The mechanical properties of the β-form are associated with its peculiar broad lamellae morphology. The lamellae form coplanar stacks where the plane twists along the growth direction and the β-spherulites form exhibit 3D banded structure lamellae. A schematic of α and β crystals of PP is shown in Figure 1.
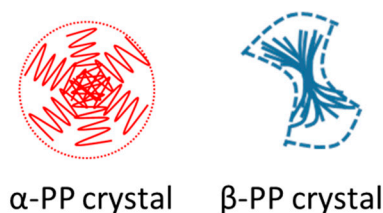
Figure 1. Schematic representation of α and β crystals of polypropylene (PP) showing a spherical and banded structure, respectively, as they would be seen under polarized light microscopy. The dotted lines contour the simulated PP chain to highlight their different arrangements in the two crystals.

As a load is applied on β-i-PP above the necking point, the banded lamellae start to separate and defold, undergoing a β- to α-phase transition. This leads to a slight increase in tensile stress (strain hardening), especially at low deformation rates. The necked specimen then deforms to break at relative high stress [7–10]. Furthermore, Jacoby et al. have reported that the coupling between the crystalline and amorphous regions in β-i-PP is weaker than in α-i-PP, thus enhancing the mechanical damping behavior of the β-form [11]. The combination of lamellae morphology, the β- to α-phase transition, and damping behavior make β-i-PP tougher than α-i-PP.

Several methodologies, including shear-induced crystallization [12–16], crystallization in a temperature field gradient, quenching from the melt, vibration-induced crystallization, ultraviolet (UV) irradiation, and the addition of specific nucleating agents have all been applied in the past years to produce β-i-PP ([10] and references therein). Previous studies have reported that the addition of 1D/2D nanomaterials to i-PP promote the nucleation and growth of β-spherulites, such as clay [17], octadecylamine-functionalized single-walled carbon nanotube (SWCNTs) [18], and graphite [19]: However, the effect of graphene nanoplatelets (GNPs) has been reported much less [3]. It has been reported that GNPs promote α-nucleating formation in PP composites prepared by twin-screw extrusion [3].

In this work, composites of i-PP and GNPs were prepared by melt mixing techniques (i.e., extrusion and injection molding) in order to study the effect of GNP addition as a β-nucleating agent for PP. We show a correlation between mixing, depending on extruder type, and the β-nucleating efficiency of GNP. As research efforts on functional composites with carbon additives continue to increase unabated for a range of diverse applications (e.g., automotive, electronics, tissue engineering) [20–23], it is essential to understand the effects of processing on the properties of the final composites. Therefore, this study aimed to correlate the effect of GNP addition on the crystallization behavior of PP and understand the role that the processing conditions employed in composite preparation play in inducing PP crystallization.

2. Materials and Methods

PP (material grade 1063L1, melt flow rate (MFR) = 8.0 g/10 min as reported in the data sheet provided by the supplier) was purchased from ExxonMobil, Baytown, TX, USA, and delivered in pellet form. GNP powder was kindly provided by Thomas Swan & Co. Ltd, Consett, UK, and had an average lateral size on the order of 10 μm and a thickness in the range of 100 nm to 200 nm.

The PP was cryo-milled to a powder in a freezer mill (SPEXSamplePrep) before being dry-mixed manually with the GNP powder. Composites of PP with GNPs up to 5 wt % were first prepared using a laboratory scale extruder (Thermo Scientific, HAAKE Lab, Waltham, MA, USA), which was fitted with twin conical screws (nonmodular, screw diameter = 5/14 mm (conical), screw length = 109.5 mm). Each composition post-melt mixing was fed directly to a microinjection molding machine (Thermo Scientific, Multijet Plus, Waltham, MA, USA) to prepare test specimens for characterization. Table 1 lists the processing conditions used to produce all samples.

Table 1. Laboratory scale microextruder and mini-injection molding processing conditions.

T (°C) Extrusion Barrel	Injection Molding *T* (°C)-Harvesting Cylinder	Injection Molding *T* (°C)-Mold Holder	Injection Pressure (bar)	Pressure after Injection (bar)	Time of Pressing (s)
175	190	50	600	200	5

The same compositions were also prepared using a 16-mm co-rotating parallel twin screw extruder (PRISM ThermoFischer Scientific), $L/D = 40$. The screws were fitted with feed screw (FS) 45/45 forward and mixing elements properly oriented to each other to guarantee optimal mixing conditions. In particular, the adopted screw configuration starting from the feeding zone to the die was as follows:

- 10 FS followed by 0–90°/4/12, 0°/4/12, and 90–0°/4/12 mixing elements, with respect to the last FS element offset;
- 6 FS elements followed by 0°/6/18 mixing elements;
- 9 FS elements followed by 0°/4/12, 0–90°/8/24 mixing elements;
- 7 FS elements to close the screws assembling.

The orientation of the mixing elements was based on the optimization of the highest mixing conditions (0–90°) with the lowest one (0°), as suggested by the manufacturer. The advantage of the parallel twin screw extruder over the conical one was its ability to modulate the screw configuration according to the desired properties.

The temperature profile used from the feed to the die end was set to 170 °C, 180 °C, 185 °C, 190 °C, 190 °C, 195 °C, 195 °C, 200 °C, 205 °C. The molten composite filament was drawn from the extruder, cooled in a water bath, and pelletized using a laboratory pelletizer. The pellets were collected and processed using the same microinjection molding machine and processing conditions, as per Table 1.

In both instances, disks 25 mm in diameter and 1.7 mm thick were prepared, and samples were taken from these discs for scanning electron microscopy (SEM), differential scanning calorimetry (DSC), and X-ray diffraction (XRD) measurements.

SEM imaging was carried out using a Zeiss Sigma field emission instrument, provided with a Gemini column. The images were recorded using an InLens detector, a working distance of 3.2 mm, and an acceleration voltage of 5 kV. The samples were cryo-fractured and placed on a carbon adhesive tape mounted on an aluminum SEM stub. Before testing, the samples were sputter-coated (10 nm) using a Pd/Pt metal target (Cressington 108 auto), provided with a thickness controller. The coating was applied to minimize charging on the surface of the sample due to the backscattering of the electron beam when hitting non-electrically conductive materials and under a weak argon atmosphere.

The crystalline structure of the samples was analyzed by wide-angle X-ray diffraction (WAXD), using a PANalytical Empyrean X-ray diffractometer. The instrument was equipped with a Co ($K_{\alpha 1}$ (λ) = 1.789 Å) source, a PIXcel3D detector, a tube voltage of 45 kV, and a current of 40 A. The tests were set in reflectance mode with a stage speed of 1 rps.

The thermal properties of all composites, including melting temperature (T_m), crystallization temperature (T_c), and degree of crystallinity (X_c), were measured by differential scanning calorimetry (DSC) using a Mettler Toledo DSC1. Two cycles were realized through heating from 25 °C to 200 °C at 10 °K/min and cooling to room temperature at 10 °K/min. The samples were held for 2 min at 200 °C before the cooling step and for 1 min at room temperature before the second heating cycle. The crystallinity fraction (X_c) was calculated according to the following equation:

$$X_c(\%) = \frac{\varphi_{PP} \cdot \Delta H_c}{\Delta H_{c,\infty}}, \tag{1}$$

where φ_{PP} is the mass fraction of PP in the mixture, ΔH_c is the enthalpy of crystallization during the first cooling, and $\Delta H_{c,\infty}$ is the enthalpy of crystallization of a theoretical PP crystal of infinite dimensions (207.1 J/g, [24]).

3. Results and Discussion

Figure 2 shows representative SEM images of the composite of PP with 5 wt % of GNPs prepared with a laboratory scale extruder (Figure 2a–c) and the 16-mm extruder (Figure 2d–f). The differently designed extruders imparted different levels of shear stress on the composites during melt mixing, resulting in different levels of GNP dispersion and distribution per unit volume of PP matrix. This contributed to the nucleation efficiency of GNPs for PP, particularly at low GNP loading.
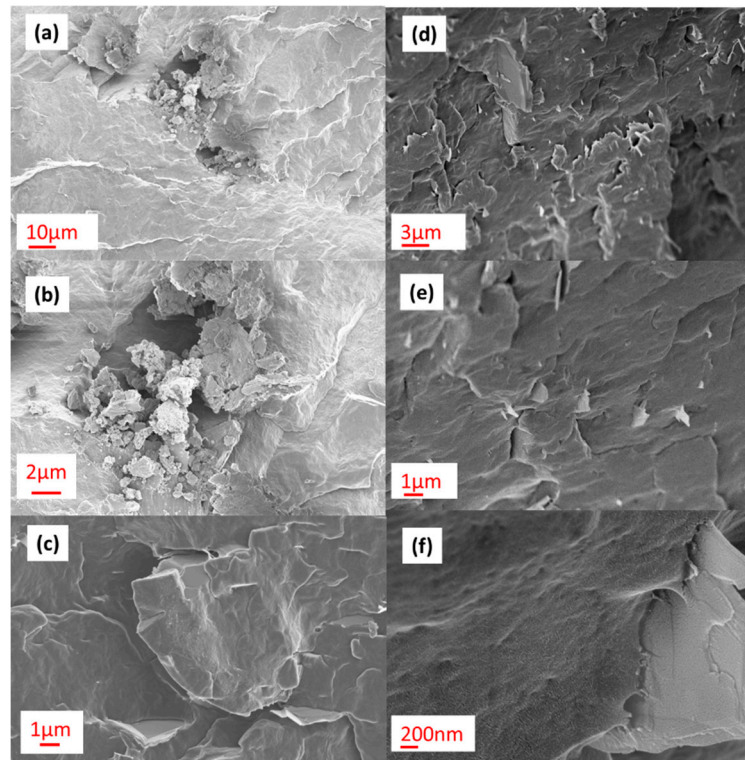
Figure 2. Scanning electron microscopy (SEM) images of a composite of PP and 5 wt % graphene nanoplatelets (GNPs) prepared by the laboratory scale extruder (**a**–**c**) and the 16-mm extruder (**d**–**f**) at different magnifications.

Irrespective of the extruder used, it became more challenging to effectively disperse the GNPs with increased loading. At 5 wt %, agglomerates of GNPs could be seen in the composite prepared by the laboratory scale extruder (Figure 2a–c). In contrast, good distribution of the GNPs in the polymer matrix was achieved when using the 16-mm extruder (Figure 2d–f) when this was examined across the length scales. The application of shear and some extensional flow in the parallel twin-screw extruder was more effective at higher GNP loadings for breaking down the GNP agglomerates during mixing in PP, with flakes of ca. 90-nm thickness observed (Figure 2f). The mixing efficiency of the two extruders influenced the crystallization behavior of PP upon addition of GNPs.

Figure 3a,b shows the XRD patterns registered for neat PP, GNPs, and their composites at different GNP loadings prepared with both extruders. The fraction of PP β-phase formed (K_β) for the composites prepared with the two different extruders as a function of GNP loading was estimated using Equation (2) [25,26]:

$$K_\beta = \frac{H_\beta}{H_\beta + H\alpha_1 + H\alpha_2 + H\alpha_3},$$ (2)

where H_β is the intensity of the β(300) peak in the XRD pattern, and $H\alpha_1$, $H\alpha_2$, and $H\alpha_3$ are the intensities of the α(100), α(040), and α(130) peaks, respectively.

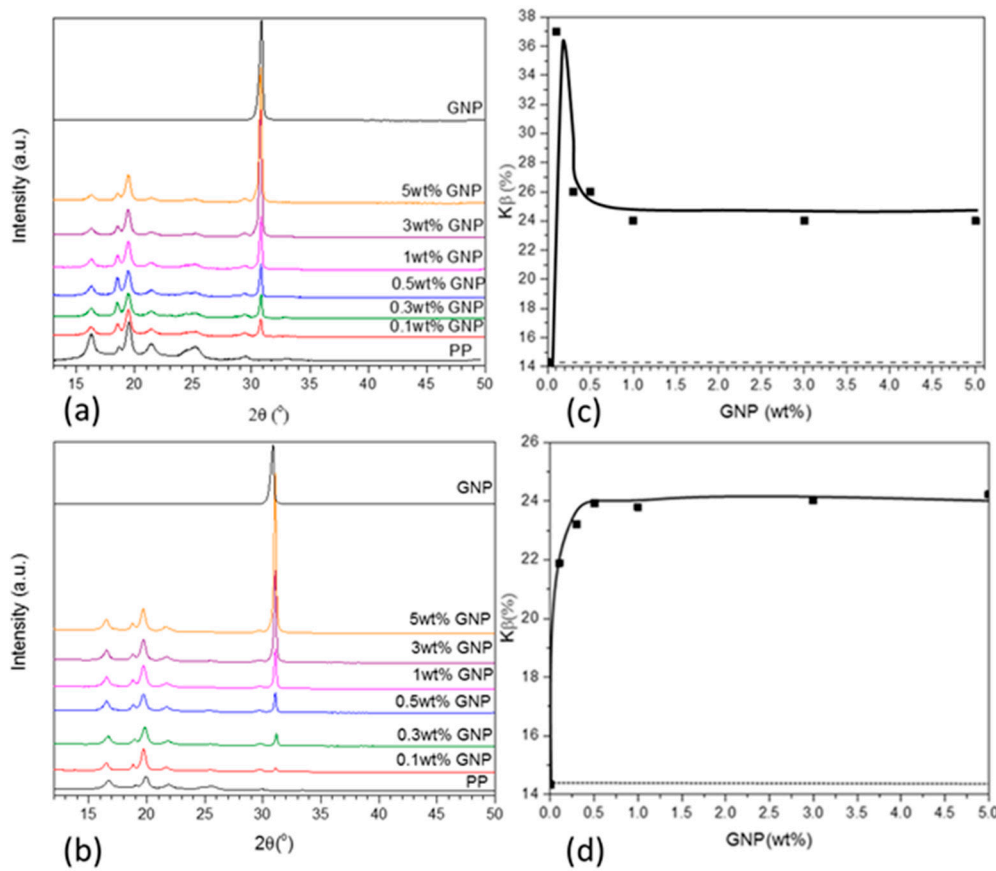**Figure 3.** XRD patterns of PP, GNPs, and their composites at different GNP loadings prepared with (**a**) a laboratory scale extruder and (**b**) a 16-mm extruder, and the fraction of β-polymorph formed (K_β) as a function of GNP loading for composites prepared by (**c**) a laboratory scale extruder and (**d**) a 16-mm extruder.

The XRD patterns reported in Figure 3a,b showed the most intense peaks for PP at 2θ = 16.5° α(100), 19.2° β(300), 20° α(040), 22° α(130), and for the GNPs at 2θ = 32° (002). The registered peaks may have been shifted compared to those reported in other studies, since the X-ray source used in this work was cobalt, $K_{\alpha 1}$ (λ) = 1.789 Å [1,27]. The intensity of the single peak in the GNP pattern at 2θ = 32° due to the crystallographic plane (002) increased with increasing GNP loading, as expected. Furthermore, the peak at 2θ = 19.2° β(300) also increased with increasing GNP content, confirming the GNPs had a β-nucleating effect on this PP, irrespective of the extruder used to prepare the composites. This observation was more evident from a plot of K_β (i.e., total fraction of β-polymorph formed) as a function of GNP content in the composite. Specifically, the K_β calculated for the composites prepared by the laboratory scale extruder had a maximum of 37% at 0.1 wt % GNP, before decreasing to 24% at 0.3 wt % GNP and then remaining constant with increasing GNP loading up to 5 wt %. In contrast, the K_β calculated for the composites prepared using the 16-mm extruder increased up to 24% at GNPs = 0.5 wt % and remained constant at higher GNP loading. The difference in K_β at low GNP loading was associated with the more effective combination of GNP dispersion and particularly distribution in the 16-mm extruder. This created a system where there was greater interfacial interaction between GNP filler particles and polymers, which in turn hindered polymer chain dynamics, thus favoring the growth of β-crystallites [1]. However, the difference in K_β was evident only for GNP ≤0.3 wt %, since at higher GNP loadings, K_β was constant at 24%, regardless of the extruder used. Clearly, above

a critical GNP loading of 0.5 wt %, further successive additions of GNP had no further effect on β-nucleation, but it hindered polymer chain dynamics. GNP particles constrained the movement and alignment of PP chains on GNP platelets, thus limiting the formation of more β-crystals, regardless of the processing method employed. There was no further β-nucleation above 0.5 wt % GNP [1], and β-crystallite growth was more sensitive to processing at low filler concentration. It should be noted that the values for K_β may have had contributions from both processing effects and the incorporation of GNPs in PP. It has also been reported previously that injection molding can facilitate the formation of β-crystals. The melt-flow realized inside the mold upon injection creates a sample with a so-called "skin-core" morphology, where the skin is subject to high shear. That is, the skin of the sample is richer in β-spherulites, whereas the core is richer in α-spherulites [7]. In Figure 2c,d, the K_β for the neat PP is 14% (dashed line), derived from both the pre-existent β-crystals in the as-received raw material and the β-crystals formed upon injection molding. Therefore, any further increase in K_β was solely due to the β-nucleation effect upon GNP addition.

The thickness of α- and β-spherulites within neat PP and its composites at different GNP loadings was calculated using Scherrer's equation [28]:

$$L_{hkl} = \frac{k\lambda}{\beta_{hkl}cos\theta_{hkl}}, \tag{3}$$

where k is a constant depending on the modeled shape of the crystallites, with values between 0.89–0.94. In this case, a k value of 0.90 was used, as pseudospherical-shaped crystallites were considered [29,30]. Here, β_{hkl} is the FWHM (i.e. the full width at half maximum in rad) of the peak corresponding to the plane (*hkl*), and θ is the diffraction angle (rad) of that plane. The thickness of the spherulites was calculated along the (040) and (300) directions related to the crystalline planes α(040) and β(300), respectively. Regardless of the extruder employed, the thicknesses were estimated as 20 nm for the β-spherulites and 10 nm for the α-spherulites, in good agreement with the Transmission Electron Microscopy (TEM) evidence reported in Reference [31]. Therefore, since K_β increased with GNP loading up to 0.5 wt % GNPs and no change in the thickness of the β-lamellae was detected, it is possible to assert that GNPs facilitated the formation of either larger lamellae or a higher number of comparable/smaller lamellae than neat PP. Table 2 summarizes the main results from the XRD analysis.

Table 2. X-ray diffraction (XRD) results summary.

Material	2θ (°)	Crystalline Planes
	16.5	α(100)
	19.2	β(300)
	20	α(040)
PP	22	α(130)
	25	α(111) + β(301)
	25.7	α(041) + α(131)
	30	α(060)
GNPs	32	(002)
K_β	24% at GNP ≥ 0.5 wt %	
L_{hkl}	β-spherulites = 20 nm (0–5 wt % GNP) α-spherulites = 10 nm (0–5 wt % GNP)	

Figure 4 shows the DSC curves for neat PP and composites of PP with different loadings of GNPs.
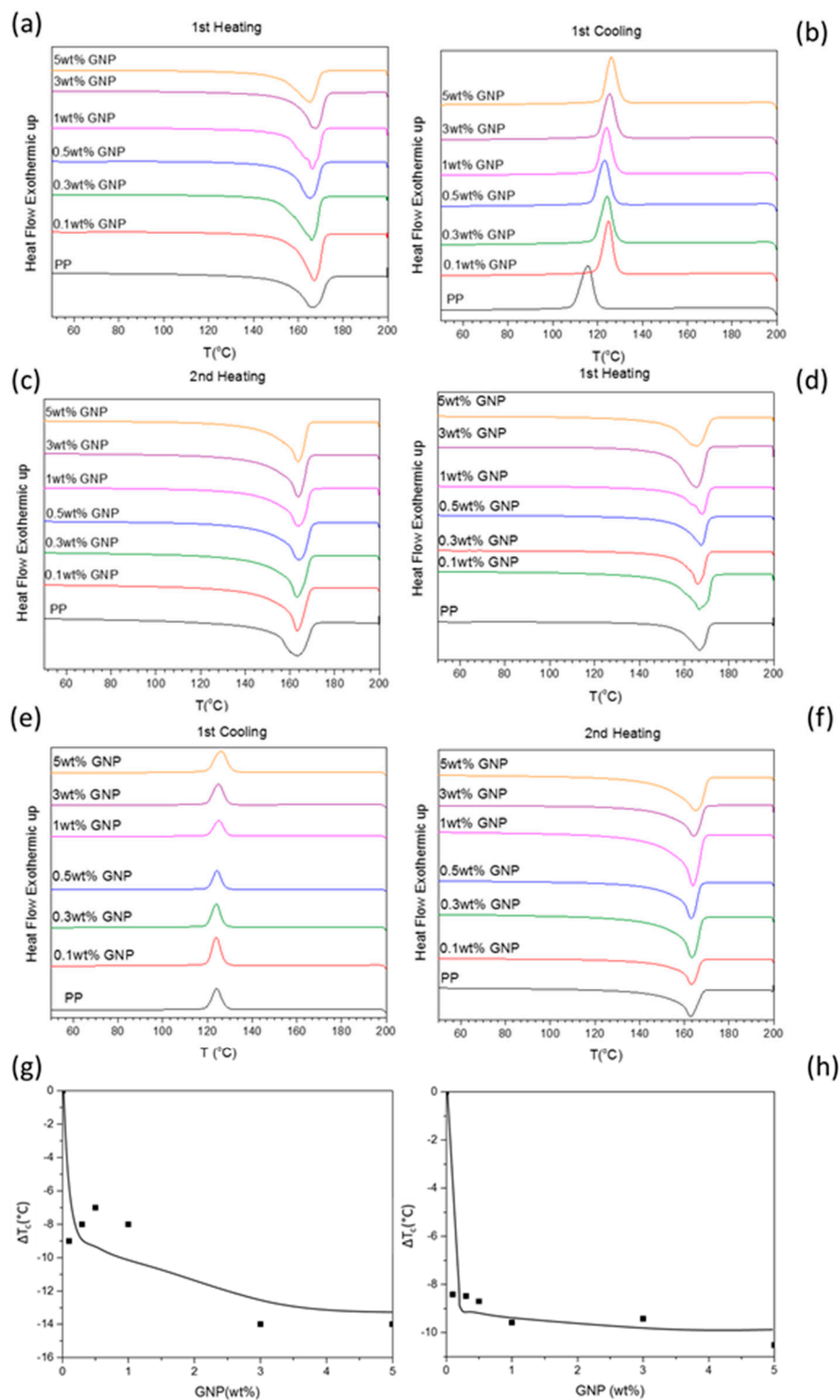
Figure 4. Differential scanning calorimetry (DSC) thermograms (heating and cooling) of composites of PP with GNPs at different loadings prepared using a laboratory scale extruder (**a**–**c**) and a 16-mm extruder (**d**–**f**) and the change in crystallization temperature (ΔT_c) as a function of GNP loading for the samples prepared with a laboratory scale extruder (**g**) and a 16-mm extruder (**h**).

The first heating thermograms (Figure 3a,d) show broad and asymmetric peaks confirming the coexistence of α-PP and β-PP crystals, as evident from the shoulder in the melting peaks at around

165.5 °C, for a GNP loading of 1 wt % for the samples prepared with the laboratory scale extruder and 0.1 wt % and 0.3 wt % for the ones prepared with the twin-screw extruder. These results suggest a change in PP polymorphism upon filler incorporation, as previously confirmed by XRD experiments. However, the β-PP polymorph content increased from the neat PP to the composites with 0.5 wt % GNPs in the XRD spectra, but a similar trend was not visible in the DSC thermograms. The reason for this discrepancy may have been due to the β−α phase transition during the first heating step in the DSC experiment, which resulted in overlapping of the peaks associated with the two polymorphic forms [3].

The first cooling thermograms (Figure 4b,e) show a shift toward higher temperatures upon GNP incorporation. In particular, T_c increased from 116 °C for the neat polymer to 132 °C and 126 °C for the composites with 5 wt % of GNPs prepared by the laboratory scale extruder and the 16-mm extruder, respectively. For composites prepared using the 16-mm extruder, the nucleation of PP upon addition of GNPs manifested as an increase in the T_c of PP, obtained for a GNP loading as low as 0.1 wt % GNP. Further increasing the loadings of GNPs did not result in more nucleation or increased T_c. This may have been associated with the even distribution of GNPs throughout the PP matrix, which constrained PP chains in a confined space delimited by filler particles, thus delaying crystallization with no further increase in T_c.

The second heating thermograms (Figure 4c,f) show broad peaks after GNP addition, yet are more symmetric than those obtained during the first heating. The controlled cooling cycle realized during the DSC measurements produced a material with a narrower crystallite size distribution compared to the material cooled by injection molding (i.e., narrower peaks should have been recorded during the second heating cycle). However, the melting peaks (T_m) of the composites in the second heating thermograms (Figure 4c,f) are as broad as the ones in the first heating curves. This was because of the β−α phase transition, which caused superimposing of the peaks related to the β−α phase transition and α-spherulite melting [10,26].

The variation in crystallization temperature (ΔT_c) recorded during the first cooling cycle (for the composites prepared with both extruders) as a function of GNP loading is reported in Figure 4g,h. A nucleating effect (ΔT_c increase) was detected for the samples prepared using both extruders: However, ΔT_c increased by up to 14 °C and 10 °C for the composites prepared using the laboratory scale and 16-mm extruder, respectively, for a GNP loading of 5 wt %. The thermal properties determined from the DSC measurements are listed in Table 3.

Table 3. Melting temperature (T_m) and enthalpy of melting (ΔH_m) from the second heating; crystallization temperature (T_c), enthalpy of crystallization (ΔH_c), and crystallinity ($X_c\%$) from the first cooling at different GNP loadings; a/b = samples prepared by 16-mm extruder/samples prepared by laboratory scale extruder.

Filler Content (wt %)	T_m (°C) Second Heating (a/b)	ΔH_m (J/g) Second Heating (a/b)	T_c (°C) First Cooling (a/b)	ΔH_c (J/g) First Cooling (a/b)	X_c (%) First Cooling (a/b)
0	170	102	116	97	47
0.1	163/163	109/101	124/125	100/97	48/47
0.3	163/163	111/106	124/124	103/99	50/47
0.5	163/164	110/103	124/123	102/95	49/45
1	164/164	109/106	125/124	99/97	47/46
3	164/164	105/101	125/130	94/94	44/44
5	165/164	102/98	126/130	93/90	43/41

In Table 3, it should be noted that the T_m of PP after the second heating cycle decreased by 5 °C when 5 wt % GNPs were added, regardless of the extruder type employed. The addition of corrugated GNP platelets [32] may have hindered the crystallization of polymer chains, especially at higher filler loadings, and thus a larger fraction of PP amorphous phase formed and T_m was depressed. This phenomenon was evident from the change in crystalline content ($X_c\%$), which increased to 50% when

GNPs were added at 0.5 wt % before decreasing to 43% when GNPs were added at loadings up to 5 wt % for the samples prepared by the 16-mm extruder. At GNPs $\leq$ 0.5 wt %, PP chains were free to crystallize in a defined geometry, which was more unlikely to happen at higher filler loadings >0.5 wt % due to the constraint realized by GNP particles [1]. Furthermore, GNP particles are thermally conductive (values of up to 7000 W/mK at room temperature have been reported [33,34]), whereas PP is a thermal insulator: Thus, a more efficient thermal dissipation was realized during the cooling cycle where GNP particles were present, forcing nearby neighbor PP chains to crystallize faster than those further away. This might have contributed to the formation of the amorphous phase. Crystallinity (%) did not follow any particular (allowing for DSC error) trend for the samples prepared with the laboratory scale extruder, perhaps due to variable and non-uniform distribution of GNPs in PP.

The values of T_c and the degree of crystallinity (%) for PP upon GNP addition revealed that the most effective nucleating effect occurred for a GNP loading of 0.5 wt %, which coincided with a saturation of the β-nucleating effect (detected from XRD measurements) (Figure 3). However, it was not possible to make informed conclusions on the β-nucleation of PP by GNPs from the DSC results, as the heating and cooling cycles resulted in an overlapping of the α–β transition and the α-polymorph crystallization during the first cooling, regardless of the type of extruder used [7,10]. ΔH_m and ΔH_c of the composites prepared using the 16-mm extruder increased upon addition of up to 0.5 wt % GNPs to PP (i.e., either thicker or larger lamellae formed during the heating and cooling cycles. When 5 wt % GNPs were added, ΔH_m and ΔH_c decreased, probably due to the increase in the amorphous phase. This trend was not detected for the samples prepared by the laboratory scale extruder due to the inhomogeneity of the samples obtained with this process (GNP agglomeration, see Figure 2).

4. Conclusions

GNPs readily nucleated the β-polymorph of PP regardless of the extruder type used to prepare their composites (i.e., laboratory scale twin-screw (conical) extruder and L/D = 16 twin-screw (parallel) extruder; see XRD). Furthermore, the mixing efficiency when preparing composites of PP and GNPs at low filler loadings (<0.5 wt %) influenced the formation of β-crystals within the PP matrix. For low GNP loadings (<0.5 wt %), dispersion and distribution of GNPs was optimal, PP chain mobility was more hindered, and the formation of the β-conformation was preferred. However, the mixing efficiency was less relevant at higher filler loadings (i.e., >0.5 wt %), since above this the GNP loading saturation of the β-nucleating effect was obtained. For that reason, no further increase of the β-fraction (K_β) at GNP loadings >0.5 wt % was observed, irrespective of the extruder used (i.e., low and high mixing efficiency; see SEM, XRD), with a saturation value of 24% (see XRD).

The nucleating effect of GNPs on PP was also confirmed from the DSC experiments, with an increase in T_c of ca. 14 °C and 10 °C for the samples prepared using the laboratory scale extruder and the 16-mm extruder, respectively. For the composites prepared with the latter, the 10 °C increase in the T_c of PP was obtained with just 0.1 wt % GNPs, and further successive increasing loadings of GNPs up to 5 wt % had little or no effect (allowing for instrument error) on T_c. The GNPs were more widely distributed within the PP matrix, and the polymer chains were more constrained, which delayed crystallization. The addition of GNPs at ca. 0.5 wt % increased the PP crystallinity to ca. 50% when using the 16-mm extruder, whereas no difference was detected when using the laboratory scale extruder, probably due to the high filler agglomeration in PP (see SEM). At filler loadings >0.5 wt %, the crystallinity decreased and a higher fraction of amorphous phase formed. Moreover, during cooling, there may have been a contribution to the crystallization behavior observed given the high thermal conductivity of GNPs, which contributed to more efficient heat dissipation in the immediate environment of the GNP particles, forcing nearby PP chains to crystallize faster than those further away, leading to a reduction in crystalline content.

References

1. Kalaitzidou, K.; Fukushima, H.; Askeland, P.; Drzal, L.T. The nucleating effect of exfoliated graphite nanoplatelets and their influence on the crystal structure and electrical conductivity of polypropylene nanocomposites. *J. Mater. Sci.* **2008**, *43*, 2895–2907. [CrossRef]

2. Saraf, R.; Porter, R.S. Considerations on the structure of smectic polypropylene. *Mol. Cryst. Liq. Cryst.* **1985**, *2*, 85–93.

3. Dai, J.; Shen, Y.; Yang, J.H.; Huang, T.; Zhang, N.; Wang, Y. Crystallization and melting behaviors of polypropylene admixed by graphene and beta-phase nucleating agent. *Colloid Polym. Sci.* **2014**, *292*, 923–933. [CrossRef]

4. Tjong, S.C.; Shen, J.S.; Li, R.K.Y. Impact fracture-toughness of beta-form polypropylene. *Scr. Metall. Mater.* **1995**, *33*, 503–508. [CrossRef]

5. KargerKocsis, J.; Varga, J.; Ehrenstein, G.W. Comparison of the fracture and failure behavior of injection-molded alpha- and beta-polypropylene in high-speed three-point bending tests. *J. Appl. Polym. Sci.* **1997**, *64*, 2057–2066. [CrossRef]

6. Varga, J.; Ehrenstein, G.W.; Schlarb, A.K. Vibration welding of alpha and beta isotactic polypropylenes: Mechanical properties and structure. *Express Polym. Lett.* **2008**, *2*, 148–156. [CrossRef]

7. Varga, J. β-modification of isotactic polypropylene: Preparation, structure, processing, properties, and application. *J. Macromol. Sci.* **2002**, *B41*, 1121–1171. [CrossRef]

8. KargerKocsis, J.; Varga, J. Effects of β-α transformation on the static and dynamic tensile behavior of isotactic polypropylene. *J. Appl. Polym. Sci.* **1996**, *62*, 291–300. [CrossRef]

9. Chen, H.B.; Karger-Kocsis, J.; Wu, J.S.; Varga, J. Fracture toughness of alpha- and beta-phase polypropylene homopolymers and random- and block-copolymers. *Polymer* **2002**, *43*, 6505–6514. [CrossRef]

10. Papageorgiou, D.G.; Chrissafis, K.; Bikiaris, D.N. β-Nucleated Polypropylene: Processing, Properties and Nanocomposites. *Polym. Rev.* **2015**, *55*, 596–629. [CrossRef]

11. Jacoby, P.; Bersted, B.H.; Kissel, W.J.; Smith, C.E. Studies on the beta-crystalline form of isotactic polypropylene. *J. Polym. Sci. B* **1986**, *24*, 461–491. [CrossRef]

12. Varga, J.; KargerKocsis, J. Rules of supermolecular structure formation in sheared isotactic polypropylene melts. *J. Polym. Sci. B* **1996**, *34*, 657–670. [CrossRef]

13. Zhang, C.G.; Hu, H.Q.; Wang, D.J.; Yan, S.; Han, C.C. In situ optical microscope study of the shear-induced crystallization of isotactic polypropylene. *Polymer* **2005**, *46*, 8157–8161. [CrossRef]

14. Nogales, A.; Hsiao, B.S.; Somani, R.H.; Srinivas, S.; Tsou, A.H.; Balta-Calleja, F.J.; Ezquerra, T.A. Shear-induced crystallization of isotactic polypropylene with different molecular weight distributions: In situ small- and wide-angle X-ray scattering studies. *Polymer* **2001**, *42*, 5247–5256. [CrossRef]

15. Somani, R.H.; Hsiao, B.S.; Nogales, A.; Srinivas, S.; Tsou, A.H.; Sics, I.; Balta-Calleja, F.J.; Ezquerra, T.A. Structure development during shear flow-induced crystallization of i-PP: In-situ small-angle X-ray scattering study. *Macromolecules* **2000**, *33*, 9385–9394. [CrossRef]

16. Moitzi, J.; Skalicky, P. Shear-induced crystallization of isotactic polypropylene melts-isothermal waxs experiments with synchrotron-radiation. *Polymer* **1993**, *34*, 3168–3172. [CrossRef]

17. KargerKocsis, J. How does "phase transformation toughening" work in semicrystalline polymers? *Polym. Eng. Sci.* **1996**, *36*, 203–210. [CrossRef]

18. Grady, B.P.; Pompeo, F.; Shambaugh, R.L.; Resasco, D.E. Nucleation of polypropylene crystallization by single-walled carbon nanotubes. *J. Phys. Chem. B* **2002**, *106*, 5852–5858. [CrossRef]

19. Gopakumar, T.G.; Page, D. Polypropylene/graphite nanocomposites by thermo-kinetic mixing. *Polym. Eng. Sci.* **2004**, *44*, 1162–1169. [CrossRef]

20. Li, B.; Zhong, W.H. Review on polymer/graphite nanoplatelet nanocomposites. *J. Mater. Sci.* **2011**, *46*, 5595–5614. [CrossRef]

21. Scaffaro, R.; Maio, A.; Lopresti, F.; Botta, L. Nanocarbons in Electrospun Polymeric Nanomats for Tissue Engineering: A Review. *Polymers* **2017**, *9*, 76. [CrossRef]

22. Scaffaro, R.; Maio, A.; Botta, L.; Gulino, E.F.; Gulli, D. Tunable release of Chlorhexidine from Polycaprolactone-based filaments containing graphene nanoplatelets. *Eur. Polym. J.* **2019**, *110*, 221–232. [CrossRef]

23. Li, Y.F.; Zhu, J.H.; Wei, S.Y.; Ryu, J.; Sun, L.Y.; Guo, Z.H. Poly(propylene)/Graphene Nanoplatelet Nanocomposites: Melt Rheological Behavior and Thermal, Electrical, and Electronic Properties. *Macromol. Chem. Phys.* **2011**, *212*, 1951–1959. [CrossRef]

24. Jose, S.; Aprem, A.S.; Francis, B.; Chandy, M.C.; Werner, P.; Alstaedt, V.; Thomas, S. Phase morphology, crystallisation behaviour and mechanical properties of isotactic polypropylene/high density polyethylene blends. *Eur. Polym. J.* **2004**, *40*, 2105–2115. [CrossRef]

25. Huo, H.; Jiang, S.C.; An, L.J.; Feng, J.C. Influence of shear on crystallization behavior of the beta phase in isotactic polypropylene with beta-nucleating agent. *Macromolecules* **2004**, *37*, 2478–2483. [CrossRef]

26. Juhasz, P.; Varga, J.; Belina, K.; Belina, G. Efficiency of beta-nucleating agents in propylene/alpha-olefin copolymers. *J. Macromol. Sci. B* **2002**, *B41*, 1173–1789. [CrossRef]

27. Yi, Q.F.; Wen, X.F.; Dong, J.Y.; Han, C.C. A novel effective way of comprising a beta-nucleating agent in isotactic polypropylene (i-PP): Polymerized dispersion and polymer characterization. *Polymer* **2008**, *49*, 5053–5063. [CrossRef]

28. Guerra V, V.; Wan, C.; Sloan, J.; Degirmenci, V.; Presvytis, D.; McNally, T. 2D Boron Nitride Nanosheets (BNNS) Prepared by High-Pressure-Homogenisation: Structure and Morphology. *Nanoscale* **2018**, *10*, 19469–19477. [CrossRef]

29. Nazarov, A.S.; Demin, V.N.; Grayfer, E.D.; Bulavchenko, A.I.; Arymbaeva, A.T.; Shin, H.J.; Choi, J.Y.; Fedorov, V.E. Functionalization and dispersion of hexagonal boron nitride (h-BN) nanosheets treated with inorganic reagents. *Chem. Asian J.* **2012**, *7*, 554–560. [CrossRef]

30. Langford, J.I.; Wilson, A.J.C. Seherrer after Sixty Years: A Survey and Some New Results in the Determination of Crystallite Size. *J. Appl. Cryst.* **1978**, *11*, 102–113. [CrossRef]

31. Li, J.X.; Cheung, W.L. On the deformation mechanisms of beta-polypropylene: 1. Effect of necking on β-phase PP crystals. *Polymer* **1998**, *39*, 6935–6940. [CrossRef]

32. Preobrajenski, A.B.; Ng, M.L.; Vinogradov, A.S.; Martensson, N. Controlling graphene corrugation on lattice-mismatched substrates. *Phys. Rev. B* **2008**, *78*, 073401. [CrossRef]

33. Pop, E.; Varshney, V.; Roy, A.K. Thermal properties of graphene: Fundamentals and applications. *MRS Bull.* **2012**, *37*, 1273–1281. [CrossRef]

34. Kim, H.S.; Bae, H.S.; Yu, J.; Kim, S.Y. Thermal conductivity of polymer composites with the geometrical characteristics of graphene nanoplatelets. *Sci. Rep.* **2016**, *6*, 26825. [CrossRef]

Fused deposition modelling (FDM) of composites of graphene nanoplatelets and polymers for high thermal conductivity: a mini-review

Valentina Guerra, Chaoying Wan and Tony McNally[*]

Abstract

Composites of polymers and the graphene family of 2D materials continue to attract great interest due their potential to dissipate heat, thus extending the in-service life of electronic and other devices. Such composites can be 3D printed using Fused Deposition Modelling into complex bespoke structures having enhanced properties, including thermal conductivity in different directions. While there are controversial opinions on the limitations of FDM for large-scale and high volume production (e.g. long production times, and expensive printers required), FDM is an innovative solution to the manufacture of small objects where effective thermal management is required and it is a valid alternative for the manufacture of (micro)-electronic components. There are few papers published on the FDM of functional composite materials based on graphene(s). In this mini-review, we describe the many technical challenges that remain to successful printing of these composites by FDM, including orientation effects, void formation, printing and feeding rates, nozzle and printing bed temperatures and the role each has in determining the thermal conductivity of any composite product made by FDM. We also compare these initial reports with those on FDM of other and related carbonaceous fillers, such as multi-walled carbon nanotubes and carbon fibre.

Keywords: 3D printing, Fused deposition modelling (FDM), Composites, Graphene nanoplatelets (GNP), Multi-walled carbon nanotubes (MWCNTs), Carbon fibre (CF), Polymers, Thermal conductivity (TC)

Introduction

The need for flexible devices driven by the exigence to fulfil requirements from an immense variety of customers is pushing technology companies towards the manufacture of soft substrates, which can be folded, rolled, are portable and environmentally friendly (e.g. recyclable, low energy consuming and low waste). Flexible nanotechnology is considered a new frontier for the production of what are by now considered "primary" goods such as smart phones, tablets and computers, in particular towards the idea to "transform" one object into another by simple folding, connecting them or rolling

them. However, when scaling down the dimensions of an object, for instance in an electronic device, the heat generated during operation can represent an issue if the material the device is made from is not able to efficiently dissipate heat. Indeed, the excess heat trapped inside the object might lead to thermal degradation [1–5].

Composites of graphene nanoplatelets (GNP) and polymers continue to arouse great interest as possible route to dissipating heat, thus extending the in-service life of the final product. In a crystalline material (regular homogeneous structure) the phonons propagates as harmonic waves and the heat dissipates with no energy loss along the thermal path. In polymeric systems, the amorphous regions generates discontinuities (heterogeneous points) where the phonons scatter, thus, disrupting the thermal

* Correspondence: ▮▮▮▮▮▮▮▮▮▮▮▮
International Institute for Nanocomposite Manufacturing (IINM), WMG, University of Warwick, Coventry CV4 7AL, UK

path [6] (and references therein). For that reason, polymers are thermal insulators yet the addition of functional fillers such as GNPs, which are thermal conductors, to polymers may allow the manufacturing of thermally conductive composites. The basic concept is to create a 3D conductive interconnecting GNP network dispersed and distributed throughout the polymer matrix so that the external thermal impulse is transferred from the polymer chains to the GNP particles throughout the composite [3, 7, 8], with negligible phonon scattering.

Fused deposition modelling (FDM) may be employed as a manufacturing process to create highly thermally conductive objects for applications such as flexible nanotechnology. To the best of our knowledge, just a few papers have been published on GNP composites with thermoplastics processed by FDM [9, 10]. In this short review, we highlight the role of FDM as an innovative process and describe the technical challenges still to be overcome to produce objects with enhanced thermal conductivity (TC) made from composites of GNP and thermoplastics by FDM.

Fused deposition model (FDM)

The ability to build up complex functional structures in a relatively fast and inexpensive manufacturing process makes additive manufacturing (AM) technology, commonly known as 3D printing, very attractive to both industry and academia [11–15]. It allows for objects to be built layer-by-layer based on Computer-Aided Design (CAD) software where the objects are modelled as a series of cross-section slices [15]. With the increase demand for light-weight materials having tailored properties suitable for specific applications, there continues to intense interest in thermoplastics processed by AM. While the AM approach has limitations currently with regard large-scale production as well as with high volumes of bulky objects (i.e. long production times and, bespoke expensive printers are required), it is an innovative solution to manufacturing micro-size objects [16, 17]. Indeed, the ability to control the size of objects on small-scale dimensions renders AM a valid alternative in application areas such as microelectronics.

To date, polymers such as acrylonitrile butadiene styrene (ABS), poly(lactic acid) (PLA), poly (caprolactone) (PCL), poly (carbonate) (PC) and poly (ether-ether-ketone) (PEEK) among others have been printed by FDM, a specific AM technique usually employed for thermoplastics [11, 18, 19]. In the FDM process with a platform moving in the direction perpendicular to the nozzles (z direction), a polymer filament is fed to the printer by a roller mechanism and addressed to a liquefier where it is heated above its glass transition temperature (T_g). The filament, still solid, acts as a piston pushing the molten polymer through the head print nozzle, which moves in

the x-y plane, thus placing the material onto a sliding platform moving in vertical direction (z). When the first layer is completed, the platform slides down allowing a second layer to be placed onto the previous one. The layers adhere to each other as they cool down and the process ends once the entire CAD-programmed structure has been built [9, 20, 21]. The FDM process is represented in Fig. 1 [22].

Requirements for FDM processing

FDM is basically an extrusion process where the homogeneity of the feedstock material as well as the thermal, mechanical and rheological properties are key features to guarantee the continuity of the printing process and the quality of the final product [10].

(Nano) filler distribution and dispersion

The printing ability of thermoplastic composites is highly affected by filler dispersion and distribution in the polymer matrix since the filler particles can agglomerate and may clog the print head nozzles causing print jam [10]. This is detrimental for continuity of the process hence the quality of the final product, since any interruption during the printing process produces poor quality products [10]. Therefore, a preliminary mixing step is required for filled thermoplastic polymers to obtain homogeneous composites. By way of example, extrusion is the most common technique used to process thermoplastics and their composites since it is relatively cheap and environment-friendly, thus very attractive to industry. In particular, twin-screw extruders are largely employed as they are effective mixer and have devolatilization capability. Moreover, the ability to modify the shape of the die makes extrusion a flexible process to manufacture material in long filaments with a desired diameter suitable for feeding to FDM printers [23–26].

It is important to highlight that filler dispersion and distribution in the polymer matrix depends on several factors. Besides processing, compatibility between composite components, surface interaction and filler particle geometry are also key factors to consider in trying to achieve homogeneous composites having enhanced chemical, physical and mechanical properties [6, 27, 28] (and references therein).

Thermal properties of the feedstock

An understanding of the thermal properties of the feedstock composite material is also essential. The material must be heated above the glass transition temperature (T_g) of the polymer matrix when extruded through the nozzles and has to remain soft during printing to guarantee a suitable flow, without degrading.

For semi-crystalline polymers, the nozzle temperature is set close to the melting temperature T_m (glass
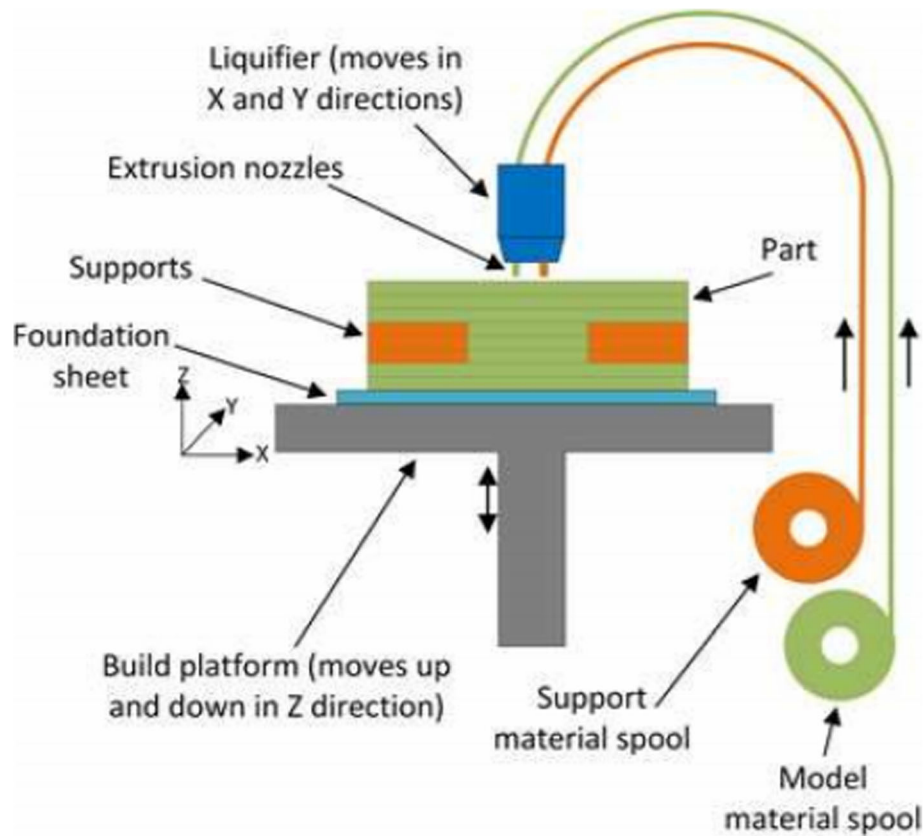
Fig. 1 Schematic diagram showing the important components of a FDM printer [20]

transition temperature (T_g), for amorphous polymers), which has not to be high, to prevent severe processing conditions. On the contrary, the degradation temperature T_{deg} should be high enough and not fall within the processing temperature range [29]. After printing, the material is cooled down below its crystallization temperature T_c (T_g in case of amorphous polymers). It is important that the printed layer is still slightly warm but not totally molten when the next layer is deposited, to allow adhesion between the layers without shape deformation. Experimental evidence has shown that for a successful printing procedure T_c and T_m should differ by about 5–10 °C [30].

Choosing the right range of temperature could be challenging when it comes to processing composites since the filler may alter the properties of the neat polymer. For instance, GNP may increase both T_g and T_m of the polymer [31–33], but not the T_{deg}, thus reducing the range of processing temperatures available. Therefore, the choice of the right polymer matrix having a sufficient high T_{deg} must also be considered for the FDM process.

To facilitate the printing procedure, the coefficient of thermal expansion (CTE) of the material has to be low. That is, neither expansion nor contraction has to occur during processing [34]. This is important to guarantee a

consistent output when the material is extruded through the nozzle and to achieve a consistent geometry when the material cools down [10].

Rheology

The rheology of the composite material is critical in controlling FDM processing in terms of product flow consistency and continuity. The viscosity of the material to be printed has to remain as constant as possible during processing, since any fluctuation with temperature and time results in inconsistent flow and the amount of material deposited while printing. Additionally, the melt viscosity has to be low enough, in the range of experimental temperatures to guarantee ease of extrusion through the nozzle head, thus avoiding high pressure at the exit, which may damage the printer. The high flowability is not only essential to effectively extrude the composite material through the nozzle, it also improves the adhesion between the printed layers when they cool down, thus minimizing the number of interfaces (voids generated between two or more touching filaments) [20, 33, 35].

Keeping composite viscosity constant within the range of operation temperatures is not easy due to the viscoelastic properties of the polymer matrix. The viscosity of

the composite may change by passing from the liquefier to the printing support (different temperatures) as well as by changing the printing speed (deformation speed). When the molten composite is extruded from the nozzles at a defined speed, it passes through high shear stress regions (i.e. walls of the nozzles), which deform the flowing material at a certain rate (shear rate). An increase or decrease of the printing speed alters the shear rate in the material being processed. As the viscosity of non-Newtonian polymers depends on the shear rate, a change in printing speeds may affect the viscosity of the filament being printed [36, 37]. It follows that only a range of optimal viscosities under the operative conditions can be defined, which depends on several parameters such as polymer matrix molecular weight, filler/polymer interaction and filler concentration [20]. For a given polymer/filler system (i.e. defined polymer molecular weight and polymer/filler thermodynamics), the viscosity increases with filler content and reaches the highest value when a percolated network of filler particles is formed in the matrix. Therefore, the main challenge to obtaining a consistent flow of thermally conductive composite during printing is to achieve percolation at low filler content to keep the viscosity within workable range. Therefore, to enhance TC, a low thermal percolation threshold is necessary in order to process the composite by FDM [38]. Different parameters play a key role in defining the optimal percolation value such as the cost of the functional material, the 3D printer specifications (e.g. maximum acceptable pressure at the nozzle head nozzle) and the polymer/filler system (i.e. the percolation threshold will change depending on the polymer/filler system).

Mechanical properties
The mechanical properties of the composites of interest must also be studied before printing. Flexibility is necessary to covert the composite material to filament before being fed in to the FDM printer, but it has to be rigid enough with high mechanical strength to draw it from the feeding system without being plastically deformed. However, brittleness is not desired, since the material cannot break while being pulled from the feeding system. Finally, the material has to be hard enough to prevent surface wearing and tearing [30]. The number of parameters to consider is significant since they depend on the polymer/filler system and the 3D printer specifications. Moreover, authors usually pay attention to the properties of the printed product and very few papers report the characteristics of the feeding material [9, 21, 39].

Influence of FDM parameters on thermal conductivity
The different parameters discussed above affect the TC of the FDM printed object although, it is not easy to compare quantitatively the effect of each parameter on the TC after FDM since the printed samples can be highly anisotropic. Moreover, the effects of voids and printing orientation, feeding and printing rates, nozzle and printing bed temperature also need to consider as they too contribute to the final TC of the printed object.

Void formation and printing direction effects on TC
The layer-by-layer deposition of the composite material is a key factor in modulating the properties of the final product since different morphologies at the interfaces are created. The molten material assumes a spherical shape when it is extruded from the printer nozzle but, it becomes more elliptical as deposited onto the substrate, thus, creating voids between adjacent printed filaments. The voids break the continuity of the material as insulating walls against thermal flow. However, if the voids are aligned along a specific direction a continuous thermal pathway is realized along the direction perpendicular to that one. For instance, when an external heat stimulus is applied to a 3D system x-y-z, a smooth constant thermal conductive flow is realized along the y-axis if the voids are all aligned in the x-z direction [9, 40]. It is possible to control the alignment of voids, hence the thermal flow, by properly tuning the printing direction as shown in Fig. 2:

It is evident that when the three layers are all printed along the y-axis, the voids are oriented in the x-z directions and a continuous pathway for thermal flow is realized along the y-axis (Fig. 2 (a) and (b)). If one of the three layers, the middle one in Fig. 2(c) is not aligned in the same direction, then that specific layer becomes a discontinuity to the heat flow and thermal conduction along y-axis is lower, see Fig. 2 (d). In particular, for the middle layer the voids are aligned along the y-axis and act as insulating "bubbles" on the thermal flow along that direction. Shemelys et al. [41] prepared both composites of ABS with graphite and with CNTs by extrusion and post-processed them by FDM. The wide distribution of the voids created upon printing resulted in poor thermal conduction of the final printed composite (TC method: hot-disk). Yunchao et al. [40] were able to improve the TC of polyamide 6 (PA6) with inclusion of 50 wt% graphite from 0.5 W/mK to 6 W/mK when printing the layers along the same direction (TC method: hot disk).

It must be highlighted that two conditions are necessary to achieve a thermal pathway along the printing direction (y in the example above). Besides the alignment of voids along the appropriate directions (x and z in the example above), filler particle alignment along the printing direction is also essential. Indeed, no thermal flow can be realised along a given axis if the conductive particles are not aligned along that axis and form an
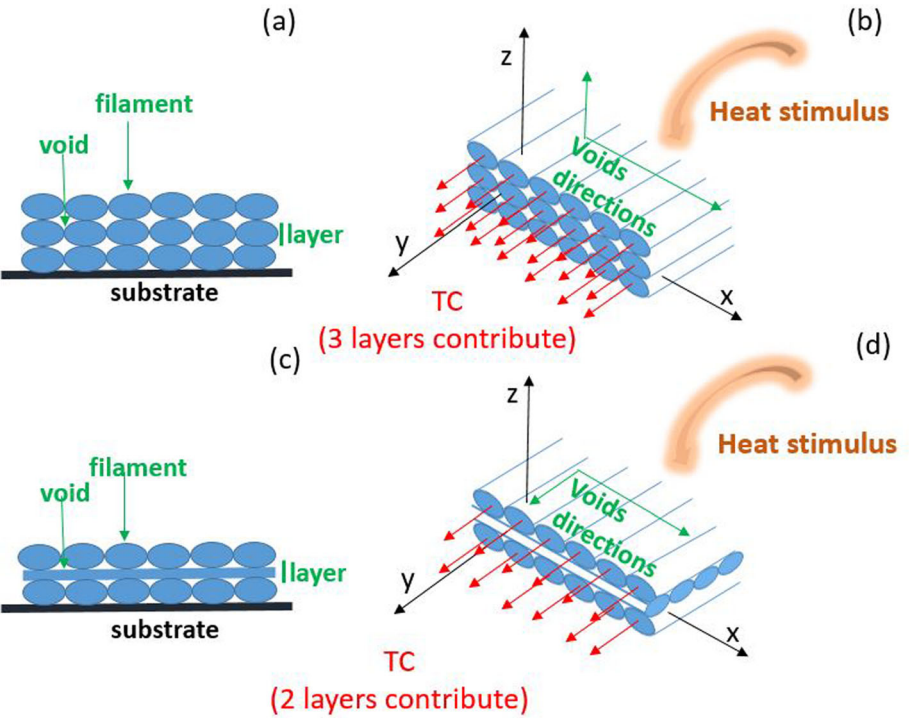
Fig. 2 Schematic diagram illustrating the effect of voids and printing direction on TC. **a**, **b** filaments printed with the same orientation generate voids perpendicularly arranged (x-z directions), with respect to the thermal conduction direction (y-direction) thus maximizing TC along the conductive axis (y-axis) and **c**, **d**, filaments printed in different orientations generate voids along the thermal conduction direction, thus reducing TC along the conductive axis (y-axis)
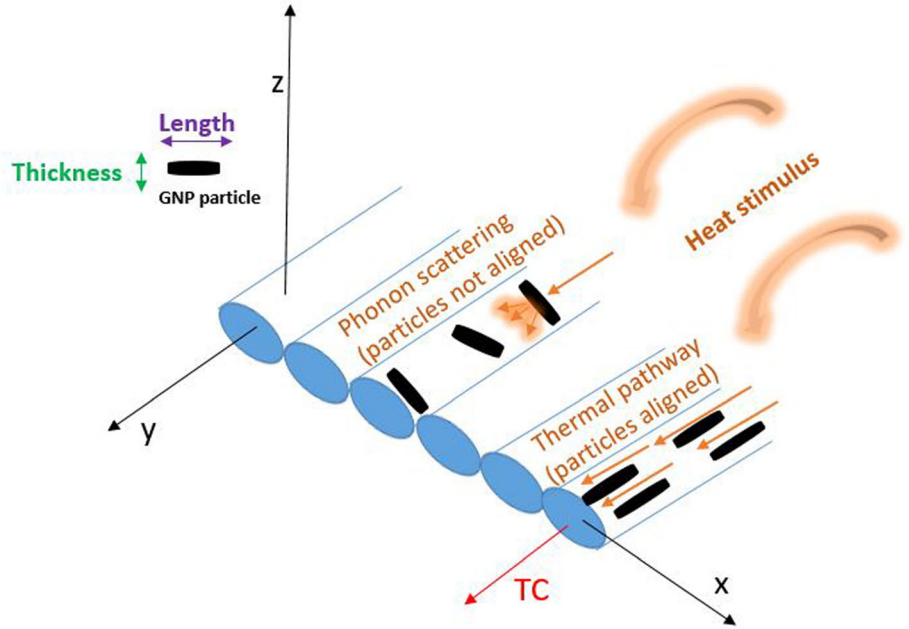

Fig. 3 Schematic illustration of thermal conduction within printed filaments of a composite of GNP and a polymer. When the GNPs are aligned along the conductive axis (y-axis) TC is detected

interconnected 3D network within the matrix (percolated structure) with negligible phonon scattering [6] (and references therein). When dealing with 2D materials like GNPs, defining the concept of particle alignment is crucial to understanding the thermal conductivity of their composites. Thermal conduction is maximum along GNP particle length and minimum along its thickness due to phonon scattering, which decreases with the reduction in the number of layers (thickness) [42–46]. It is essential for GNP composites to be conductive along a specific direction such that the GNP particles are arranged with the platelets facing along that direction [47]. Figure 3 shows a schematic of GNP particle alignment in a 3D printed layer:

When the GNP particles are aligned in a way that their length lies along the y-axis, a thermal pathway is realized, given there is a greater chance the particles are touching then TC is detected along the y-axis when a heat stimulus is applied. In contrast, if GNP particles are not properly aligned along the y-axis, phonon scattering dominates upon application of heat and no TC can be detected in they-axis direction [40].

The alignment of filler particles in the printing direction can be achieved by orienting the polymer chains [48, 49]. Polymer chains stretch as they are forced to pass through the printer head nozzle acting as an orienting pulling force onto filler particles and causing their alignment in the printing direction [9, 50]. By way of example, Zhu et al. [51] prepared composites of PA12 with GNP (6 wt%) with a co-rotating twin screw extruder (screw diameter = 20 mm; L/D ratio = 40) and post-processed them by compression moulding and FDM. The FDM samples showed higher through-in-plane TC than the compression moulded ones (1.2 W/mK and 0.2 W/mK respectively, TC method: laser flash) due to the alignment of GNP along the printing direction. Liao et al. [52] prepared composites of PA12 with carbon fibre (10 wt%) with a co-rotating twin screw extruder (screw diameter = 35 mm, L/D = 28) and fed the filament to the FDM machine. The through-in-plane TC of the final sample improved from 0.2 W/mK to 0.8 W/mK when the carbon fibres were arranged in a way to create an oriented path, thus facilitating thermal flow. However, the overall TC value was low probably due to the voids in the TC direction (TC method: laser flash). In some instances, the nature and the shape of the filler particles prevents their alignment, as reported by Dorigato et al. [53], who prepared composites of ABS with CNTs (6 wt%) by using a twin screw extruder (screw diameter = 16 mm, L/D = 25), before feeding the filaments to a FDM. The final composites had a low thermal conductivity (*ca* 0.25 W/mK) probably due to the unfavourable orientation of the CNTs in ABS after printing (TC method: laser flash).

An interconnected system of filler particles (3D network) is needed to create a conductive path. Lebedev et al. [38] prepared composites of PLA with graphite and CNTs using a mixer having counter-rotating blades before post-processing by FDM. They were able to obtain a TC of 4 W/mK for composites with 30 wt% graphite and 1 wt% CNTs (TC method: hot wire). The authors asserted that the CNT bridged the graphite particles, thus creating a three-dimensional hybrid network, which ultimately improved the TC of the final composites. Singh et al. [54]improved the TC of ABS with exfoliated graphite (22 wt%) by adding the filler to a slurry of ABS and acetone. The mixture was dried and the resulting composites (recovered as a lump of materials) was broken in to smaller pieces before extrusion. The extruded filament was printed and the final material had a TC of 17.60 W/mK (TC method: hot disk). The corresponding composites prepared by direct mixing of the same graphite with ABS had a TC of 4.65 W/mK. It appears that the sludge of ABS and acetone somehow better facilitated the formation of a conductive graphite network.

Effect of printing and feeding rates on TC

The printing rate (speed at which a filament is deposited) and feeding rates (speed at which the material is loaded into the nozzle) [20] influence the thermal conduction of the final composite in terms of filament adhesion when printing. Layers not properly adhered to each other create large interfaces (voids) which lead to phonon scattering, hence low thermal conduction [40, 41]. Overall, the higher the printing and feeding rates, the better the adhesion, hence the smaller the interfaces between the printed layers. In fact, high printing rate assures that the temperature of the extruded material is closer to the T_g (T_m for semi-crystalline materials) than the one printed using a slower printing rate, as the former results in better interactions and bonding among adjacent filaments [9, 55]. Likewise, for a given printing rate (feeding rate), high feeding rate (low printing rate) allows printing of thicker filaments, which are able to adhere better than thinner ones, even though there is a loss in geometrical resolution [9, 56].

Effect of nozzle and cooling bed temperature on TC

Nozzle temperature and the building platform temperature (cooling bed) are crucial in determining the quality of the final product since they influence the physical properties of the printing materials in terms of viscosity and crystallization [10, 20, 21]. Overall, a constant flow through the nozzle due to an appropriate viscosity guarantees a uniform material with a low concentration of defects, both on the microscopic (i.e. voids, polymer chain adhesion) and

macroscopic (i.e. constant shapes and regular amounts of deposited material) level [56]. This reduces the probability of phonon scattering hence better thermal conduction is achieved [40]. Indeed, as explained before, the presence of defects generate structural discontinuities inside of the material, thus, disrupting the phonon path, which ultimately causes phonon scattering, hence low thermal conduction [6] (and references therein). Additionally, crystallization realized under controlled conditions produces more highly crystalline materials, known to dissipate heat more efficiently [39, 57].

The nozzle temperature has to be set in a way to ensure that the composite matrix material is fully molten since the presence of un-melted polymer leads to uneven temperatures inside the nozzle, which may cause a reduction in crystallinity upon material solidification [39]. Indeed, polymer chains will not behave uniformly when they are not subject to the same temperature regime during printing, since they will experience different crystallization rates when cooling. Some chains may crystallize from very high temperatures, while others crystallize from lower temperatures, leading to a product with non-homogeneous properties [21]. Furthermore, the nozzle temperature has to guarantee an easy flow of the material as well as having a viscosity to keep shape after printing [30].

The bed temperature mainly influences the crystallization process. When the bed temperature is much lower than the nozzle temperature, the printed material will experience non-isothermal crystallization, which may reduce polymer crystallinity. By contrast, if the cooling temperature is closer to the nozzle temperature, the printing material will experience a quasi-isothermal crystallization, which ultimately may produce a highly crystalline material [21].

Figure 4 shows a schematic diagram of the optimal nozzle/ and bed temperature ranges for semi-crystalline polymers, constructed from experimental evidence reported in literature.

Summary of composites of polymers and carbonaceous additives prepared by FDM

Table 1 lists the main properties of 3D printed (FDM) of composites of polymers with carbonaceous additives reported in literature at the time of writing.

As evident from Table 1, composites of polymers and GNP/graphene printed by FDM are seldom reported and of those only a few authors focus their research on studying TC. Likewise, the electrical properties of these FDM printed composites are also rarely analysed. Gnanasekaran et al. [39], Wei et al. [10] and Yu et al. [67], prepared composites of a polymer and graphene by FDM and obtained EC values not higher than 1 S/m. The aggregation of graphene during printing caused inhomogeneities, poor (nano) filler dispersion and distribution, which ultimately resulted in poorly performing FDM printed composites. Gnanasekaran et al. [39] also studied the properties of composite of PBT and MWCNTs and the final printed composites displayed an increase in EC up to 10 S/m. The author assigned the improved performance to the alignment of the MWCNTs upon printing.

Reports on CF based composites prepared by FDM are much more common and the natural alignment of CF along the printing filaments confers the final products with exceptional mechanical properties (see Table 1). However, GNP is a valid alternative to manufacturing functional materials by FDM as proven by Dingchun et al. [51], who prepare composites of PA12 and GNP (6 wt%) showing similar mechanical properties to the composites of PA12 with CF (6 wt%) prepared by Liao *et. al.* [52] Indeed, the concurrent alignment of the voids and GNP particles in the tensile direction resulted in an increase in Young's modulus of *ca* 50% with respect to the neat PA12 and an increase of 7% compared to the
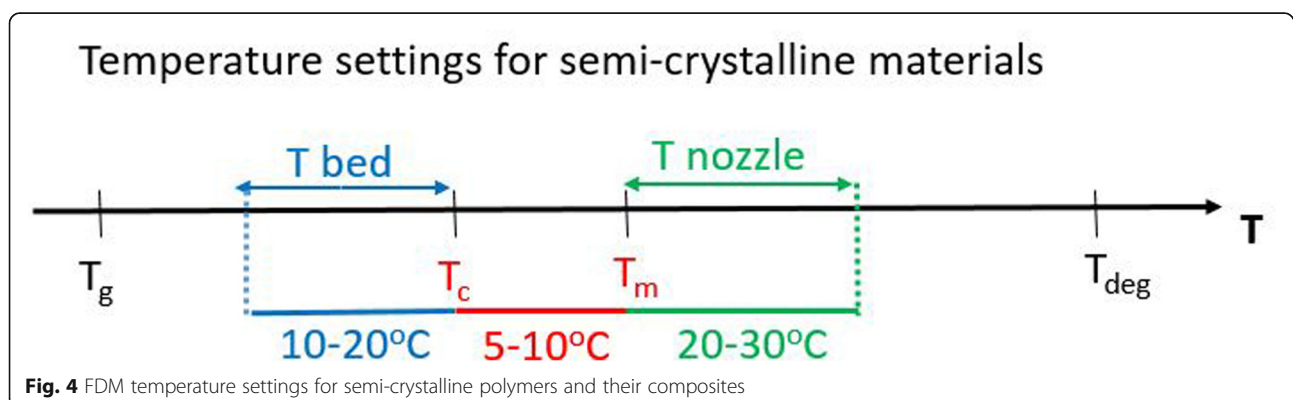

Fig. 4 FDM temperature settings for semi-crystalline polymers and their composites

Table 1 Main properties of composites of polymers with carbonaceous additives prepared by FDM as reported in literature. [a] CF: carbon fibre, [b] CNT/MWCNTs: carbon nanotube/multi-walled carbon nanotubes, [c] CB: carbon black, [d] PEI: Poly(ether imide)

Matrix	Filler	Properties	References
Thermal properties			
ABS	[a]CF(13 wt%)	CTE(μm/m°C):9.85; TC (W/mK):0.4 (in-plane)	[58]
PLA	[b]Graphite (30 wt%)/CNT(1 wt%)	TC(W/mK):5	[38]
PLA	Graphene	ΔT(°C): 0.5; (Voltage applied: 10 V, time: 300 s)	[59]
PA6	Graphite (50 wt%)	TC(W/mK):5.5 (through-plane)	[40]
ABS	CNT(8 wt%)	ΔT(°C):250; (Voltage applied:24 V,10s)	[53]
ABS	Graphite (4.3vol%) CF(1.7vol%)	TC(W/mK):0.4 (in-plane) TC(W/mK):0.2 (in-plane)	[41]
ABS	Graphite (21.7w%)	TC(W/mK):17.60	[54]
PA12	GNP(10 wt%)	TC(W/mK):1.2	[51]
PA12	CF(10 wt%)	TC(W/mK):0.8	[52]
Electrical properties			
ABS	CNT (10 wt%)	EC (S/cm):3.3×10^{-6}	[60]
PLA	[b]MWCNT (10 wt%)	EC (S/cm):6×10^3	[61]
PCL	[c]CB (15 wt%)	Electrical resistance (kΩ): 19 (60s)	[62]
Epoxy	CNF(4 wt%)	Surface resistivity (Ω/sq.):1000; Volume resistivity (Ωcm):1000	[63]
TPU	MWCNT (3 wt%)	Relative resistance (R/R0):6 (tensile strain: 50%, 20 cycles)	[64]
PLA	CF(20 wt%)	Relative resistance (R/R0):3.5 (tensile strain:1.7%, stress: 20 MPa) Relative resistance (R/R0):1.2 (tensile strain:5%, Force (N):100)	[65]
ABS	CNT(8 wt%)	Electrical resistivity (Ωcm):1	[53]
[d]PEI	MWCNT	Resistance (Ω):15.37 (220 s under cyclical mechanical loading)	[66]
PBT	CNT(0.04vol%)	EC(S/m):10	[39]
	Graphene (0.09vol%)	EC(S/m):1	
ABS	Graphene (8 wt%)	EC(S/m):0.01	[10]
PLA	Graphene (8 wt%)	EC(S/m):1	[67]
	CNT(8 wt%)	EC(S/m):1	
ABS	CB(1.32vol%)	EC(S/cm):10^{-8}	[68]
	CNT(1.38vol%)	EC(S/cm):0.01	
ABS	CB(15 wt%)	Resistivity (Ω·m):120@1 Hz	
PLA	GNP(8 wt%)	Capacitance (μF): 28@0.5 μA	[69]
PMMA	GNP (10 wt%)	EC(S/cm):14.2	[70]
Mechanical properties			
ABS	MWCNT (10 wt%)	E (MPa): 1600; σ(MPa): 56; ε(%): 5	[60]
ABS	CNT (3 wt%) + CF	E (MPa): 3400	[71]
PLA	CF (6.6 vol%)	E (MPa): 20000; σ(MPa):180; ε(%): 1	[72]
ABS	CF (10 wt%)	E (MPa):7900; σ(MPa):37.4; ε(%): 5	[73]
PLA	Graphene (0.5 wt%)	E (MPa):2000; σ(MPa):40; ε(%): 25	[74]
PLA	MWCNT (0.5 wt%)	E (MPa):2500; σ(MPa):40; ε(%): 25	[74]
ABS	CF(7.5 wt%)	E (MPa):2500; σ(MPa):25; Ductility (%): 3	[75]
PLA	CF (13 wt%)	E increase (%):350; σ(MPa):200	[76]
ABS	CF (30 wt%)	E (MPa):13000; σ(MPa):60	[77]
Epoxy	CF	E (GPa):161.4;σ(MPa):793	[78]
		Flexural modulus (GPa):144; Flexural strength (MPa):202	

Table 1 Main properties of composites of polymers with carbonaceous additives prepared by FDM as reported in literature. [a] CF: carbon fibre, [b] CNT/MWCNTs: carbon nanotube/multi-walled carbon nanotubes, [c] CB: carbon black, [d] PEI: Poly(ether imide) *(Continued)*

Matrix	Filler	Properties	References
PLA	CF	Flexural modulus (GPa): 10; Flexural strength (MPa):180 ($T_{liquefier}$ = 210 °C, layer thickness = 0.5 mm)	[20]
PLA	Modified CF	Flexural modulus (MPa):91; Flexural strength (MPa):156	[79]
Epoxy	SiC/C (31vol%)	E (GPa):24.5; σ(MPa):66.2	[80]
Nylon	CF (34.5vol%)	σ (MPa):500; ε(%): 1.7 (6CF layers)	[81]
ABS	CF(1.4vol%)	σ (kN):1.5; Stroke (mm):4.5	[82]
TPU	MWCNT(3 wt%)	σ(MPa):3; ε(%):50 (20 cycles, linear biaxial sensor)	[64]
ABS	CF(13 wt%)	E (MPa):71; σ(MPa):7	[58]
PLA	CF(20 wt%)	σ(MPa):32.5; ε(%): 1.7	[65]
		Flexural strength (MPa):68.2; Flexural strain(%):5	
PEI	CNT	σ(MPa):120; ε(%):5	[66]
PLA	Graphene(8 wt%)	σ(MPa):60; ε(%):4	[50]
ABS	Graphene (8 wt%)	E (MPa):3500;σ(MPa):2700	[9]
ABS	CF(18 wt%)	σ(MPa):58.6	[30]
PLA	Recycled CF	E (GPa):20;σ(MPa):250	[83]
		Flexural modulus (GPa):13;Flexural strength (MPa):250	
ABS	CNT(8 wt%)	σ(MPa):37;ε(%):7	[53]
ABS	Graphite(4.3vol%)	σ(MPa):37.55; ε(%):6	[41]
	CF(1.7vol%)	σ(MPa):35.73; ε(%):10	
PA12	GNP(6 wt%)	E (MPa):2252; σ(MPa):41; ε(%):12	[51]
PA12	CF(6 wt%)	E (MPa):2700; σ(MPa):80; ε(%):5	[52]
PLA	Graphene	E (GPa):4; Nanohardness (MPa):146	[84]
		Wear volume loss (mm^3):3.5 (20 N, 30s)	
		Creep displacement (μm):0.3 (25mN, 1 s)	
PLA	Graphene (2 wt%)	E (MPa):900; σ(MPa):60	[67]
		Flexural modulus (MPa):3070; Flexural strength (MPa):94.2	
	CNT (2 wt%)	Flexural modulus (MPa):2620; Flexural strength (MPa):82	
PA6	CF(25vol%)	E (GPa):53	[85]
PEEK	MWCNT(5vol%)	Ultimate strength (MPa): 105	[86]
PA6	CF(40vol%)	E (GPa):68 ± 6; σ(MPa):700 ± 70	[87]
TPU/ PLA	GO(5 wt%)	E (MPa): 55	[88]
PEEK	CF(28vol%)/GNP(5vol%)	E (GPa): 7	[89]
EVA	Graphite (40 wt%)	Compressive strength (MPa): 30; Hardness (Shore D): 28	[90]
PLA	GNP(10 wt%)	E:2.4 GPa; σ: 40 MPa	[91]
ABS	MWCNT(8 wt%)	E (MPa): 2150 ± 80; σ(MPa): 46.9 ± 0.9; ε(%): 4.0 ± 0.7	[92]
PLA	GNP(12 wt%)	E (GPa): 3.5 ± 0.048 ± 0.257	[93]

correspondent compression moulded sample. The value of E reported (2252 MPa) is close to that obtained by Liao *et. al* [52] (2700 MPa). In some instances, a combination of CF and GNP can improve the mechanical properties of the matrix they are added to. Indeed, Papageorgiou *at al* [89]. increased the value of E for PEEK by

adding GNP (5 vol%) and CF (28 vol%) and the authors proposed that the high aspect ratio of both CF and GNP limited the mobility of PEEK chains, thus increasing the stiffness. GNP has also been added to biocompatible polymers such as PLA and printed by FDM. By way of example, Prashantha et al. [91] improved the mechanical

properties of PLA by preparing composites with GNP (10 wt%) by FDM and the authors proposed that this improvement was derived from the compatibility between GNP and PLA, which in turn facilitated GNP dispersion in the matrix. Composites of PLA with GNP were also used to prototype capacitors manufactured by FDM. Foster et al. [69] added GNP (8 wt%) to PLA and manufactured a pseudo-capacitor by FDM which had a capacitance of *ca* 28 µF (under a current of 0.5 µA). The authors asserted that even though the value obtained was not as competitive as current capacitors on the market, FDM presents an alternative route to prepare such electronic devices.

Other authors have explored the viability of FDM to print composites of polymer blends and modified GNP. Chen et al. [88] prepared composites of TPU/PLA with GO (5 wt%) and they obtained improvement mechanical properties which the authors ascribed to reduced porosity of the printed part achieved by modulating the printing direction of the filaments.

Conclusions

FDM may be employed to print composites of thermoplastics with GNP and other carbonaceous fillers (e.g. MWCNTs, CF), in order to obtain objects with improved TC and potentially other properties. To the best of our knowledge, just a few papers have been published on FDM of composites of polymers and graphene(s), yet the concept is routinely proposed as a route to manufacture products that not only could have enhanced properties but also have functional properties in different directions in the same product, e.g. in battery applications. The technical challenges to successfully 3D print filled polymers by FDM still remain and, there is an immediate need for both innovative solutions and systematic studies that address these challenges.

In this mini-review, we have discussed the key parameters that must be considered to successfully produce a product from GNP filled polymers by FDM, with the target of achieving enhanced TC. Ostensibly, FDM is an extrusion process where the homogeneity of the feedstock material and the thermal, mechanical and rheological properties of the composite material are key to ensuring continuity of the printing process and the quality and functionality of the final product.

Furthermore, there are a number of FDM processing parameters that must be considered and which ultimately will determine the TC value obtained, including the presence of voids, orientation effects, feeding and printing rates, nozzle and printing bed temperatures. The voids break the continuity of the printing material acting as insulating walls against thermal flow. However, if the voids are aligned in a specific direction a continuous thermal pathway is realized in the perpendicular

direction. The printing and feeding rates influence the thermal conduction of the final composite in terms of filament adhesion during printing the material. Layers not properly adhered to each other create large interfaces which lead to phonon scattering, hence low thermal conduction. Overall, the higher the printing and feeding rates, the better the adhesion, hence the smaller the interfaces between printed layers. Nozzle temperature and cooling bed temperature are crucial in determining the quality of the final product since they influence the physical properties (i.e. melt viscosity and crystallization of the composite material. When the composite matrix is a semi-crystalline polymer, the nozzle temperature should be set close to the T_m (up to *ca* 30 °C higher), while the bed temperature should be set *ca* 10-20 °C below the T_c.

While the published literature on FDM of carbon fibre based composites is more common and to a lesser extent on CNTs, FDM of GNP based composites is a viable alternative to preparing bespoke complex products having functional properties. Indeed, the alignment of GNP in the printing direction will lead to products with combinations of remarkable properties and in different directions if required, e.g. thermal and mechanical properties. However, if the hype is to be overcome a more fundamental understanding of processing-structure-property relationships is required if GNP filled polymers can be printed by FDM in to useful products.

Authors' contributions
TMcN conceived the topic; TMcN and VG drafted the article; TMcN, VG and CW reviewed and corrected the article. The authors read and approved the final manuscript.

Availability of data and materials
All data generated or analyzed during this study are included in this published article.

Competing interests
The authors declare that they have no competing interests.

References

1. D. Akinwande, N. Petrone, J. Hone, Nat. Commun. **5** (2014)
2. H.Y. Chang, S.X. Yang, J.H. Lee, et al., ACS Nano **7**, 6 (2013)
3. S. Das, R. Gulotty, A.V. Sumant, et al., Nano Lett. **14**, 5 (2014)
4. G.H. Lee, Y.J. Yu, X. Cui, et al., ACS Nano **7**, 9 (2013)
5. J. Lee, T.J. Ha, H.F. Li, et al., ACS Nano **7**, 9 (2013)
6. V. Guerra, C.Y. Wan, T. McNally, Prog. Mater. Sci. **100** (2019)
7. W. Zhou, S. Qi, H. Li, et al., Thermochim. Acta **452**, 1 (2007)
8. S.G. Mosanenzadeh, H.E. Naguib, Compos. Part B-Eng. **85** (2016)
9. S. Dul, L. Fambri, A. Pegoretti, Composites Part A-Appl. Sci. Manufacturing **85** (2016)
10. X.J. Wei, D. Li, W. Jiang, et al., Sci. Rep. **5** (2015)
11. R.D. Farahani, M. Dube, D. Therriault, Adv. Mater. **28**, 28 (2016)
12. S. Shaffer, K.J. Yang, J. Vargas, et al., Polymer **55**, 23 (2014)
13. S.H. Masood, W.Q. Song, Mater. Des. **25**, 7 (2004)
14. M. Nikzad, S.H. Masood, I. Sbarski, Mater. Des. **32**, 6 (2011)
15. A. de Leon, Q.Y. Chen, N.B. Palaganas, et al., React. Funct. Polym. **103** (2016)
16. S.Y. Wu, C. Yang, W.Y. Hsu, et al., Microsyst. Nanoengineering **1** (2015)
17. R.D. Sochol, E. Sweet, C.C. Glick, et al., Microelectron. Eng. **189** (2018)
18. K. Fu, Y.G. Yao, J.Q. Dai, et al., Adv. Mater. **29**, 9 (2017)
19. H. Ota, S. Emaminejad, Y.J. Gao, et al., Adv. Mat. Technol. **1**, 1 (2016)
20. X.Y. Tian, T.F. Liu, C.C. Yang, et al., Composites Part A-Appl. Sci. Manufacturing **88** (2016)
21. C. Yang, X. Tian, D. Li, et al., J. Mater. Process. Technol. **248** (2017)
22. A.W. Gebisa, H.G. Lemu, Materials **11**, 4 (2018)
23. S. Hansch, R. Socher, D. Pospiech, et al., Compos. Sci. Technol. **72**, 14 (2012)
24. K.B. Nie, X.J. Wang, L. Xu, et al., Mater. Des. **36** (2012)
25. T. Sakai, Polimery **58**, 11–12 (2013)
26. T. Villmow, P. Potschke, S. Pegel, et al., Polymer **49**, 16 (2008)
27. A.K. Naskar, J.K. Keum, R.G. Boeman, Nat. Nanotechnol. **11**, 12 (2016)
28. A.J. McNamara, Y. Joshi, Z.M.M. Zhang, Int. J. Therm. Sci. **62** (2012)
29. E. Bassoli, A. Gatto, L. Iuliano, et al., Rapid Prototyp. J. **13**, 3 (2007)
30. W. Zhong, F. Li, Z. Zhang, et al., Mater. Sci. Eng. A **301**, 2 (2001)
31. T. Ramanathan, A.A. Abdala, S. Stankovich, et al., Nat. Nanotechnol. **3**, 6 (2008)
32. T. Ramanathan, S. Stankovich, D.A. Dikin, et al., J. Polymer Sci. Part B-Polymer Phys. **45**, 15 (2007)
33. S. Vadukumpully, J. Paul, N. Mahanta, et al., Carbon **49**, 1 (2011)
34. C. Heo, H.G. Moon, C.S. Yoon, et al., J. Appl. Polym. Sci. **124**, 6 (2012)
35. Q.F. Xu, B. Mondal, A.M. Lyons, ACS Appl. Mater. Interfaces **3**, 9 (2011)
36. M. Faes, H. Valkenaers, F. Vogeler, et al., in *3rd Cirp Global Web Conference - Production Engineering Research Advancement beyond State of the Art*, ed. by A. Caggiano, vol 28 (2015), p. 76
37. H.W. Lin, C.P. Chang, WH Hwu *et al.* J. Mater. Process. Technol. **197**, 1–3 (2008)
38. S.M. Lebedev, O.S. Gefle, E.T. Amitov, et al., Polym. Test **58** (2017)
39. K. Gnanasekaran, T. Heijmans, S. van Bennekom, et al., Appl. Mater. Today **9** (2017)
40. Y.C. Jia, H. He, Y. Geng, et al., Compos. Sci. Technol. **145** (2017)
41. C. Shemelya, A. De La Rosa, A.R. Torrado, et al., Addit. Manuf. **16** (2017)
42. E. Pop, V. Varshney, A.K. Roy, MRS Bull. **37**, 12 (2012)
43. J.D. Renteria, D.L. Nika, A.A. Balandin, Appl. Sci.-Basel **4**, 4 (2014)
44. A.A. Balandin, Nat. Mater. **10**, 8 (2011)
45. J.W. Jiang, B.S. Wang, J.S. Wang, et al., J. Phys. Condens. Matter **27**, 8 (2015)
46. G. Chen, Int. J. Therm. Sci. **39**, 4 (2000)
47. C. Yuan, B. Xie, M. Huang, et al., Int. J. Heat Mass Transf. **94** (2016)
48. P. Zhao, K. Wang, H. Yang, et al., Polymer **48**, 19 (2007)
49. E.T. Thostenson, T.W. Chou, J. Phys. D-Appl. Phys. **35**, 16 (2002)
50. D. Zhang, B.H. Chi, B.W. Li, et al., Synth. Met. **217** (2016)
51. D.C. Zhu, Y.Y. Ren, G.X. Liao, et al., J. Appl. Polym. Sci. **134**, 39 (2017)
52. G. Liao, Z. Li, Y. Cheng, et al., Mater. Des. **139** (2018)
53. A. Dorigato, V. Moretti, S. Dul, et al., Synth. Met. **226** (2017)
54. R. Singh, G.S. Sandhu, R. Penna, et al., Materials **10**, 8 (2017)
55. B.G. Compton, B.K. Post, C.E. Duty, et al., Addit. Manuf. **17** (2017)
56. O.S. Carneiro, A.F. Silva, R. Gomes, Mater. Des. **83** (2015)
57. N. Burger, A. Laachachi, M. Ferriol, et al., Prog. Polym. Sci. **61** (2016)
58. L.J. Love, V. Kunc, O. Rios, et al., J. Mater. Res. **29**, 17 (2014)
59. Y. Zhuang, W.T. Song, G. Ning, et al., Mater. Des. **126** (2017)
60. J. Jyoti, S. Basu, B.P. Singh, et al., Composites Part B-Engineering **83** (2015)
61. G. Postiglione, G. Natale, G. Griffini, et al., Composites Part A-Appl. Sci. Manufacturing **76** (2015)
62. S.J. Leigh, R.J. Bradley, C.P. Purssell, et al., PLoS One **7**, 11 (2012)
63. J. Czyzewski, P. Burzynski, K. Gawel, et al., J. Mater. Process. Technol. **209**, 12–13 (2009)
64. J.F. Christ, C.J. Hohimer, N. Aliheidari, et al., in *Sensors and Smart Structures Technologies for Civil, Mechanical, and Aerospace Systems 2017*, ed. by J. P. Lynch, vol 10168 (2017)
65. X.H. Yao, C.C. Luan, D.M. Zhang, et al., Mater. Des. **114** (2017)
66. JM Gardner, G Sauti, JW Kim *et al.*, Additive Manufacturing 12, (2016)
67. W.W. Yu, J. Zhang, J.R. Wu, et al., J. Appl. Polym. Sci. **134**, 15 (2017)
68. D.P. Schmitz, L.G. Ecco, S. Dul, et al., Materials Today Communications 15 (2018)
69. C.W. Foster, M.P. Down, Y. Zhang, et al., Sci. Rep. **7** (2017)
70. V.B. Mohan, B.J. Krebs, D. Bhattacharyya, Materials Today Communications **17** (2018)
71. G Tsiakatouras, E Tsellou, and C Stergiou, 12, (2014)
72. R. Matsuzaki, M. Ueda, M. Namiki, et al., Sci. Rep. **6** (2016)
73. M.L. Shofner, K. Lozano, F.J. Rodriguez-Macias, et al., J. Appl. Polym. Sci. **89**, 11 (2003)
74. M. Plymill, Greeley, et al., *University of Tennessee Honors Thesis Projects* (2016)
75. F.D. Ning, W.L. Cong, J.J. Qiu, et al., Composites Part B-Engineering **80** (2015)
76. T. Hofstätter, W.I. Gutmann, T. Koch, et al., *Proceedings of ASPE Summer Topical Meeting 2016: Dimensional Accuracy and Surface Finish in Additive Manufacturing ASPE – The American Society for Precision Engineering* (2016)
77. H.L. Tekinalp, V. Kunc, G.M. Velez-Garcia, et al., Compos. Sci. Technol. **105** (2014)
78. W.F. Hao, Y. Liu, H. Zhou, et al., Polym. Test. **65** (2018)
79. N.Y. Li, Y.G. Li, S.T. Liu, J. Mater. Process. Technol. **238** (2016)
80. B.G. Compton, J.A. Lewis, Adv. Mater. **26**, 34 (2014)
81. K. Fvd, Y. Koga, A. Todoroki, et al., Open J. Compos. Mater. **6** (2016)
82. K.I. Mori, T. Maeno, Y. Nakagawa, in *11th International Conference on Technology of Plasticity, Ictp 2014*, ed. by T. Ishikawa, K. I. Mori, vol 81 (2014), p. 1595
83. X.Y. Tian, T.F. Liu, Q.R. Wang, et al., J. Clean. Prod. **142** (2017)
84. J. Bustillos, D. Montero, P. Nautiyal, et al., Polym. Compos. **39**, 11 (2018)
85. T.F. Liu, X.Y. Tian, M.Y. Zhang, et al., Composites Part A-Appl. Sci. Manufacturing **114** (2018)
86. S. Berretta, R. Davies, Y.T. Shyng, et al., Polym. Test. **63** (2017)
87. J. Justo, L. Tavara, L. Garcia-Guzman, et al., Compos. Struct. **185** (2018)
88. Q.Y. Chen, J.D. Mangadlao, J. Wallat, et al., ACS Appl. Mater. Interfaces **9**, 4 (2017)
89. D.G. Papageorgiou, M.F. Liu, Z.L. Li, et al., Compos. Sci. Technol. **175** (2019)
90. N. Kumar, P.K. Jain, P. Tandon, et al., J. Braz. Soc. Mech. Sci. Eng. **40**, 4 (2018)
91. K. Prashantha, F. Roger, J. Macromol. Sci. Part A-Pure Appl. Chem. **54**, 1 (2017)
92. S. Dul, L. Fambri, A. Pegoretti, Nanomaterials **8**, 1 (2018)
93. T. Batakliev, V. Georgiev, E. Ivanov, et al., J. Appl. Polym. Sci. **136**, 13 (2019)